The Evolution of a Turbulent Isothermal Jet in a Uniform Turbulent External Coflow

by

William James Van Heyst

A thesis
presented to the University of Waterloo
in fulfilment of the
thesis requirement for the degree of
Doctor of Philosophy
in
Mechanical Engineering

Waterloo, Ontario, Canada, 1997

The University of Waterloo requires the signatures of all persons using or photocopying this thesis. Please sign below, and give address and date.

Abstract

An experimental investigation is presented that examines the effects of external turbulence on the development and evolution of a turbulent isothermal coflowing jet. Three intensities of external turbulence, two different jet model diameters, and two initial jet velocities were combined to obtain data for twelve different experimental conditions. The measured instantaneous velocity data resulting from these experiments were statistically processed to obtain mean velocities, Reynolds normal and shear stresses, integral length scales, and energy spectra both within the jet and in the external flow. The experimental results indicate that the presence of external turbulence begins to affect the development of a jet in the range of 15 to 25 momentum radii downstream from the jet exit by enhancing the diffusion of jet momentum.

A new entrainment velocity function is developed for use in an integral model to predict the effects of external turbulence on the evolution of a coflowing jet. The resulting predictions are compared with experimental data and yield accurate predictions for the radial spread and velocity decay for a jet in a laminar external coflow while yielding relatively good agreement for a jet in a turbulent external coflow.

Acknowledgements

The research that is contained within the covers of this thesis could not have been completed without the aid and moral support of a great many people as well as the financial support of the Natural Science and Engineering Research Council of Canada (NSERC).

To begin, I wish to express my sincere thanks to my supervisors, Dr. Al Strong and Dr. Pete Slawson, for their continual guidance, supervision, and encouragement throughout the course of this research. Special thanks are also extended to Mr. Gord Hitchman and to Ms. Anita Fonn for their great assistance.

I am also indebted to my fellow graduate students for not only their friendship but also for their insight. I especially wish to thank Duncan Phillips, Jake Friedman, Mahmud Ashrafizaadeh, Gord Poole, John Stokes, Steve Dajka, Chris Ireland, and Dr. Tony Straatman.

I also owe a dept of thanks to my family and friends outside the university who helped see me through graduate school. Above all, I would like to thank my wife, Sandra, and my daughter, Aidan, for their continual patience and emotional support in this endeavour.

"I don't know what I may seem to the world, but as to myself, I seem to have been only like a boy playing on the seashore and diverting myself now and then finding a smoother pebble or a prettier shell, whilst the great ocean of truth lay all undiscovered before me."

Sir Isaac Newton, 1642-1727

Dedicated to the memory of my father

Contents

List of Tables

List of Figures

Nomenclature

a	minor diameter of the elliptical control volume
b	grid bar width or radial length scale of the jet
B	fixed or bias errors
B_e	resolution bandwidth
B_r	half-power point bandwidth
c, c_1, c_2	constants as defined in the text
C_{uv}	correlation coefficient for the Reynolds shear stress
d_j	diameter of the model jet
E_{rr}	radial or transverse power spectral density function
E_{xx}	streamwise power spectral density function
f	frequency
f_c	reference clock frequency
f_D	Doppler frequency
f_L	high pass filter frequency setting
f_U	low pass filter frequency setting
$f(\ )$	similarity mean velocity profile function
$g_{11}(\ ), g_{22}(\ ), g_{12}(\ )$	similarity Reynolds stress profile functions
$I, I^*, I_r, I_r^*, I_x, I_x^*$	local turbulent intensities used in the uncertainty analysis
k	wavenumber
K	effective eddy diffusivity
l	mixing length scale
l_e	external turbulence length scale
L	length scale

L_e	generic integral length scale in the external turbulence field
L_o	jet velocity half width
L_{rr}	radial or transverse integral length scale
L_{xx}	streamwise integral length scale
m	exponent or number of fringes required for a valid Doppler signal
M	grid mesh spacing (*ie.* the centre-to-centre bar separation distance)
M_o	momentum integral
n	exponent or order of smoothing polynomial
n_d	number of distinct subgroups in a record
n_l	number of data points to the left of the current data point
n_r	number of data points to the right of the current data point
N	number of sampler
$\dot{N}$	mean valid signal arrival rate
N_e	Doppler burst intensity
p	exponent
P	pressure
q	arbitrary experimental result
q_e	turbulent kinetic energy of the external flow
r	radial or transverse position
r_o	arbitrary reference point in jet
R	radius of the jet
R_j	radius of the jet model
R_{rr}	radial or transverse autocorrelation function
R_{xx}	streamwise autocorrelation function
Re_b	grid Reynolds number ($Re_b=U_e b/\nu$)
Re_T	turbulent Reynolds number ($Re_T=U_o L_o/\nu_T$)
S	random or precision errors
t	time or student-t multiplier
t_o	start time of an averaging period

T	averaging time period
T_1, T_2	terms in the integral momentum equation
T_r	radial or transverse turbulent intensity in grid-generated turbulence
$\overline{T}_r$	average radial or transverse turbulent intensity in grid-generated turbulence
T_x	streamwise turbulent intensity in grid-generated turbulence
$\overline{T}_x$	average streamwise turbulent intensity in grid-generated turbulence
$\mathfrak{T}_{rr}$	radial or transverse integral time scale
$\mathfrak{T}_{xx}$	streamwise integral time scale
$\mathfrak{T}_\lambda$	Taylor micro time scale
u	streamwise fluctuating velocity
$\tilde{u}$	turbulent velocity scale
$\mathbf{U}$	instantaneous velocity
U	streamwise mean velocity
$\overline{U}$	streamwise top-hat mean velocity
$\tilde{U}$	mean velocity scale
U_c	mean convection velocity
U_{cl}	centerline mean velocity
U_e	external streamwise mean velocity
$\overline{U}_e$	average external streamwise mean velocity
U_j	average jet exit velocity
U_o	centerline excess mean velocity
$\overline{U}_o$	centerline excess top-hat mean velocity
$\overline{u\,v_r}$	Reynolds shear stress
v	arbitrary turbulent velocity
v_e	entrainment velocity function
v_r	radial or transverse fluctuating velocity
v_ϕ	azimuthal fluctuating velocity
V_r	radial or transverse mean velocity
V_ϕ	azimuthal mean velocity

$VR=U_j/U_e$	initial velocity ratio
w	weighting function
x	streamwise position
x_o	virtual origin for the jet
y_j	arbitrary measured value
$z_{\alpha/2}$	standard normal variate for a (100−α)% confidence interval

Greek Symbols

α	entrainment constant (initial phase)
β	entrainment constant (intermediate phase)
γ	entrainment constant (final phase)
δ	total uncertainty
ϵ	rate of energy dissipation per unit mass
η	normalized radial position
θ	momentum radius or laser beam intersection angle
ν	kinematic viscosity
ν_T	turbulent eddy viscosity
π	3.141593265...
ρ	fluid density
σ	grid solidity
τ	time lag or shear stress
ϕ	azimuthal position

Subscripts

d	dissipative eddies
e	external
fin	final phase
g	grid
int	intermediate phase
j	jet
l	large grid or large eddies
lam	initial phase or laminar external
o	jet centerline
r	radial component
s	small grid
x	streamwise component
ϕ	azimuthal component

Acronyms

CV	control volume
CS	clock synchronization
EN	electronic noise
FFT	fast Fourier transform
FS	fringe spacing
HWA	hot wire anemometry
LB	location bias
LDA	laser Doppler anemometry
PM	photomultiplier

PSD	power spectral density
rms	root-mean square
RSS	root-sum square
SNR	signal-to-noise ratio
TL	threshold limit

Chapter 1: Introduction

1.1 Motivation and Scope of Research

Historically, mankind has relied on the immense volume of the atmosphere and oceans to dilute pollutants that arise from our everyday lives. As the global population continues to grow and the rate at which new technology is introduced continues to accelerate, the effects of releasing more and more pollutants into the atmosphere and oceans is of growing concern. Economics and government legislation will continue to contend with each other to dictate the level of pollutant emissions that are deemed controllable and acceptable. Unfortunately, this means that there will always be some level of pollutants released into the natural environment. In addition, accidental releases, such as the Bhopal disaster in India and the Chernobyl accident in the Ukraine, rely solely on the diffusive nature of the natural environment to dilute and reduce the level of contaminants released. Thus our understanding of the behaviour of such plumes and jets interacting with the natural environment is of great importance in predicting pollutant transport and contaminant levels.

Intuitively one would postulate that the effects of atmospheric turbulence on the evolution of a jet or plume would be to increase the dispersion of pollutants and thus cause an increase in the radial

spread and perhaps change the trajectory of the jet or plume. Very little experimental data exists, however, to support this supposition. The main reason for this is that typical jets and plumes released into the natural environment are extremely complex. As an illustrative example, consider a smoke stack emission released into the planetary boundary layer. In this layer of the atmosphere the mean wind and its turbulence structure depend, in varying degrees, on convective forces due to atmospheric heating, local topography, large scale horizontal pressure gradients, Coriolis forces, and vertical temperature stability. The source can also introduce complexities such as buoyancy into the flow. Thus in order to conduct experiments to increase our understanding of how the evolution of jets and plumes is affected by an interacting turbulent background flow, the problem needs to be simplified and the numerous variables controlled. Realistically, this can only be accomplished at the laboratory scale since accurate and controlled full scale experiments are both difficult and expensive to conduct due to the uncooperative nature of the atmosphere and due to the limitations of the present meteorological and remote sensing instrumentation.

Thus laboratory scale experiments are required that emphasize the interaction of a jet or plume with a turbulent external flow. Since little experimental data exists for interacting turbulent flows, the experiments should reduce the complexity of the two flow fields by using the simplest possible flows in order to first elucidate the mechanisms involved in the interaction of the two turbulent fields. To this end, grid-generated turbulence will be used to model the atmospheric or environmental turbulence and a simple isothermal turbulent coflowing jet will be used to model the pollution source. One advantage of using these simple flows is that, individually, they are well documented in the literature thus providing a useful benchmark for the experimental results.

These experiments are also required to postulate and validate predictive models for jets and plumes issuing into a turbulent background flow. One common predictive model, used by government and industry, for this type of flow is the integral model which requires the specification of an entrainment velocity function. In spite of their relatively simplistic formulation, which is based on the Navier-Stokes equations with realistic simplifying assumptions, the integral model represents a sound engineering compromise between the complex physics of the flow and the ease of applying

the model to predict the overall dispersion in a flow field.

Traditionally, however, integral models have largely disregarded the increased rate of dispersion produced by the turbulence in the natural environment when modelling a jet or plume released into the natural environment. This exclusion can again be attributed to the fact that little experimental data exists to quantify the effects of environmental turbulence and thus the few models that put forth theoretical-based conjecture to account for its effects cannot be verified. It is the purpose of this work to conduct laboratory experiments to provide the means to evaluate and understand the physics of the interacting turbulent flows. From this, an integral model with an entrainment velocity function can be further developed and validated which will account for the effects of external turbulence on the evolution of jets and plumes.

1.2 Objectives of the Thesis

The main objectives for this thesis are thus twofold and can be stated as:

1. To acquire a new data base for turbulent isothermal jets released into uniform turbulent external coflows that incorporates a range of characteristic turbulent scales both within the jet and the external coflow.

2. To develop a new entrainment velocity function, to be incorporated into an integral model, that accounts for the interaction of the coflowing jet with the turbulent external coflow by determining the correct length and velocity scales that dominate the diffusion process as the jet evolves downstream.

1.3 Outline of Thesis

The thesis is divided into three main parts. The first part, given in Chapter 2, presents a review of the theory and literature which forms the basis for the present work. The second part consists of three chapters and deals with the experimental aspects of the current research. Chapter 3 gives a brief overview of the experimental equipment, the experimental methodology, and the level of experimental uncertainty contained within the results. Chapter 4 reports the experimental results for the external flow both in the absence and presence of turbulence generating grids and Chapter 5 details the experimental findings of the various coflowing jet runs in various levels of external turbulence. The third part of the thesis, given in Chapter 6, develops a predictive integral model and compares the predictions to the experimental data for a coflowing jet using a new entrainment velocity function. The thesis is concluded with Chapter 7 which details the main conclusions and contributions of the present research as well as recommendations for future work.

Chapter 2: Background and Literature Review

2.1 Introduction

The literature pertaining to turbulent fluid motion and diffusion is vast and varies from application to application. G.I. Taylor (1922), while studying smoke stack emissions, appears to be one of the first researchers to note that "turbulent motion is capable of diffusing heat and other diffusible properties through the interior of a fluid in much the same way that molecular agitation gives rise to molecular diffusion." Since then, there has been a multitude of research devoted to the study of turbulence.

The aim of this chapter is to review the theory and literature pertaining to the mechanisms of interacting turbulent flow fields. To start, a brief overview of the quantities used to characterize turbulent flows will be given. Reviews of theoretical and experimental studies of grid-generated turbulence will be given next. This will be followed by a similar examination of isothermal, coflowing jets in a laminar external flow as well as in a turbulent external flow. The chapter will conclude with a summary of the current research objectives.

2.2 Relevant Turbulence Background

Turbulence is one of the chief outstanding difficulties in the area of fluid mechanics (Bradshaw, 1994). It has been defined by Hinze (1975) as "an irregular condition of flow in which the various quantities show a random variation with time and space coordinates, so that statistically distinct averages can be discerned." Other researchers, such as Tennekes and Lumley (1972) avoid giving a precise definition of turbulence but instead list characteristics of turbulent flows.

In spite of this lack of conformity on the definition of turbulence, it is almost universally accepted that turbulent fluid motion satisfies, at every moment in time and space, the complete instantaneous unsteady and non-linear Navier-Stokes equations. Unfortunately, the computational requirements to directly solve these equations at realistic Reynolds numbers are still beyond current capacities.

A common alternative approach, often termed the deterministic approach, is to describe turbulent flows in terms of classical statistical concepts of random variables where the statistical quantities are determined in both the amplitude domain (mean and turbulent velocities) and in the time domain (autocorrelations and turbulent energy spectra). These quantities can, in turn, be used to derive other useful parameters. The turbulence statistics to be used in this thesis are defined in the next sub-sections.

2.2.1 Amplitude Domain Statistics

The two most common amplitude domain statics used to describe a turbulent flow are the time-mean average velocity (hereafter referred to as simply the mean velocity), which gives an indication of the bulk motion of the fluid flow, and the root-mean-square (rms) or turbulent velocity, which gives a measure of the magnitude of the turbulence in a flow. To obtain these values, the instantaneous velocity signal from the turbulent flow, U, must first be decomposed into an average value, U, and a fluctuating component, u, where:

$$\mathbf{U} = U + u \tag{2.1}$$

The average velocity is statistically defined over a finite time interval, T, as:

$$U = \frac{1}{T}\int_{t_o}^{t_o+T} \mathbf{U}\,dt \tag{2.2}$$

where t_o is the start time of the averaging period. The averaging period, T, should be sufficiently large such that the derivative of the mean velocity with respect to time is zero for steady state flows or negligibly small for flows with slightly varying mean velocities (Hinze, 1975).

Since the mean of the fluctuating velocity must be identically equal to zero by definition, it is not a suitable parameter to characterize the intensity of the turbulence. Instead, the root-mean-square (rms) velocity is used and is statistically defined as:

$$\sqrt{\overline{u^2}} = \left(\frac{1}{T}\int_{t_o}^{t_o+T} u^2\,dt \right)^{1/2} \tag{2.3}$$

Similar definitions to equations (2.2) and (2.3) are obtainable in the other coordinate directions.

2.2.2 Time Domain Statistics

Most signals arising from physical processes, including those from random processes, have some structure in time (Castro, 1989). For turbulent flows, one method used to determine the degree of dependence between the turbulent velocity at one point in time and the same turbulent velocity at later times is to evaluate the autocorrelation function which is defined, assuming the mean flow is in the x direction, for the streamwise direction as:

$$R_{xx}(\tau) = \frac{\overline{u(x;t)\,u(x;t+\tau)}}{\overline{u^2}} \tag{2.4}$$

and for the transverse or radial direction, which is taken cross stream to the mean flow, as:

$$R_{rr}(\tau) = \frac{\overline{v_r(x;t)\,v_r(x;t+\tau)}}{\overline{v_r^2}} \tag{2.5}$$

where u and v_r are the fluctuating velocities in the streamwise and transverse or in this case radial directions, x is the downstream position, t is the time, and τ is the time lag between the velocity signals being correlated.

An alternative but complementary way of describing the time domain dependence in turbulent flows is from a turbulent energy spectrum. Turbulent energy is comprised of vortices of various frequencies containing a certain amount of turbulent kinetic energy. At any position in the flow there is an energy content of the turbulence associated with a given frequency (or size) of the eddy. If the energy density content of a turbulent signature is determined over a range of predetermined frequencies, the result will give a distribution or energy density spectrum over the range of frequencies measured. The spectrum thus represents the distribution of turbulent kinetic energy across the various frequencies of the flow. In particular, the streamwise power spectral density (PSD) function, $E_{xx}(f)$, is defined such that $E_{xx}(f)df$ is the turbulent energy contributed by the streamwise component of the turbulent flow over the frequency range of $f-df/2$ to $f+df/2$. The radial or transverse PSD function, $E_{rr}(f)$, has a similar definition. The integral of the PSD over the range of frequencies is the turbulent kinetic energy per unit mass of the original turbulent signature.

The autocorrelation function and the power spectral density function are not independent of each other but form an exact Fourier transform pair. Thus specification of one specifies the other.

2.2.3 Integral Scales of Turbulence

Physical limitations of the experimental equipment only allow for time series to be measured at a single point in space at any one time. Thus any statistics determined from the time series will be temporal and Eulerian in nature.

Using the autocorrelation equations, integral time scales can be calculated using:

$$\Im_{xx} = \int_0^\infty R_{xx}(\tau)\, d\tau \tag{2.6}$$

for the streamwise direction and:

$$\Im_{rr} = \int_0^\infty R_{rr}(\tau)\, d\tau \tag{2.7}$$

for the radial or transverse direction.

Unfortunately, integral time scales are difficult to physically interpret and are thus usually converted to spatial scales using Taylor's theory of frozen turbulence. This hypothesis assumes that "the fluctuations at a fixed point of the field may be imagined to be caused by the whole turbulent flow field passing that point as a 'frozen' field" (Hinze, 1975, page 46). Taylor's hypothesis is only an approximation and valid only when the convecting mean velocity is constant and when $U \gg (\overline{u^2})^{1/2}$. Thus its application to shear flows should be viewed with some caution since the convecting mean velocity varies with position and the turbulent velocities can be fairly large in comparison to the mean velocity.

The integral length scale in the streamwise direction is therefore given by:

$$L_{xx} = U\Im_{xx} \tag{2.8}$$

and is generally considered to be typical of the average to larger sized energy containing eddies whose history is determined by the geometric or production scales of the flow.

The integral length scale in the transverse or radial direction is not as straight forward since there is no obvious choice for a convecting velocity in the radial direction. If, however, it is assumed that the turbulence structure remains frozen over the integral time scale as it is convected downstream by the mean streamwise velocity, then a radial integral length scale can be defined as:

$$L_{rr} = U\Im_{rr} \tag{2.9}$$

Strictly speaking, this is not a true radial integral length scale since it is dependent on the convecting streamwise velocity. It is, however, the integral length scale that is representative of the correlation between the radial turbulent velocities. In Chapter 5, it will be shown after the fact that the length scale defined by equation (2.9) does scale with the radius or geometric scale of the jet.

The choice of U to be used in the above equations is somewhat dependent on the flow. For the external grid generated turbulence, the mean velocity is constant throughout the flow field and is thus the obvious choice. In a coflowing jet, the convection velocity is dependent on both the streamwise and radial positions. Antonia and Bilger (1973) have evaluated streamwise integral length scales on the centerline of the jet and use the local mean velocity, U, (which in this case is the local centerline velocity) as the convecting velocity. Smith and Hughes (1977) evaluate the convecting velocity to be 0.9 times that of the local mean velocity based on separation techniques using hot wires. Biringen (1986) calculates the convecting velocity, U_c, using:

$$U_c = U\left(1 + 2\frac{\overline{u^2}}{U^2}\right) \tag{2.10}$$

According to the literature on coflowing jets, there is no apparent standard choice for the convecting velocity. If the mean velocity profiles within the jet can be shown to be similar, then all

the jet mean velocities can be related back to each other. Thus the choice of a convecting velocity becomes somewhat arbitrary since it can be related to any other mean velocity in the jet by similarity relations.

Following Antonia and Bilger (1973), the present study will use the local mean velocity as the convecting velocity in all cases.

2.3 Grid-Generated Turbulence

In a 1951 paper, Baines and Paterson stated paradoxically that grids and screens could be used in a fluid flow field to either generate or reduce turbulence and to either create or eliminate large scale velocity or pressure non-uniformities. With such a wide range of applications, the present literature review will concentrate solely on turbulence that is generated by the wakes and momentum jets formed behind grids.

Turbulence generating grids exist in a wide variety of geometric configurations ranging from biplanar arrays of round or square bars to perforated plates. The conventional method of describing a grid is by the bar width, b, the centre to centre mesh spacing, M, and the grid solidity, σ, which is defined by the projected area per unit total area and can be calculated from:

$$\sigma = \frac{b}{M}\left(2 - \frac{b}{M}\right) \tag{2.11}$$

Experimental evidence suggests that significant flow instabilities result when σ>0.50 (Roach, 1987).

An excellent review of grid-generated turbulence theory is given in Hinze (1975). Typically, the behaviour of the streamwise turbulent velocity, $(\overline{u^2})^{1/2}$, and integral length scale, L_{xx}, are described by power laws of the form:

$$\left(\overline{u^2}\right)^{1/2} \propto x_g^{n/2} \tag{2.12}$$

and,

$$L_{xx} \propto x_g^p \tag{2.13}$$

where x_g is the streamwise distance from the grid plane and where the exponents obey the theoretical conjugate relationship (Lewalle, 1990):

$$p = 1 + \frac{n}{2} \tag{2.14}$$

To appreciate the range in the different theoretical values, without going into the theoretical detail, Hinze (1975) states that $n/2=-0.5$ and $p=0.5$ for the case of complete self-preservation of turbulence, $n/2=-0.6$ and $p=0.4$ when Saffman's invariance is assumed, and $n/2=-0.714$ and $p=0.286$ when Loitsianskii's invariance assumed.

George (1992), in a re-analysis of homogeneous isotropic turbulence (based on a more general form of self-preservation theory using higher order momentum similarity), has shown that the decay of the turbulent energy in grid-generated turbulence is, in part, continuously determined by the initial conditions of the flow. No single universal state of self-preservation can thus be obtained unless the grid Reynolds number is infinite at which point the flow becomes independent of the initial conditions. George (1992) has derived for this case of infinite grid Reynolds number a theoretical upper limit on the decay exponent as $n/2=-0.5$ and also notes that there is some experimental evidence to suggest that $n/2$ increases towards -0.5 as the grid Reynolds number increases.

Excellent reviews of grid-generated turbulence experiments are also given in Hinze (1975) as well as Roach (1987). Hinze (1975) summarizes the experimental data by stating the range for the exponents as $-0.675 \leq n/2 \leq -0.600$ and $0.30 \leq p \leq 0.53$ while Roach (1987) suggests using

$n/2=-0.714$ and $p=0.5$ as the average of the experimental data.

The present study uses grids composed of a biplanar array of square bars since the location of the flow separation on the bar is not sensitive to the Reynolds number of the flow as in the case of round rods. A list of other grid-generated turbulence experiments using this same grid configuration is given in Table 2.1 which summarizes the working medium and the initial conditions of the experiments. The last column in the table gives the grid Reynolds number which is defined as $Re_b=U_e b/\nu$ where U_e is the streamwise mean velocity in the flow and ν is the kinematic viscosity of the fluid. In addition, for this configuration, Fink (1977) and Johnson and Johnston (1989) have demonstrated that the flow behind the grid is uniform and homogeneous in planes parallel to the

Reference	Fluid	b (cm)	M (cm)	σ	U_e (m/s)	Re_b
Present	water	1.27	5.08	0.44	0.0721	900
		2.54	10.16	0.44	0.0713	1800
Comte-Bellot and Corrsin (1966)	air	0.477	2.54	0.34	20	6400
Fink (1977)	air	1.0	4.0	0.44	7	4700
Johnson and Johnston (1989)	water	1.27	6.35	0.36	0.152	2100
Nakamura and Ohya (1983)	air	2.5	13.0	0.35	10	16700
Sato (1951)	air	0.5	2.5	0.36	5	1650
		0.5	2.5	0.36	10	3300
Sirivat and Warhaft (1983)	air	0.476	2.54	0.34	3.4	1000
		0.476	2.54	0.34	6.3	1800
Tan and Ling (1963)	water	1.88	5.08	0.60	0.0292	550
		0.706	1.905	0.60	0.0318	230
Warhaft and Lumley (1978)	air	0.476	2.54	0.34	6.5	1900

Table 2.1: Summary of the geometric and flow conditions for square bar grid experiments.

grid after 40 bar widths downstream from the grid.

For square bar grids, Roach (1987) suggests the following semi-empirical fits to the turbulent intensities:

$$T_x = \frac{\sqrt{\overline{u^2}}}{U_e} = 1.13\left(\frac{x_g}{b}\right)^{-0.714} \qquad \& \qquad T_r = \frac{\sqrt{\overline{v_r^2}}}{U_e} = 1.01\left(\frac{x_g}{b}\right)^{-0.714} \tag{2.15}$$

and to the integral length scales:

$$\frac{L_{xx}}{b} = 0.20\left(\frac{x_g}{b}\right)^{0.50} \qquad \& \qquad \frac{L_{rr}}{b} = 0.10\left(\frac{x_g}{b}\right)^{0.50} \tag{2.16}$$

The data from the experiments listed in Table 2.1 and equations (2.15) and (2.16) will be used to check the validity of the present experimental results for grid-generated turbulence in Chapter 4.

The present study also proposes to use water as a working medium. Table 2.1 indicates that only Tan and Ling (1963) and Johnson and Johnston (1989) have previously used water, neither of which made comparisons to similar results obtained in wind tunnel experiments. Note, however, that the grid solidity of Tan and Ling (1963) is 0.6 and thus the results are not reliable due to the flow instabilities introduced when σ>0.5 (Roach, 1987). Comparison of the air and water results, at a given grid Reynolds number, should thus indicate similar characteristics for grid-generated turbulence.

In addition, the grid Reynolds number range, excluding that of Tan and Ling (1963), varies from 900 up to 16700. This may provide a sufficiently broad range to verify if the initial conditions of the flow, and thus the grid Reynolds number, have a continuous effect on the downstream development of the turbulence as postulated by George (1992).

2.4 Analytical Models for Coflowing Jets

In the field of pollution dispersion modelling, the average behaviour of jets and plumes can be described by knowledge of the trajectory and spread (see, for example, Slawson and Csanady, 1967 and 1971.) These two parameters describe respectively the mean path that the jet or plume follows in the environment and the degree of transverse dispersion or dilution about the mean path. The spread and trajectory are assumed to be average quantities which, if obtained by field measurements, would require fifteen minutes to an hour averaging time frame in the planetary boundary layer.

If an isothermal jet in a uniform external coflow is taken to be a simplified version of real environmental situations then its mean behaviour should also be satisfactorily predicted by its trajectory and spread. Since the jet orientation is horizontal and since the jet fluid is isothermal, the mean path of the jet exhausting into the coflow is simply the horizontal extension of the axis of the jet model into the external coflow. There can, however, be a significant decay in the streamwise mean velocity, U, of the jet with distance downstream. Thus, in order to estimate the distance travelled by fluid elements within the jet, the mean velocity decay must be predicted. In the atmosphere, this is commonly avoided by invoking the *bent-over plume assumption* whereby it is assumed that the mean velocity of the jet or plume is equal to that of the mean wind. In addition, the behaviour of the jet radius, R, as a function of the distance downstream is also required to give an estimate of the spread. Predicting the mean behaviour of an isothermal jet in an external coflow can thus be translated into predicting $U=f(x)$ and $R=g(x)$.

The axial mean velocity and the radius are both mean quantities which depend on the turbulence structure within the jet which, in turn, is responsible for entraining the slower external fluid at the edge of the jet. The slower entrained external fluid results in a decrease in the mean jet velocity and an increase in the jet radius. When the external coflow is also turbulent, the effect on the mean velocity and radius of the jet will be dependent on the interaction of the turbulence within the jet with that in the external coflow. Thus, in modelling the jet in an external coflow which is turbulent,

both the mean quantities and the turbulent statistics of the jet and the external coflow must be considered.

2.4.1 Similarity Considerations

A jet in a coflowing external stream is representative of a developing flow since, depending on the downstream location, the behaviour of the jet falls somewhere between that of a jet in a quiescent surrounding and that of small velocity excess jet similar to a small defect wake except opposite in sign. As a result, the radial profiles of the mean velocity and turbulent velocities are dependent on both the radial position and the downstream location.

Similarity theory suggests that for many flows the profiles of the mean and turbulent velocities maintain the same functional form with only the radial length scale and scales of the velocities changing with downstream distance (Townsend, 1976). For similarity to occur in a coflowing jet, the variation of the streamwise mean velocity and the turbulent stresses must be of the form:

$$\begin{aligned} U &= U_e + \tilde{U} f(\eta) \\ \overline{u^2} &= \tilde{u}^2 g_{11}(\eta) \\ \overline{v_r^2} &= \tilde{u}^2 g_{22}(\eta) \\ \overline{uv_r} &= \tilde{u}^2 g_{12}(\eta) \end{aligned} \qquad (2.17)$$

where $\eta = r/b$, b is a scale of radial length and is dependent on the velocity profile assumed, U_e is the constant velocity in the external coflow, $\tilde{U}$ is some scale of the mean velocity, $\tilde{u}^2$ is a scale of the turbulent stresses and f, g_{11}, g_{22}, and g_{12} are the functions defining the radial distribution for the various variables. Note that b, $\tilde{U}$, and $\tilde{u}^2$ are functions of x only and that the turbulent stresses are allowed to have a scale factor which is independent of the scale factor for the mean velocity.

Typically, the next step is to investigate under what conditions, if any, the similarity distributions given by equation (2.17) satisfy the equations for the conservation of mass and x-momentum. The

simplified conservation of mass equation is given by (see Appendix A for a complete derivation including turbulence terms):

$$\frac{\partial U}{\partial x} + \frac{1}{r}\frac{\partial}{\partial r}\left(r V_r\right) = 0 \tag{2.18}$$

which can be solved for the radial mean velocity, V_r, to give:

$$-V_r = \frac{1}{r}\int_0 \frac{\partial U}{\partial x} r\, dr \tag{2.19}$$

The simplified x-momentum equation is given by:

$$U\frac{\partial U}{\partial x} + V_r\frac{\partial U}{\partial r} + \frac{\partial}{\partial x}\left(\overline{u^2} - \overline{v_r^2}\right) + \frac{1}{r}\frac{\partial}{\partial r}\left(r\overline{uv_r}\right) = 0 \tag{2.20}$$

Substituting equation (2.17) into equation (2.19), and recalling that the partial derivatives with respect to x and r can be converted to partial derivatives with respect to η using the chain rule of derivatives to get:

$$\begin{aligned} \frac{\partial(\,)}{\partial x} &= -\frac{\eta}{b}\frac{db}{dx}\frac{\partial(\,)}{\partial \eta} \\ \frac{\partial(\,)}{\partial r} &= \frac{1}{b}\frac{\partial(\,)}{\partial \eta} \end{aligned} \tag{2.21}$$

then the radial velocity will have the form of:

$$-V_r = \frac{1}{b}\frac{d\left(\tilde{U}b^2\right)}{dx}\frac{1}{\eta}\int_0 f\eta\, d\eta - \tilde{U}\frac{db}{dx}\eta f \tag{2.22}$$

Substituting this expression for V_r along with the similarity expressions given by equation (2.17) into equation (2.20), results in:

$$\underset{\text{I}}{\left\{\frac{b\,U_e}{\tilde{u}^2}\frac{d\tilde{U}}{dx}\right\}}[f]+\underset{\text{II}}{\left\{\frac{b\,\tilde{U}}{\tilde{u}^2}\frac{d\tilde{U}}{dx}\right\}}[f^2]-\underset{\text{III}}{\left\{\frac{\tilde{U}}{\tilde{u}^2 b}\frac{d(\tilde{U}b^2)}{dx}\right\}}\left[\frac{f'}{\eta}\int_0 f\eta\,d\eta\right]-$$

$$\underset{\text{IV}}{\left\{\frac{U_e\tilde{U}}{\tilde{u}^2}\frac{db}{dx}\right\}}[\eta f']+\underset{\text{V}}{\left\{\frac{b}{\tilde{u}^2}\frac{d\tilde{u}^2}{dx}\right\}}[g_{11}-g_{22}]- \qquad (2.23)$$

$$\underset{\text{VI}}{\left\{\frac{db}{dx}\right\}}\left[\eta\left(g_{11}'-g_{22}'\right)\right]+\underset{\text{VII}}{\left[\frac{1}{\eta}\frac{\partial(\eta g_{12})}{\partial\eta}\right]}=0$$

where primes denote differentiation with respect to η. The terms in the square brackets are functions of η only and the terms in the curly brackets are functions of x only. If the flow is to display similarity, then the value of each term must be identical for all values of x and η. Since there is no term in curly brackets in the seventh term on the left hand side, similarity is only possible if the six other terms in curly brackets are all constant.

The sixth term in curly brackets on the left hand side therefore gives $b \propto x$ and, as a consequence, the fourth term results in $U_e\tilde{U}/\tilde{u}^2$ being a constant. $\tilde{u}^2$ can then be replaced by $U_e\,\tilde{U}$ and the first and fifth terms then give:

$$\frac{b}{\tilde{U}}\frac{d\tilde{U}}{dx} = \text{constant} \qquad (2.24)$$

while the second term gives:

$$\frac{b}{U_e}\frac{d\tilde{U}}{dx} = \text{constant} \qquad (2.25)$$

The above two conditions can only be satisfied if $\tilde{U}$ is a constant which gives a zero value for the derivative. However, the remaining terms in square brackets in equation (2.23) can only be satisfied if $\tilde{U} \propto U_e$. Thus the only solution that can be obtained from the conservation of mass and x-momentum equation are for similarity distributions with scale factors of $\tilde{U} \propto U_e$, $\tilde{u}^2 \propto \tilde{U}^2$, and $b \propto x$.

This describes the case of a jet with an initial velocity ratio of unity and does not, in general, reflect the true development of jet in a uniform external coflow as observed in experiments. In fact, previous experimental studies on jets with initial velocity ratios greater than unity, indicate that the scale factor that collapses the radial profiles of the mean velocity is the centerline excess mean velocity, U_o, which is defined as the difference between the mean velocity at the jet centerline and that of the external coflow and, as such, is a function of distance downstream. It must therefore be concluded that complete mathematical similarity for a jet in a uniform coflow does not exist.

Similarity theory, however, can provide two useful asymptotic limits on the behaviour of U_o and R if the condition that U_e is a constant is relaxed and allowed to be a function of x (Hill, 1965, Newman, 1967, and Hinze, 1975). The similarity analysis (see Newman, 1967, for the complete analysis) then yields the condition that $\tilde{U}/U_e$ is a constant. The first asymptotic limit is given by a very strong jet in a comparatively weak external coflow where $U_e/U_o \ll 1$. Under these conditions, the expected development of the jet corresponds to $U_o \propto x^{-1}$ and $R \propto x$. This behaviour has been observed in jets issuing into quiescent backgrounds (Hussein *et al*, 1994) as well as in coflowing jets close to the jet exit (Biringen, 1986). The second asymptotic limit is given by a very weak jet in a comparatively strong background flow where $U_e/U_o \gg 1$. Under these conditions, the expected development of the jet becomes $U_o \propto x^{-2/3}$ and $R \propto x^{1/3}$. Limited experimental data exists for the verification of this final stage asymptote since the condition that $U_e/U_o \gg 1$ is only realized far downstream from the jet exit. Biringen (1986) and Nickels and Perry (1996) have stated that their far field data appears to approach the above trends.

2.4.2 Integral Models for a Jet in a Nearly Laminar Coflow

Most analytical models for a jet in a nearly laminar (*i.e.* very low turbulence levels) coflow begin the model development by assuming partial similarity in that the mean axial velocity profiles become self-similar by a certain distance downstream from the jet exit. Using a characteristic length (*i.e.* the jet velocity half width, L_o, or the jet radius, R) and a characteristic mean velocity (*i.e.* the

centerline excess mean velocity, U_o, or the top-hat mean velocity, $\overline{U}$), the radial profile of the axial mean velocity can then be specified, for example, by:

$$U = U_e + U_o f(\eta); \qquad \text{where } \eta = \frac{r}{L_o} \tag{2.26}$$

where $f(\eta)$ is some universal function. This recasts the problem into solving for the characteristic length and velocity.

An integral momentum equation is then developed using the conservation of mass and the streamwise momentum equation along with simplifying assumptions. The resulting equation can then be used to determine the relationship between local values of U_o and L_o. As a simple illustrative example, take a high Reynolds number flow where viscous effects can be ignored and in addition assume that the momentum contribution from any turbulence quantity is small in comparison to the momentum contribution from the mean quantities. The resulting integral momentum equation for such a case is (Hinze, 1975):

$$\int_0^\infty U(U - U_e) r\, dr = \frac{M_o}{2\pi\rho} \tag{2.27}$$

where M_o is the momentum integral constant.

As a brief aside, the momentum integral constant can be used to define a useful length scale commonly referred to as the momentum thickness in planar flows (see, for example, Tennekes and Lumley, 1972). The momentum thickness is the length scale that compares the excess momentum flux of the jet to that of the background flow by equating M_o to an equivalent momentum flux using the external mean velocity, U_e, and a radius, θ, such that:

$$\theta = \left(\frac{M_o}{\pi \rho U_e^2} \right)^{1/2} \tag{2.28}$$

To keep the physical significance of θ as clear as possible, it will be referred to as a momentum radius rather than a thickness. Since θ defines a length scale which is characteristic of a particular combination of a jet and an external flow, it can be used as a normalizing length scale in order to compare results from different experiments.

The integral momentum equation, given by equation (2.27), is used for illustration purposes only since the assumptions used in the development exclude any effects of turbulence, both within the jet and within the external coflow. Substituting the velocity profile assumption, equation (2.26), into equation (2.27) gives:

$$\int_0^\infty \eta f^2(\eta)\, d\eta + \frac{U_e}{U_o}\int_0^\infty \eta f(\eta)\, d\eta = \frac{M_o}{2\pi\rho\left(U_o L_o\right)^2} \qquad (2.29)$$

If the streamwise mean velocity profiles are self-preserving, and providing that $f(\eta)$ is known, equation (2.29) can be integrated from the centerline to the edge of the jet to yield an equation relating local values of U_o and L_o.

An additional equation, however, is required to determine the axial variation of the mean velocity scale and the scale of jet spread. Several methods, detailed in the literature, have been used to obtain this second equation and are briefly outlined below.

2.4.2.1 Double Momentum Integral Technique

One of the first techniques, introduced by Squire and Trouncer (1944), uses a second momentum integral evaluated from the centerline to the jet velocity half width, L_o. Evaluation of this second integral requires an estimate of the shear stress, τ, at $r=L_o$. Squire and Trouncer (1944) used Prandtl's mixing length theory to approximate the shear stress as:

$$\tau = -\rho \overline{u v_r} = \nu_T \frac{\partial U}{\partial r} \qquad \text{where } \nu_T = \rho l^2 \left| \frac{\partial U}{\partial r} \right| \tag{2.30}$$

and is the phenomenological turbulent eddy viscosity. In addition, they assumed that the mixing length, l, was always a constant proportion of the width of the flow. This effectively results in $\nu_T \propto U_o L_o$ (Hill, 1965) and the turbulent Reynolds number, defined by:

$$Re_T = \frac{U_o L_o}{\nu_T} \tag{2.31}$$

becomes a constant throughout the flow. This is physically unrealistic for a jet in a coflow since the turbulent Reynolds number should decrease with increasing distance (Antonia and Bilger, 1974). Forstall and Shapiro (1950) have shown that the method of Squire and Trouncer (1944) does predict the general order of magnitude of U_o and L_o but presents a false picture of the way in which they vary with the streamwise distance.

2.4.2.2 Higher Moments of the Momentum Equation

A second method for obtaining a second equation involves multiplying the momentum equation by $U^m r^n$ where m and n are integers. Hill (1965) used m=0 and n=2 to obtain a moment-of-momentum equation. The set of equations can be solved for x and R as functions of the mean velocity ratio to give:

$$\frac{x}{\theta} = 6.39\left(\frac{U_e}{U_o} + 0.468\right)^{\frac{3}{2}} + 5.38\left(\frac{U_e}{U_o} + 0.468\right)^{\frac{1}{2}} + 1.76\left(\frac{U_e}{U_o} + 0.468\right)^{\frac{1}{2}} - 8.30$$

$$\frac{R}{\theta} = \frac{\frac{U_e}{U_o}}{\left(2\pi\left(0.095\frac{U_e}{U_o} + 0.0445\right)\right)^{\frac{1}{2}}} \tag{2.32}$$

where θ is the momentum thickness. All the constants in the solutions are evaluated based on experimental data for jets issuing into a quiescent background (*i.e.* a very strong jet). Hill (1965) found that his solution adequately predicted experimental data for a jet in a coflow provided $U_j/U_o<1$ but failed in predicting data when the jet degenerated into a weak jet. Since the constants in the equation are determined from data for a jet in a quiescent background, its not surprising to see good agreement with data from strong jets. One advantage of this solution over the double integral method is that it is independent of any phenomenological turbulence theories such as eddy viscosities and mixing lengths.

In addition to a moment-of-momentum equation, Hill (1965) suggests an energy integral equation where $m=1$ and $n=0$. No solution, however, is presented for this case. It should be noted that the choice of m and n in this method is somewhat arbitrary since if the exact solution is known it would satisfy any of the higher moment equations.

2.4.2.3 The Energy Equation with a Shear Stress Model

Fink (1977) uses the energy equation to obtain the second equation relating the local radial length scale and mean velocity scale. In using the energy equation, however, a Reynolds shear stress term emerges which must be modelled. Fink (1977) uses a turbulent eddy viscosity model so that:

$$\frac{\tau}{\rho} = \overline{u v_r} \approx \nu_T \frac{\partial U}{\partial r} \tag{2.33}$$

where:

$$\nu_T = c_1 \theta U_e \tag{2.34}$$

and c_1 is an entrainment constant and θ is the momentum radius.

Fink (1977) appears to obtain good agreement between experimental data and the predicted values

for the decay of the mean velocity. No comparison, however, is made for the radial spread of the jet even though the spread and the mean velocity decay are coupled through the integral momentum equation. One serious flaw of the above model is that it relies on the radial gradient of the streamwise mean velocity which becomes zero at the jet centerline and at the edge of the jet.

2.4.2.4 Townsend's Hypothesis of Large Eddy Equilibrium

A fourth method for obtaining the second equation involves using Townsend's hypothesis of large eddy equilibrium. This hypothesis assumes that the largest eddies of the turbulent shear flow are in approximate energy equilibrium throughout a significant part of their existence. This leads to a relationship between the mean rate of shear strain and the Reynolds shear stress which involves the scales of the largest eddies (Gartshore, 1966). In this method the turbulent Reynolds number, Re_T, is allowed to vary with distance downstream in a particular flow as well as from one flow to another with the variation related to $(\partial U/\partial x)/(\partial U/\partial r)$ at $r=L_o$. A double integral technique similar to Squire and Trouncer(1944) is also employed. The resulting set of equations is solved numerically using a Runge-Kutta scheme and requires the input of two empirical constants (Newman, 1967). In spite of the added sophistication and the additional assumptions regarding the large eddy equilibrium hypothesis, the method does not show good agreement with experimental data (Patel, 1971).

2.4.2.5 Auxiliary Growth Equations

The use of auxiliary growth equations stems from the assumption that the spatial rate of growth of a mixing layer is dependent on the level of turbulence within the mixing layer which, in turn, is dependent on the mean velocity. Newman (1967), in an analogy to a derivation of Abramovich (1963) for mixing layers in constant pressure, proposes an auxiliary equation for plane jets in an external coflow of the form:

$$\frac{dL_o}{dx} = c_1 \frac{|U_o|}{U_e + \frac{U_o}{2}} \tag{2.35}$$

This auxiliary equation is identical to that proposed by Townsend (1976) who arrived at it from considering the entrainment into the shear flows and termed c_1 the *entrainment constant.* Patel (1971), however, has shown that this auxiliary equation corresponds to an approximately constant eddy viscosity Reynolds number. To allow for variation in the turbulent Reynolds number, Patel (1971) has suggested an auxiliary equation of the form:

$$\frac{dL_o}{dx} = c_2 \frac{U_o}{U_e + U_o} \tag{2.36}$$

Although there is only slight qualitative differences in the auxiliary equations, equation (2.36) does give the correct values for the turbulent Reynolds number for a strong plane jet and a weak plane jet. Antonia and Bilger (1974) have extended the method of Patel (1971) to an axisymmetric jet. The auxiliary equation has the same form as equation (2.36) although the value of the constant c_2 is chosen to satisfy the growth rate of a strong axisymmetric coflowing jet. Antonia and Bilger (1974) have concluded that this method of using an auxiliary equation is satisfactory when U_e/U_o is small but is not acceptable when U_e/U_o is large since the influence of the initial conditions is not destroyed.

2.4.2.6 Entrainment Hypothesis

The use of an entrainment hypothesis, although quite similar to the auxiliary growth equation technique, originates in the field of air pollution dispersion modelling (see, for examples, Morton *et al*, 1956, and Slawson and Csanady, 1967 and 1971) and is still commonly employed in atmospheric integral models. The method assumes that the radial inflow velocity at the edge of the jet is the result of entrainment of ambient fluid due to the action of turbulence. The turbulent

velocities responsible for the entrainment of ambient fluid are assumed to be proportional to some mean velocity or mean velocity difference within the jet. The entrainment hypothesis is usually contained within the continuity equation which can be rewritten in the form:

$$\frac{d}{dx}\int_0^{R(x)} U(x,r)\,r\,dr = R\,v_e \tag{2.37}$$

where v_e is the entrainment velocity. Typically, the mean velocity within the jet is assumed to have a top-hat distribution such that when $0 \le r \le R$, $U=\overline{U}$ and when $r \ge R$, $U=U_e$. The integral in equation (2.37) can then be evaluated to give:

$$\frac{d}{dx}\left(R^2\,\overline{U}\right) = 2\,R\,v_e \tag{2.38}$$

The entrainment hypothesis is then contained within the entrainment velocity. Morton (1961) and Maczynski (1962) have both suggested that $v_e=\alpha(\overline{U}-U_e)$ where α is the entrainment constant. Maczynski (1962) has shown however that, given the above entrainment hypothesis, α cannot remain a constant but must increase between the initial region of the jet and the region far downstream of the exit. Maczynski (1962) states the reason for this is that in the initial region the jet velocity is large and may inhibit mixing while farther downstream, the jet velocity decreases and the flow is more like that of a wake which is known to have a greater value of α than a jet issuing into a quiescent background.

Van Heyst (1992) has proposed that $v_e=\alpha\overline{U}$ which gives a closed form analytical solution of $R \propto x$ and $\overline{U} \propto x^{-1}$ which is the asymptotic limit for a strong jet in a weak coflow. As might be expected, this entrainment hypothesis satisfactorily predicts the flow near the jet but fails to yield the correct asymptotic limit far downstream where the jet has degenerated into a very weak jet.

2.4.2.7 Other Analytical Models

Antonia and Bilger (1974) have applied a two parameter turbulence model developed by Rodi and Spalding (1970) and Spalding (1971). In the turbulence model, the turbulent kinetic energy and a turbulence length scale are determined from the differential transport equations for these quantities. There is however no physical basis for the differential equation for the turbulence length scale which is derived by analogy to the turbulent kinetic energy equation. The method gives good predictions for the mean velocity decay and for the spread of the jet while giving adequate predictions of the turbulent velocities and the Reynolds stress for values of U_j/U_e as low as three. The apparent success of the model is diminished, however, by the non-physical nature of the turbulence length scale equation, by the uncertainty in determining some of the constants to be used in the equations, and by the possible dependency that these constants have on flow parameters.

Nickels and Perry (1996) have used coherent structures to model a coflowing jet in which they assume that the flow is dominated by double-roller eddies which are inclined to the streamwise direction. The characteristic velocity of the coherent structures is proportional to the centerline excess mean velocity and the characteristic length scale is proportional to the radius. Nickels and Perry (1996) try many different eddy shapes but choose the one that gives the correct Reynolds stress ratios and reasonably good shapes for the spectra. The model shows reasonable agreement between the predicted values and experimental data for the Reynolds stresses and mean velocities but only fair agreement between turbulent energy spectra. The authors consider the chosen eddy shape a "first stab" which gives results which are fairly consistent with the data, but admit that other possible shapes still need to be explored.

2.4.3 Models Including the Effects of External Turbulence

Slawson and Csanady (1967 and 1971) have proposed a zone model where a turbulent jet or plume undergoes three distinct phases of growth. In the initial phase, the self-generated turbulence within

the plume or jet dominates the mixing and the growth. As distance from the source is increased, an intermediate phase is entered where the external turbulence in the inertial subrange dominates the mixing. The final phase is entered when the mixing becomes dominated by the energy containing eddies within the external flow. The existence of three distinct phases is a considerable simplification since in reality there is likely to be significant overlap in growth mechanisms between the phases. Slawson and Csanady (1971) have incorporated the entrainment of external fluid into the jet or plume that is the result of the external turbulence by using an entrainment hypothesis which is dependent on the growth phase of the jet or plume. In the intermediate phase, Slawson and Csanady (1971) have proposed that $v_e=\beta\epsilon^{1/3}R^{4/3}$ and in the final phase, $v_e=\gamma vL/R$ where β and γ are entrainment constants for each phase, ϵ is the rate of energy dissipation per unit mass, R is the jet or plume radius, v is a turbulent root-mean-square velocity in the external coflow, and L is the length scale of the energy containing eddies in the external coflow.

Fink (1977) uses the zone model proposed by Slawson and Csanady (1971) but uses an eddy viscosity model to represent the self-generated diffusion of the jet and the added diffusion caused by the turbulence in the external coflow rather than an entrainment hypothesis. The added eddy viscosity that is due to the effects of the external turbulence, $\nu_{T,e}$, are modelled by $\nu_{T,e}\approx 0$ for the initial zone, and by $\nu_{T,e}\propto\epsilon^{1/3}(L_o)^{4/3}$ for the intermediate zone. Fink (1977) did not include a final phase portion in his model. For a turbulent external flow, the added eddy viscosity due to the external turbulence is linearly summed with that due to the jet in equation (2.34). Fink (1977) concludes, however, that the overall enhanced axial development of a jet in a turbulent coflow is poorly predicted by assuming a constant total eddy viscosity composed of a self-generated part and a supplement which is only influenced by the characteristics of the eddies in the inertial subrange of the external coflow.

Scahtzmann (1979), in developing an integral model for plume rise, allows the entrainment velocity to have several terms, each reflective of a specific entrainment mechanism. This allows for some overlapping between the various phases of plume and jet growth. The term which models the atmospheric phase has the same form as that proposed by Slawson and Csanady (1971) for the final

phase. However, due to lack of experimental data on jets and plumes in external turbulence fields, the value of the constant is left undetermined.

Wright (1994), in order to account for the effects of external turbulence generated by a bed of gravel on a coflowing jet, also uses an entrainment velocity function similar to the final phase of Slawson and Csanady (1971) but sets the characteristic turbulent velocity equal to the wall shear stress velocity at the gravel bed. A linear summation for the laminar and turbulent entrainment functions is also used. Wright (1994) obtains fair agreement to the radial spread of the jet but makes no comparison with the mean velocity decay.

2.4.4 Current Integral Model

To predict the behaviour of the mean velocity and the jet radius as a function of downstream distance, the current integral model, to be developed in Chapter 6, will use the entrainment velocity approach for the additional equation needed to relate the streamwise development of the mean velocity and the spread of the jet. This choice is based, in part, on the fact that the entrainment velocity has a physically based meaning and that it is used in existing environmental integral models. In addition, it can easily be modified to account for the effects of external turbulence as demonstrated by Slawson and Csanady (1967 and 1971).

2.5 Coflowing Jet Experiments

One of the first experimental investigations into coflowing jets is that of Squire and Trouncer (1944) who used the coflowing configuration as an extension to the problem of a jet issuing into quiescent background. Since then, there have been a number of experimental studies regarding coflowing jets. The ones most relevant to the present study have their initial conditions summarized in Table 2.2. The table presents the type of jet used, the working fluid, the measurement technique

Study	Jet Type	Fluid	Measuring System	d_j (cm)	U_j (m/s)	U_e (m/s)	$VR=U_j/U_e$	External Turbulence
Present	long pipe	water	LDA	0.953 & 2.223	varied	~0.07	~3 & ~6	yes
Van Heyst (1992)	short pipe	water	LDA	1.905	0.22	~0.072	~3	yes
Biringen (1986)	long pipe with nozzle	air	HWA (x-wire)	0.5 & 1.0	43.8	varied	3.33, 5, & 10	no
Fink (1977)	long pipe	air	pitot tubes & HWA	0.6	varied	~7.0	3.1, 4.1, & 5.75	yes
Smith & Hughes (1977)	long pipe with nozzle	air	HWA	5.0	35 & 70	~20	1.75 & 3.50	no
Antonia & Bilger (1973)	long pipe with nozzle	air	pitot tubes & HWA	0.528	91.3 & 137	~30.5	3.0 & 4.5	no
Reichardt (1965) (from Rodi, 1972)	?	air	HWA	?	?	?	1.67, 2.75, 4.24, & 7.94	no

Table 2.2: Summary of initial conditions for coflowing jet experiments. (LDA-laser Doppler anemometry; HWA-hot wire anemometry)

employed as well as the specific diameter of the jet model, d_j, the average mean velocity at the jet exit, U_j, the external mean velocity, U_e, and the initial velocity ratio, VR. The last column indicates whether or not a turbulent external coflow was also considered.

Note that only Van Heyst (1992) and Fink (1977) have employed a turbulent external flow and that, in both cases, this was achieved using only one turbulence generating grid. In each of these studies it was concluded that the presence of turbulence in the external flow caused the mean velocities in the jet to decrease more rapidly and the jet characteristic widths to increase more rapidly over the case of a jet in a nearly laminar external flow. In addition, an increase in the magnitude of the streamwise turbulent velocities and an increase in the magnitude of the streamwise integral length scales were also observed in the jet when the external flow was turbulent.

Fink (1977) has pointed out that turbulent mixing processes interact most effectively when the characteristic scales of turbulence are on the same order of magnitude. One shortcoming of both the experiments of Van Heyst (1992) and Fink (1977) is that only one turbulence generating grid is employed which limits the external turbulence to a single characteristic length scale and a single characteristic velocity scale, both of which evolve with downstream distance. In addition, both Van Heyst (1992) and Fink (1977) use only one jet diameter, although Fink (1977) uses three different initial jet velocities. Thus the characteristic scales of turbulence in the jet, especially the characteristic length scale, are limited in range in these experiments. To expand the range of characteristic turbulence scales in the experiments, multiple grids having different bar widths and multiple jet models having different jet diameters as well as several initial jet velocities should be used. This would result in experimental data that covers a range of characteristic turbulence scales both within the jet and in the external flow which would better elucidate the mechanisms involved in two interacting turbulent flow fields.

2.6 Research Objectives

Upon review of the relevant background and literature, the primary objectives of the current research can be restated as:

1. To acquire a new data base for turbulent isothermal jets released into uniform turbulent external coflows that incorporates a range of characteristic turbulent scales both within the jet and the external coflow.

2. To develop a new entrainment velocity function, to be incorporated into an integral model, that accounts for the interaction of the coflowing jet with the turbulent external coflow by determining the correct length and velocity scales that dominate the diffusion process as the jet evolves downstream.

with the secondary objectives being:

1. To determine if the initial conditions of the grid, especially the grid Reynolds number, have a continuous effect on the behaviour of grid-generated turbulence at finite grid Reynolds numbers as suggested by George (1992).

2. To investigate and perhaps determine the appropriate scaling for the mean and turbulent velocities in the coflowing jet.

Chapter 3: Experimental Apparatus, Methods, and Uncertainty

3.1 Introduction

This chapter provides a brief discussion and overview of the equipment used to obtain experimental data for both the grid-generated turbulence investigation and the coflowing jet experiments. Attention is focused on the water flume test facility, the turbulence generating grids, the coflowing jet models, and the laser Doppler anemometer (LDA) system. This is followed by a discussion of the experimental methodology employed to obtain accurate results and the level of experimental uncertainty contained within the results.

3.2 Experimental Apparatus

The principal components of the experimental apparatus are of the water flume facility, the

turbulence generating grids, and the coflowing jet models which will be discussed in detail in this section. The details of the laser Doppler anemometry (LDA) system and the traversing rigs used to locate the LDA are left to the next section for discussion.

The schematic given in Figure 3.1 illustrates the test section of the water flume and the relative placement of the turbulence generating grids and the coflowing jet models with respect to each other and with respect to the free surface and floor of the flume.

3.2.1 Water Flume

All the experiments were conducted in the water flume test facility located in the Fluid Mechanics Laboratory at the University of Waterloo. The closed-loop water flume is 12.2 m long with a cross section of 1.2 m wide by 0.8 m nominal operating depth. This large cross sectional area provides

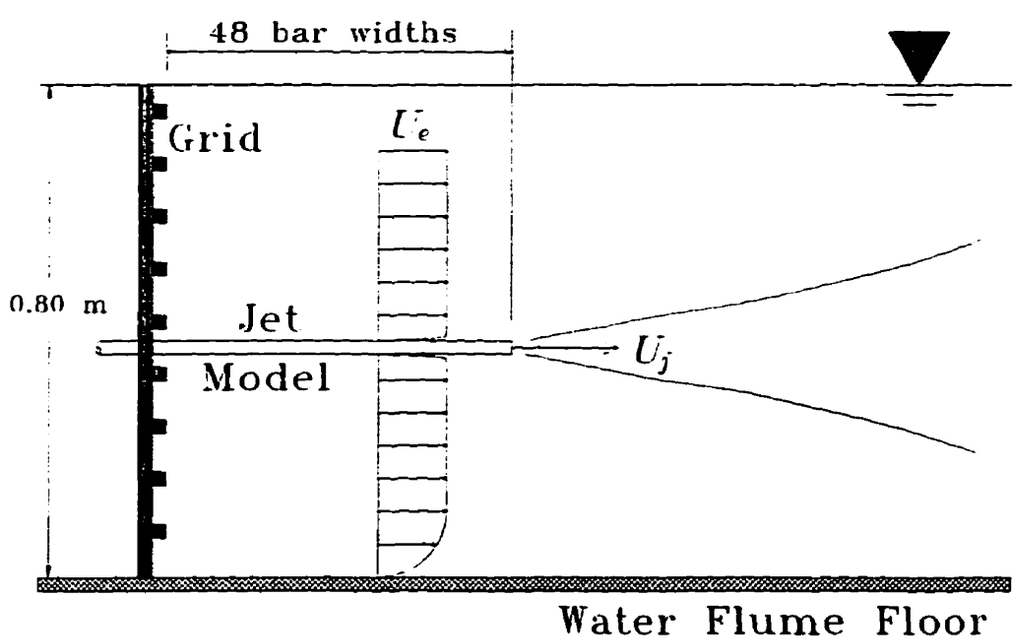

Figure 3.1: Schematic of the test section of the water flume with a jet model and a turbulence generating grid installed.

a central working core free from free-surface effects as well as blockage effects due to boundary layer development on the floor and sidewalls. Plexiglass sidewalls, spanning the entire test section, facilitate the use of a laser Doppler anemometer (LDA).

The water supply for the flume originates in a 90 m^3 storage sump located beneath the pump room in the Fluid Mechanics Laboratory. The water is pumped from the sump to a 24 m^3 constant volume head tank, equipped with an overspill weir, located directly above the pump room. From the head tank, the water passes through a control valve and into a cylindrical head tank located at the start of the flume after which the water enters the channel portion of the water flume.

A series of baffles, screens and a honeycomb located in the first two metres of the water flume effectively reduce all scales of turbulence which results in a very low turbulent flow. A restriction plate, located at the end of the water flume, provides sufficient resistance for the flow to obtain a nearly uniform mean velocity profile in the test section.

Once the water passes through the restriction plate at the end of the flume, it returns to the storage sump via a trench located below the water flume facility.

3.2.2 Turbulence Generating Grids

The turbulent energy in the water flume is increased by inserting one of two different turbulence generating grids upstream from the test section. Each grid is composed of a biplanar array of square aluminum bars with bar widths of b_s=1.27 cm and b_l=2.54 cm and mesh spacings of M_s=5.08 cm and M_l=10.16 cm where the subscripts s and l refer to the small and large grid respectively. The grid solidity for both grids is σ=0.44. The grid Reynolds numbers, based on the bar width and the mean velocity, are $Re_{b,s} \approx 900$ and $Re_{b,l} \approx 1800$. Square bars were used for the construction of the grids due to their insensitivity to Reynolds number variation since the location of flow separation is fixed for a square bar (Comte-Bellot and Corrsin, 1966). This is not the case for round rods

where the location of flow separation is strongly dependent on the Reynolds number of the flow.

The location of the grids upstream from the jet exit is set at 48 bar widths to ensure that the turbulence generated by the grids is approximately homogeneous (see, for example, Johnson and Johnston, 1989) in planes parallel to the grid by the location of the jet exit.

3.2.3 Coflowing Jet Models

Two coflowing jet models have been designed and constructed out of plexiglass tubing with inner diameters of 0.953 cm and 2.223 cm and a wall thickness of 0.159 cm. Both models are 1.3 metres in length and could be suspended in the water flume by two sets of thin wires with one set being located at the upstream start of the model and the other being located 30 cm upstream from the jet exit. Each set of mounting wires consists of four wires that are attached to the jet models at a 45° angle from the principal coordinate axes so that the wakes generated by the wires did not interfere with the jet in the measurement planes. This mounting configuration allows the jet to be aligned accurately with the flow and ensures that the jet is held rigidly in place.

To reduce flow separation around the jet exit due to the thickness of the plexiglass tube wall, the end of the models have been machined to produce a gradual taper to the exit. The boundary layer thickness along the jet models is estimated to be between 7 and 10 mm thick based on velocity traverses taken 2 mm down from the jet exit. The thickness of the boundary on the jet models does not appear to be dramatically affected by the levels of turbulence in the external flow and thus all experimental runs using the same jet model have approximately the same initial conditions at the jet exit.

For the small jet with an approximate initial velocity ratio (VR) of 3, the jet Reynolds number, based on the average mean velocity at the jet exit and the jet model diameter, is approximately 2000. To guarantee that the flow leaving this jet is turbulent, small screens had to be inserted into the model

tube upstream of the jet exit. The jet Reynolds number for the other experimental runs are on the order of 4000 or greater which is large enough to ensure the flow leaving the pipe is turbulent (Munson *et al*, 1990).

The water flow to the jet model is regulated using a calibrated flow meter and is set by the desired initial jet velocity ratio so that the flow rate leaving the jet model, divided by the model's cross-sectional area, gives an average velocity equal to the initial velocity ratio times the external mean velocity.

3.3 Velocity Measuring System

The primary component used to measure the instantaneous velocities in the water flume is the laser Doppler anemometry (LDA) system. The LDA employed in the current study is set up as a two-

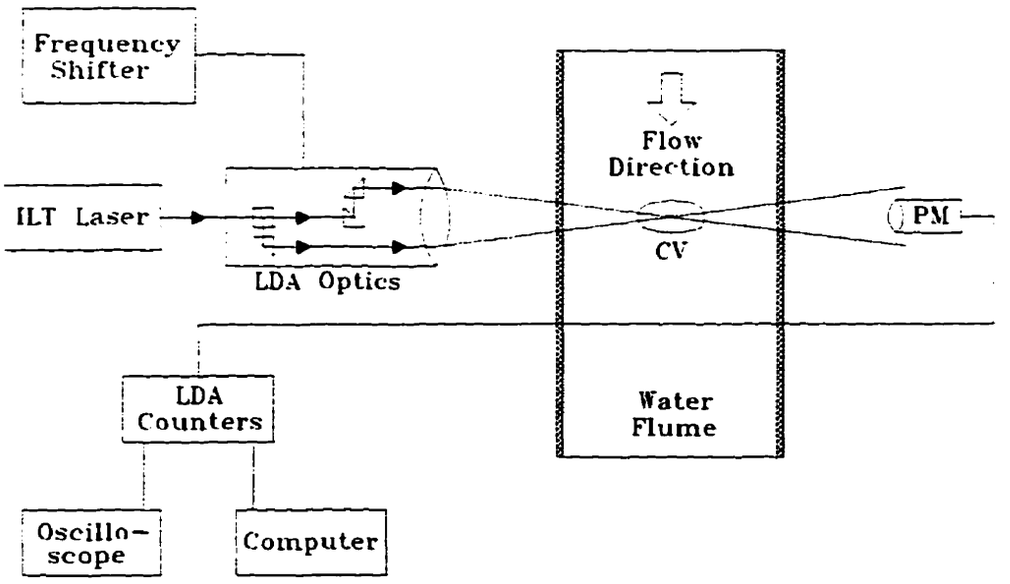

Figure 3.2: Schematic of the LDA system operating in forward scatter mode.

component two-colour forward scatter system as illustrated by the schematic in Figure 3.2. The system consists of an argon-ion laser, two-component modular optics, a photomultiplier (PM), an electronic frequency shifter, counters, an oscilloscope, and a data acquisition computer. The other major component of the measuring system is the traversing rigs on which the LDA system and the PM are mounted.

3.3.1 Laser Doppler Anemometry (LDA) System

The Ion Laser Technology (ILT) model 5500A laser is an air-cooled coherent light source capable of generating laser light in the 457 nm to 514.5 nm regime of the electromagnetic spectrum. The operating output power of the unit can be adjusted from 10 mW to 500 mW. Typical laser power in the experiments ranged between 200 mW and 300 mW as dictated by the quality of the signal being received at the PM from the control volume (CV).

The Dantec 55X modular optics are assembled into a two-component, two-colour forward scatter system. This optical arrangement allows for the simultaneous measurements of the streamwise and transverse instantaneous velocities in the control volume and has a better signal-to-noise ratio then the same system operating in back scatter mode.

Upon entering the LDA optics, the cyan laser beam is split into two beams of equal intensity by a neutral beam splitter. One of the beams then passes through a Bragg cell which, in conjunction with the frequency shifter, optically shifts the frequency of the laser beam by +40 MHZ. The other beam passes through a glass rod to equalize the optical lengths of the beams. Both beams then proceed through a series of beam splitters which split the cyan beams into a blue beam at 488 nm and a green beam at 514.5 nm. All four beams then pass through a beam translator which allows the beams to leave the optics at a specified separation. Finally, the beams pass through a beam expander and a 600 mm focusing lens before leaving the module.

After leaving the LDA optics, the laser beams pass through the plexiglass side wall of the water flume and intersect each other in the flow field to form a control volume. The beams continue to pass through the water and out the opposite side wall where they are blocked for safety reasons.

When two laser beams with the same frequency intersect each other, a stationary interference pattern of intensity fringes result. In highly turbulent flows and in reversing flows, this stationary interference pattern does not allow the LDA system to distinguish the flow direction and thus negative bias errors are introduced into the velocity data. However, when a frequency shifted beam and an unshifted beam intersect, the same interference pattern is produced only the fringes are no longer stationary but move with a known velocity. Thus in flows with near zero mean velocities or reversing velocities, shifting one beam enables a parallel transformation to be performed in the frequency domain that shifts the zero velocity away from the zero frequency, making it possible to determine the flow direction without introducing errors.

When the natural hydrosol or particles present in the water pass through the control volume, they scatter light from the blue and green beams' interference patterns. The photomultiplier (PM), located on the opposite side of the water flume, is focused on the control volume and detects the Doppler shift in the scattered light. The PM converts this optical velocity information to an electronic output which is sent to the two LDA counters for processing.

The output from the PM is a voltage with a frequency that is proportional to the velocity of the flow. The signal that corresponds to each particle passing through the control volume is termed a Doppler burst. The Dantec 55L90a LDA counters, operating in conjunction with the 55N10 frequency shifter, are used to find the frequency of these bursts and thus the velocity of the particle by determining the time it takes the particle to travel over eight fringes. The LDA counters also provide advanced data validation techniques as well as high-pass and low-pass filters to remove unwanted noise from the signal.

An analog frequency indication of the Doppler burst signal can be monitored using an oscilloscope

connected to the LDA counters. Simultaneously, a digital output is sent to a 286 personal computer where on-line velocity statistics are computed and where the raw data is archived in ASCII format for later processing.

In all the experiments, the sampling frequency of the LDA system is set at 250 Hz with 40960 paired instantaneous velocity measurements being collected at each position.

3.3.2 Traversing Rigs

A traversing rig for the laser and modular optics has been designed and built in-house to allow the control volume of the LDA system to be positioned anywhere within the test section of the water flume. The traversing rig has three mutually perpendicular axes which are all controlled by stepper motors where each step of the motor corresponds to a displacement of 6.35 μm (400 steps per revolution). The entire traversing rig is mounted on a sturdy steel table positioned on the concrete floor of the laboratory. The concrete floor is 0.91 metres thick and effectively isolates the traversing rig from any structural vibrations occurring in the laboratory.

A second traversing rig is used to move the PM, located on the opposite side of the flume, in series with the laser and optics. The PM traversing rig consists of two mutually perpendicular axes in the streamwise and vertical directions. Traversing in these two directions is accomplished using stepper motors in a similar manner as that of the LDA traversing rig. Since the PM contains a focusing ring to adjust for the lateral or cross stream position of the control volume, no traversing axis is required in this direction.

All stepper motors are wired to their respective drivers and power supplies which are controlled by the main data acquisition computer via the parallel printer port.

3.3.3 Noise Limitations of the LDA System

Although LDA systems offer many advantages, such as their non-intrusive measuring technique, there can be disadvantages associated with them as well. Besides the initial cost of the system, one disadvantage present in the current system, when operating in a sample-and-hold processing mode, is the introduction of random or white noise into the signal due to the random steps that occur at the arrival of new samples in the control volume (Adrian and Yao, 1987). In addition, the sample-and-hold process also tends to low-pass filter the combination of the true signal spectrum and the noise spectrum at a frequency that can be determined by the mean data rate. This low-pass filtering is attributed to the loss of information that occurs over the 'hold' periods (Adrian and Yao, 1987). As a result, measured data in low turbulent intensity flows can have their true spectra swamped by a noise spectrum at high frequencies.

One method of extracting the true spectrum from the noise-contaminated measured spectrum is to run the measured times series data through a Savitzky-Golay or least-squares filter program. The filter program assumes that the true variable is slowly varying over the measurement interval and that it is corrupted by random noise. Each data point is then replaced by a local average of the surrounding data points. Since nearby data points very nearly measure the same underlying value, averaging can reduce the level of noise without biasing the value obtained.

Appendix B gives the complete details of the noise encountered in the present low turbulent energy flows as well as the filtering techniques used to compensate for the noise contamination.

3.4 Experimental Methodology and Uncertainty

Uncertainty in measurements is due to two fundamental and distinct types of errors. The first type are random or precision errors, S, which represent the scatter about the average value and are usually the result of the characteristics of the measuring system as well as changes in the quantity

being measured. Precision errors can be quantified by using known statistical methods (see Appendix C). The second type of errors are fixed or bias errors, B, and show up in measurements as a displacement between the average measured value and the average true value. Unlike precision errors, bias errors must be estimated since no simple statistical method exists to quantify them.

The total uncertainty, δ, in a measured result is the combination of the precision errors and bias errors. The method used to combine the errors is the root-sum-square (RSS) method which is given by:

$$\delta_{RSS} = \left((tS)^2 + B^2 \right)^{1/2} \tag{3.1}$$

where the Student t multiplier is a function of the degrees of freedom used in calculating S. This method of error combination results in a 95% confidence interval on the total uncertainty. Full details of an uncertainty analysis, including error propagation into reported results, is given in Appendix C.

3.4.1 Grid-Generated Turbulence Experiments

To ensure that accurate measurements in grid-generated turbulence are obtained, six independent time series consisting of 40960 instantaneous paired velocity samples are acquired at each downstream location. The processed mean velocities, turbulent velocities, integral length scales, and energy spectra, given in Chapter 4, are thus the average of the six time series. The advantage of taking six measurements at a single location is that it effectively reduces the precision error by a factor of $1/\sqrt{6}$=0.408. The uncertainty associated with these measurements is summarized in Table 3.1 Note that the effect of taking six measurements is felt strongest in the power spectral density functions where the precision error is reduced from near 16% to approximately 6.5%.

Component	Precision Error, S	Bias Error, B	Total Error, δ_{RSS}
mean velocity, U_e	$\pm 0.002/\sqrt{6} = \pm 0.0008$	± 0.0179	± 0.018
turbulent velocities; $(\overline{u^2})^{1/2}$ & $(\overline{v_r^2})^{1/2}$	$\pm 0.0068/\sqrt{6} = \pm 0.0028$	± 0.0143	± 0.015
integral length scales; L_{xx} & L_{rr}	$\pm 0.0168/\sqrt{6} = \pm 0.0068$	± 0.0393	± 0.042
power spectral density functions; $E_{xx}(k)$ & $E_{rr}(k)$	$\pm 0.1580/\sqrt{6} = \pm 0.0645$	± 0.0200	± 0.131

Table 3.1: Summary of the normalized precision, bias, and total errors for a 95% confidence interval in the measured grid-generated turbulence quantities.

3.4.2 The Momentum Integral and the Coflowing Jet Experiments

For a jet in a coflowing external stream, one method available to determine the accuracy of the measurements is the momentum integral. This integral is a physical constraint for the flow in that the momentum added to the flow at the jet origin must be conserved across the jet at any downstream location. The momentum integral, M_o, also referred to as the excess jet momentum flux, is defined by:

$$M_o = 2\pi\rho \int_0^R \left[U(U - U_e) + \overline{u^2} - \frac{\overline{v_r^2} + \overline{v_\phi^2}}{2} \right] r\,dr = \text{constant} \qquad (3.2)$$

where ρ is the fluid density, R is the radius of the jet, U is the total mean velocity within the jet, U_e is the external coflow mean velocity, and $\overline{u^2}$, $\overline{v_r^2}$, and $\overline{v_\phi^2}$ are the square of the streamwise, radial, and azimuthal components of the turbulent velocity. The derivation of equation (3.2) is given in Appendix A.

The momentum integral, which is essentially an initial condition for the flow, provides a useful quantitative check for the measured velocity profiles since, in theory, it should be constant in the streamwise flow direction. However, in order to apply the momentum integral as defined by equation (3.2) to the present data, some simplification is necessary.

3.4.2.1 Approximation to the Momentum Integral

Since it is assumed that the jet is axisymmetric in the (r, ϕ) plane (*i.e.* no variation relative to ϕ), a measurement traverse along the centerline of the jet in a plane of symmetry is sufficient to evaluate all terms in the momentum integral. Due to the physical limitations of the laser Doppler anemometer (LDA), however, only two velocity components can be resolved at any one time (one of which must be the streamwise component) and thus an assumption must be made about the third in order to evaluate the integral. Based on the symmetry of the jet, two possibilities exist for a centerline traverse: either a vertical traverse at the lateral centre which yields streamwise and radial results or a horizontal traverse at the vertical centre which yields streamwise and azimuthal results. Figure 3.3 graphically illustrates the two traversing options. Since the primary interest of the current research is the turbulent entrainment of external fluid across the jet boundary, the velocities of primary interest are those that cross the jet boundary which are the radial velocities. The logical option for traversing is therefore the vertical traverse since it yields streamwise velocities and the desired radial velocities.

In order to evaluate the momentum integral as given in equation (3.2), an assumption regarding the behaviour of $\overline{v_\phi^2}$ must first be postulated. Ideally this general assumption would relate $\overline{v_\phi^2}$ back to either $\overline{u^2}$ or $\overline{v_r^2}$ so that equation (3.2) can be simplified with no new terms being introduced.

To determine the general behaviour of $\overline{v_\phi^2}$, a set of preliminary experiments have been conducted that entail measurement traverses in both the vertical and horizontal planes of symmetry for the small jet at a downstream location of x_j=40.2 cm with VR≈3 and 6 and in the absence of any

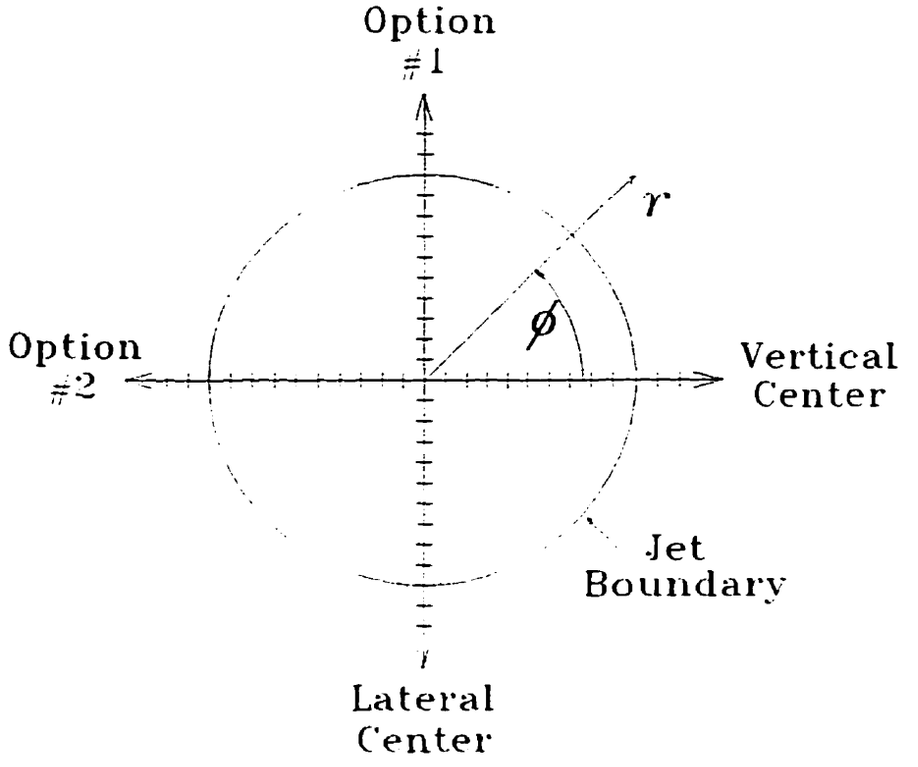

Figure 3.3: Illustration of the two traversing options available for LDA measurements on the jet centerline in the (r, ϕ) plane.

turbulence generating grids. It is found that, for a given initial velocity ratio, the mean velocity profiles exhibit the same profile shape, both in width and maximum velocity, when compared to each other thus substantiating the assumption of axisymmetry in the (r, ϕ) plane. The turbulent velocity results are presented in Figures 3.4 and 3.5 for $VR \approx 3$ and 6 respectively. Note that the axes in both plots have not been normalized so that an estimate of the relative variation between the two traversing options can be obtained from the streamwise turbulent velocity component. Although there is some minor variation in the $(\overline{u'^2})^{1/2}$ profiles between the different traversing options, they essentially have the same profile shape in magnitude and in width, which again confirms the assumption of axisymmetry in the (r, ϕ) plane. The remaining data on Figures 3.4 and 3.5 consists of $(\overline{v_r'^2})^{1/2}$ measured in the vertical traverse and $(\overline{v_\phi'^2})^{1/2}$ measured in the horizontal traverse. These profiles show good agreement with each other both in shape and in magnitude.

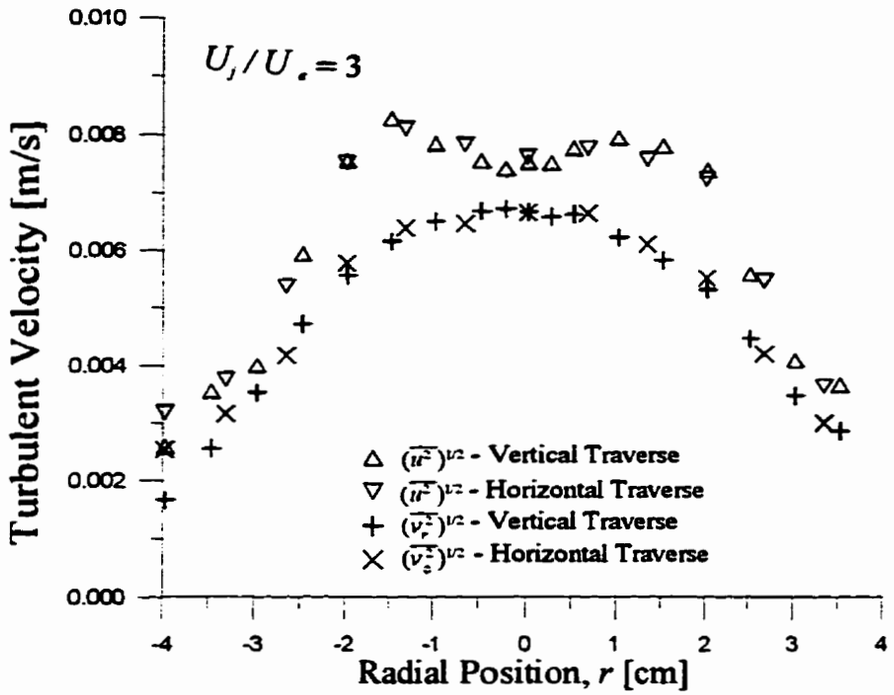

Figure 3.4: Turbulent velocity profiles for the small jet at $VR \approx 3$ and $x_j = 40.2$ cm.

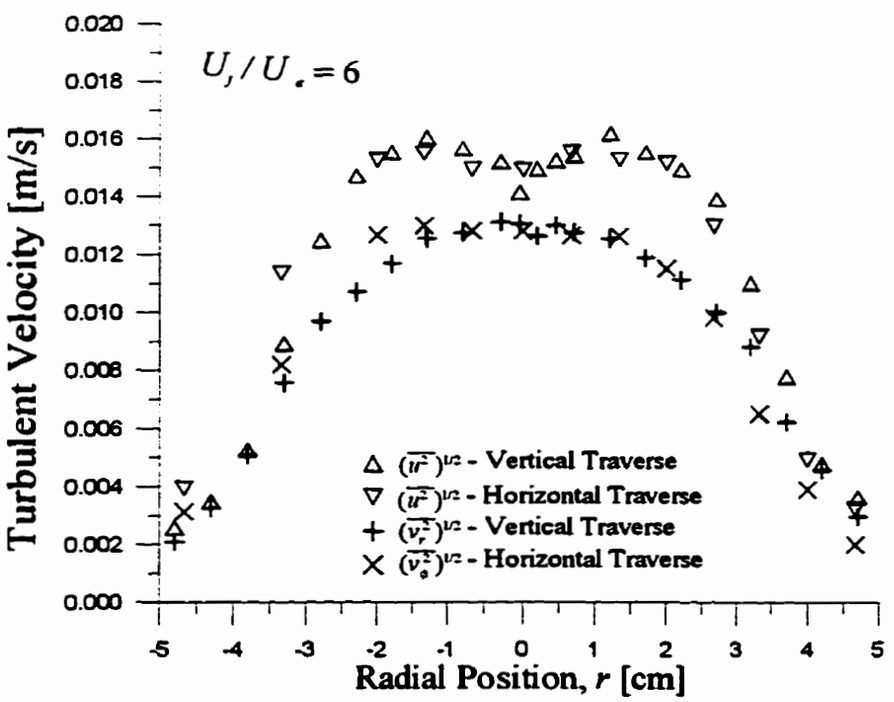

Figure 3.5: Turbulent velocity profiles for the small jet at $VR \approx 6$ and $x_j = 40.2$ cm.

It will thus be generally assumed that $(\overline{v_\phi^2})^{1/2}$ can be approximated by $(\overline{v_r^2})^{1/2}$, at least to within the relative variation as demonstrated by the streamwise components. This assumption is also supported by the radial and azimuthal turbulent velocity data of Biringen (1986) for a jet in a laminar coflow.

The momentum integral can thus be approximated by:

$$M \approx 2\pi\rho \int_0^R \left[U(U - U_e) + \overline{u^2} - \overline{v_r^2} \right] r\, dr \tag{3.3}$$

without introducing significant error.

3.4.2.2 The Momentum Integral and the Experimental Data

Using equation (3.3), the degree of conservation of initial momentum was checked at each traversing location for each of the twelve experimental runs. For the four runs with a low turbulent background (*i.e.* no turbulence generating grid installed), the initial jet momentum is conserved to within 90 percent or better up to the final traversing location. With the turbulence generating grids installed, the initial momentum of the jet is conserved to within 85 percent or better. The greater degradation of momentum conservation in the later case is in part due to the fact the equation (3.3) neglects terms that arise in the derivation due to the external turbulence (see Appendix A for details). The effect of the external turbulence is not only to augment the diffusion of jet momentum but also mask the turbulence of the jet thus making the jet momentum more difficult to experimentally detect.

In the literature, it is often assumed that the square of the turbulent velocities make a negligible contribution to the total momentum integral (see, for example, Hinze, 1975). Antonia and Bilger

(1973) and Capp (1983), however, have estimated that the contribution of the square of the turbulent velocities to the momentum integral for a coflowing jet in a laminar external flow is under ten percent based on extrapolated estimates from jets in quiescent backgrounds. The present data for a jet in an external coflow indicates that the effect of the ($\overline{u'^2} - \overline{v_r'^2}$) term in the integral is to increase the magnitude of the momentum integral between one and eight percent. This increase follows the general trend of increasing very rapidly to a maximum shortly beyond the jet exit after which it begins to diminish with increasing distance. Figure 3.6 depicts this trend in the evolution of the percent contribution of the ($\overline{u'^2} - \overline{v_r'^2}$) term in the integral to the total magnitude of the momentum integral for the four cases of a jet in a low turbulent coflow (*i.e.* no turbulence generating grid installed). The average contribution to the total momentum integral for the four cases exhibited in Figure 3.6 is only 3.6%. When the external flow is made turbulent through the use of a grid, the average percent contribution of the fluctuating terms is increased to 4.3% with

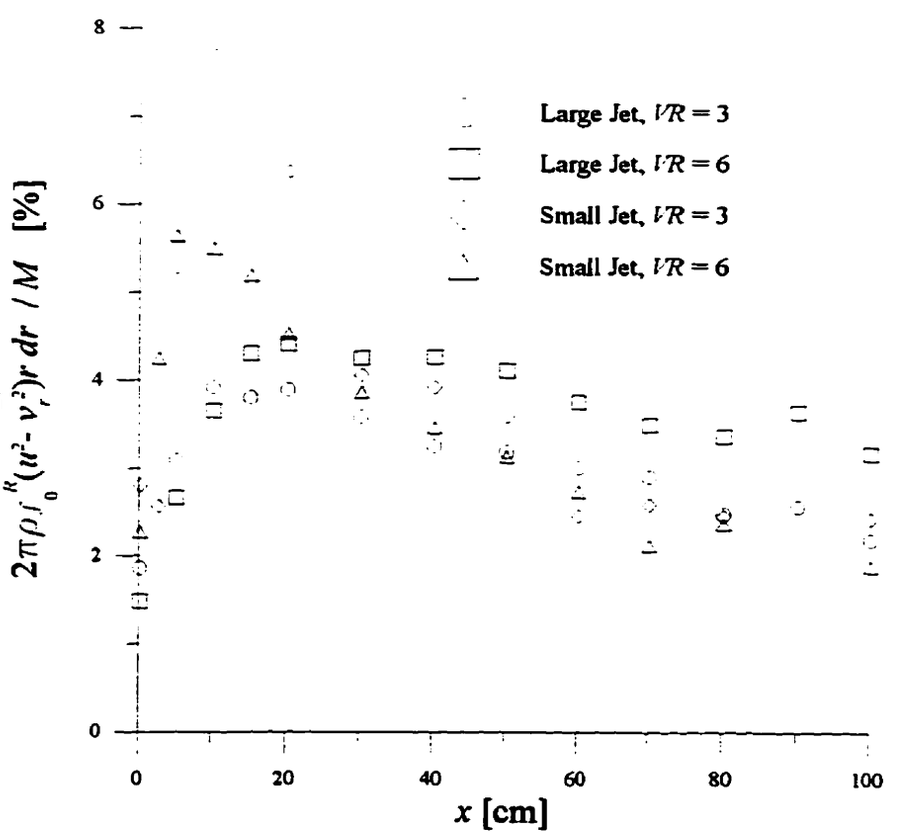

Figure 3.6: Percent contribution of the ($\overline{u'^2} - \overline{v_r'^2}$) term in the momentum integral (equation 3.3) to the total momentum for jets in a low turbulent coflow.

the small grid installed and increased further to 5.2% with the large grid installed.

3.4.2.3 Experimental Uncertainty for the Coflowing Jet

Estimates of the precision error, bias error, and total error for the principal coflowing jet quantities is summarized in Table 3.2. The difference between these errors and those presented for grid-generated turbulence is that the precision errors are given for a single time series. A detailed error analysis is given in Appendix C.

Component	Precision Error, S	Bias Error, B	Total Error, δ_{RSS}
mean velocity, U_e	±0.0020	±0.0179	±0.018
turbulent velocities; $(\overline{u^2})^{1/2}$ & $(\overline{v_r^2})^{1/2}$	±0.0068	±0.0143	±0.020
integral length scales; L_{xx} & L_{rr}	±0.0168	±0.0393	±0.052
power spectral density functions; $E_{xx}(k)$ & $E_{rr}(k)$	±0.1580	±0.0200	±0.317

Table 3.2: Summary of the normalized precision, bias, and total errors for a 95% confidence interval in the measured coflowing jet quantities.

3.5 Closure

Details of the experimental apparatus have been presented in this chapter along with the measuring techniques used to check the experimental data and the uncertainties associated with the measured data.

Chapter 4: The External Flow

4.1 Introduction

The objective of this chapter is to experimentally characterize the behaviour of the external flow field both in the absence and presence of turbulence generating grids and without the jet model installed. The mean velocity and turbulent intensities of the external flow in the absence of a grid are first examined. This is followed by an analysis of the external flow field with the small and large grids installed which details the behaviour of the turbulent intensities, integral length scales, and turbulent energy spectra. A comparison of these results to relevant data and theory in the grid-generated turbulence literature is also made. The chapter is concluded with a summary of the major findings of the present experimental study.

4.2 External Flow in the Absence of a Grid

4.2.1 Mean Velocity Profiles

Typical mean velocities, U_e, measured in the external flow in three vertical traverses in the absence of a grid, are given in Figure 4.1. The downstream locations of the traverses are near the start (x=10 cm), near the middle (x=50 cm), and near the end (x=100 cm) of the working window. This gives a representative vertical picture of the mean velocity over the entire traversing regime. All three profiles are remarkably similar to each other both in their magnitude of U_e as well as their relative profile shape. Also included in the figure is the approximate vertical location of the jet

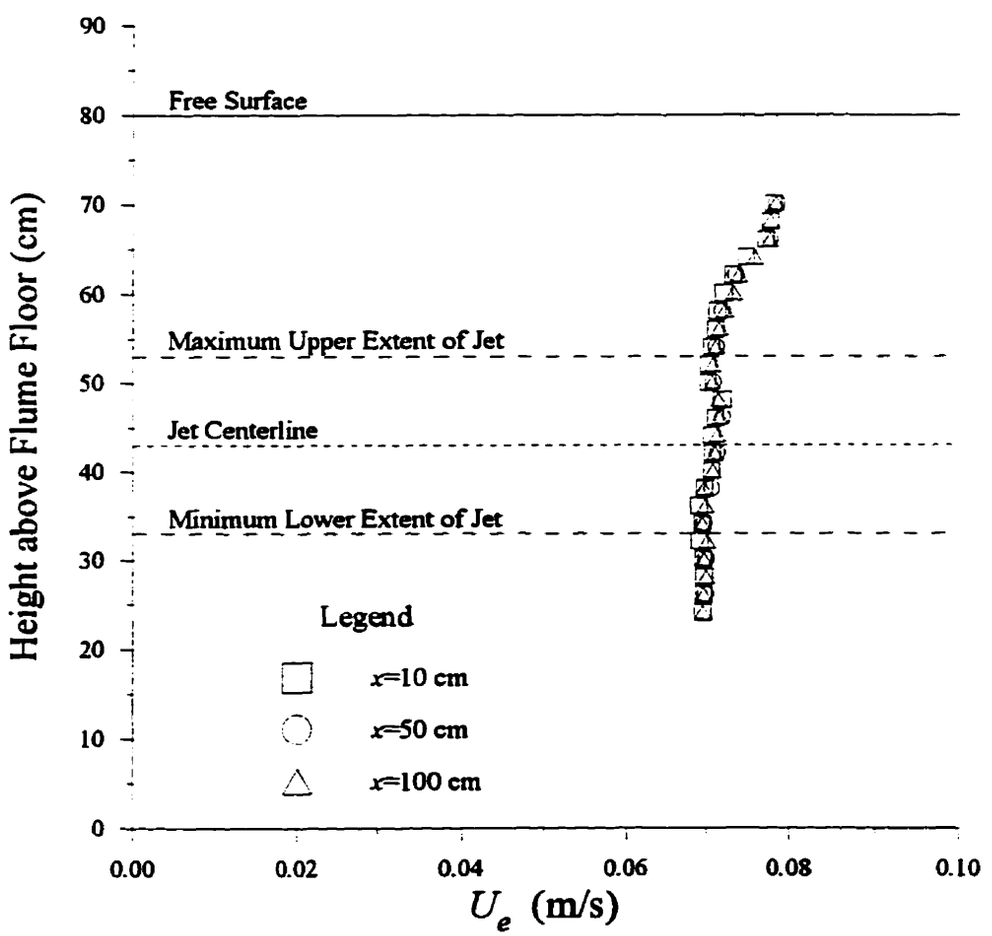

Figure 4.1: Vertical variation of the external streamwise mean velocity on the transverse centreline of the flume in the absence of any grid.

model centerline as well as upper and lower limits for the maximum jet radius conservatively estimated at ±10 cm based on the results in Chapter 5. Although the profile is not uniform over the distance covered by the limits of the jet radius, it can be approximated as such with $\overline{U}_e$=0.07055 ±0.00076 m/s where the ±0.00076 represents one standard deviation from the average value.

The lateral or cross-stream variation of U_e, although not shown graphically, can be similarly summarized by $\overline{U}_e$=0.07078±0.00055 m/s over the maximum diameter of the jet.

4.2.2 Turbulent Intensity Profiles

The streamwise and transverse (or radial) turbulent intensities, defined respectively as:

$$T_x = \frac{\sqrt{\overline{u_e^2}}}{U_e} \tag{4.1}$$

and

$$T_r = \frac{\sqrt{\overline{v_{r,e}^2}}}{U_e} \tag{4.2}$$

are given in Figures 4.2 and 4.3 for the same three vertical traverses as for the mean velocity. The average value and standard deviation for T_x over the maximum radial limits of the jet is given by $\overline{T}_x$=0.00868±0.00103 while for T_r, it is given by $\overline{T}_r$=0.00387±0.00027 for the same range. Note that the turbulent intensity in the radial direction is less than half the value in the streamwise direction and that there is significantly less scatter in T_r than in T_x as indicated by the data in the figures and by the magnitudes of the respective standard deviations. This high level of anisotropy between the two turbulent intensity components is probably caused by the honeycomb located upstream of the test section which is more effective, due to its configuration, at reducing the

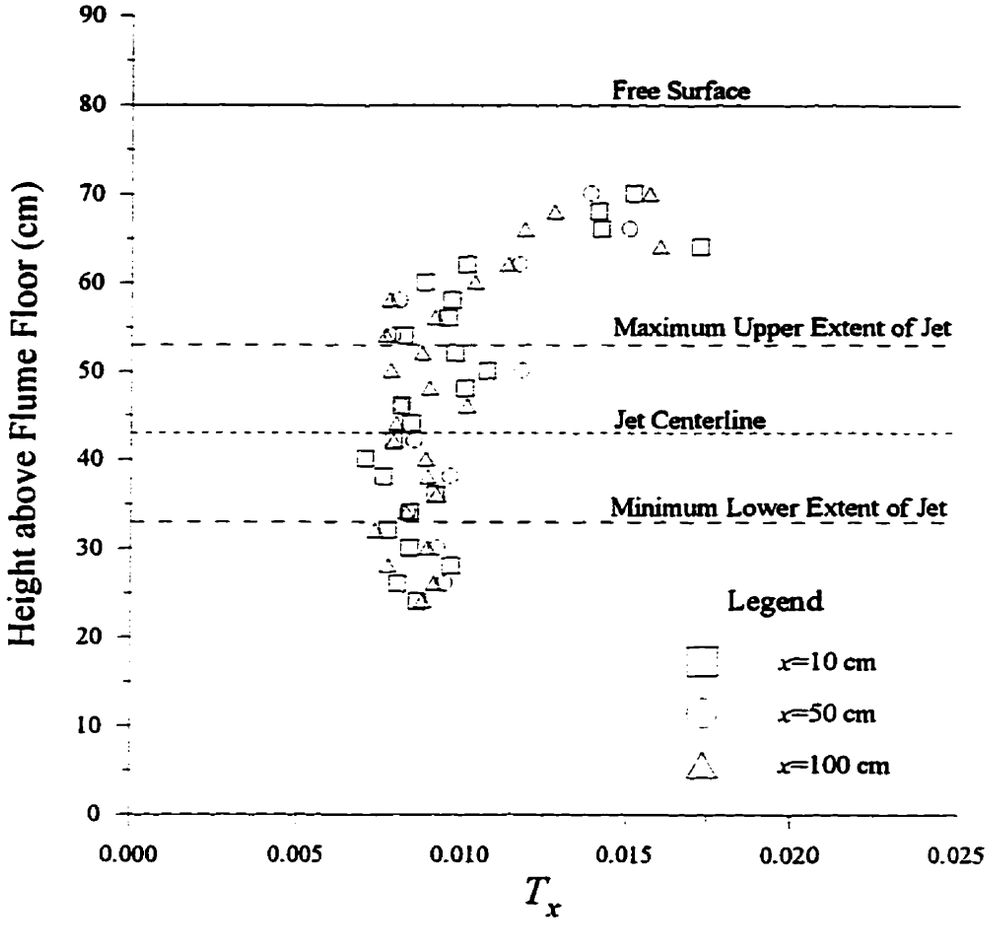

Figure 4.2: Vertical variation of the external streamwise turbulent intensity in the absence of any grid.

turbulent energy in the radial direction than in the streamwise direction.

The lateral or cross-stream variation of the two turbulent intensity components across the maximum jet diameter is given by $\overline{T}_x$=0.00782±0.00078 and $\overline{T}_r$=0.00352±0.00024 and are consistent with the trends observed for the vertical variation of the turbulent intensities.

Note that the external flow in the absence of a turbulence generating grid is not truly laminar due to the existence of small levels of turbulence. The external flow in the absence of a gird is therefore classified as a low turbulent external flow with turbulent intensities under one percent.

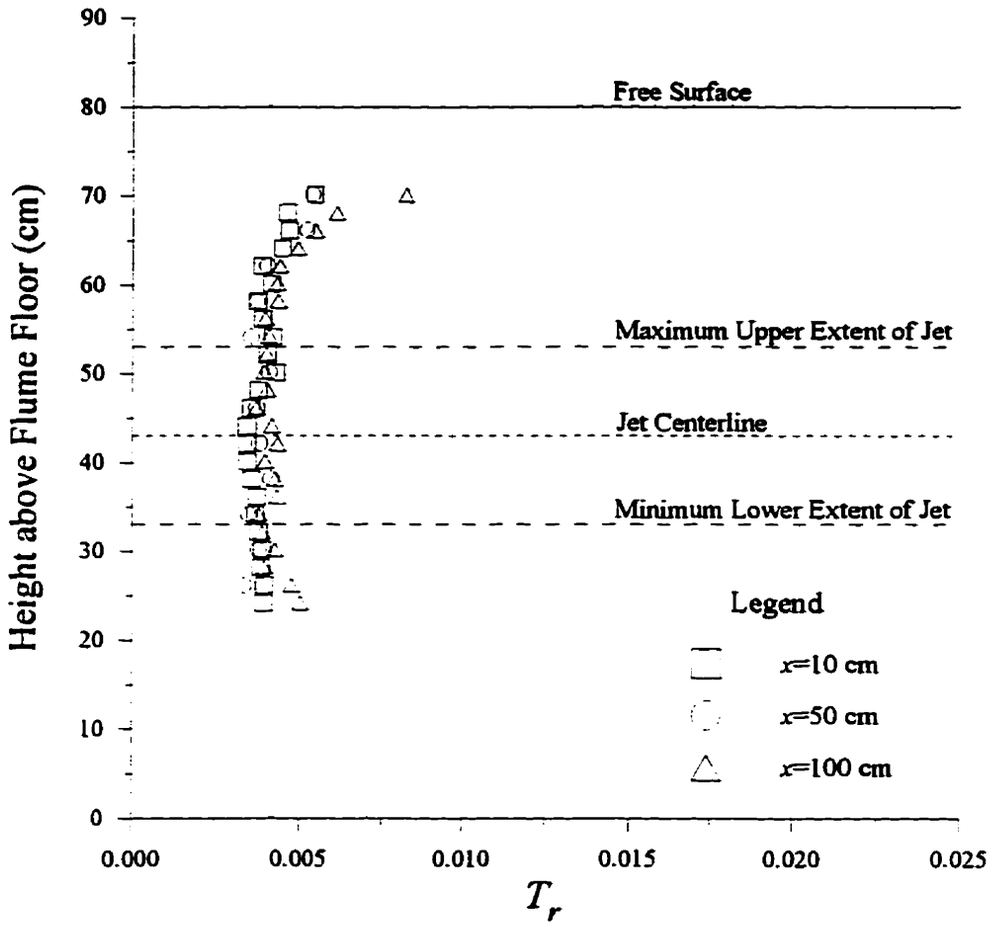

Figure 4.3: Vertical variation of the external transverse turbulent intensity in the absence of any grid.

4.2.3 Integral Length Scales and Turbulent Energy Spectra

The low levels of turbulent energy in the external flow with no grid installed coupled with the inherent low level energy noise of the LDA system made measurements of the integral length scales and turbulent energy spectra too unreliable to report meaningful results (see Appendix B for a detailed analysis of the problem).

4.3 External Flow in the Presence of Grids

In order to augment the turbulent energy of the external flow, turbulence generating grids are inserted upstream of the test section of the water flume. The turbulence is created by the wakes and momentum jets formed behind the grid which eventually coalesce downstream resulting in nearly homogeneous turbulence in planes parallel to the grid by x_g/b=40 (see, for example, Johnson and Johnston, 1989).

The traditional view of grid-generated turbulence is that the turbulent energy decay asymptotically approaches a common universal self-preserving state for all grids (see, for example, Hinze, 1975, and Roach, 1987) where the term 'self-preserving' is taken here to imply that the flow has reached an equilibrium where all the dynamical influences evolve together and no further relative dynamical readjustment is required (George, 1989). George (1992) has demonstrated, based on more general form of the traditional self-preservation theory, that the decay of turbulent energy in grid-generated turbulence is, in part, determined by the initial conditions of the flow. Thus no universal self-preserving state can exist for all grids at finite grid Reynolds numbers.

In the present study, the grid Reynolds numbers for the two grids are $Re_{b,s}$=900 and $Re_{b,l}$=1800 where the subscripts s and l refer to the small and large grids respectively. The above discussion implies that the decay of turbulent intensities, the growth of integral length scales, and the spectral decay of turbulent energy will be unique for each grid since the grid Reynolds numbers are finite.

4.3.1 Turbulent Intensities

The streamwise turbulent intensities for the small and large grids are given in Figure 4.4 as the hollow circles and squares respectively. Individual best fit power law equations to this data yield:

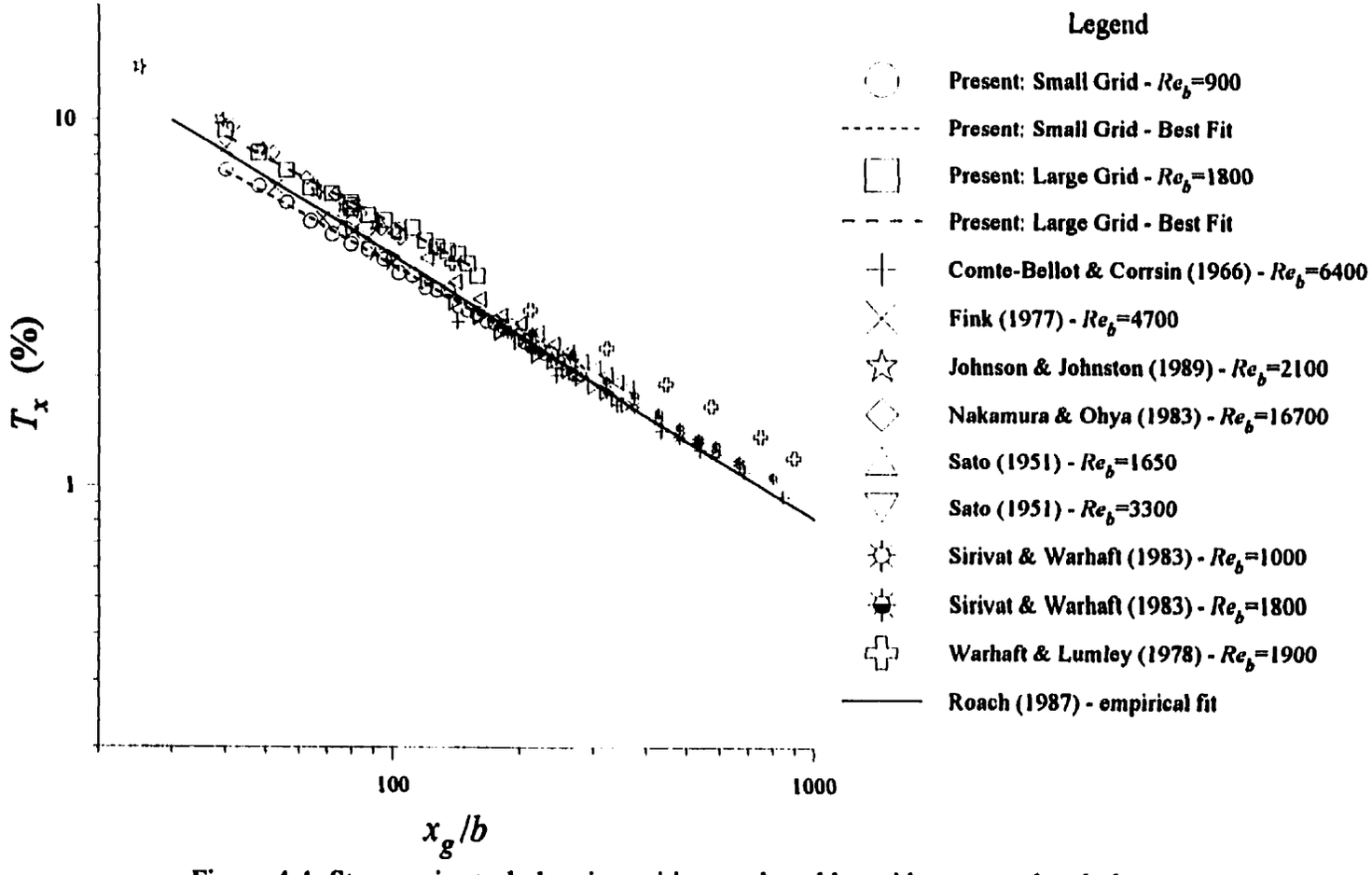

Figure 4.4: Streamwise turbulent intensities produced by grid-generated turbulence.

$$T_{x,s} = 0.784\left(\frac{x_g}{b}\right)^{-0.648} \qquad \& \qquad T_{x,l} = 0.857\left(\frac{x_g}{b}\right)^{-0.612} \tag{4.3}$$

where x_g is the distance from the turbulence generating grid. These equations are included as the dashed lines in the figure. Both exponents in equation (4.4) are within the experimental range of $-0.675 \le n/2 \le -0.50$ as reported by Hinze (1975) with the large grid exponent greater than that of the small grid. This is consistent with George (1992) in that the exponent should increase towards -0.5 as Re_b increases towards infinity.

Six other square bar experimental data sets are also included in the figure along with the empirical fit of Roach (1987) given by equation (2.15). The data for T_x follows similar decay rates as the present results although there is significant scatter in the magnitude of T_x between individual experiments at the same downstream location. Roach's empirical fit approximates the average of the data well near the grid but decays too rapidly thus underestimating T_x far downstream from the grid.

In the studies reporting results at two values of Re_b (Sato, 1951, Sirivat and Warhaft, 1983, and the present study), larger values for T_x are consistently measured at the higher Re_b experiment at the same normalized distance from the grid thus indicating that T_x is dependent on Re_b, at least over the range of $900 \le Re_b \le 3300$. This Re_b dependency is not readily apparent when the entire data set, as given in Figure 4.4, is considered. Failure of the data to collapse to a single universal state suggests that either there is considerable experimental scatter in all the data sets or that each experiment has a self-preserving state that is uniquely determined by the initial conditions of the flow as surmised by George (1992). Since the difference within individual experiments reporting results at two values of Re_b is dependent on Re_b, an initial condition of the flow, it seems most probable that the overall variation of T_x is the result of different initial conditions rather than solely experimental scatter. No discernable difference in the results, however, can be attributed solely to the working fluid of the experiments.

In a similar manner to the streamwise turbulent intensities, the present transverse turbulent intensities are given in Figure 4.5 as the hollow circles and squares for the small and large grid respectively. Individual best fit power law equations to the data, also included in the figure, yield:

$$T_{r,s} = 0.682\left(\frac{x_g}{b}\right)^{-0.641} \qquad \& \qquad T_{r,l} = 0.721\left(\frac{x_g}{b}\right)^{-0.604} \tag{4.4}$$

where the exponents are again within the range reported by Hinze (1975). In addition, the large grid exponent (larger Re_b) is greater than that for the small grid as expected based on the streamwise results and George (1992).

Experimental data from four other studies and the empirical fit of Roach (1987) (equation (2.15)) are also included in the figure and behave in much the same fashion as their streamwise counterparts given in Figure 4.4. The two studies reporting T_r results at two values of Re_b (Sirivat and Warhaft, 1983 and the present study) again consistently report larger values for T_r at any given downstream location for the higher Re_b experiment. This again points to a dependency on the initial conditions of the flow within individual experiments.

A comparison between the present results for T_x and T_r indicate that the two turbulent intensities behave similarly except that the magnitudes for T_r are smaller at any downstream location. This anisotropy, which can be characterized by the ratio of the streamwise turbulent velocity to the radial or transverse turbulent velocity, ranges from 1.07 to 1.18 for the small grid and from 1.10 to 1.20 for the large grid and are within the typical range of 1.0 to 1.5 as given by Roach (1987).

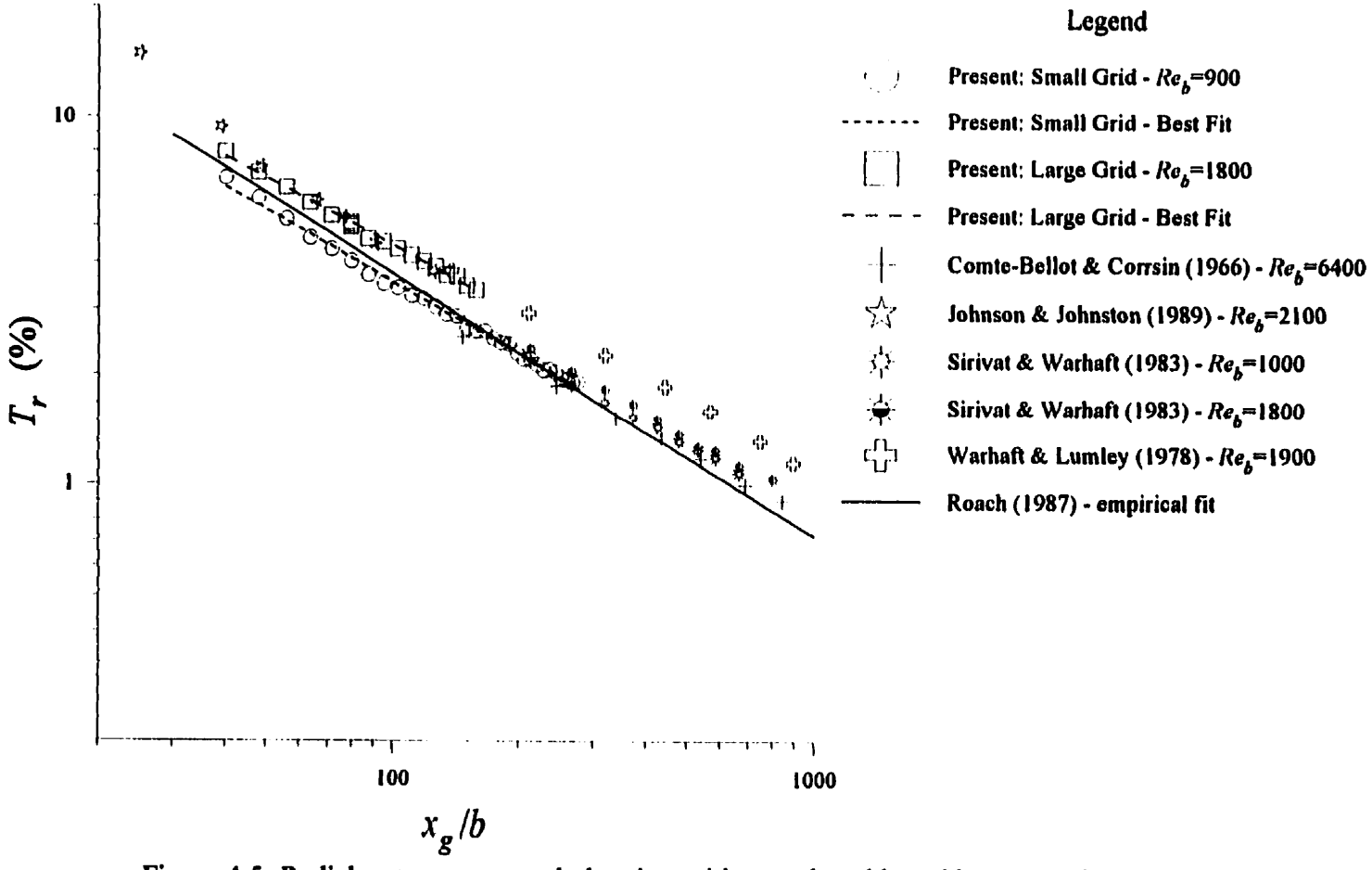

Figure 4.5: Radial or transverse turbulent intensities produced by grid-generated turbulence.

4.3.2 Turbulent Integral Length Scales

The streamwise integral length scales, L_{xx}, normalized by the grid bar width, are given in Figure 4.6 for both the small and large grid. Power law fits to the current L_{xx}/b data, included in the figure as the dashed lines, yield:

$$\frac{L_{xx,s}}{b} = 0.427\left(\frac{x_g}{b}\right)^{0.392} \qquad \& \qquad \frac{L_{xx,l}}{b} = 0.369\left(\frac{x_g}{b}\right)^{0.465} \tag{4.5}$$

where both exponents fall within the expected experimental range of $0.30 \le p \le 0.53$ as reported by Hinze (1975). Note, however, that the large grid experiences a faster rate of growth for L_{xx}/b than the small grid.

Studies reporting streamwise integral length scales appear to be limited to that of Fink (1977), Nakamura and Ohya (1983), and Sirivat and Warhaft (1983). These results are also included in the figure along with the empirical fit of Roach (1987) given by equation (2.16). In determining the empirical fit, Roach (1987) used the data of Nakamura and Ohya (1983) and Sirivat and Warhaft (1983) and thus the agreement with these two data sets is not surprising. Fink (1977) and the present results, however, show greater magnitudes for L_{xx}/b at a given non-dimensional distance downstream from the grid and an overall slower rate of growth. Examination of the initial conditions of the experiments reveals that the grid solidity of Nakamura and Ohya (1983) and Sirivat and Warhaft (1983) is σ=0.34~0.35 while the grid solidity for Fink (1977) and the present grids is much higher at σ=0.44. Thus the gird solidity (initial condition) appears to have a significant effect on the size and growth rate of the streamwise integral length scales.

In addition, the data of Sirivat and Warhaft (1983) and the present data, which report results at two values of Re_b show that, at any given downstream location, larger magnitudes of L_{xx}/b consistently correspond to the experiment at the higher Re_b thus indicating that the grid Reynolds number dependency extends to the integral length scales as well as to the turbulent intensities.

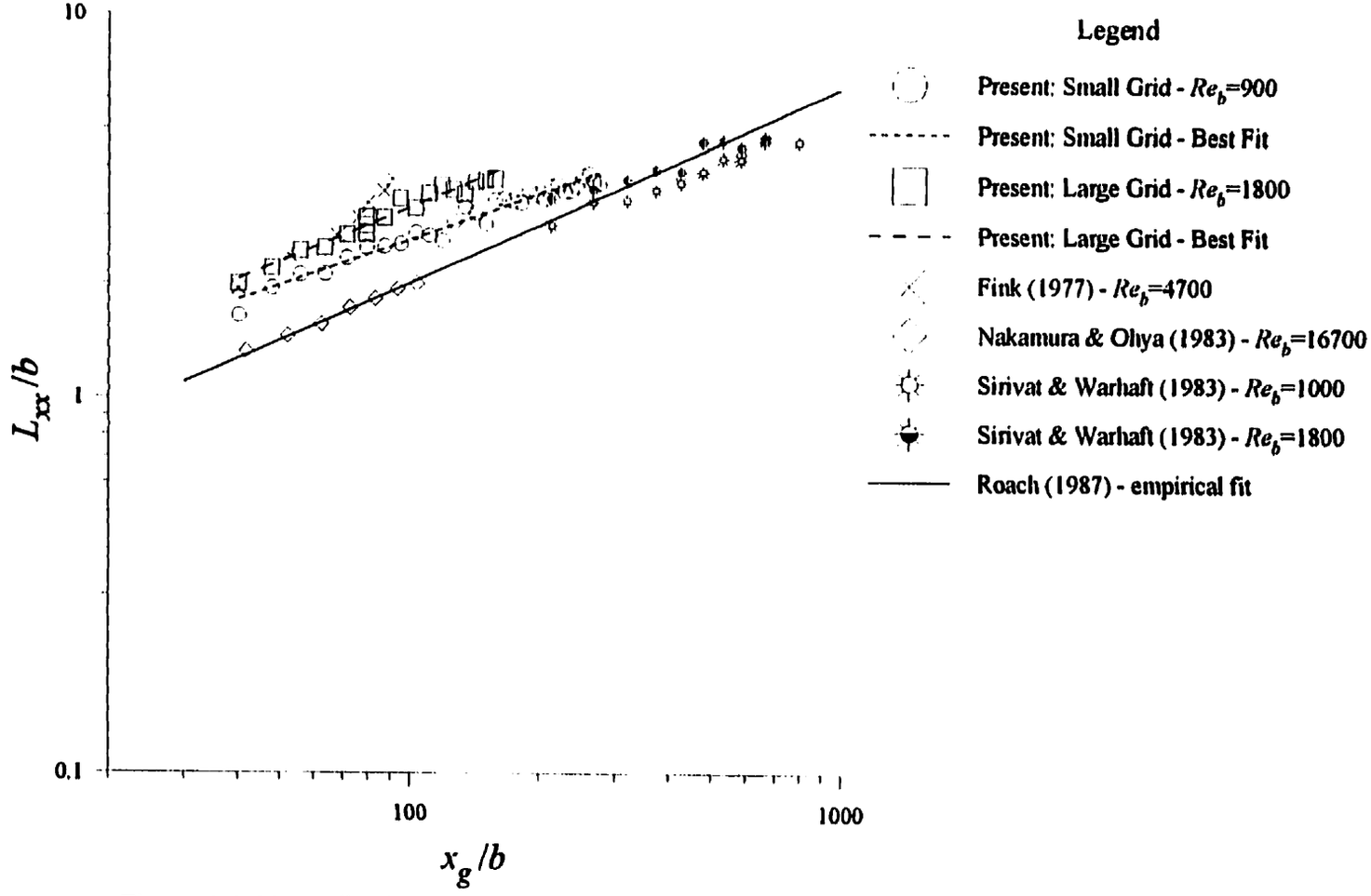

Figure 4.6: Normalized streamwise integral length scales produced by grid-generated turbulence.

The transverse integral length scales, L_{rr}, are given in Figure 4.7 for both the small and large grids normalized by the grid bar width. Note that L_{rr} by its definition (see equation (2.9)) is not strictly a true transverse integral length scale since it relies on the mean convecting streamwise velocity to convert from a temporal scale to a spatial scale. Power law fits to the present data yield:

$$\frac{L_{rr.s}}{b} = 0.196\left(\frac{x_g}{b}\right)^{0.417} \qquad \& \qquad \frac{L_{rr.l}}{b} = 0.183\left(\frac{x_g}{b}\right)^{0.448} \tag{4.6}$$

and are included in the figure as the dashed lines. Again, the exponents are within the experimental range as reported by Hinze (1975) with the larger grid (*ie.* higher Re_b) exhibiting a larger value for the growth exponent.

Other square bar grid experiments have not reported values for L_{rr}. Roach (1987) proposes an empirical fit for L_{rr}, as given by equation (2.16), by assuming that $L_{rr}=L_{xx}/2$. This empirical fit is included in the figure and displays the same relative behaviour in comparison to the present data as that of the streamwise component.

Based on the present transverse data, it is again apparent that there is a grid Reynolds number dependency since larger values of L_{rr}/b are typically obtained with the large grid (*ie.* higher Re_b value).

A comparison of the present streamwise and radial integral length scales indicates that the two components behave similarly except that the magnitudes of L_{rr}/b are nearly half that of L_{xx}/b at any downstream location. This lends credence to the assumption used by Roach (1987) in his derivation of an empirical fit to the radial or transverse integral length scales.

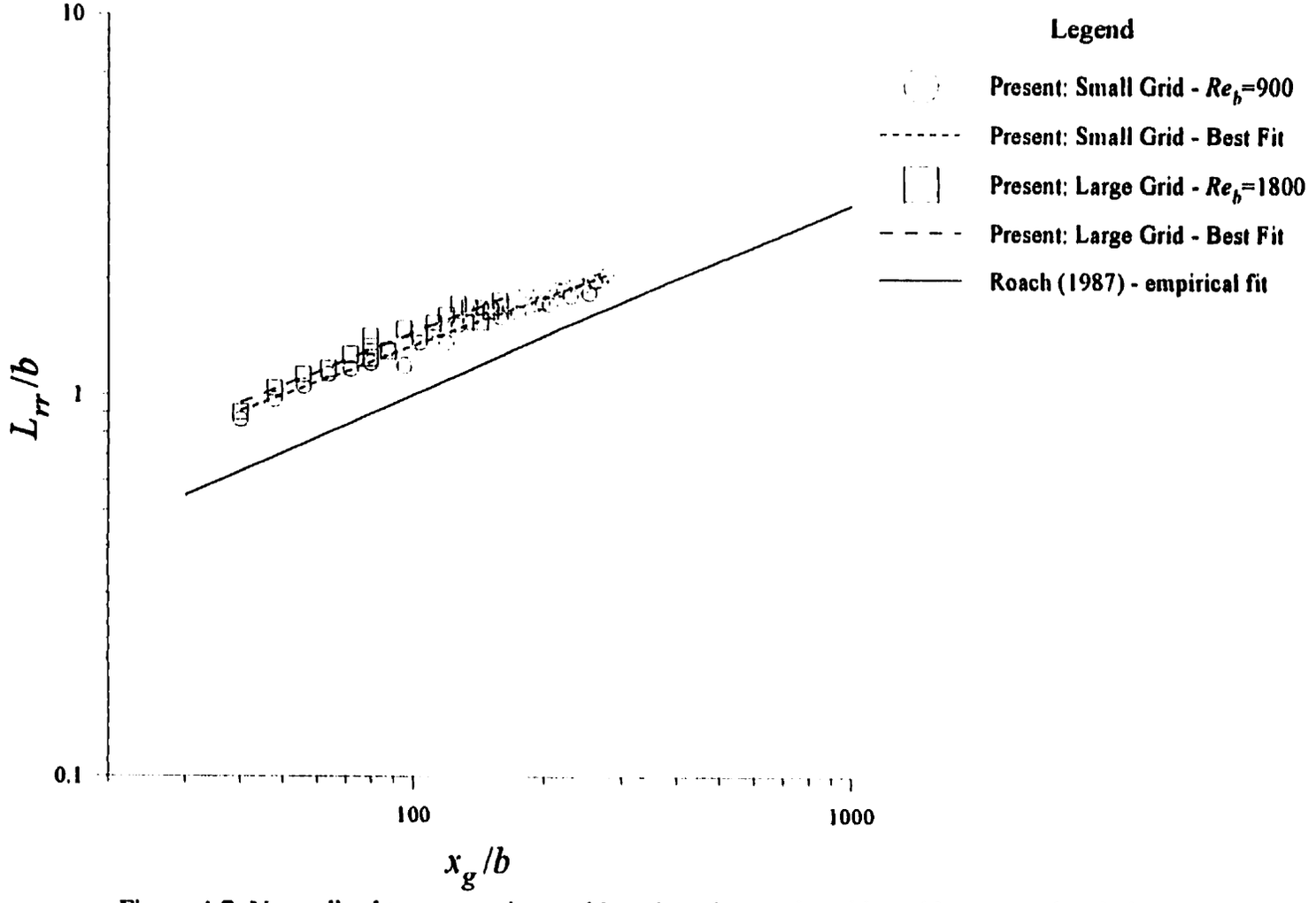

Figure 4.7: Normalized transverse integral length scales produced by grid-generated turbulence.

4.3.3 Streamwise Turbulent Energy Spectra

As a means of examining the turbulent energy content at a given wavenumber, k, the streamwise one-sided power spectra density (PSD) function, $E_{xx}(k)$, evaluated at three downstream locations for both the small and large grids, is given in the top two graphs of Figure 4.8. None of the previous studies mentioned have reported turbulent energy spectra. Thus, in order to compare the present data with other experimental data, the grid-generated turbulence spectra of Comte-Bellot and Corrsin (1971) (b=0.953 cm, M=5.08 cm, σ=0.34, U_e=12.7 m/s, and $Re_b \approx 8000$) are used and are given in the bottom graph of Figure 4.8. Note, however, that Comte-Bellot and Corrsin (1971) inserted their grid upstream of a slight contraction (1.27:1) in an attempt to make the resulting turbulence behind the grid more isotropic. In addition, the data of Comte-Bellot and Corrsin (1971) is obtained much further downstream than the present results. Also included in the three figures for reference purposes is an approximate spectrum for isotropic turbulence (Hinze, 1975) given by:

$$\frac{E_{xx}(k)}{\overline{u^2} L_{xx}} = \frac{2}{\pi\left(1 + \left(k L_{xx}\right)^2\right)} \tag{4.7}$$

This equation, however, strictly applies to homogeneous, isotropic turbulence and even then becomes invalid at very high wavenumbers. However, judging from Figure 4.8, all three sets of spectra follow the approximate spectrum for isotropic turbulence fairly well up until $kL_{xx} \approx 20$ after which the measured spectra decrease more rapidly than the approximate spectrum.

In order for a flow to be in a state of self-preservation, there can be no dynamical readjustments of the turbulent energy in the spectrum over the wavenumber regime. The three normalized spectra of Comte-Bellot and Corrsin (1971) have the same relative shape at each downstream location. It can therefore be concluded that flow has reached a state of self-preservation sometime before x_s/b=220.

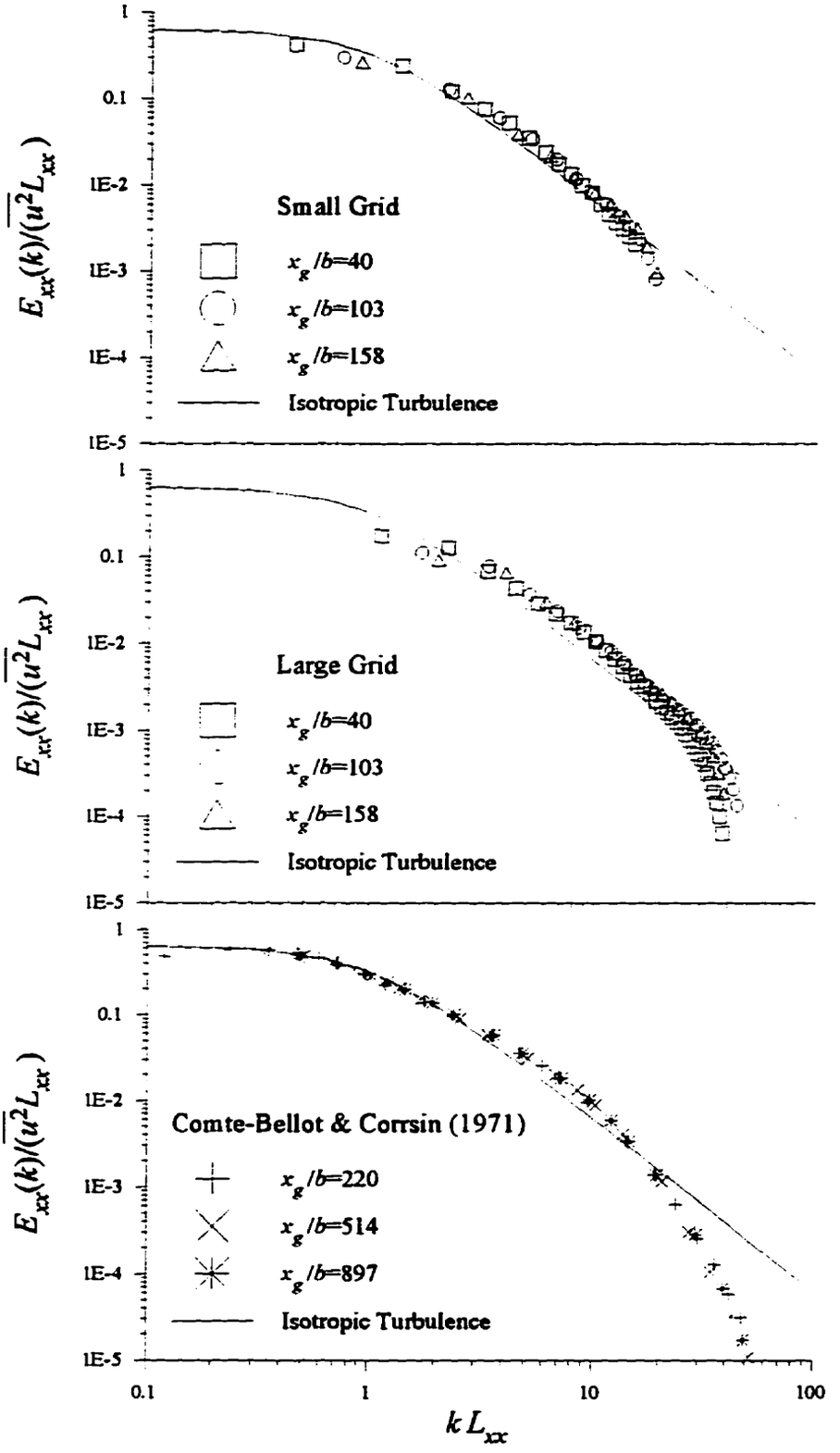

Figure 4.8: Normalized power spectra versus normalized wavenumber for grid-generated turbulence.

The normalized spectra for the large grid, given in the centre graph of Figure 4.8, illustrates that there is some readjustment of the turbulent energy at the larger normalized wavenumbers between the streamwise locations of x_g/b=40 and 103. However, by x_g/b>100, the spectra maintain the same relative shape thus indicating that the flow has become self-preserving. The normalized spectra for the small grid, given in the top graph of Figure 4.8 also indicates that a self-preserving state is reached by x_g/b=100.

In comparing the spectra between the small and large grids, it is of interest to note that the differences between the normalized spectra at x_g/b=40 and 103 are not as great for the flow with the small grid installed as they are for flow with the large grid installed, thus indicating that the flow with the small grid is able to reach a state of self-preservation earlier than the flow with the large grid. This is not unexpected since the grids tend to extract turbulent energy from the mean flow at scales typical of their geometric scales. The large grid would therefore create a greater range of wavenumbers (*ie.* from geometric scales to dissipative scales) over which the turbulent energy must readjust before becoming self-preserving.

Comparing the self-preserving spectra of the three different grid-generated turbulence experiments illustrates that each grid experiment has a unique turbulent energy spectrum although they share many of the same features. The fact that a state of self-preservation has been reached in each experiment and that there is no universal self-preserving spectrum supports the theory put forth by George (1992) in that the initial conditions play a continuous role in determining the shape of the turbulent energy spectra and thus the decay of the turbulent intensities and growth of the integral length scales.

4.3.4 Dissipation Rate per Unit Mass

The dissipation rate per unit mass, ϵ, is an important parameter characterizing the turbulence in the inertial sub-range of the external flow and is expected to be an input into the integral jet model to

be developed in Chapter 6. The dissipation rate is too complex to measure directly but can be estimated by assuming isotropic turbulence. Neglecting the energy dissipation in the lower wavenumber range, the total energy supply in the equilibrium range is practically equal to the total dissipation rate (Hinze, 1975). Thus the dissipation rate can be estimated using:

$$\epsilon_e = - U_e \frac{dq_e}{dx} \tag{4.8}$$

where q_e is the total turbulent kinetic energy per unit mass in the external flow and can be estimated, in grid-generated turbulence, by:

$$q_e = \frac{1}{2} \overline{u_e^2} + \overline{v_{r.e}^2} \tag{4.9}$$

since the turbulence is assumed homogeneous in planes parallel to the grid. Since the turbulent velocities for each grid have been fitted by power law equations (in the form of turbulent intensities), the dissipation rate per unit mass can be easily estimated if the distance from the grid plane is known.

4.4 Closure

The external flow with no grid installed is approximately uniform with a mean velocity of $\overline{U}_e$=0.0706 m/s and with turbulent intensities less than one percent over the working section of the water flume.

With the grids installed, the experimental data for the decay of the turbulent intensities and the growth of the integral length scales is well predicted by power law equations for each grid where the exponents all fall within the expected experimental range. The exponents for the large grid (*ie.* larger Re_b), however, are greater in magnitude than those for the small grid. This points to a grid Reynolds number dependency in the experimental data. In addition, the integral length scales are

strongly affected by grid solidity. Unique self-preserving turbulent energy spectra in the current study occur by $x_g/b>100$. These findings thus confirm that the initial conditions have a continuous effect on the behaviour of the grid-generated turbulence and that each grid produces a similar but unique state of self-preservation in the flow.

Chapter 5: Coflowing Jet Experimental Results

5.1 Introduction

Twelve different cases of a jet issuing into an external coflowing stream have been obtained by varying the jet model diameter and the jet exit velocity as well as by varying the turbulence level of the external coflow. The chapter starts with a summary of the initial conditions for the twelve different runs. This is followed by the presentation of the mean velocity results, including the radial spread of the jet, which in turn is followed by a section devoted to the results obtained from the Reynolds normal and shear stress data. The results for the turbulent integral length scales and turbulent power spectral density functions are next presented. The chapter concludes with a summary of the major conclusions of the experimental investigation.

5.2 Jet Initial Conditions

The initial conditions for the twelve different experimental runs are summarized in Table 5.1. The experimental runs are grouped according to the initial velocity ratio, VR, and jet radius, R_j, so that the effects of varying the external turbulence levels can be compared directly within a set. To negate some of the influences caused by the minor variations in the initial conditions, the downstream distance, x, will be normalized using the momentum radius, θ, since θ is the length scale that is characteristic of a particular combination of a jet and an external flow. A non-dimensional virtual origin, x_o/θ, has also been included in the table where an average value has been used for θ. The virtual origin offsets the effects of varying jet potential core lengths by projecting the start of a jet to an imaginary point source of momentum. The value of x_o/θ is obtained from the data by determining the x/θ intercept using a linear regression on the data points where $U_c/U_o \propto x/\theta$.

Exp't #	R_j [cm]	U_c [m/s]	$VR = U_j/U_c$	M_o [kg·m/s^2]	θ_o [cm]	x_o/θ	Turbulence Grid
1a	1.111	0.0710	6.04	0.0727	6.81	+0.68	no grid
1b	1.111	0.0689	6.06	0.0702	6.75	+0.68	small grid
1c	1.111	0.0699	6.07	0.0715	6.89	+0.68	large grid
2a	1.111	0.0699	3.29	0.0132	2.95	-1.05	no grid
2b	1.111	0.0687	3.26	0.0125	2.91	-1.05	small grid
2c	1.111	0.0698	3.17	0.0136	2.98	-1.05	large grid
3a	0.476	0.0690	5.76	0.0094	2.54	+0.59	no grid
3b	0.476	0.0662	5.64	0.0102	2.80	+0.59	small grid
3c	0.476	0.0703	5.72	0.0100	2.54	+0.59	large grid
4a	0.476	0.0686	3.32	0.0015	1.01	+0.0	no grid
4b	0.476	0.0664	3.37	0.0017	1.11	+0.0	small grid
4c	0.476	0.0703	3.21	0.0016	1.01	+0.0	large grid

Table 5.1: Initial conditions for the twelve experimental runs.

Note that the virtual origin remains constant for a given VR and R_j no matter the level of external turbulence.

5.3 Mean Velocity Results

In this section, the mean velocity profiles are used to confirm the radial similarity of the excess mean velocity profiles at various downstream locations. In addition, the decay of the centerline excess mean velocity for the jets in a low turbulent coflow will be compared with similar results from the literature as well as with the same jets in turbulent external flows. Finally, the radial growth of the jets, based on a contour surface defined by a percentage of the excess mean velocity, will be compared with the literature data as well as within each set of jet experiments.

5.3.1 Similarity of the Excess Mean Velocity Profiles

The practical purposes of demonstrating the radial similarity of the excess mean velocity, $U-U_e$, are two-fold. The first is to use radial similarity as a benchmark for the present data since similarity has been reported by Antonia and Bilger (1973), Smith and Hughes (1977) and Biringen (1986) for jets in laminar coflows and by Fink (1977) for jets in turbulent coflows. The second purpose comes from a physical modelling point of view since similarity will allow all the excess mean velocity information contained within a radial profile to be distilled to a single characteristic velocity scale and a single characteristic length scale without major loss of experimental information except perhaps at the edge of the jet. Previous studies on coflowing jets (Antonia and Bilger, 1973, and Biringen, 1986) have used the centerline excess mean velocity, U_o, and the jet velocity half width, L_{σ} for these scales. The excess mean velocity at a downstream location can then be described by:

$$\frac{U-U_e}{U_o} = f(\eta)\,; \quad \eta = \frac{r}{L_o} \tag{5.1}$$

where $f(\eta)$ is a universal function, typically a Gaussian function defined by:

$$f(\eta) = e^{-c\eta^2} \tag{5.2}$$

where c is a constant given by $c=ln(2)=0.69$ since by definition $e^{-c}=0.5$ at $r=L_o$. The Gaussian function has been shown to give a satisfactory fit to the non-dimensionalized excess mean velocity profiles (So and Hwang, 1989) and thus is a useful qualitative check for the present data.

Figures 5.1 to 5.4 contain selected non-dimensionalized radial profiles of the excess mean velocity for the twelve experimental runs with initial conditions listed in Table 5.1. To reduce the number of data points presented, only the positive half of each profile has been plotted since the jet centerline is an axis of symmetry. To give a representative picture of the downstream development of the excess mean velocity, six profiles have been selected starting at a downstream location of x=10.2 cm and ending at x=100.2 cm for each run. Also included in the caption for each figure is the approximate non-dimensional distance downstream given by $(x-x_o)/\theta$ where the value of θ is the average of the local value for the three runs in each figure.

Figure 5.1 contains the profiles for the large jet at $VR\approx6$ and represents the group of experiments that are closest to the jet exit in non-dimensional terms. As noted by other researchers, the Gaussian function gives a very good fit to the experimental data. Increasing the level of external turbulence by installing a grid appears to have little effect on the non-dimensional excess mean velocity profiles, even by the final downstream location of $(x-x_o)/\theta=15.4$, thus indicating that, close to the exit, the jet is unaffected by external turbulence. Profiles for the large jet at $VR\approx3$ are given in Figure 5.2 and also show good agreement with the Gaussian function. With a grid installed, the plots for the final two $(x-x_o)/\theta$ stations show an increase in the data scatter at the edge of the jet and, to a lesser extent, at the jet centerline. This is more noticeable when the large grid is installed since the entrained external flow has more turbulent energy located at larger length scales which affects the jet development more than the external flow with the small grid installed or with no grid installed.

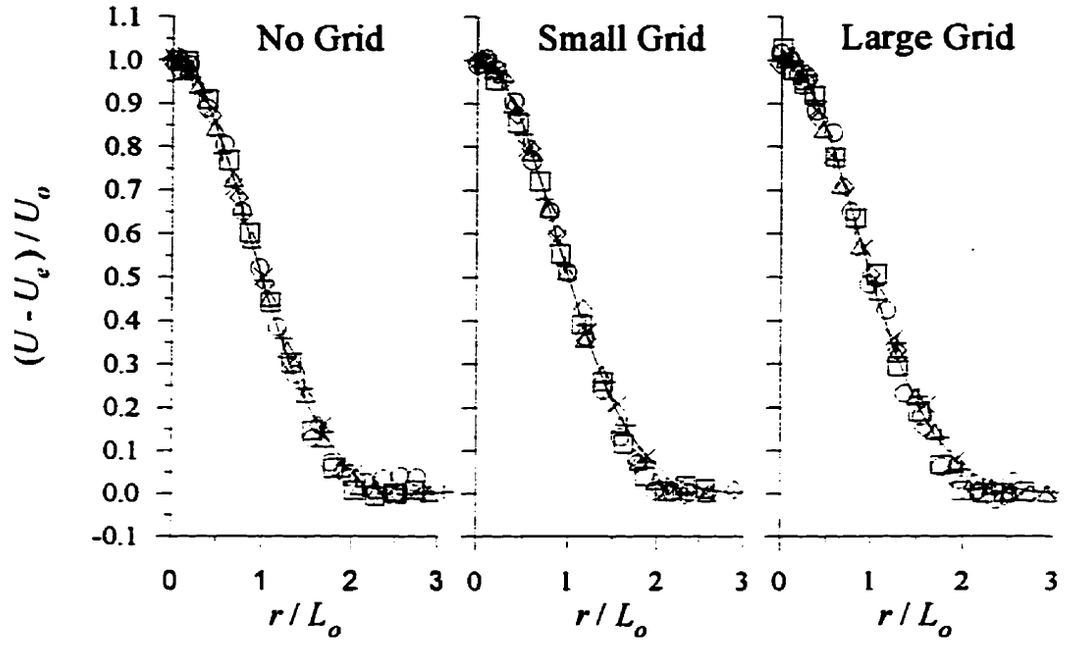

Figure 5.1: Excess mean velocity profiles for the large jet with $VR \approx 6$. x (cm): +, 10; ×, 20; △, 40; ◇, 60; □, 80; ○, 100. $(x-x_o)/\theta$: +, 0.8; ×, 2.3; △, 5.2; ◇, 8.6; □, 11.8; ○, 14.8. ——, Gaussian function.

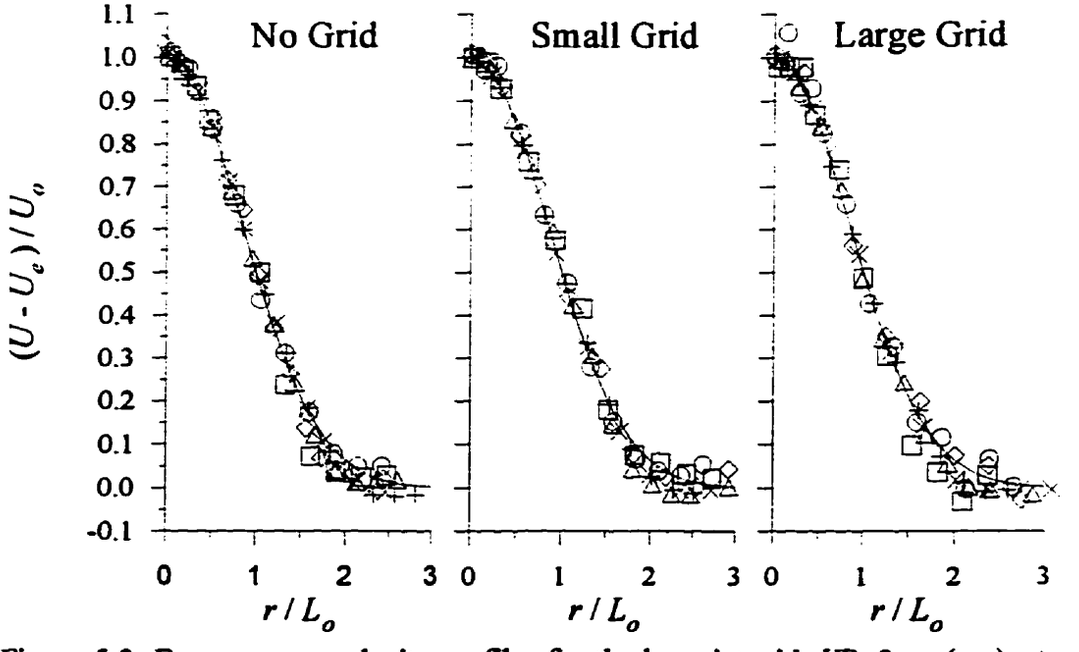

Figure 5.2: Excess mean velocity profiles for the large jet with $VR \approx 3$. x (cm): +, 10; ×, 20; △, 40; ◇, 60; □, 80; ○, 100. $(x-x_o)/\theta$: +, 4.6; ×, 8.1; △, 15.2; ◇, 22.2; □, 29.2; ○, 36.2. ——, Gaussian function.

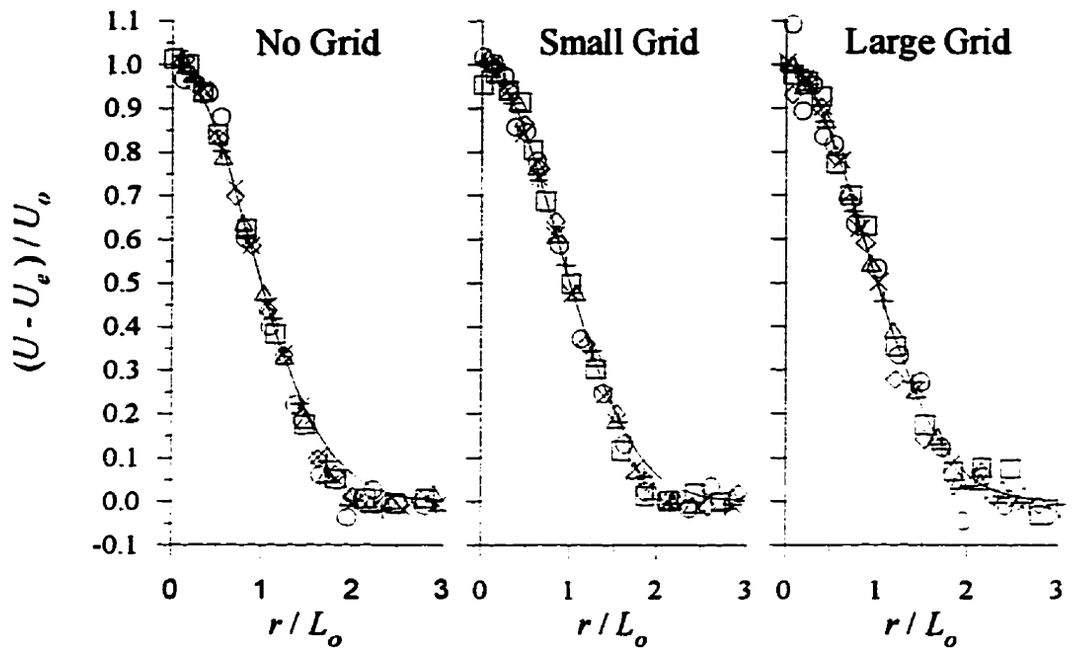

Figure 5.3 : Excess mean velocity profiles for the small jet with $VR \approx 6$. x (cm): +, 10; ×, 20; △, 40; ◇, 60; □, 80; ○, 100. $(x-x_o)/\theta$: +, 3.3; ×, 7.3; △, 15.2; ◇, 23.4; □, 32.4; ○, 40.7. ——, Gaussian function.

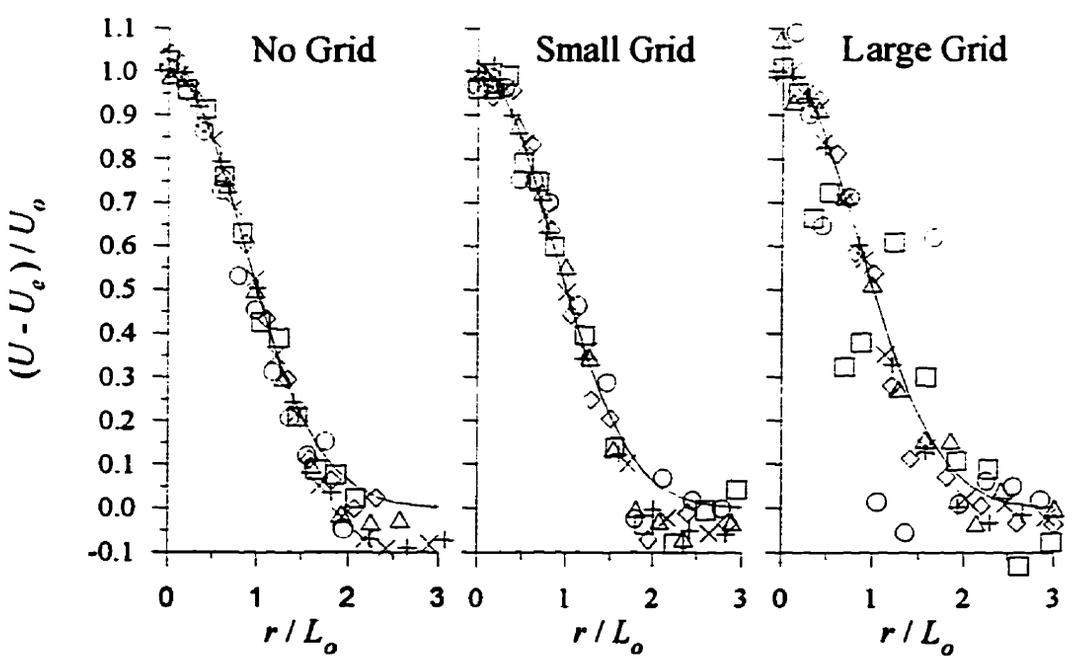

Figure 5.4: Excess mean velocity profiles for the small jet with $VR \approx 3$. x (cm): +, 10; ×, 20; △, 40; ◇, 60; □, 80; ○, 100. $(x-x_o)/\theta$: +, 9.9; ×, 19.6; △, 39.5; ◇, 60.3; □, 81.8; ○, 105.7. ——, Gaussian function.

The non-dimensional profiles of the excess mean velocity for the small jet are given in Figures 5.3 and 5.4 for $VR \approx 6$ and 3 respectively. The profiles for the small jet at $VR \approx 6$ show approximately the same pattern and degree of scatter in the experimental data as for the large jet at $VR \approx 3$ (Figure 5.2). This is not unexpected since the non-dimensional downstream distance is approximately the same for both cases. The small jet at $VR \approx 3$, however, travels the farthest non-dimensional distance from the jet exit and displays the greatest amount of scatter in the experimental data. The level of scatter is so great for the case of the large grid installed that the assumption of radial similarity becomes questionable by the last two traversing locations. This is again the effect of entraining external fluid which has greater levels of turbulent energy at larger length scales when the large grid is installed.

Two trends emerge from the above figures. The first is that, for a given external flow, the farther the non-dimensional distance travelled from the jet exit, the greater the scatter in the profile. The second trend is that, for a given location past $(x-x_o)/\theta > 20$, the jet with the large grid installed displays the greatest scatter in the profile data followed by the jet with the small grid installed.

5.3.2 Behaviour of the Jet Centerline Excess Mean Velocity

To establish confidence in the present data, the behaviour of the centerline excess mean velocity is compared to other data available in the literature. In Figure 5.5, the present data for U_e/U_o has been plotted against $(x-x_o)/\theta$ for the four runs without a grid installed with similar results from six other studies on coflowing jets. A virtual origin, x_o, is used for each data set where x_o has been extrapolated from the data based on a linear regression. As can be seen from the figure, the majority of the data sets, after passing through an initial development zone for the potential core, collapse to a single trend for the development of U_e/U_o. Since the data is plotted on a log-log plot, the slope of the line, which is approximately unity for the data in the figure, corresponds to an exponent in a power law relationship. Thus it is found find that $U_e/U_o \propto x$ throughout most of the experimental regime for all seven studies listed in the legend in Figure 5.5.

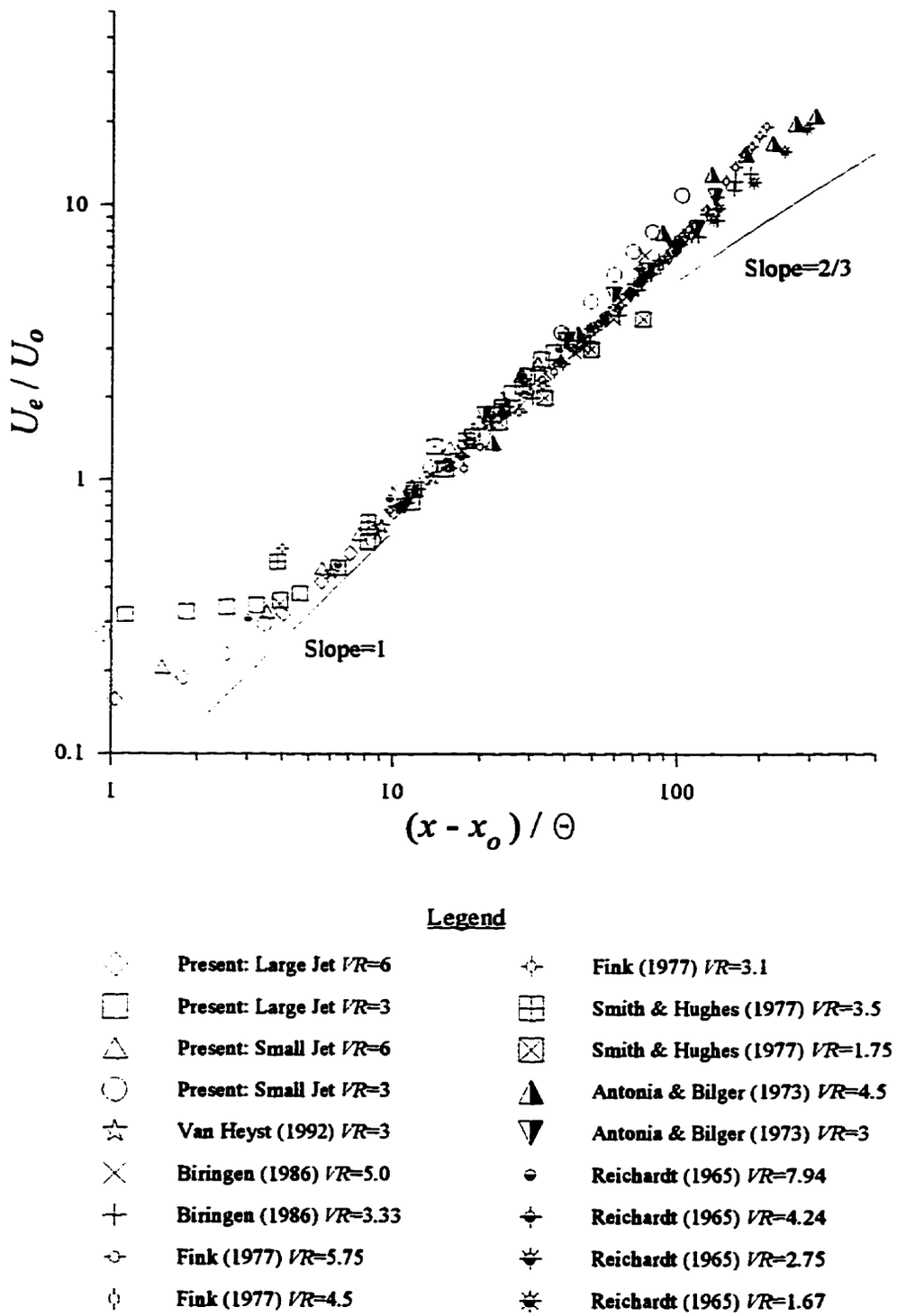

Figure 5.5: Jet centerline excess mean velocity behaviour in a laminar external coflow.

Chapter 2 presented two theoretical asymptotic limits for the behaviour of U_o in a coflowing jet in a laminar external flow. The limits, arrived at using similarity considerations, are dependent on the magnitude of U_e/U_o. If $U_e/U_o \ll 1$ then the jet is strong in comparison to the external flow and the expected behaviour is $U_o \propto x^{-1}$. If $U_e/U_o \gg 1$ then the jet is weak in comparison to the external flow and the expected behaviour is $U_o \propto x^{-2/3}$. For reference purposes, lines with slopes of unity and 2/3 have been included in Figure 5.5. Typically, very small values of U_e/U_o are only obtainable very close to the jet exit. Experimental profiles of the mean velocity in this region, however, are not self-similar due to the flow readjusting from the potential core where U_e/U_o would be a constant. Adherence to the asymptotic limit, therefore, can only be expected after a short development length which the experimental data in Figure 5.5 supports. In spite of this, the experimental data indicates that $U_o \propto x^{-1}$ up to $U_e/U_o \sim 20$ (or $(x-x_o)/\theta \sim 200$) with little indication of an imminent change in slope to 2/3 except for the data of Antonia and Bilger (1973) at $VR=4.5$. The absence of a universal $U_o \propto x^{-2/3}$ behaviour is either the result that insufficient distance has been travelled downstream to reach $U_e/U_o \gg 1$ or that the limit itself is not physically realistic for a coflowing jet in a uniform external flow (see §2.4.1).

Figure 5.5 also indicates that the magnitude of U_e/U_o for the present small jet at $VR \approx 3$ begins to increase over the other data at approximately $(x-x_o)/\theta \approx 40$. This increase in U_e/U_o is the result of the low levels of turbulent energy in the external flow when no grid is installed (*i.e.* turbulent intensities of $T_x \sim 1\%$) affecting the development of the jet far downstream from the exit. The literature data sets have been obtained in wind tunnels where the turbulent intensities can typically be an order of magnitude less than that in a water flume (see, for example, Antonia and Bilger (1973) where $T_x=0.1\%$) and thus do not affect the development of the jet.

A comparison between the behaviour of the centerline excess mean velocity in the absence and presence of turbulence generating grids is given in Figure 5.6 for the four sets of experimental runs. Before commenting on the results, however, the issue of experimental uncertainty needs to be addressed. Until this point, the information that has been gleaned from the presented results for the coflowing jets has been more of a check to make certain the present experiments are consistent with

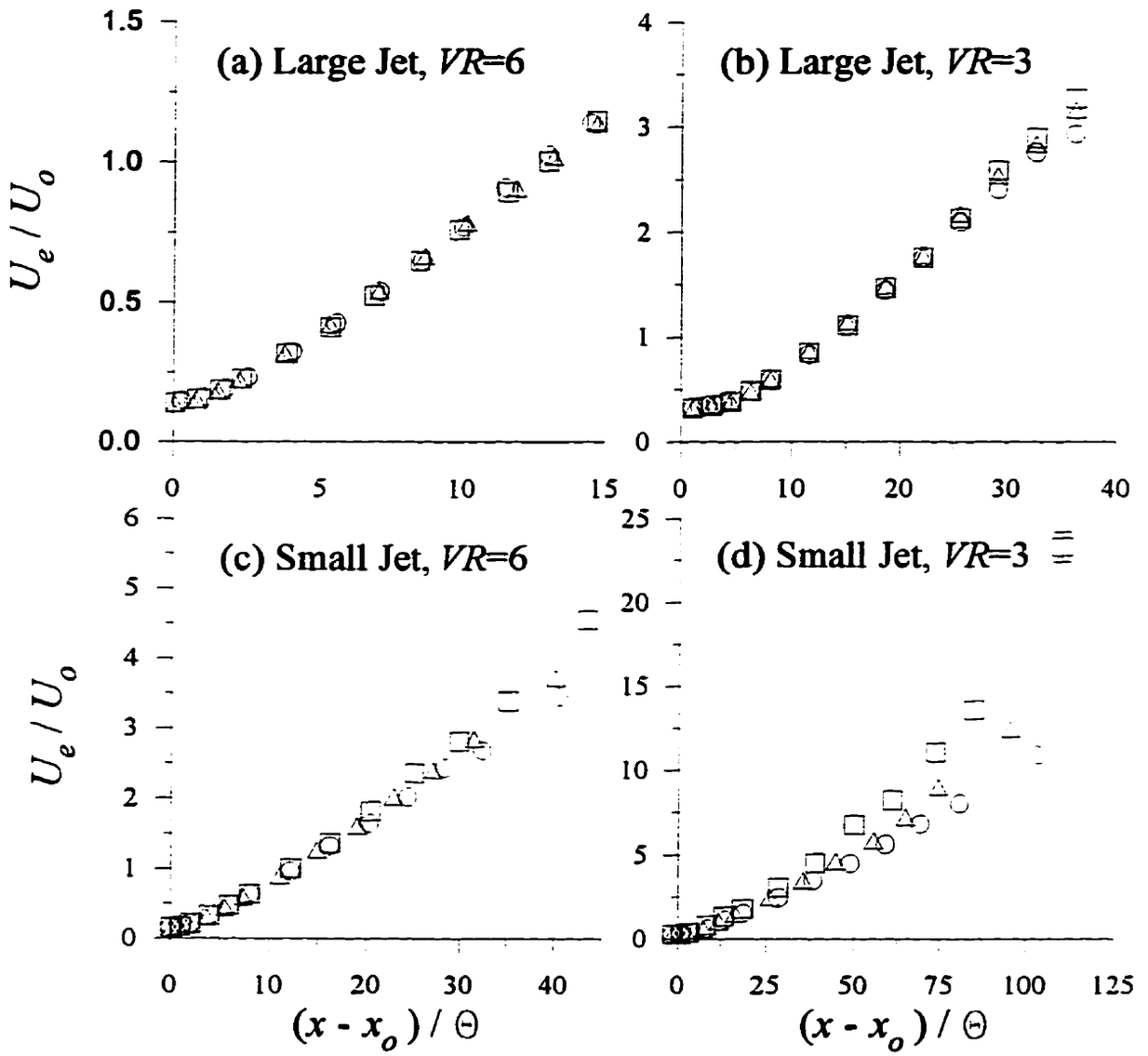

Figure 5.6: Centerline excess mean velocity behaviour. Symbols refer to the grid installed: ○, no grid; △, small grid; □, large grid. Error bars are for precision errors only and are included only on data points where the error bar exceeds the limits of the data symbols.

established results. The data presented in Figure 5.6, however, is a direct comparison of results within an experimental set which will pinpoint a downstream location where the effects of external turbulence first become significant. The level of experimental uncertainty contained within the presented data thus becomes extremely important as it will determine where the effects become statistically significant.

The total uncertainty within a measured value is composed of bias or fixed errors and precision or random errors (see Appendix C). Since each experimental set is conducted using the same jet and measurement system, the bias errors are considered to be the same no matter the level of external turbulence. Since the bias errors represent an offset between the measured and the true value and since it is the same for all three cases in each of the experimental sets, a comparison of the results within a set need not account for the bias error. Precision errors, on the other hand, do need to be accounted for due to their random nature. In Figure 5.6, the error bars for the precision errors are all within the limits of the data symbols except for the small jet at $VR \approx 3$ with the large grid installed at the very last traversing location. An error bar has been included for this point.

Figure 5.6a presents the experimental data for the large jet at $VR \approx 6$ for the three levels of external turbulence. The figure indicates that there is no significant variation in U_e/U_o over the non-dimensional experimental regime that can be attributed to the level of external turbulence. In the three remaining experimental groups, the presence of a grid results in a statistically significant increase in the growth of U_e/U_o by $(x-x_o)/\theta \approx 25$ with a greater increase corresponding to the jet with the large grid installed. By taking the inverse of the relationships, the effects of the external turbulence can be translated into a decrease in the centerline excess mean velocity by $(x-x_o)/\theta \approx 25$. Since the external flow with the large grid installed contains more turbulent energy, which diffuses jet momentum away from the centerline, than that with the small grid installed, which in turn contains more than that with no grid installed, it makes physical sense to expect a faster decrease in U_o when more turbulent energy is present in the external flow.

5.3.3 Behaviour of the Jet Radius

The true radius of the jet, R, is defined by the radial location where the excess mean velocity diminishes to zero. The drawback of this definition for the jet radius is that it is very difficult to realize experimentally since the excess mean velocity approaches a value of zero slowly at the edge of the jet. Due to the scatter and uncertainty associated with experimental data, it therefore

becomes very difficult to determine the precise location where $U-U_e=0$. An alternative definition, put forth by Keffer and Baines (1963), is to use the radial location where the excess mean velocity drops to ten percent of the centerline value. This radial location can be more accurately determined from experimental data then the location where $U-U_e=0$ since there is still a well defined gradient in the excess mean velocity profile (see, for example, Figure 5.1).

As with the centerline excess mean velocities, the present jet radii with no grid installed are first compared to the literature data to establish confidence in the current results. Most of the jet radial development reported in the literature is limited to the jet velocity half widths. By assuming a Gaussian profile for the radial distribution of the excess mean velocity, and by using the reported centerline value, the jet velocity half widths have been converted to effective jet radii and are presented, along with the present results, in Figure 5.7. This collection of data, plotted on a log-log plot, indicates that all the radii follow approximately the same trend. Note that the degree of scatter in the radius data is greater than that in the centerline excess mean velocity data given in Figure 5.5.

Despite the higher level of scatter, the radii, after an initial development zone, can be described by a line on the log-log plot with a slope approximately equal to 2/3. At approximately $(x-x_o)/\theta=100$, the slope of the line appears to decrease to approximately 1/3 although there is insufficient experimental data past $(x-x_o)/\theta=300$ to confirm this extrapolation.

In Chapter 2, the two asymptotic limits for the radial behaviour of a coflowing jet are given as: when $U_e/U_o \ll 1$, then $R \propto x$ and when $U_e/U_o \gg 1$, $R \propto x^{1/3}$. For comparison purposes, two lines with slopes of unity and 1/3 are also shown in Figure 5.7. The experimental data, however, does not support the asymptotic limit of $R \propto x$ when $U_e/U_o \ll 1$ although this is probably due to the readjustment zone in the potential core where the mean velocity profiles are not similar and thus similarity limits would not apply. Some of the data, however, indicates that $R \propto x^{1/3}$ once $(x-x_o)/\theta>100$. This corresponds to the approximate location where $U_e/U_o \sim 8$ from Figure 5.5. In the transition region between that of a strong jet in a weak coflow and that of a weak jet in a strong coflow, the radii follow $R \propto x^{2/3}$.

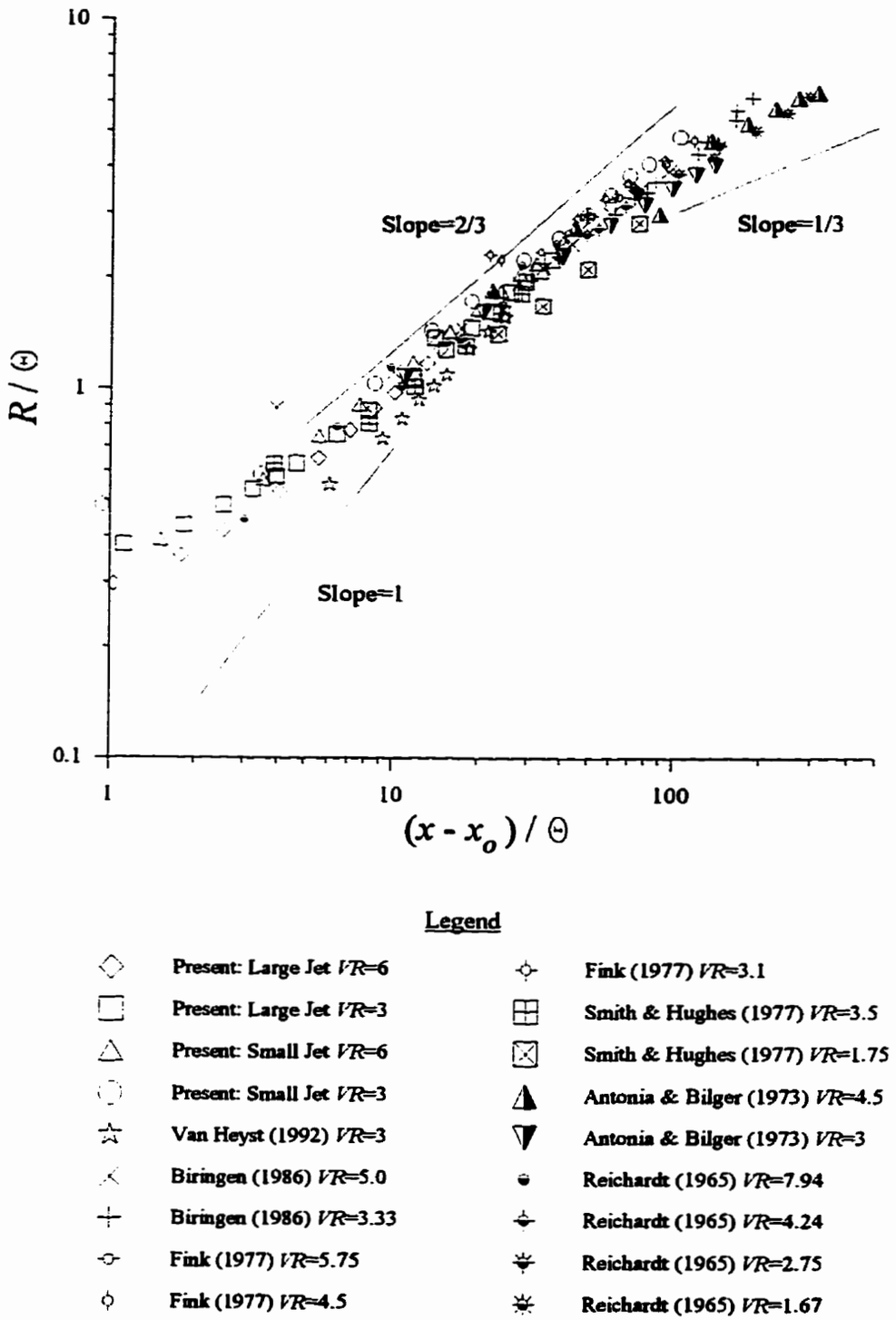

Figure 5.7: Jet radial behaviour in a laminar external coflow.

Since the centerline excess mean velocity decays more quickly for the current small jet at $VR \approx 3$ than the other data in Figure 5.5 after $(x-x_o)/\theta > 40$, its corresponding radius should increase more rapidly than the other data in order to be consistent with continuity. Figure 5.7 shows that the radius for the small jet at $VR \approx 3$, while not immensely greater than the other data, is still one of the largest.

To determine the effects that external turbulence has on the development of the jet radius, Figure 5.8 contains plots of the four sets of experimental runs. As with the centerline excess mean velocity plots, only the precision errors are shown and only for the data points where the error bars extend beyond the limits of the data symbol. For the case of the large jet at $VR \approx 6$, given in Figure 5.8a, the effect of adding external turbulence is to increase the magnitude of the radius after $(x-x_o)/\theta \sim 13$, although the effects are still fairly small. As the non-dimensional distance is increased, as in Figures 5.8b and 5.8c, the effects of external turbulence become statistically more significant until in Figure 5.8d, the radius of the jet with the large grid installed is on the order of one and a half times larger than the same jet with no grid installed by the final traversing station.

The general trend that emerges from the figure is that the radius begins to show a marked increase in magnitude when a grid is installed over no grid after $(x-x_o)/\theta \sim 20$. The larger increase in jet radius corresponds to the jet with the large grid installed. When the small grid is installed, there is an increase in the radius over the case with no grid installed but it is not as marked as the case with the large grid installed.

5.3.4 Summary of Mean Velocity Results

The present excess mean velocity profiles display radial similarity when plotted as r/L_o versus $(U-U_c)/U_c$. Once radial similarity is obtained after the potential core, it is maintained for all levels of external turbulence except at large values of $(x-x_o)/\theta$ with the large grid installed.

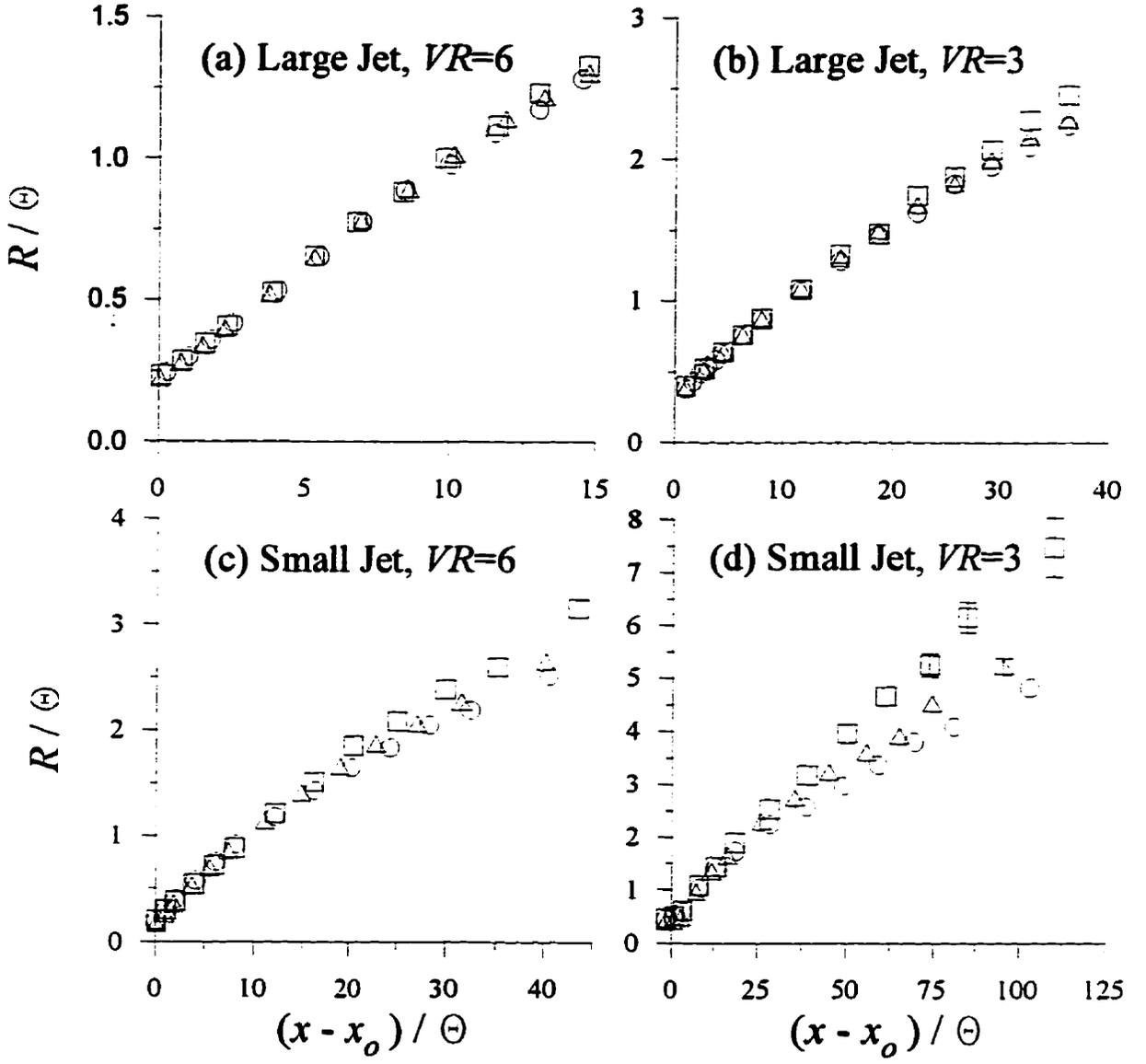

Figure 5.8: Normalized radial behaviour. Symbols refer to the turbulence generating grid installed: ○, no grid; △, small grid; □, large grid.

The present experimental data for the behaviour of U_c/U_o and R/θ for coflowing jets in the absence of any grids agree with similar results in the literature. The results show that $U_o \propto x^{-1}$ up to $U_c/U_o \sim 20$ or $(x-x_o)/\theta \sim 300$ and that $R \propto x^{2/3}$ up to $U_c/U_o \sim 8$ or $(x-x_o)/\theta \sim 100$ after which there is some evidence to suggest that $R \propto x^{1/3}$. This is not entirely the expected behaviour based on asymptotic limits arrived at using similarity hypotheses.

The effects of external turbulence are to reduce U_o and increase R more quickly than the case with no grid installed starting after $(x-x_o)/\theta \sim 20$ to 25. The jet with the large grid installed experiences the greatest changes in U_o and R.

5.4 Reynolds Stress Results

The Reynolds stress results can be subdivided into normal stresses given by $\overline{u^2}$ and $\overline{v_r^2}$ and a shear stress given by $\overline{u\,v}_r$. Physically, the normal stresses represent directional components of the total turbulent kinetic energy vector while the shear stress represents the transfer of turbulent momentum from one component to the other. Since it is more common in the literature to report turbulent velocities rather than normal shear stresses, the current data will be presented as turbulent velocities, $(\overline{u^2})^{1/2}$ and $(\overline{v_r^2})^{1/2}$.

This section first looks at some considerations arising from similarity theory in order to obtain a velocity scale to non-dimensionalize the data. This is followed by the experimental results for the radial profiles and centerline behaviour of the streamwise turbulent velocity which is followed by similar results for the radial turbulent velocity. Radial profiles and centerline behaviour for the Reynolds shear stress follow with a brief summary of the results.

5.4.1 Considerations from Similarity Theory

The conventional method of plotting radial profiles of the turbulent velocities, $(\overline{u^2})^{1/2}$ and $(\overline{v_r^2})^{1/2}$, is to normalize them using the centerline excess mean velocity, U_o, with the radial distance normalized by L_σ. This produces profiles of local turbulent intensity versus non-dimensional radius. The underlying philosophy of this method is that since similarity theory indicates that the scale factor for the mean velocity and turbulent velocities must be identical (see §2.4.1) and since U_o is the scale factor for the excess mean velocity profiles, then it must also be the scale factor for the

turbulent velocity profiles. Numerous studies have shown that, using U_o to non-dimensionalize the turbulent velocity profiles, similarity is only obtained very far downstream, if ever, with the centerline magnitude reaching various asymptotic values. One case in point is the data from Antonia and Bilger (1973). For their jet at VR=3, similarity for $(\overline{u^2})^{1/2}/U_o$ profiles was not obtained until x>100 cm (corresponding to x/θ~150) with the centerline value reaching a constant of $(\overline{u^2_o})^{1/2}/U_o$=0.50. For their jet at VR=4.5, Antonia and Bilger claim similarity is obtained by x=80 cm (x/θ~75) although there is still an increasing trend to be seen in the data right to the end of the traversing regime of x=140 (x/θ~130). The quoted asymptotic centerline value for this case is $(\overline{u^2_o})^{1/2}/U_o$=0.29. Another case is Biringen (1986) who found similarity for two out of three of his experimental runs. The centerline asymptotic values found were: for the jet at VR=10, $(\overline{u^2_o})^{1/2}/U_o$=0.30 by x/θ~25 and for the jet at VR=5, $(\overline{u^2_o})^{1/2}/U_o$=0.34 by x/θ~50. The jet at VR=3.3 did not reach similarity by the end of the traversing regime at x/θ~100.

However, since similarity distributions do not, even approximately, satisfy the governing equations of motion (except for the case of the two asymptotic limits) the result that the scale factors for the mean velocity and the turbulent velocities must be the same is not applicable to a jet in a uniform coflow. In fact, both Hinze (1975) and Townsend (1976) suggest that there can be multiple velocity scales in a single flow. The problem now is the choice of a new scale factor in lieu of U_o which will make the turbulent velocity profiles similar.

A jet in a uniform coflow has two distinct mean velocities: that of the external coflow and that of the jet itself. The easiest method of combining these velocities is to take the difference which results in an excess mean velocity whose value at the centerline is given by U_o. However, in the integral momentum equation, the mean velocities are combined as $U(U-U_e)$ which is balanced in the integral by the difference in the square of the turbulent velocities. Thus another choice for a velocity scale factor becomes $(U(U-U_e))^{1/2}$, or, after replacing U by the centerline value of U_o+U_e, the new velocity scale factor becomes $(U_o(U_o+U_e))^{1/2}$. Another interpretation of the new velocity scale factor is as an average velocity scale for the two distinct velocity fields. Incidently, for a jet in a quiescent background (U_e=0), this new velocity scale reduces to U_o which is equivalent to the

conventional velocity scale for this particular flow.

In the sections to follow, the radial profiles and centerline behaviour of both the streamwise and radial turbulent velocities will be presented by normalizing the data with U_o, the conventional method, and with $(U_o(U_o+U_e))^{1/2}$, the new scale factor. This results in two plots for each set of jet runs. These plots are presented on the same page with the same scales for the abscissa and ordinate axes to emphasize the difference in the normalizing schemes.

5.4.2 Streamwise Turbulent Velocity

5.4.2.1 Similarity of Radial Profiles

The radial profiles of the streamwise turbulent velocity have been presented in a similar manner to that used for the excess mean velocity profiles in that six profiles have been selected to represent the downstream development for each jet run and only the positive half is presented in the figure since the centerline is an axis of symmetry.

The radial profiles of streamwise turbulent velocity for the large jet at $VR \approx 6$ are normalized by U_o in Figure 5.9 and by $(U_o(U_o+U_e))^{1/2}$ in Figure 5.10. The difference between the two normalizing schemes is immediately apparent. When the profiles are normalized by the conventional velocity scale, U_o, the profiles do not reach a state of similarity by the last traversing location while the profiles normalized by the new velocity scale, $(U_o(U_o+U_e))^{1/2}$, become approximately similar by $(x-x_o)/\theta \sim 5.2$. The effects of external turbulence, however, are more apparent when the profiles are normalized by U_o. In Figure 5.9, there is a notable increase in the turbulent velocity at the final traversing location for the jet with the large grid installed over that with no grid installed. In Figure 5.10, however, the same profile is still very similar to the other profiles. This effect will become more apparent as the non-dimensional distance downstream is increased.

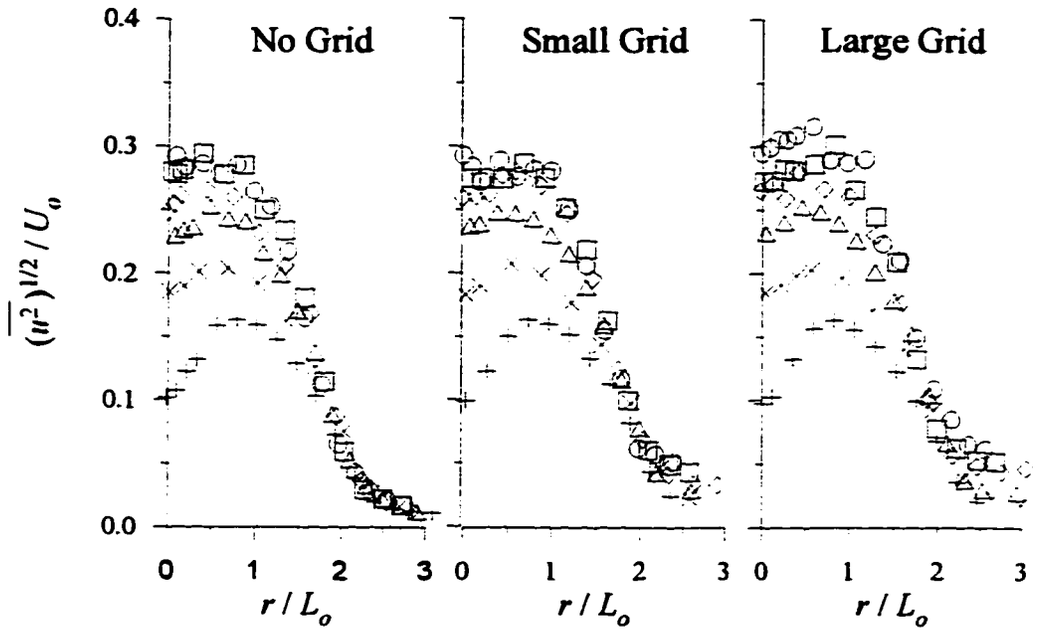

Figure 5.9: Streamwise turbulent velocity profiles for the large jet with $VR \approx 6$ normalized by U_o. x (cm): +, 10; ×, 20; △, 40; ◇, 60; □, 80; ○, 100. $(x-x_o)/\theta$: +, 0.8; ×, 2.3; △, 5.2; ◇, 8.6; □, 11.8; ○, 14.8.

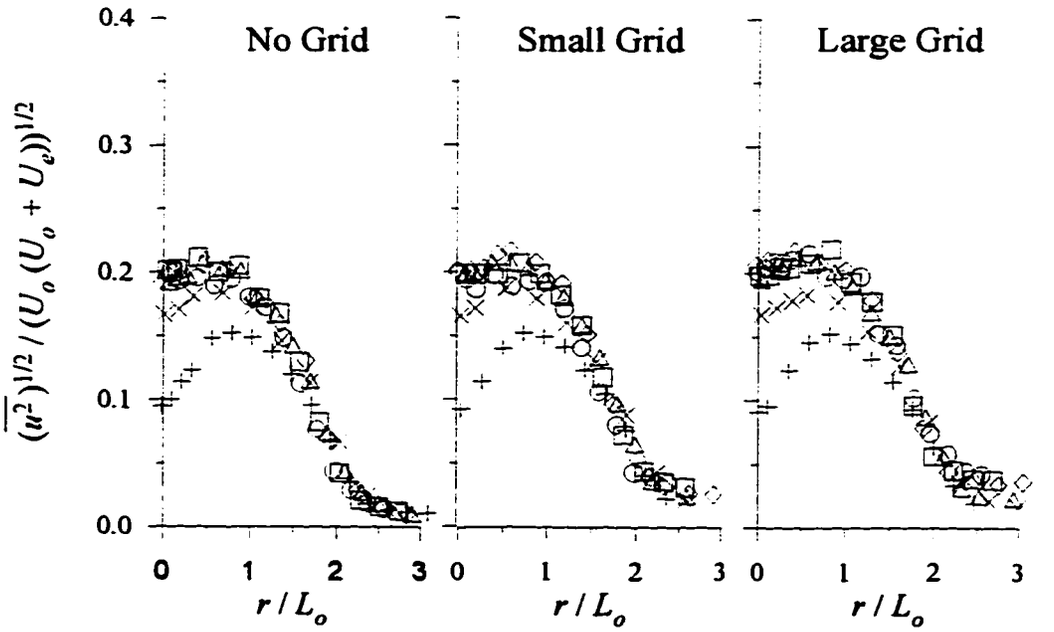

Figure 5.10: Streamwise turbulent velocity profiles for the large jet with $VR \approx 6$ normalized by $(U_o(U_o+U_e))^{1/2}$. x (cm): +, 10; ×, 20; △, 40; ◇, 60; □, 80; ○, 100. $(x-x_o)/\theta$: +, 0.8; ×, 2.3; △, 5.2; ◇, 8.6; □, 11.8; ○, 14.8.

Figures 5.11 and 5.12 show the radial profiles of $(\overline{u^2})^{1/2}$ for the large jet at $VR\approx3$ using the conventional and new normalizing techniques respectively. Again, it is apparent that using U_o, similarity is not achieved over the experimental regime while using $(U_o(U_o+U_e))^{1/2}$ results in similar profiles by $(x-x_o)/\theta=8.1$ although there is slightly more scatter in the plot for the jet with the large grid installed than in the other two plots. The effects of external turbulence can best be observed in Figure 5.11 where a noticeable difference in the profiles begins to occur after $(x-x_o)/\theta=15.2$ where the jet with the large grid installed exhibits the largest magnitudes for $(\overline{u^2})^{1/2}/U_o$ followed by the jet with the small grid installed for a given downstream location.

Figures 5.13 and 5.14 present the corresponding information for the small jet at $VR\approx6$. The same trends are again apparent: with the conventional normalization, similarity is not achieved, especially when a grid is installed, while with the new normalization, similarity in all three external turbulence levels is achieved after $(x-x_o)/\theta=7.3$ although the level of scatter in the no grid case is fairly high in comparison to the other two cases. This higher level of scatter in the no grid case is unexpected since typically a higher degree of scatter corresponds to a higher level of external turbulence. The effects of external turbulence, best seen in Figure 5.13, become apparent after $(x-x_o)/\theta=7.3$ where the largest magnitudes of $(\overline{u^2})^{1/2}/U_o$ again correspond to the jet with the large grid installed.

Lastly, Figures 5.15 and 5.16 present the streamwise turbulent velocity profiles for the small jet at $VR\approx3$. This is the most striking case since it covers the greatest non-dimensional distance downstream. The trend noted in the above three experimental sets can again be observed in this data set. Using conventional normalization, the profiles again fail to reach a state of similarity while using the new normalization, the profiles become similar by $(x-x_o)/\theta=19.6$. Figure 5.15 shows quite dramatically the effects that the external turbulence, which occur after $(x-x_o)/\theta=19.6$, have on the streamwise velocity profiles. Again the largest magnitudes of $(\overline{u^2})^{1/2}/U_o$ occur for the jet with the large grid installed. In fact, by the last traversing location with the large grid installed, it is difficult to discern the typical hump in the profile that is usually associated with the jet fluid, thus indicating that the turbulent velocity within the jet is becoming indistinguishable from that in the external flow.

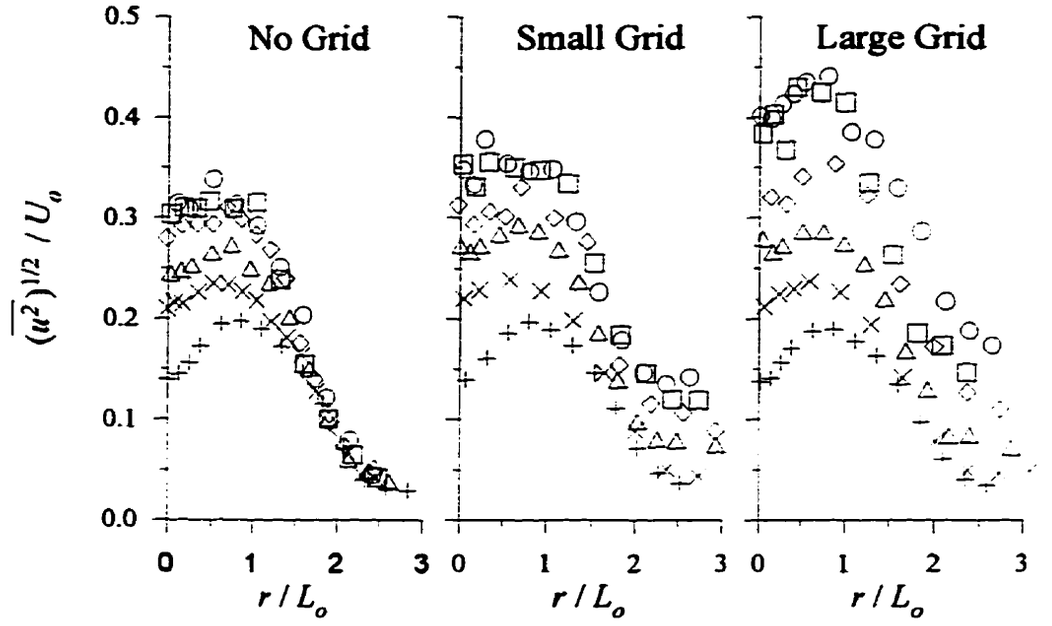

Figure 5.11: Streamwise turbulent velocity profiles for the large jet with $VR \approx 3$ normalized by U_o. x (cm): +, 10; ×, 20; △, 40; ◇, 60; □, 80; ○, 100. $(x-x_o)/\theta$: +, 4.6; ×, 8.1; △, 15.2; ◇, 22.2; □, 29.2; ○, 36.2.

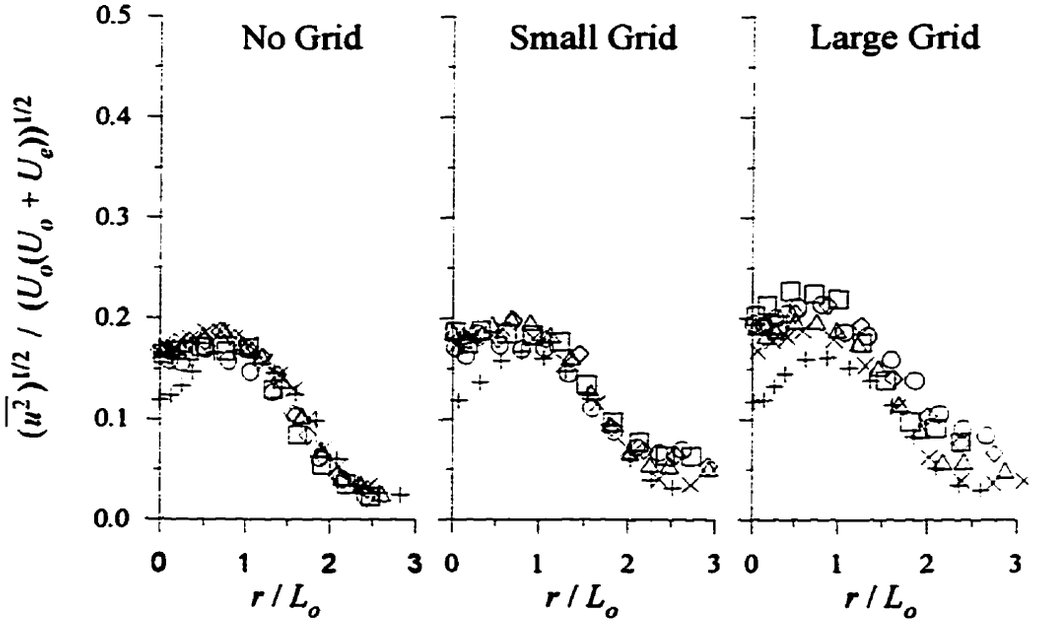

Figure 5.12: Streamwise turbulent velocity profiles for the large jet with $VR \approx 3$ normalized by $(U_o(U_o+U_e))^{1/2}$. x (cm): +, 10; ×, 20; △, 40; ◇, 60; □, 80; ○, 100. $(x-x_o)/\theta$: +, 4.6; ×, 8.1; △, 15.2; ◇, 22.2; □, 29.2; ○, 36.2.

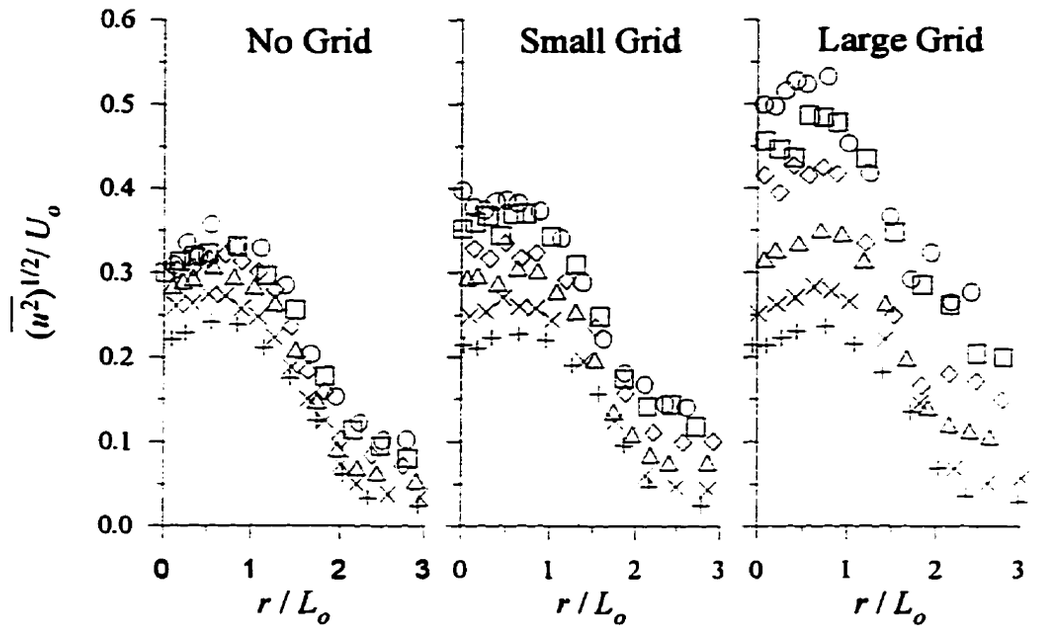

Figure 5.13: Streamwise turbulent velocity profiles for the small jet with $VR \approx 6$ normalized by U_o. x (cm): +, 10; ×, 20; △, 40; ◇, 60; □, 80; ○, 100. $(x-x_o)/\theta$: +, 3.3; ×, 7.3; △, 15.2; ◇, 23.4; □, 32.4; ○, 40.7.

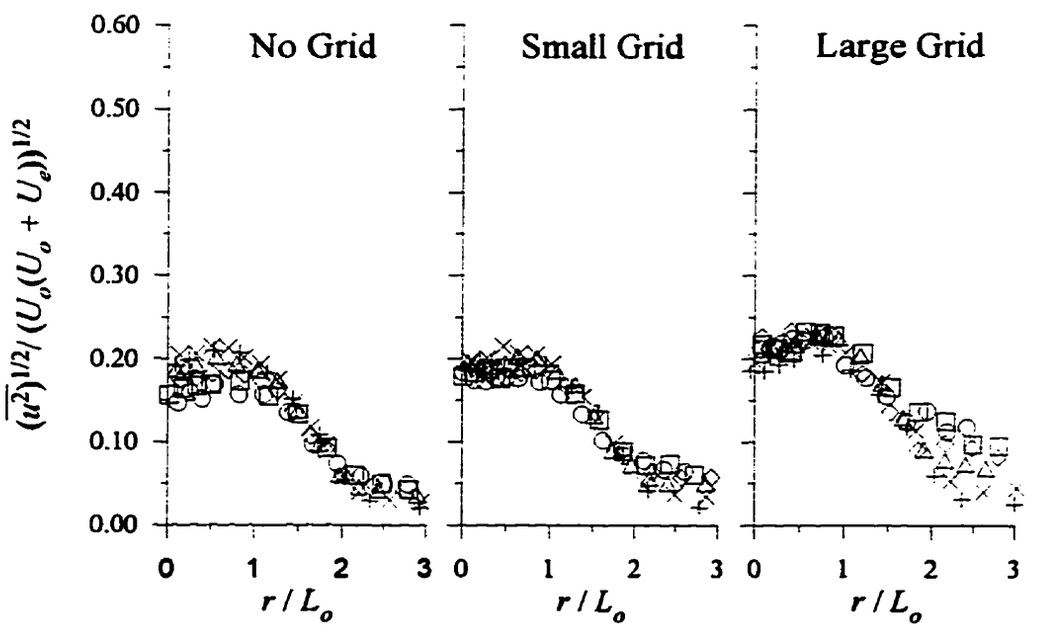

Figure 5.14: Streamwise turbulent velocity profiles for the small jet with $VR \approx 6$ normalized by $((U_o+U_e))^{1/2}$. x (cm): +, 10; ×, 20; △, 40; ◇, 60; □, 80; ○, 100. $(x-x_o)/\theta$: +, 3.3; ×, 7.3; △, 15.2; ◇, 23.4; □, 32.4; ○, 40.7.

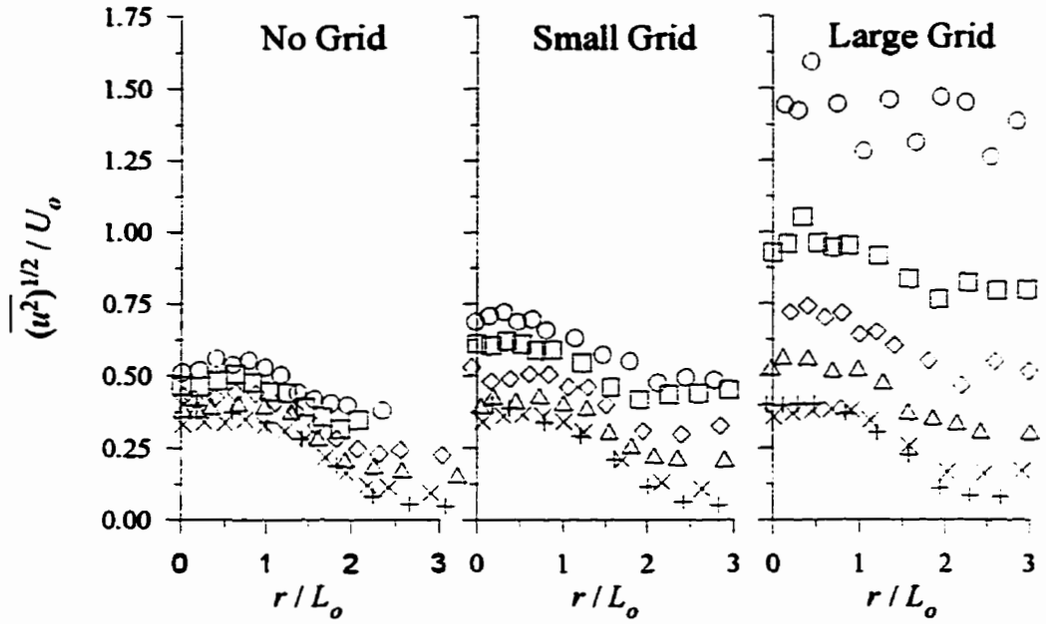

Figure 5.15: Streamwise turbulent velocity profiles for the small jet with $VR \approx 3$ normalized by U_o. x (cm): +, 10; ×, 20; △, 40; ◇, 60; □, 80; ○, 100. $(x-x_o)/\theta$: +, 9.9; ×, 19.6; △, 39.5; ◇, 60.3; □, 81.8; ○, 105.7.

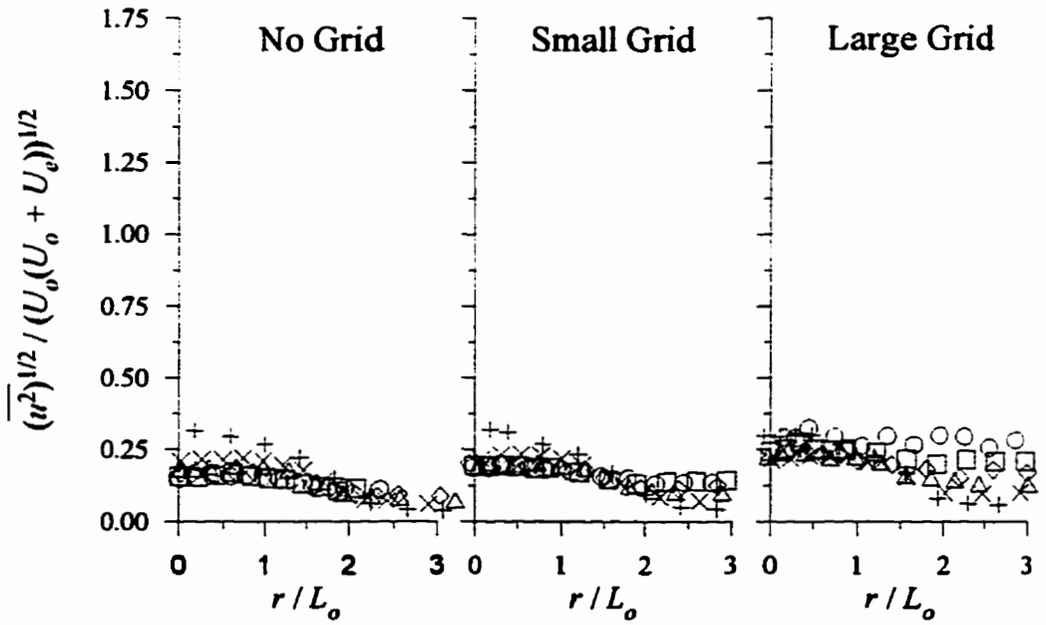

Figure 5.16: Streamwise turbulent velocity profiles for the small jet with $VR \approx 3$ normalized by $(U_o(U_o+U_e))^{1/2}$. x (cm): +, 10; ×, 20; △, 40; ◇, 60; □, 80; ○, 100. $(x-x_o)/\theta$: +, 9.9; ×, 19.6; △, 39.5; ◇, 60.3; □, 81.8; ○, 105.7.

In the majority of cases, especially those close to the jet exit, the radial profile of the normalized streamwise turbulent velocity reach a maximum peak value in the range of $0.7 \leq |r/L_o| \leq 1.0$ giving the profiles a saddle-shaped appearance. This peak corresponds to the normalized radial position in the excess mean velocity profiles where the absolute value of the gradient of the excess mean velocity is a maximum.

5.4.2.2 Centerline Behaviour

The behaviour of the centerline streamwise turbulent velocity, $(\overline{u_o^2})^{1/2}$, is given in Figure 5.17 normalized by U_o and in Figure 5.18 normalized by $(U_o(U+U_e))^{1/2}$. Unlike the radial profiles in the previous section, the centerline data from all the traversing locations have been included. Again only the precision errors are reported for a given experimental set and only for those data points with error bars that extend beyond the limits of the data symbol. This occurs only in the case of $(\overline{u_o^2})^{1/2}$ normalized by U_o for the small jet at $VR \approx 3$ with the large grid installed at the last traversing location.

In addition to the jet centerline values, the external streamwise turbulent velocities have been included in the two figures, also normalized by U_o and $(U_o(U_o+U_e))^{1/2}$, to indicate the relative behaviour of the streamwise turbulent velocities in the external flow.

In Figure 5.17a (large jet, $VR \approx 6$), the magnitudes of $(\overline{u_o^2})^{1/2}/U_o$ are not greatly affected by either the absence or presence of grids in the external flow. This is attributed to the fact that the jet centerline value of $(\overline{u_o^2})^{1/2}/U_o$ is always much greater than the external value of $(\overline{u_e^2})^{1/2}/U_o$ at any given downstream location. The turbulent velocity scales in the two flow fields are thus sufficiently different that they do not significantly influence each other. As the non-dimensional distance from the jet exit is increased, as in Figures 5.17b and 5.17c, the magnitudes of $(\overline{u_e^2})^{1/2}/U_o$ begin to reach levels that influence the corresponding value on the jet centerline. This is especially the case when the large grid is installed. These two plots clearly indicate that $(\overline{u_o^2})^{1/2}/U_o$ increases for the jet with

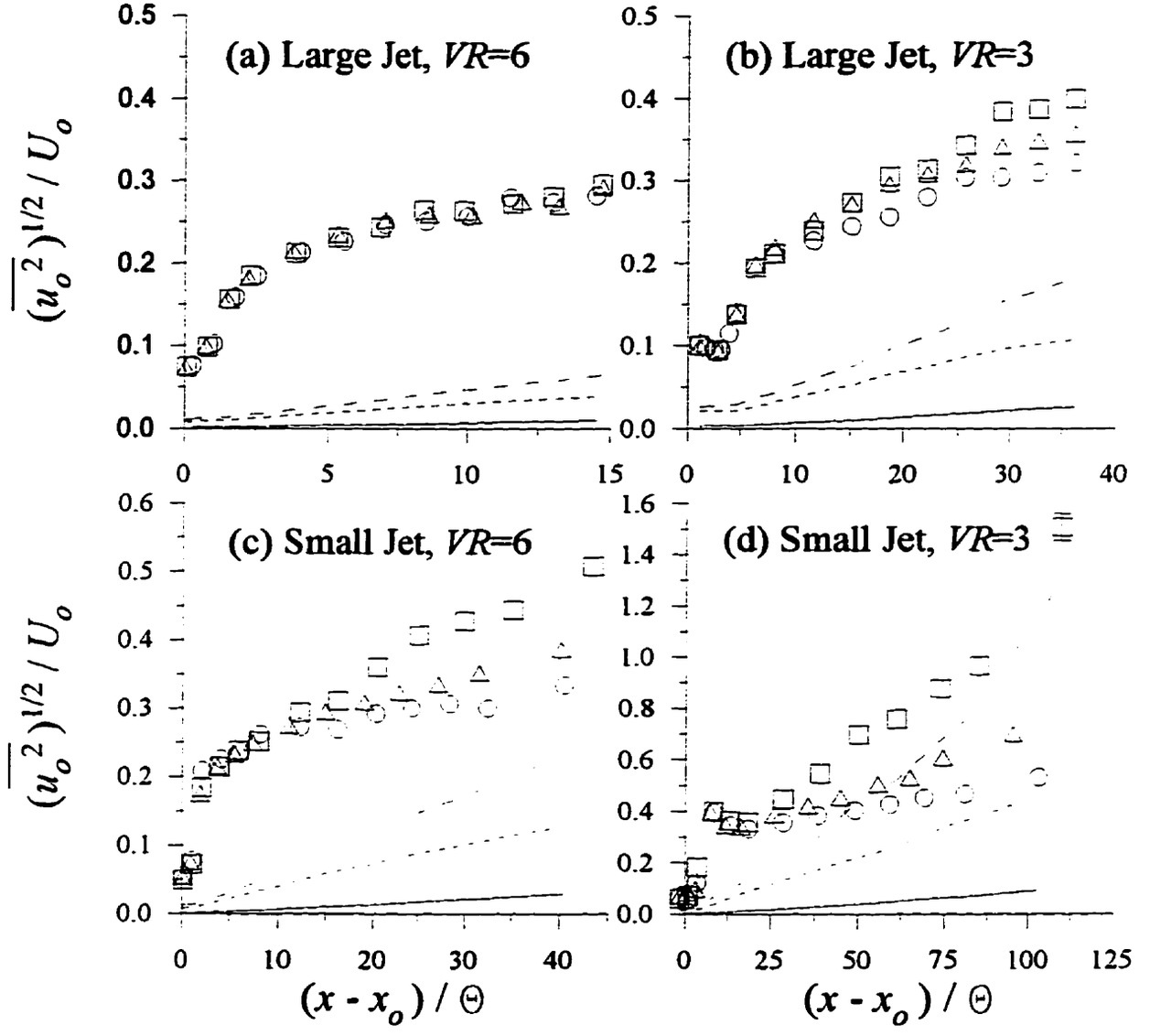

Figure 5.17: Jet centerline and external streamwise turbulent velocities normalized by U_o. Symbols refer to the jet centerline for a given grid: ○, no grid; △, small grid; □, large grid. Lines refer to the external levels: ——, no grid; ----, small grid; – – –, large grid.

either grid installed over that of the jet with no grid installed by $(x-x_o)/\Theta \approx 15$. As the non-dimensional distance is increased further still, as in Figure 5.17d (small jet, $VR \approx 3$), the values of $(\overline{u_e^2})^{1/2}/U_o$ in the external with the large grid installed become larger than $(\overline{u_o^2})^{1/2}/U_o$ for the jet with no grid installed by 50 momentum radii. The growth of $(\overline{u_o^2})^{1/2}/U_o$ for the jet with the large grid installed clearly indicates the influence that the external flow field has on its development.

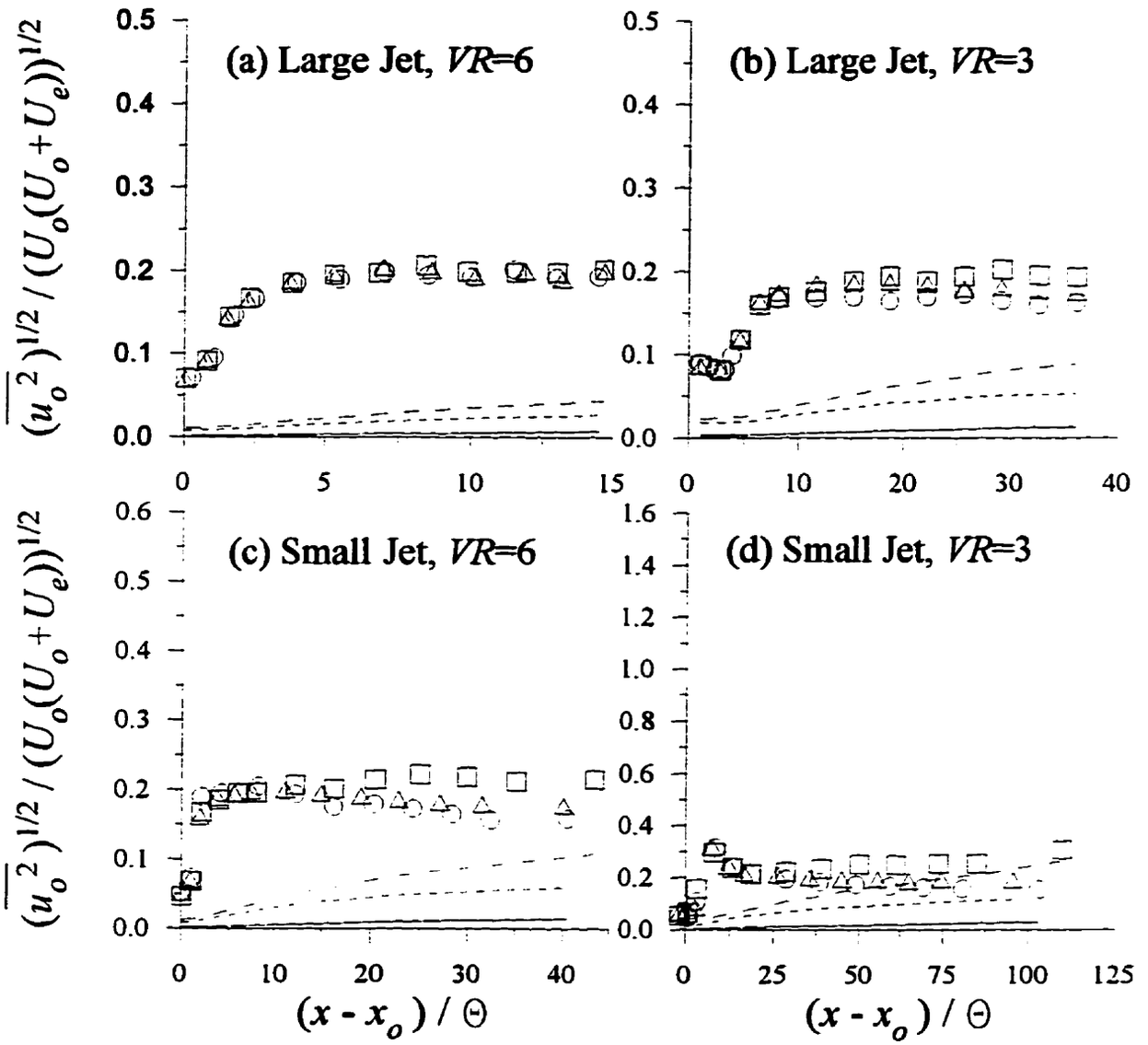

Figure 5.18: Jet centerline and external streamwise turbulent velocities normalized by $(U_o(U_o+U_e))^{1/2}$. Symbols refer to the jet centerline for a given grid: ○, no grid; △, small grid; □, large grid. Lines refer to the external levels: ——, no grid; ----, small grid; – – –, large grid.

The increase in the jet centerline value of $(\overline{u_o^2})^{1/2}/U_o$ when a grid is installed is the result of the jet entraining additional turbulent energy with the external fluid. For the jet with a grid installed, this results in an increase in $(\overline{u_o^2})^{1/2}/U_o$ over the jet with no external turbulence. As noted in the previous section, the jet centerline values do not reach an asymptotic limit when normalized by the conventional velocity scale, U_o, for any of the cases given in Figure 5.17.

Figure 5.18 presents the same data as Figure 5.17 but with $(\overline{u'^2_o})^{1/2}$ normalized by $(U_e(U_o+U_e))^{1/2}$ rather than U_o. Note also that the axes scales are identical to emphasis the differences in the two normalizing techniques. All error bars for the precision errors are within the limits of the data symbols and thus not displayed on the plots. The striking feature about this figure is that all the data appears to approach an asymptotic state. This asymptotic limit falls within the range given by $(\overline{u'^2_o})^{1/2}/(U_o(U_o+U_e))^{1/2} \approx 0.190 \pm 0.024$ where larger values tend to correspond to a more turbulent external coflow. The exception to this is the small jet at $VR \approx 3$ with the large grid installed where there is a slight rising trend in the centerline magnitude due to the increasing external value.

5.4.3 Radial Turbulent Velocity

5.4.3.1 Similarity of Radial Profiles

As with the streamwise components, radial profiles of the radial turbulent velocity, $(\overline{v'^2_r})^{1/2}$, are presented in Figures 5.19 through 5.26. The same trends observed in the streamwise components are also apparent in the behaviour of the radial turbulent velocity. The graphs, however, are still presented for completeness.

When the radial turbulent velocities are normalized by the conventional scale factor, U_o, the radial profiles fail to reach a state of similarity. By normalizing with the new scale factor, $(U_o(U_o+U_e))^{1/2}$, a state of similarity is achieved although the downstream location at which this occurs is somewhat dependent on the experimental set but typically occurs between six and eight momentum radii from the jet exit. The small jet at $VR \approx 3$, however, requires a greater distance of approximately 20 momentum radii before similarity occurs. Normalizing with U_o, however, better emphasizes the effects of external turbulence which is to increase the magnitude of $(\overline{v'^2_r})^{1/2}/U_o$ of the jet with a grid installed over that of the jet with no grid installed by $(x-x_o)/\theta \approx 15$. At a given downstream location, the larger increase corresponds to the jet with the large grid installed in the external coflow. Finally, for the small jet at $VR \approx 3$ with the large grid installed, the values of $(\overline{v'^2_r})^{1/2}/U_o$ in the jet are

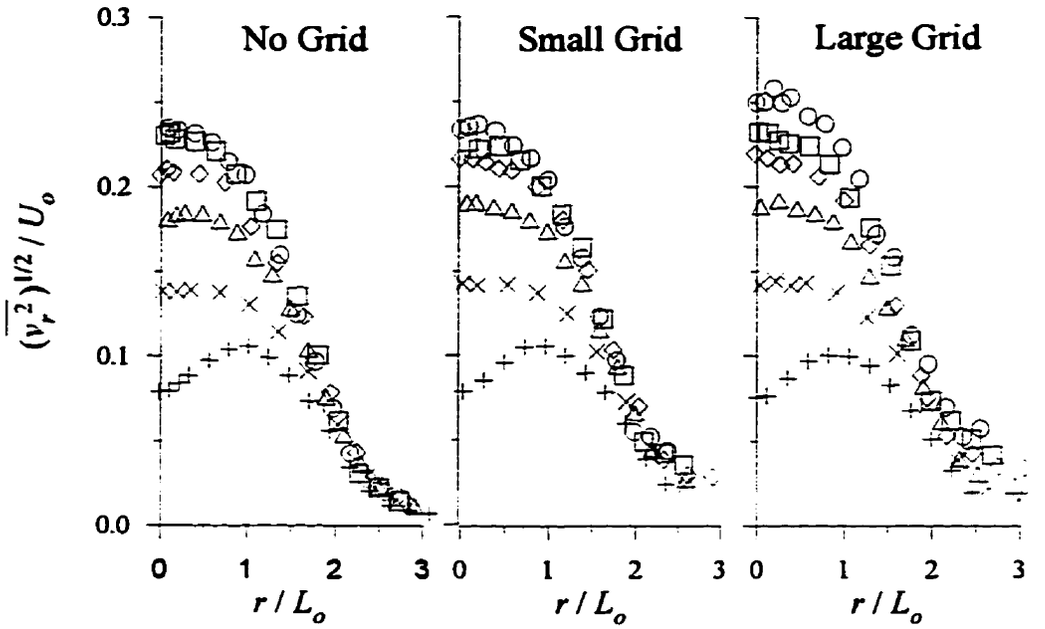

Figure 5.19: Radial turbulent velocity profiles for the large jet with $VR \approx 6$ normalized by U_o. x (cm): +, 10; ×, 20; △, 40; ◇, 60; □, 80; ○, 100. $(x-x_o)/\theta$: +, 0.8; ×, 2.3; △, 5.2; ◇, 8.6; □, 11.8; ○, 14.8.

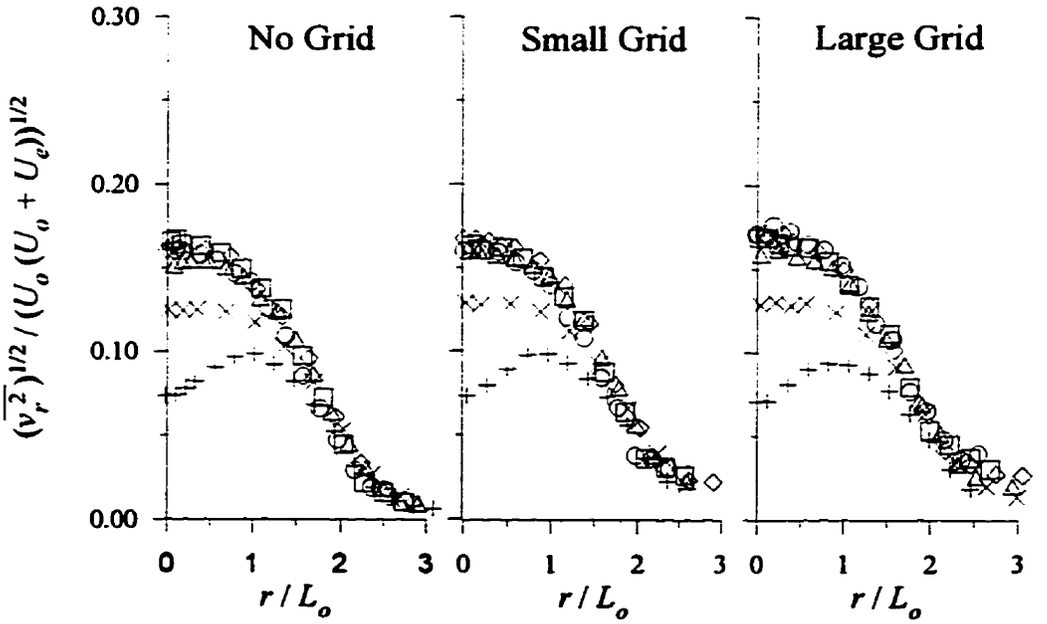

Figure 5.20: Radial turbulent velocity profiles for the large jet with $VR \approx 6$ normalized by $(U_o(U_o+U_e))^{1/2}$. x (cm): +, 10; ×, 20; △, 40; ◇, 60; □, 80; ○, 100. $(x-x_o)/\theta$: +, 0.8; ×, 2.3; △, 5.2; ◇, 8.6; □, 11.8; ○, 14.8.

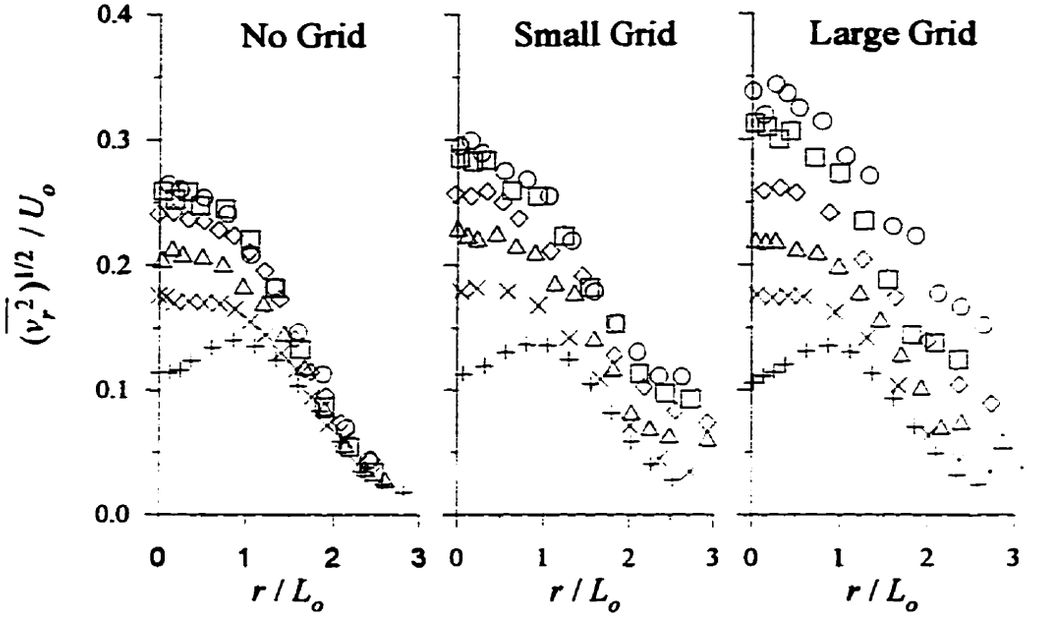

Figure 5.21: Radial turbulent velocity profiles for the large jet with $VR \approx 3$ normalized by U_o. x (cm): +, 10; ×, 20; △, 40; ◇, 60; □, 80; ○, 100. $(x-x_o)/\theta$: +, 4.6; ×, 8.1; △, 15.2; ◇, 22.2; □, 29.2; ○, 36.2.

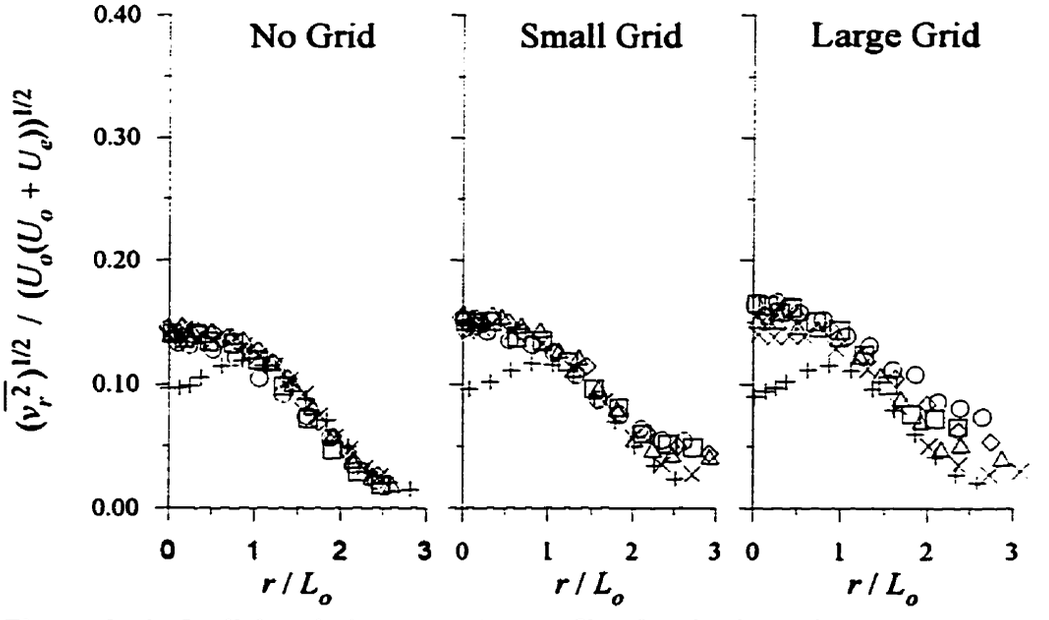

Figure 5.22: Radial turbulent velocity profiles for the large jet with $VR \approx 3$ normalized by $(U_o(U_o+U_e))^{1/2}$. x (cm): +, 10; ×, 20; △, 40; ◇, 60; □, 80; ○, 100. $(x-x_o)/\theta$: +, 4.6; ×, 8.1; △, 15.2; ◇, 22.2; □, 29.2; ○, 36.2.

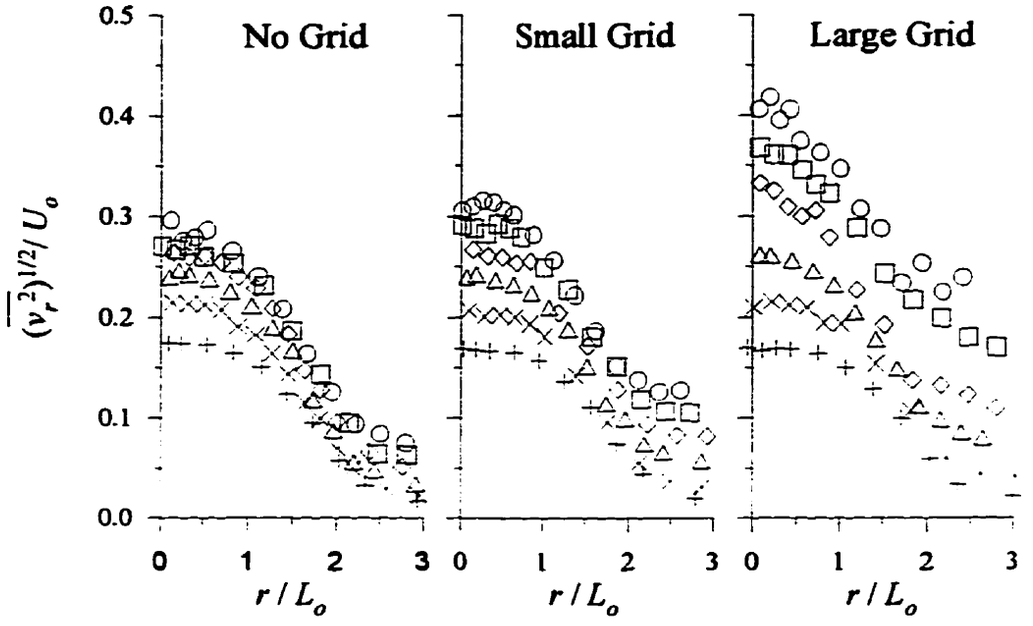

Figure 5.23: **Radial turbulent velocity profiles for the small jet with $VR \approx 6$ normalized by U_o.** x **(cm):** +, 10; ×, 20; △, 40; ◇, 60; □, 80; ○, 100. $(x-x_o)/\theta$: +, 3.3; ×, 7.3; △, 15.2; ◇, 23.4; □, 32.4; ○, 40.7.

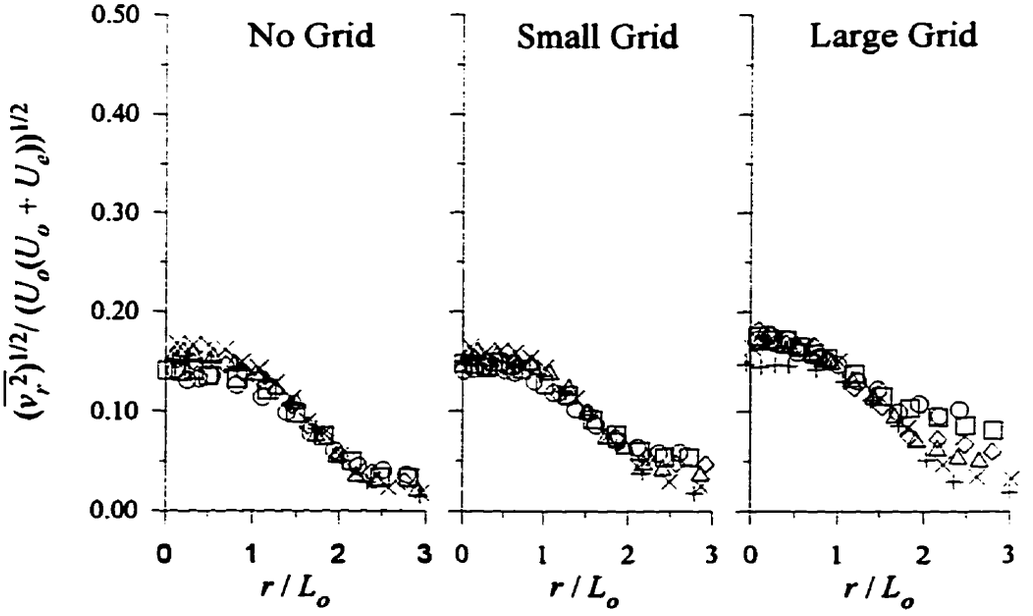

Figure 5.24: **Radial turbulent velocity profiles for the small jet with $VR \approx 6$ normalized by $(U_o(U_o+U_e))^{1/2}$.** x **(cm):** +, 10; ×, 20; △, 40; ◇, 60; □, 80; ○, 100. $(x-x_o)/\theta$: +, 3.3; ×, 7.3; △, 15.2; ◇, 23.4; □, 32.4; ○, 40.7.

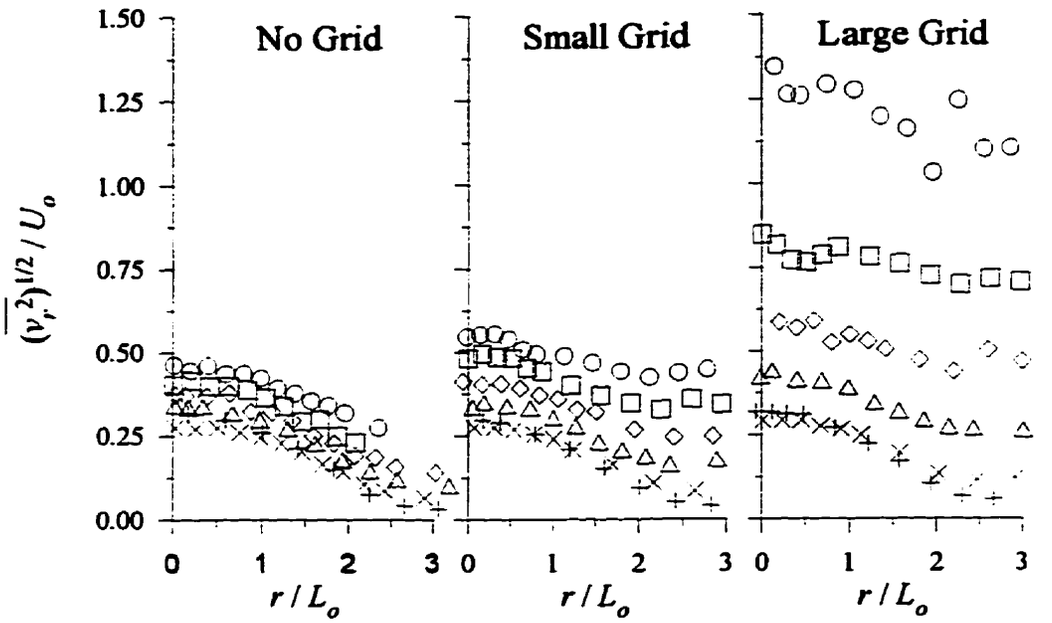

Figure 5.25: **Radial turbulent velocity profiles for the small jet with $VR \approx 3$ normalized by U_o. x (cm): +, 10; ×, 20; △, 40; ◇, 60; □, 80; ○, 100. $(x-x_o)/\theta$: +, 9.9; ×, 19.6; △, 39.5; ◇, 60.3; □, 81.8; ○, 105.7.**

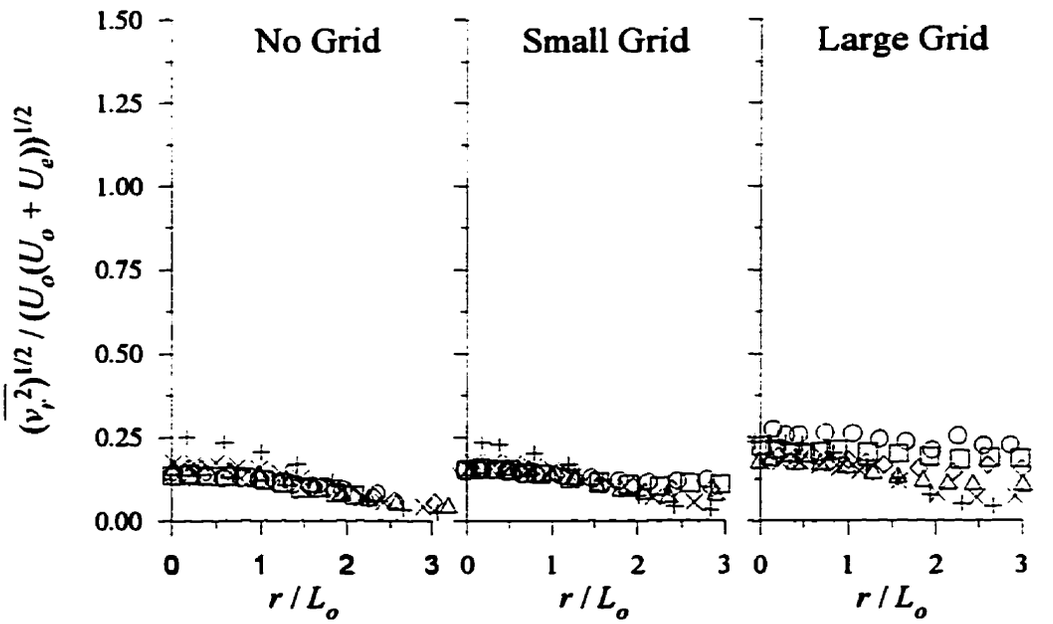

Figure 5.26: **Radial turbulent velocity profiles for the small jet with $VR \approx 3$ normalized by $(U_o(U_o+U_e))^{1/2}$. x (cm): +, 10; ×, 20; △, 40; ◇, 60; □, 80; ○, 100. $(x-x_o)/\theta$: +, 9.9; ×, 19.6; △, 39.5; ◇, 60.3; □, 81.8; ○, 105.7.**

approximately that of the external coflow by the last few traversing locations. This again suggests that the turbulence structure within the jet is slowly taking on the characteristics of the external coflow.

In general, the radial turbulent velocities are typically smaller in magnitude and display a flatter central core (after a few momentum radii from the jet exit) than their corresponding streamwise components.

5.4.3.2 Centerline Behaviour

The behaviour of the centerline radial turbulent velocity, $(\overline{v_{r,o}^2})^{1/2}$ is given in Figure 5.27 normalized by U_o and in Figure 5.28 normalized by $(U_o(U_o+U_e))^{1/2}$. The error bars for the precision errors are all within the limits of the data symbols and thus not reported on the two figures with the exception of the last data point for the small jet at $VR\approx3$ in Figure 5.27. In addition, the radial components of the turbulent velocity in the external flow are included for all levels of external turbulence.

The two figures bear a remarkable resemblance to the corresponding plots for the streamwise turbulent velocity component. Figure 5.27 indicates again that close to the jet exit, the magnitudes of the radial turbulent velocities on the jet centerline and in the external coflow are sufficiently different that any interaction is minimized. As the non-dimensional distance downstream is increased, the levels in the external coflow increase to a level where they begin to influence the magnitude on the jet centerline. Based on the bias errors, this becomes statistically significant at $(x-x_o)/\theta\approx15$. The largest changes on the jet centerline again correspond to the case when the large grid is installed. For the small jet at $VR\approx3$, the external level of $(\overline{v_{r,e}})^{1/2}/U_o$ again surpasses that of the jet with no grid installed by $(x-x_o)/\theta\approx50$. This results in a dramatic increase in $(\overline{v_{r,o}^2})^{1/2}/U_o$ for the jet with the large grid installed. Again note that centerline values do not reach an asymptotic limit over the experimental regime when normalized by the conventional scale factor, U_o.

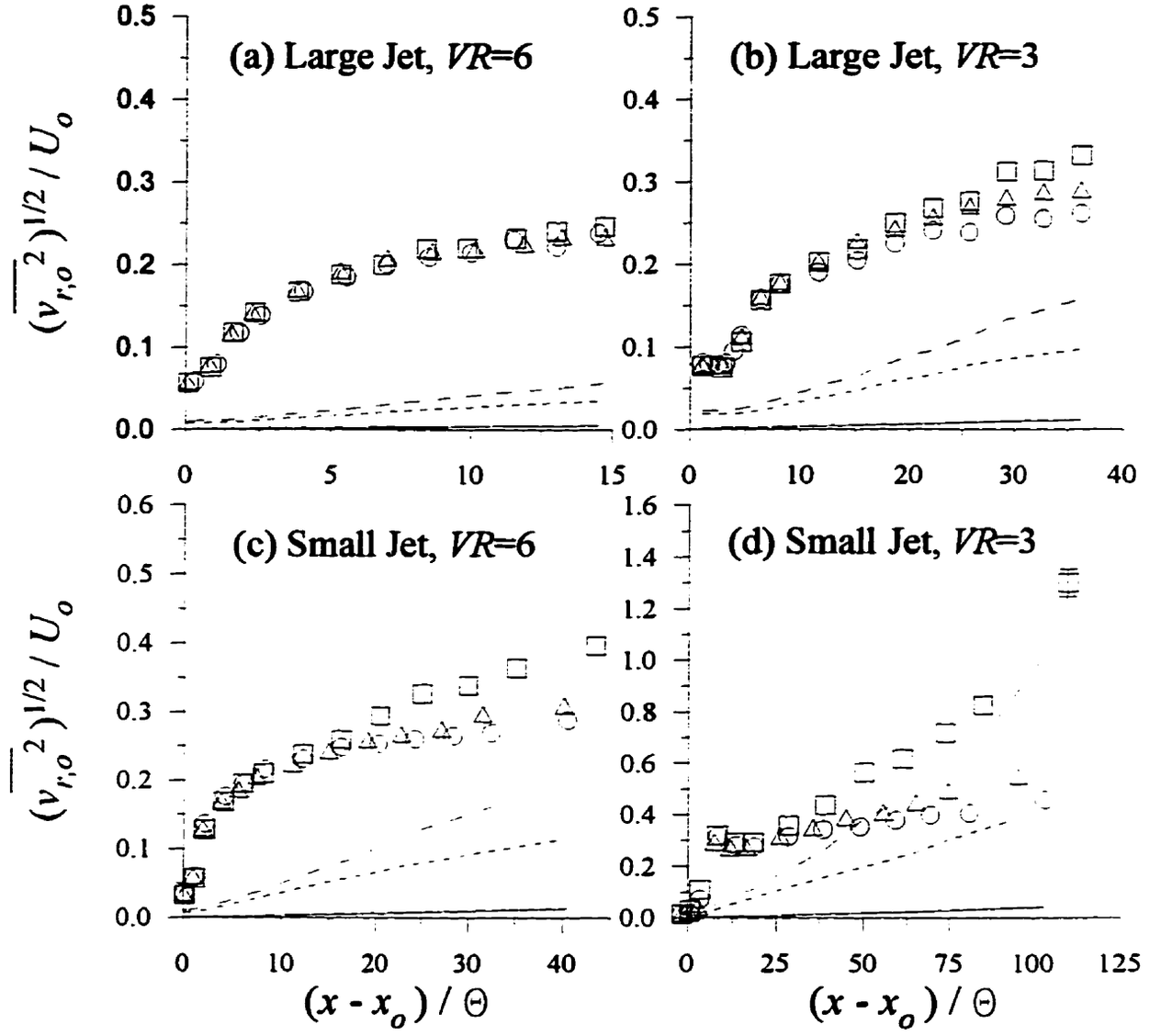

Figure 5.27: Jet centerline and external radial turbulent velocities normalized by U_o. Symbols refer to the jet centerline for a given grid: ○, no grid; △, small grid; □, large grid. Lines refer to the external levels: ——, no grid; ----, small grid; – – –, large grid.

Figure 5.28 illustrates again that by normalizing the data with the new scale factor, $(U_o(U_o+U_e))^{1/2}$, an approximate asymptotic value is reached of $\overline{(v_{r,o}^2)}^{1/2}/(U_o(U_o+U_e))^{1/2} \approx 0.156 \pm 0.017$ in nearly all the experimental cases. The exception to this is again the small jet at $VR \approx 3$ with the large grid installed where there is a slight increasing trend in the data due to the increasing values in the external coflow. As with the streamwise direction, a higher level of external turbulence typically corresponds to a higher asymptotic limit.

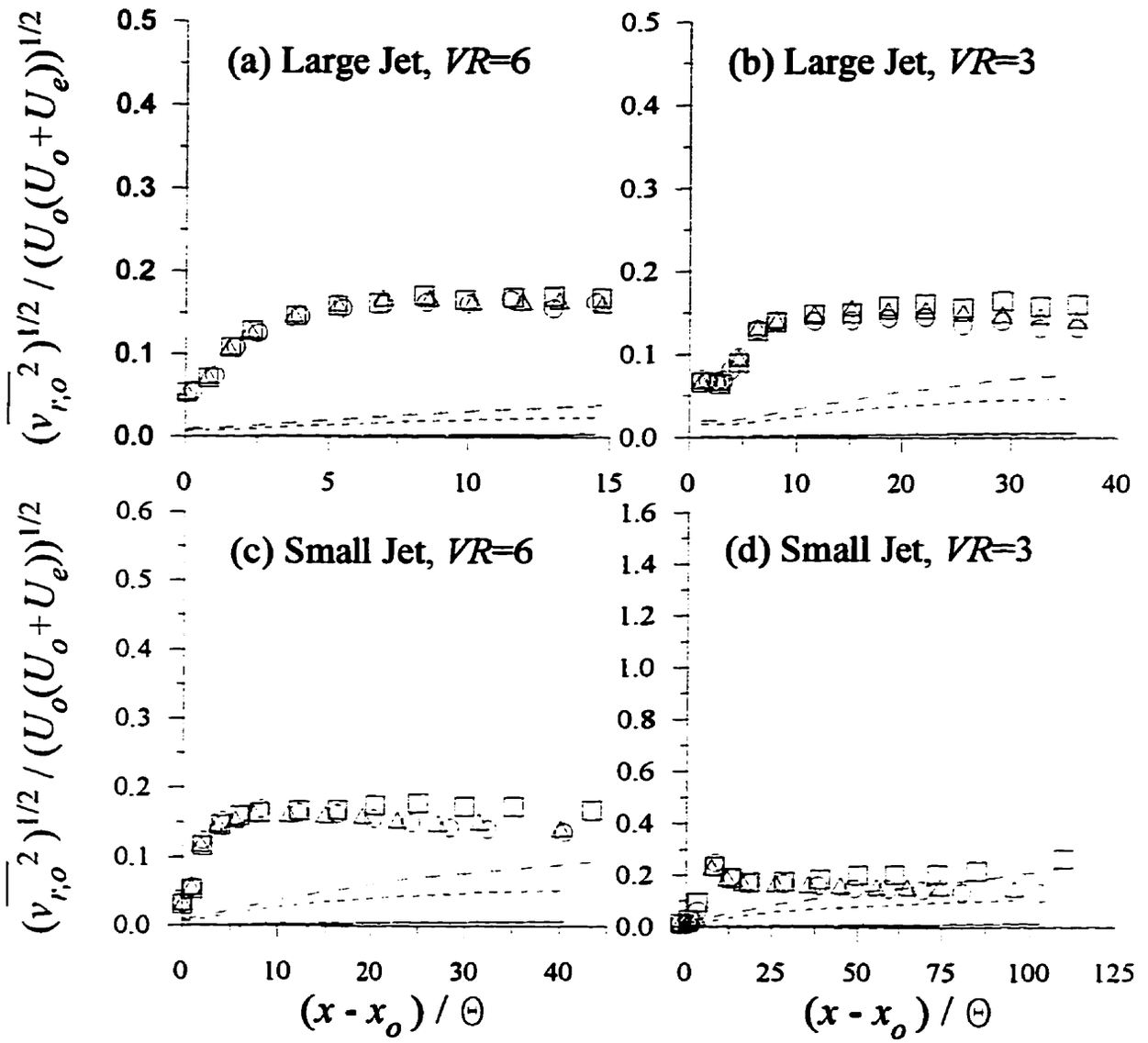

Figure 5.28: Jet centerline and external radial turbulent velocities normalized by $(U_o(U_o+U_e))^{1/2}$. Symbols refer to the jet centerline for a given grid: ○, no grid; △, small grid; □, large grid. Lines refer to the external levels: ——, no grid; ----, small grid; – – –, large grid.

5.4.4 Reynolds Shear Stress

5.4.4.1 Similarity of Radial Profiles

As with the turbulent velocity, the radial profiles of the Reynolds shear stress, $\overline{u\,v}_r$, are normalized by the conventional method using U_o^2 and by the new method using $U_o(U_o+U_e)$. This results in two plots, again given on the same page for ease of comparison, for each set of jet experiments. These plots are given in Figures 5.29 to 5.36.

In order to better illustrate the radial behaviour of $\overline{u\,v}_r$, r/L_o extends to both the positive and negative halves of the jet. The resulting distributions show a positive maximum for $\overline{u\,v}_r$ when r/L_o is negative and a negative maximum for $\overline{u\,v}_r$ when r/L_o is positive. The location of the maxima occurs in the range $0.7 \le |r/L_o| \le 1.0$ which corresponds to the peaks in the streamwise turbulent velocity profiles and the location of the maximum gradient in the excess mean velocity profiles.

The trend in the Reynolds shear stress profiles are similar to those observed in the streamwise and radial turbulent velocity profiles. When normalized by U_o^2, the conventional scale factor, the profiles fail to obtain a state of similarity and when normalized by $U_o(U_o+U_e)$, the new scale factor, the profiles obtain a reasonable state of similarity after only a few momentum radii downstream from the jet exit. The exception to this is again the small jet at $VR \approx 3$ which displays similarity after $(x-x_o)/\theta \approx 10$. The effects of external turbulence are best illustrated when the radial profiles of $\overline{u\,v}_r$ are normalized by U_o^2. As expected from the turbulent velocity results, external turbulence increases the magnitude of $\overline{u\,v}_r/U_o^2$ after $(x-x_o)/\theta \approx 15$. The largest increase in $\overline{u\,v}_r/U_o^2$ again occurs in the jet with the large grid installed. This is most dramatically illustrated by the results for the small jet at $VR \approx 3$ given in Figure 5.35. For the jet with the large grid installed the measured levels of $\overline{u\,v}_r/U_o^2$ are approximately five times larger than the other two cases thus making it necessary to increase the scale on the ordinate axis for this particular case.

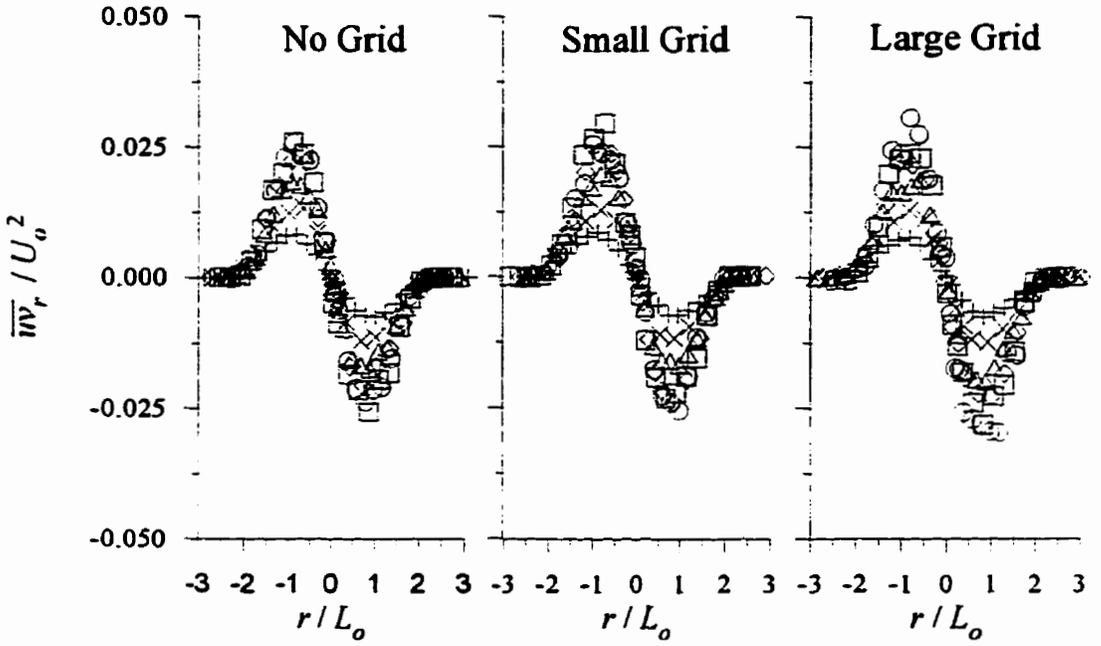

Figure 5.29 : Reynolds shear stress profiles for the large jet with $VR \approx 6$ normalized by U_o^2. x (cm): +, 10; ×, 20; △, 40; ◇, 60; □, 80; ○, 100. $(x-x_o)/\theta$: +, 0.8; ×, 2.3; △, 5.2; ◇, 8.6; □, 11.8; ○, 14.8.

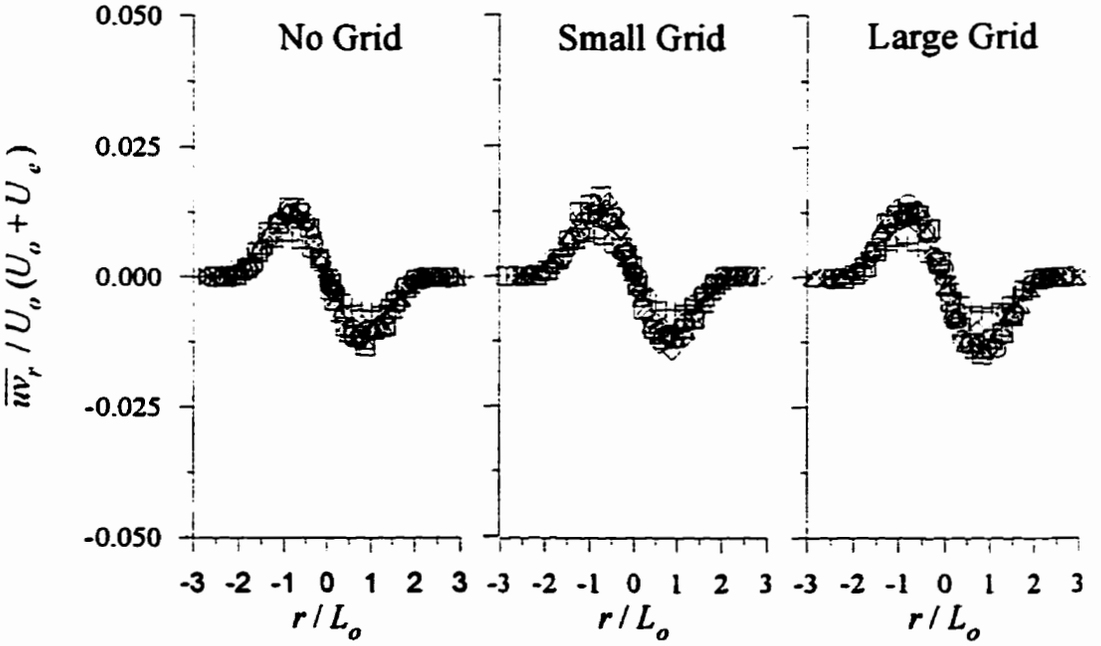

Figure 5.30 : Reynolds shear stress profiles for the large jet with $VR \approx 6$ normalized by $U_o(U_o+U_e)$. x (cm): +, 10; ×, 20; △, 40; ◇, 60; □, 80; ○, 100. $(x-x_o)/\theta$: +, 0.8; ×, 2.3; △, 5.2; ◇, 8.6; □, 11.8; ○, 14.8.

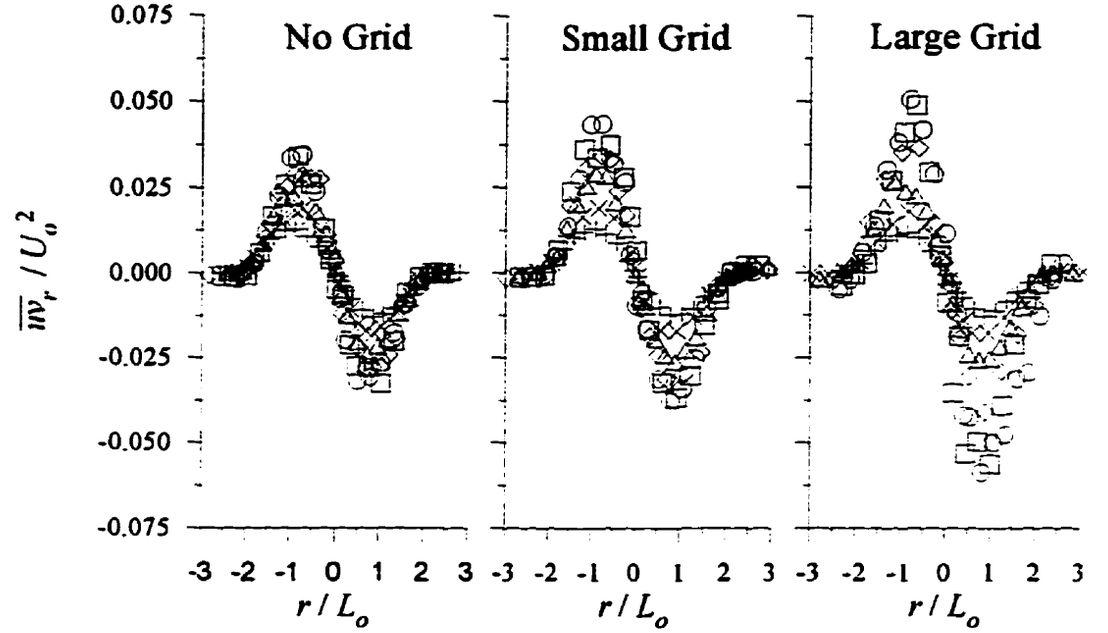

Figure 5.31 : Reynolds shear stress profiles for the large jet with $VR \approx 3$ normalized by U_o^2. x (cm): +, 10; ×, 20; △, 40; ◇, 60; □, 80; ○, 100. $(x-x_o)/\theta$: +, 4.6; ×, 8.1; △, 15.2; ◇, 22.2; □, 29.2; ○, 36.2.

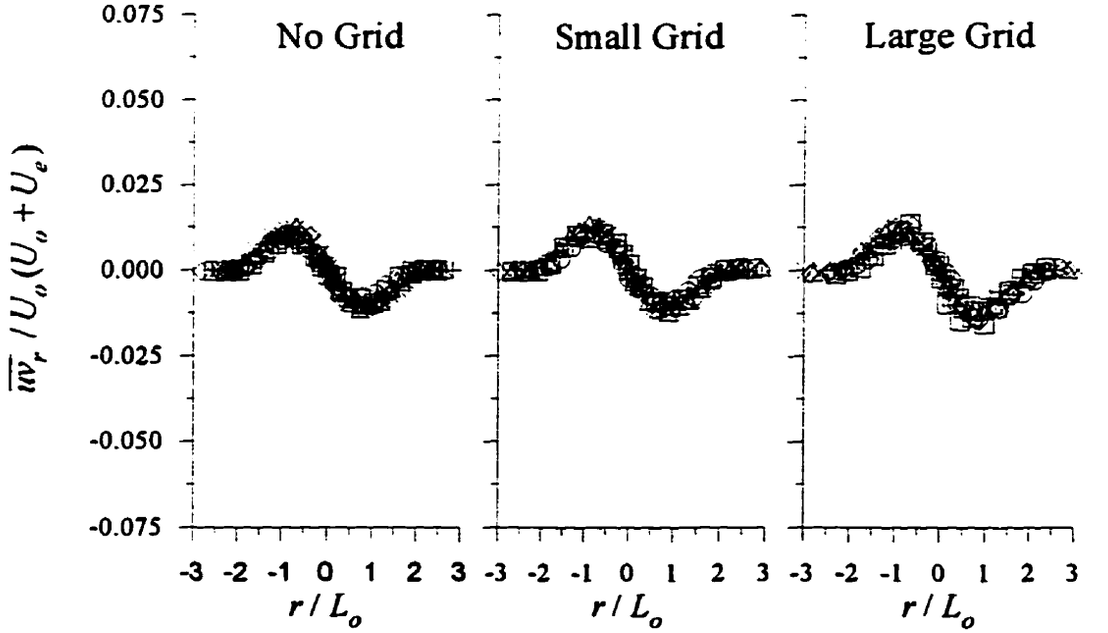

Figure 5.32 : Reynolds shear stress profiles for the large jet with $VR \approx 3$ normalized by $U_o(U_o+U_e)$. x (cm): +, 10; ×, 20; △, 40; ◇, 60; □, 80; ○, 100. $(x-x_o)/\theta$: +, 4.6; ×, 8.1; △, 15.2; ◇, 22.2; □, 29.2; ○, 36.2.

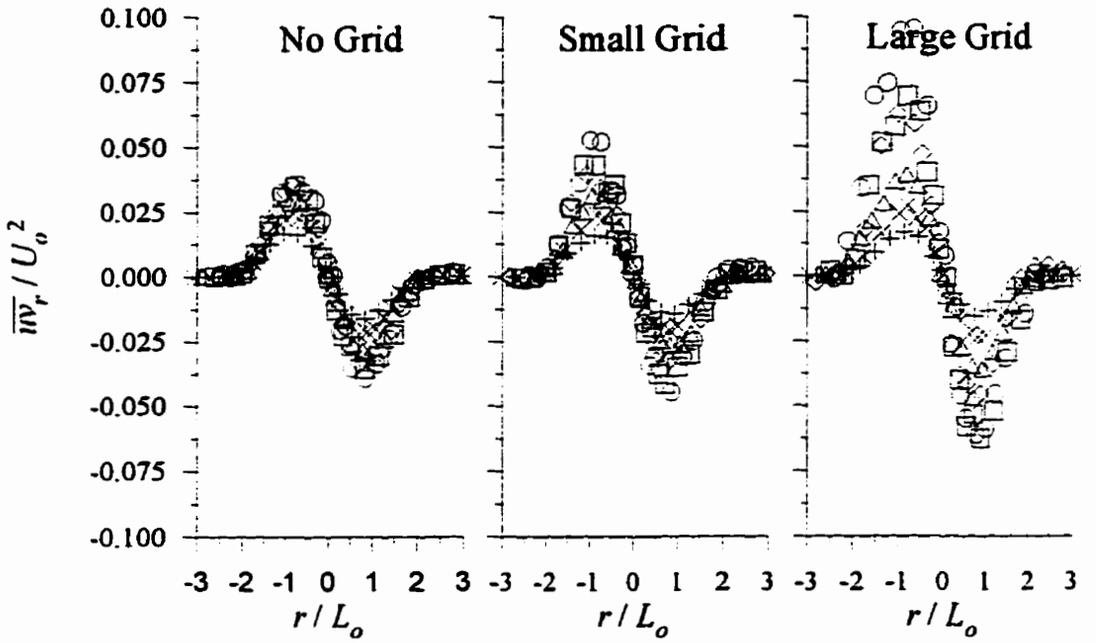

Figure 5.33 : Reynolds shear stress profiles for the small jet with $VR \approx 6$ normalized by U_o^2. x (cm): +, 10; ×, 20; △, 40; ◇, 60; □, 80; ○, 100. $(x-x_o)/\theta$: +, 3.3; ×, 7.3; △, 15.2; ◇, 23.4; □, 32.4; ○, 40.7.

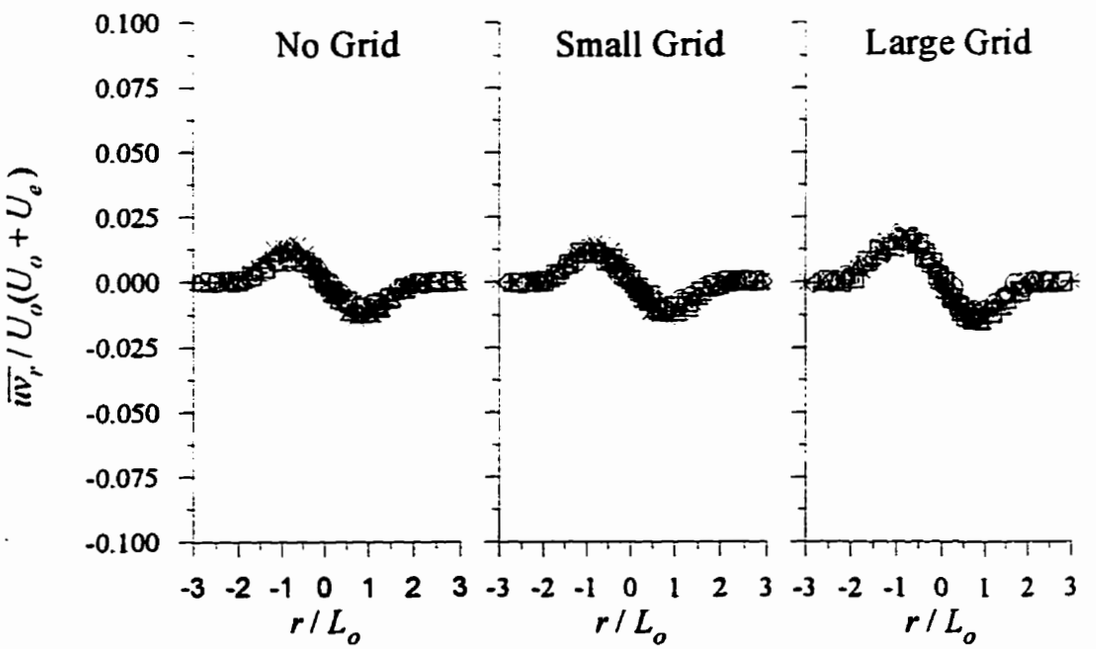

Figure 5.34 : Reynolds shear stress profiles for the small jet with $VR \approx 6$ normalized by $U_o(U_o+U_e)$. x (cm): +, 10; ×, 20; △, 40; ◇, 60; □, 80; ○, 100. $(x-x_o)/\theta$: +, 3.3; ×, 7.3; △, 15.2; ◇, 23.4; □, 32.4; ○, 40.7.

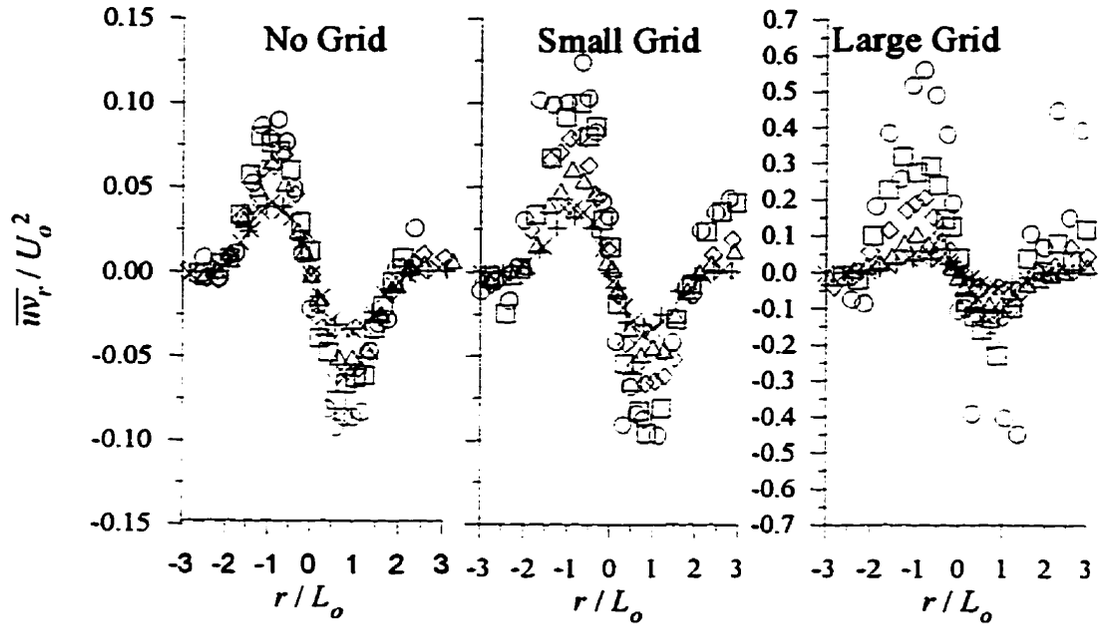

Figure 5.35 : Reynolds shear stress profiles for the small jet with $VR \approx 3$ normalized by U_o^2. x (cm): +, 10; ×, 20; △, 40; ◇, 60; □, 80; ○, 100. $(x-x_o)/\theta$: +, 9.9; ×, 19.6; △, 39.5; ◇, 60.3; □, 81.8; ○, 105.7.

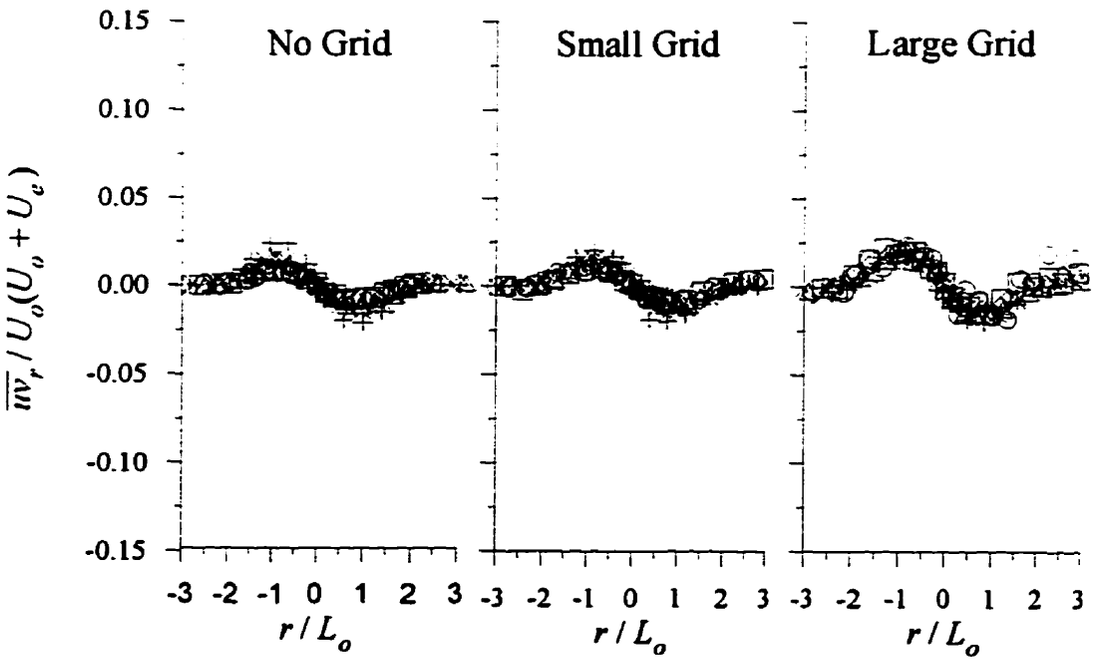

Figure 5.36 : Reynolds shear stress profiles for the small jet with $VR \approx 3$ normalized by $U_o(U_o+U_e)$. x (cm): +, 10; ×, 20; △, 40; ◇, 60; □, 80; ○, 100. $(x-x_o)/\theta$: +, 9.9; ×, 19.6; △, 39.5; ◇, 60.3; □, 81.8; ○, 105.7.

5.4.4.2 Average Maximum Behaviour

The absolute maximum value of the Reynolds shear stress, $|\overline{uv_r}|_{max}$, taken as the average of the two experimental maxima on both the positive and negative r-sides of the jet, are plotted in Figure 5.37 normalized by U_o^2 and in Figure 5.38 normalized by $U_o(U_o+U_e)$. Also included in the figures is the approximate level of Reynolds shear stress in the external coflow, $|\overline{u\,v_r}|_e$, for reference purposes. Error bars have been included for data points that have precision error bars that extend beyond the limits of their symbols.

When the maximum Reynolds shear stress is normalized by U_o^2, as in Figure 5.37, the data fails to reach an asymptotic level which would indicate a state of similarity. The effects of introducing a grid into the external flow is to increase the magnitude of $|\overline{u\,v_r}|_{max}/U_o^2$ by a downstream location of approximately $(x-x_o)/\theta \approx 15$. The largest increase again corresponds to the jets with the large grid installed. It is of interest to note that the external levels of the Reynolds shear stress are relatively small in comparison to the jet maxima. (The external levels with no grid installed actually fall on the horizontal axis of the graph.) The exception to this is the small jet at $VR \approx 3$ with the large grid installed. This would seem to indicate the Reynolds shear stresses in the jet are not greatly affected by their corresponding external levels, but depend on other quantities within the jet. Physically this makes sense since the Reynolds shear stress terms are responsible for the transfer of turbulent momentum between the streamwise and radial Reynolds normal stress terms. Thus, the magnitude of $\overline{u\,v_r}$ in the jet is more dependent on the levels of the normal stresses than the shear stresses in the external coflow.

Normalizing the maximum Reynolds shear stress using $U_o(U_o+U_e)$, as in Figure 5.38, shows that the approximate asymptotic limits are reached although there is a slight hump in the profile over the range of $5 \le (x-x_o)/\theta \le 20$. In addition, the presence of a grid in the external coflow results in a slightly higher asymptotic limit after $(x-x_o)/\theta \approx 15$. The overall average asymptotic limit, excluding the run for the small jet at $VR \approx 3$ with the large grid installed, is $|\overline{uv_r}|_{max}/(U_o(U_o+U_e)) = 0.012 \pm 0.002$. The limit for the small jet at $VR \approx 3$ with the large grid installed is 0.019.

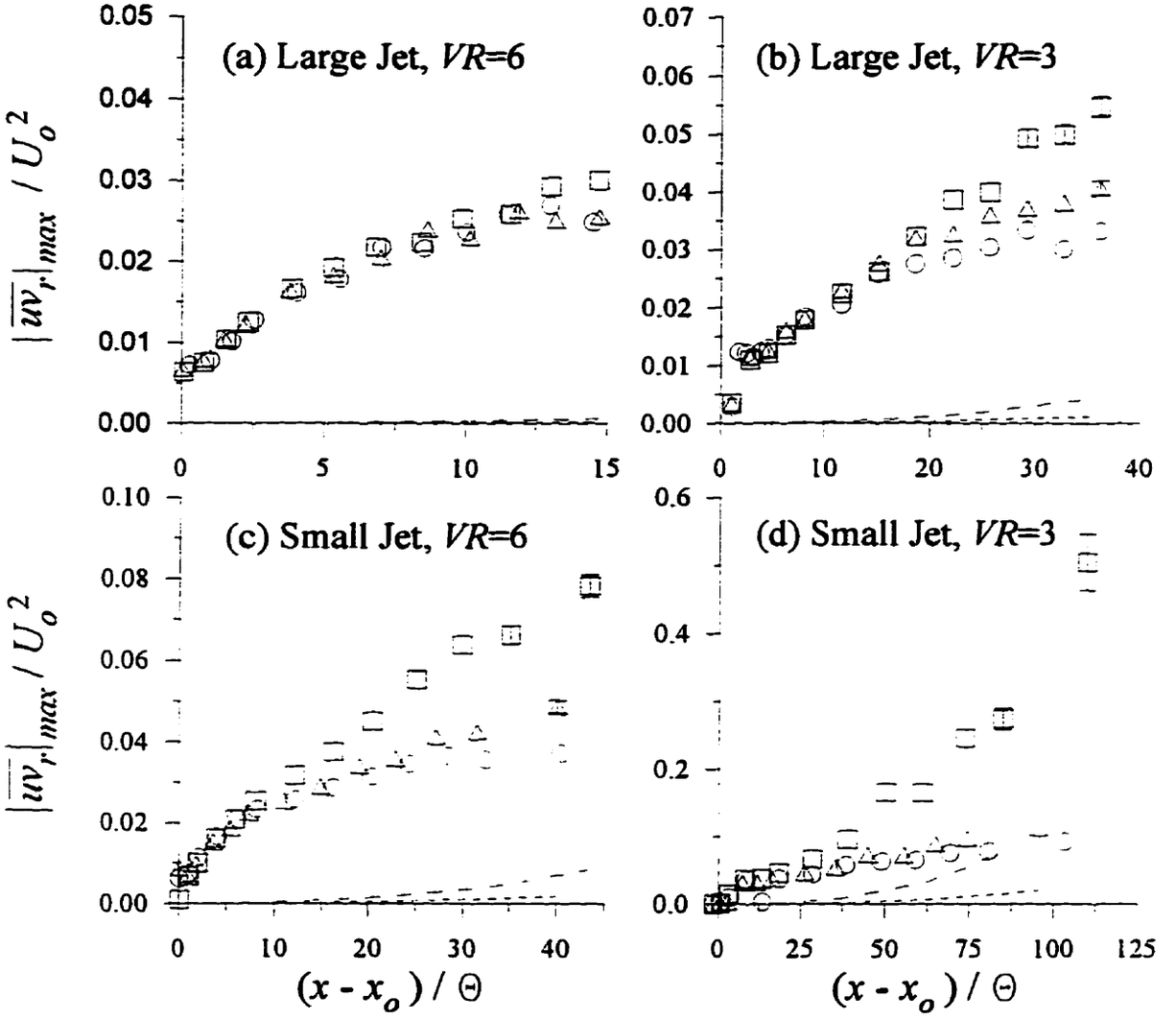

Figure 5.37: Average maximum Reynolds shear stress normalized by U_o^2. Symbols refer to the jet for a given grid: ○, no grid; △, small grid; □, large grid. Lines refer to external levels: ——, no grid; - - - -, small grid; – – –, large grid.

5.4.5 Summary of Reynolds Stress Results

When the Reynolds stresses are normalized by the conventional method (turbulent velocities by U_o and Reynolds shear stresses by U_o^2), the distributions fail to reach a state of similarity over the downstream regime covered by the four sets of jet experiments. Normalizing the Reynolds stresses with the new method (turbulent velocities by $(U_o(U_o+U_e))^{1/2}$ and Reynolds shear stresses by

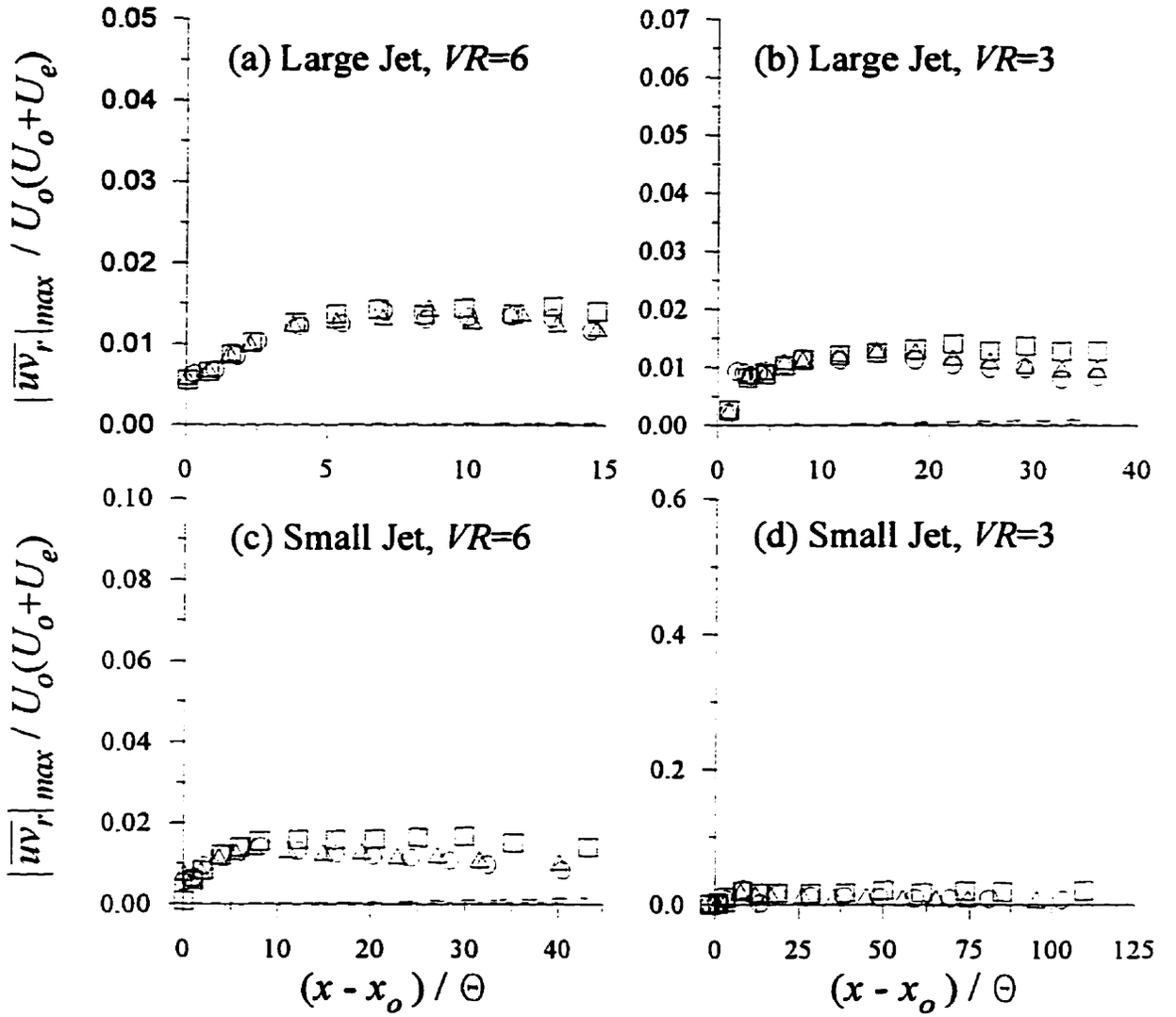

Figure 5.38: Average maximum Reynolds shear stress normalized by $U_o(U_o+U_e)$. Symbols refer to the jet for a given grid: ○, no grid; △, small grid; □, large grid. Lines refer to external levels: ——, no grid; - - - -, small grid; – – –, large grid.

$U_o(U_o+U_e)$) effectively makes the distributions similar often within the first ten momentum radii from the jet exit. It can therefore be concluded that the Reynolds stresses (both normal and shear) in a coflowing jet scale with ($U_o(U_o+U_e)$) and not with U_o^2 which is the conventional method of scaling Reynolds stresses. Thus the new scale factor is the appropriate scale factor for normalizing Reynolds stresses. This is advantageous in a modelling sense since the turbulent velocities are now directly proportional to the new mean velocity scale and can thus be replaced by it in the equations of motion.

The asymptotic limits for the centerline turbulent velocities are given approximately by:

$$(\overline{u_o^2})^{1/2}/(U_o(U_o+U_e))^{1/2} \approx 0.190 \pm 0.024 \text{ m/s}$$

$$(\overline{v_{r,o}^2})^{1/2}/(U_o(U_o+U_e))^{1/2} \approx 0.156 \pm 0.017 \text{ m/s}$$

while the asymptotic limit for the maximum Reynolds shear stress is given approximately by:

$$|\overline{uv_r}|_{max}/(U_o(U_o+U_e)) \approx 0.012 \pm 0.002 \text{ m}^2/\text{s}^2.$$

Introducing a turbulence generating grid into the external coflow results in larger magnitudes for the turbulent velocities and Reynolds shear stresses starting in the range of $15 \le (x-x_o)/\theta \le 20$ with the largest magnitudes corresponding to the case with the large grid installed.

5.5 Integral Length Scales

The streamwise and radial integral length scales, L_{xx} and L_{rr}, obtained by multiplying the integral time scales of the streamwise and radial turbulent velocities by the local mean velocity, provide an indication of how the average to larger energy containing eddies within the jet vary with distance downstream. Precision errors on individual values of the integral length scale, normalized by the jet radius, range between 2% and 20% depending on the jet initial conditions, distance downstream from the jet exit, and the level of turbulence both within the jet and the external coflow. To reduce the magnitude of this error, an average integral time scale is obtained for a given jet cross section which is then converted to an integral length scale using the average or top-hat mean velocity, $\overline{U}$, for the given jet cross section. This not only reduces the precision error by a factor of $1/\sqrt{n}$, where n is the number of data points used in the average, but makes the convecting velocity equal to the average velocity within the jet.

The streamwise integral length scales normalized by the jet radius, R, are given in Figure 5.39 while the radial components are given in Figure 5.40. The symbols give the average value of the integral length scale over a given jet cross section normalized by the jet radius. All precision error bars are found to be within the limits of the data symbols and thus not reported on the figures. The dashed

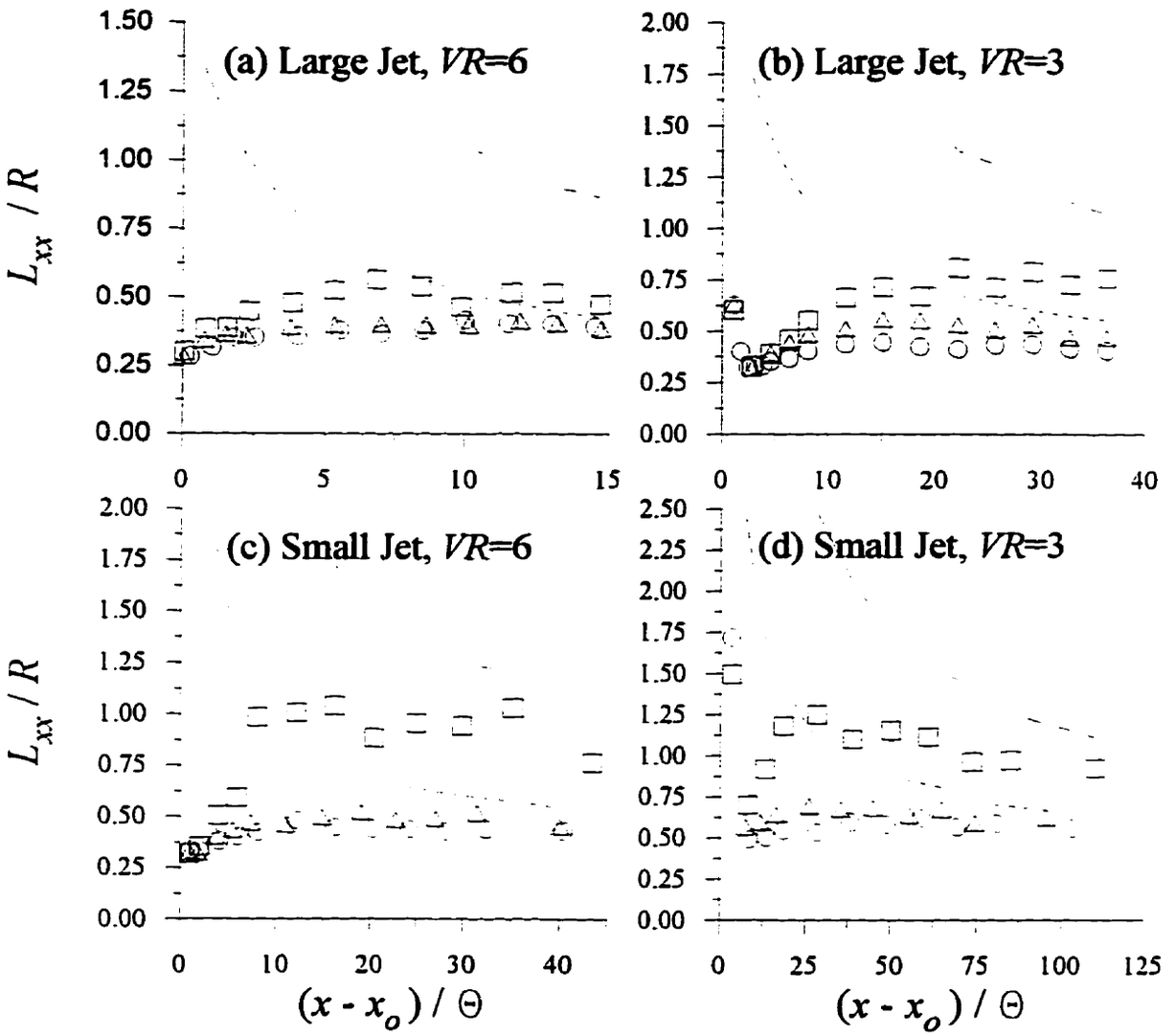

Figure 5.39: Average streamwise integral length scales normalized by the jet radius. Symbols refer to the jet for a given grid: ○, no grid; △, small grid; □, large grid. Lines refer to levels in the external flow also normalized by R: - - - -, small grid; – – –, large grid.

lines give the magnitude of the integral length scales in the external flow, also normalized by the jet radius at a given downstream location. Accurate values for the integral length scales in the absence of grid-generated turbulence are not obtainable due to the low turbulence levels coupled with the low energy noise of the LDA system.

For the jet without a grid installed, all four plots in Figure 5.39 indicate the streamwise integral

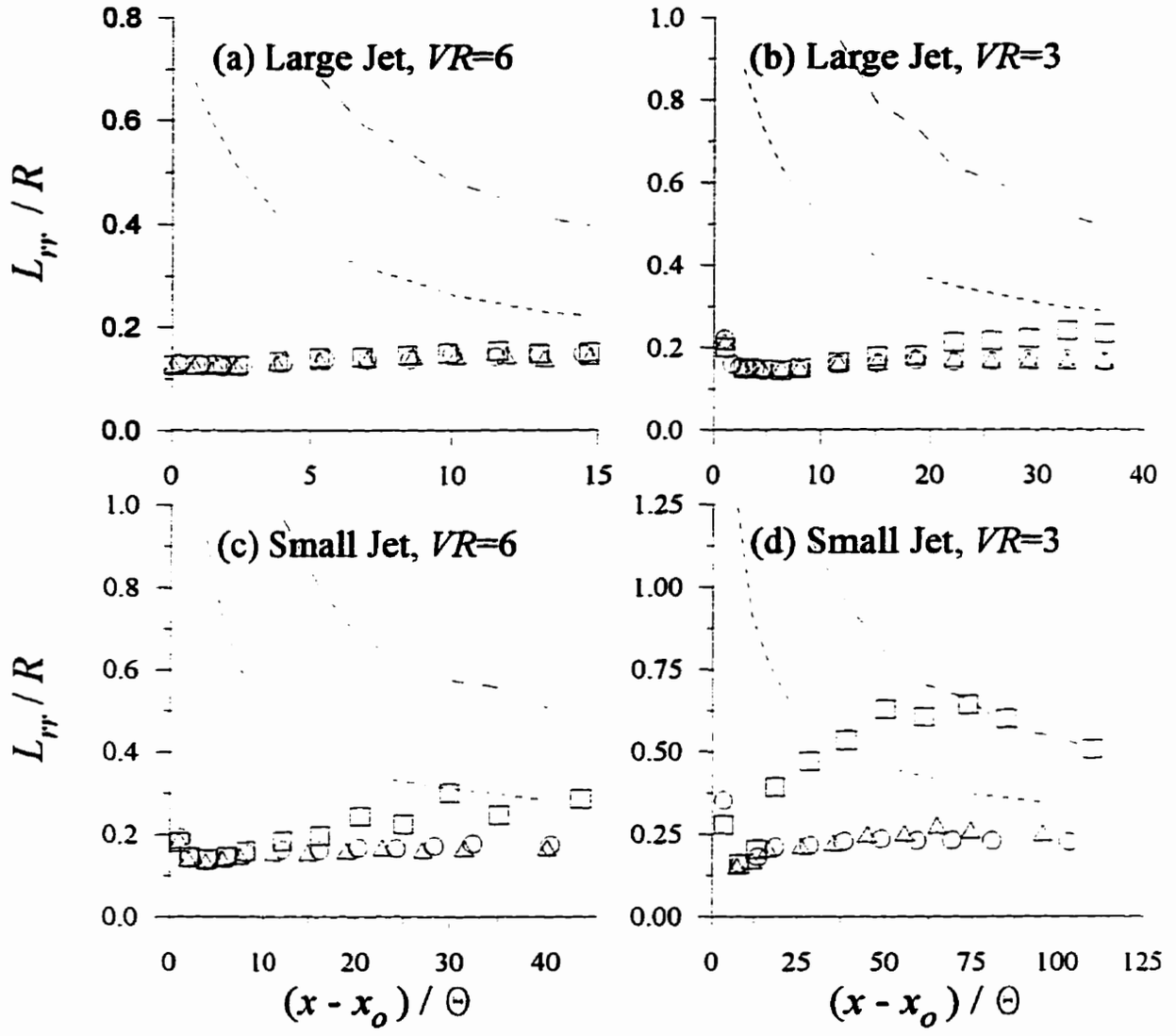

Figure 5.40: Average radial integral length scales normalized by the jet radius. Symbols refer to the jet for a given grid: ○, no grid; △, small grid; □, large grid. Lines refer to levels in the external flow also normalized by R: - - - -, small grid; – – –, large grid.

length scale is directly proportional to the jet radius which is the radial geometric scale of the flow. The asymptotic value of L_{rr}/R varies from 0.39 for the large jet at $VR \approx 6$ up to 0.57 for the small jet at $VR \approx 3$ with an average value of approximately 0.46.

When the large grid is installed in the external flow, the external values of $L_{rr,e}/R$ are quite large in comparison to the average value in the jet with no grid installed. As a result, an increase in the

magnitude of L_{xx}/R in the jet occurs in all the experimental sets very shortly after the jet exit, roughly around $(x-x_o)/\theta \approx 5$. For the large jet at $VR \approx 6$, the magnitude of L_{xx}/R is only slightly larger than that for the jets with no grid and small grid installed. As the non-dimensional distance is increased, as in Figures 5.39b and 5.39c, the magnitude of L_{xx}/R in the jet with the large grid installed increases towards the external level. In Figure 5.39c, the last two data points actually decrease in magnitude at a rate similar to that of the external flow. This is more apparent in Figure 5.39d where there is an initial rise in L_{xx}/R in the jet up until $(x-x_o)/\theta \approx 25$ after which L_{xx}/R decays as the level in the external coflow is approached.

When the small grid is installed, the external value of $L_{xx,e}/R$ drops to within the same order of magnitude as the average values within the jet with no grid installed, typically by 5 to 15 momentum radii downstream from the jet exit. In fact, by the last traversing location in each of the experimental sets, the level of $L_{xx,e}/R$ in the external for the small grid has decreased almost to the point as that found in the jet without a grid installed. Thus it is not surprising that the values for L_{xx}/R in the jet with the small grid installed are only slightly larger than those for the jet with no grid installed.

For the radial integral length scales, Figure 5.40 indicates again that for the jet with no grid installed, the integral length scales are proportional to the radius of the jet. This result is not too surprising since one could intuitively guess that the radial integral scale would be proportional to the radial geometric scale. Recall, however, that L_{rr} by its definition (see Chapter 2) is not strictly a true radial scale since it relies on the average mean streamwise velocity for conversion from a temporal scale to a spatial scale. The asymptotic value of L_{rr}/R for the jet with no grid installed ranges from 0.14 for the large jet at $VR \approx 6$ to 0.23 for the small jet at $VR \approx 3$ with an average value of 0.18. On average, the radial integral length scales are approximately 40% the magnitude of the corresponding streamwise components.

When the large grid is installed in the external, the level of $L_{rr,e}/R$ is roughly half an order of magnitude larger than the average level in the jet with no grid installed which is the same trend

observed for the streamwise component. Despite this similarity in the external values, the behaviour of L_{rr}/R for the jet with the large grid installed is, however, somewhat different than its streamwise counterpart. The magnitude of L_{rr}/R does not start to increase above the jet with no grid installed until $(x-x_o)/\theta \approx 15$, which corresponds to the downstream location where the turbulent velocities for the jet with the large grid installed began to deviate from the no grid case. In addition, there is only a modest increase in L_{rr}/R with the large grid installed for the large jet at $VR \approx 3$ and the small jet at $VR \approx 6$ in comparison to their streamwise components. However, for the small jet at $VR \approx 3$, the increase in L_{rr}/R is quite significant with the last three data points actually falling on the curve for the external levels of L_{rr}/R thus indicating that the jet with the large grid installed is acquiring the characteristics of the external flow.

When the small grid is installed, the external levels of $L_{rr,e}/R$ again drop to within the same order of magnitude as the average values in the jet with no grid. Thus there is only a minor increase in L_{rr}/R for the jet with the small grid installed over the no grid case.

In summary, both the average streamwise and radial integral lengths for the jet with no grid installed in the external flow are proportional to the radius of the jet. Increasing the level of turbulence in the external flow with the small grid results in only minor increases in the average integral length scales within the jet over that of the jet with no grid installed. By inserting the large grid in the external flow, however, the average streamwise integral length scales become larger than those for the jet with no grid installed by $(x-x_o)/\theta \approx 5$. The average radial integral length scales did not begin to do this until $(x-x_o)/\theta \approx 15$. Also, by the final three traversing locations for the small jet at $VR \approx 3$, the magnitude of the average integral length scales in the jet are comparable to those in the external flow, especially in the radial direction.

5.6 Power Spectral Density (PSD) Functions

The streamwise and radial power spectral density functions, $E_{xx}(f)$ and $E_{rr}(f)$, obtained from the measured instantaneous velocity time series, represent the distribution of turbulent kinetic energy over the range of frequencies that comprise the velocity signal. The precision error associated with a signal spectrum is approximately 32% which makes comparison with other spectra questionable, especially if the spectra have only slightly different energy levels. To reduce this high level of precision error, an average turbulent energy spectra has been calculated for a given jet cross section. This reduces the precision error by $1/\sqrt{n}$ where n is the number of spectra used in the average. Typically, n varies between 15 to 20 thus giving a precision error on the order of 8% for the average spectra.

The spectra have also been converted from the frequency domain, f, to the wavenumber domain, k, since the turbulent energy content of eddies with diameters of order k^{-1} can be determined directly from the spectrum. As with the integral scales of motion, a spatial measurement is easier to interpret than a temporal or frequency based measurement. To convert from the frequency domain to the wavenumber domain, use is again made of Taylor's theory of frozen turbulence, namely:

$$k = \frac{2\pi}{\overline{U}} f \tag{5.2}$$

and:

$$E(k) = \frac{\overline{U}}{2\pi} E(f) \tag{5.3}$$

where the convecting velocity is again assumed to be equal to the average mean velocity, $\overline{U}$, across the jet cross section. It should be kept in mind that Taylor's theory of frozen turbulence is only an approximation that is reasonable in homogeneous turbulence and thus should be viewed with some caution when applied in shear flows.

The average turbulent energy spectrum represents the average distribution of turbulent energy per unit mass over the eddy sizes that comprise the flow at a given downstream location. These spectra can therefore by used to illustrate how the turbulent energy distribution changes with downstream location as well as with different turbulent energy levels in the external coflow. The resulting streamwise turbulent energy spectra, $E_{uu}(k)$, are given in Figures 5.41 to 5.44 for each of the experimental sets. To give a representative depiction of the downstream development, six profiles have been selected for each level of external turbulence. In addition, the approximate location of the integral length scales ($L_{uu} \propto k^{-1}$) have been included on the spectra for reference purposes to mark the evolution of the larger energy containing eddies. Also included in the figures are the turbulent energy spectra for the external flow with the small and large grids installed. Typical precision errors for these external spectra are on the order of 13%. A reasonably accurate turbulent energy spectrum for the external flow with no grid installed could not be obtained due to the low level of turbulent energy coupled with the low energy noise of the LDA system.

Close to the jet exit, as for the large jet at $VR \approx 6$ given in Figure 5.41, the average turbulent energy within the jet is far greater than that in any of the external coflows. Thus the relative downstream evolution of the average spectra within the jet are virtually unaffected by the presence of turbulence in the external flow. At farther non-dimensional distances from the jet exit, as for the large jet at $VR \approx 3$ and the small jet at $VR \approx 6$ given respectively in Figures 5.42 and 5.43, the average turbulent energy within the jet decreases to a level where the turbulent energy within the external coflow begins to affect the behaviour of the average jet spectra. This is evidenced by the increase in the turbulent energy content at the smaller wavenumbers (or larger length scales) within the average jet spectra when a grid is installed in the external flow. At the farthest non-dimensional locations, as for the small jet at $VR \approx 3$ given in Figure 5.44, the average turbulent energy within the jet has decreased to the levels in the external coflow when a grid is installed. At the farthest point, the average spectra of the jet, although containing slightly more turbulent energy at all wave-numbers, has acquired the same spectral shape as that in the turbulent external coflow. The greatest influence of the external turbulence on the evolution of the average turbulent energy spectra occur when the large grid is installed in the external flow.

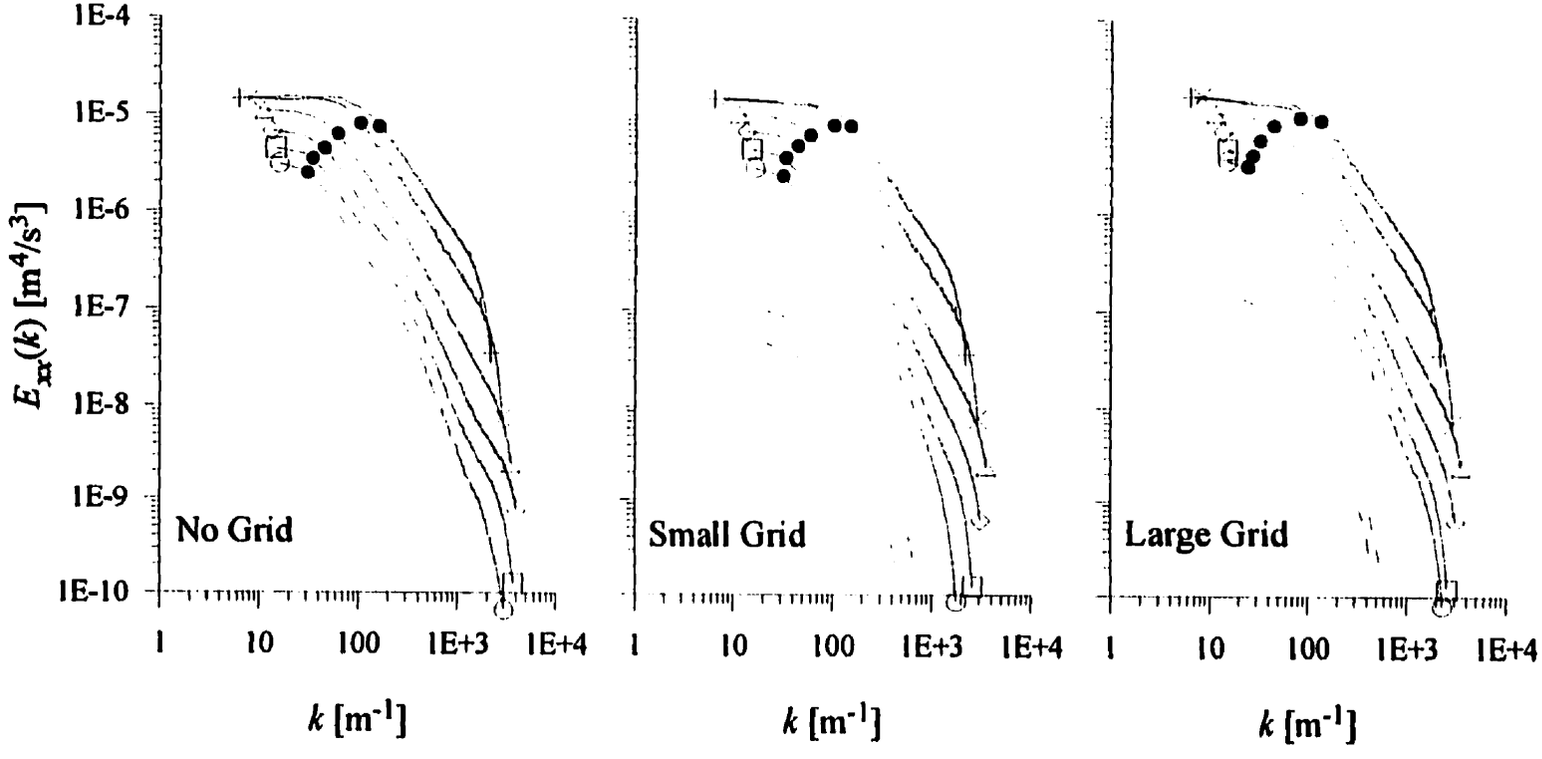

Figure 5.41: Average streamwise turbulent energy spectra for the large jet at $VR \approx 6$. x (cm): +, 10; ×, 20; △, 40; ◇, 60; □, 80; ○, 100. $(x-x_o)/\theta$: +, 0.8; ×, 2.3; △, 5.2; ◇, 8.6; □, 11.8; ○, 14.8. External spectra range: - - - -, small grid; – – –, large gird. Solid bullets, ●, give approximate locations of L_{xx} on spectra.

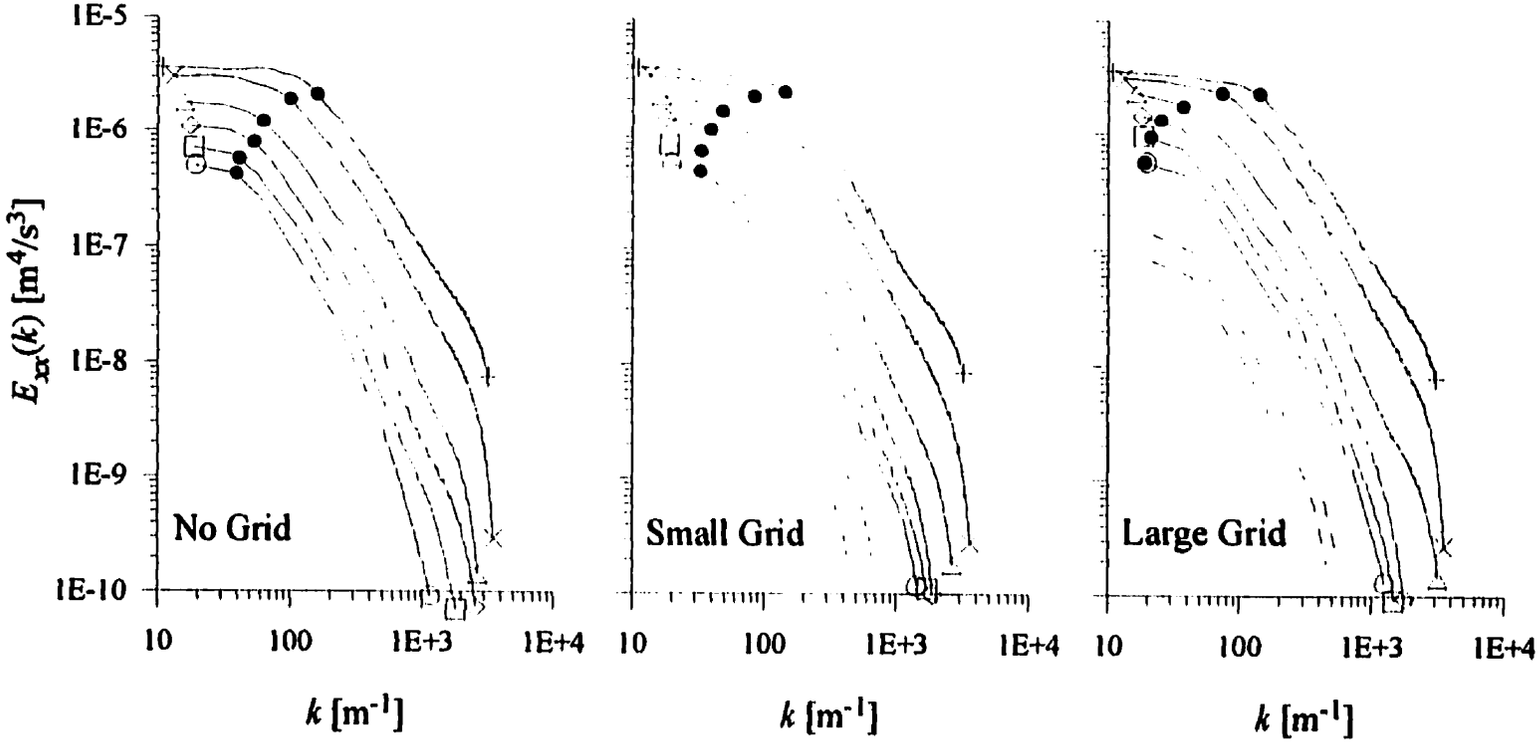

Figure 5.42: Average streamwise turbulent energy spectra for the large jet at $VR \approx 3$. x (cm): +, 10; ×, 20; △, 40; ◇, 60; □, 80; ○, 100. $(x-x_o)/\theta$: +, 4.6; ×, 8.1; △, 15.2; ◇, 22.2; □, 29.2; ○, 36.2. External spectra range: - - - -, small grid; – – –, large gird. Solid bullets, ●, give approximate locations of L_{xx} on spectra.

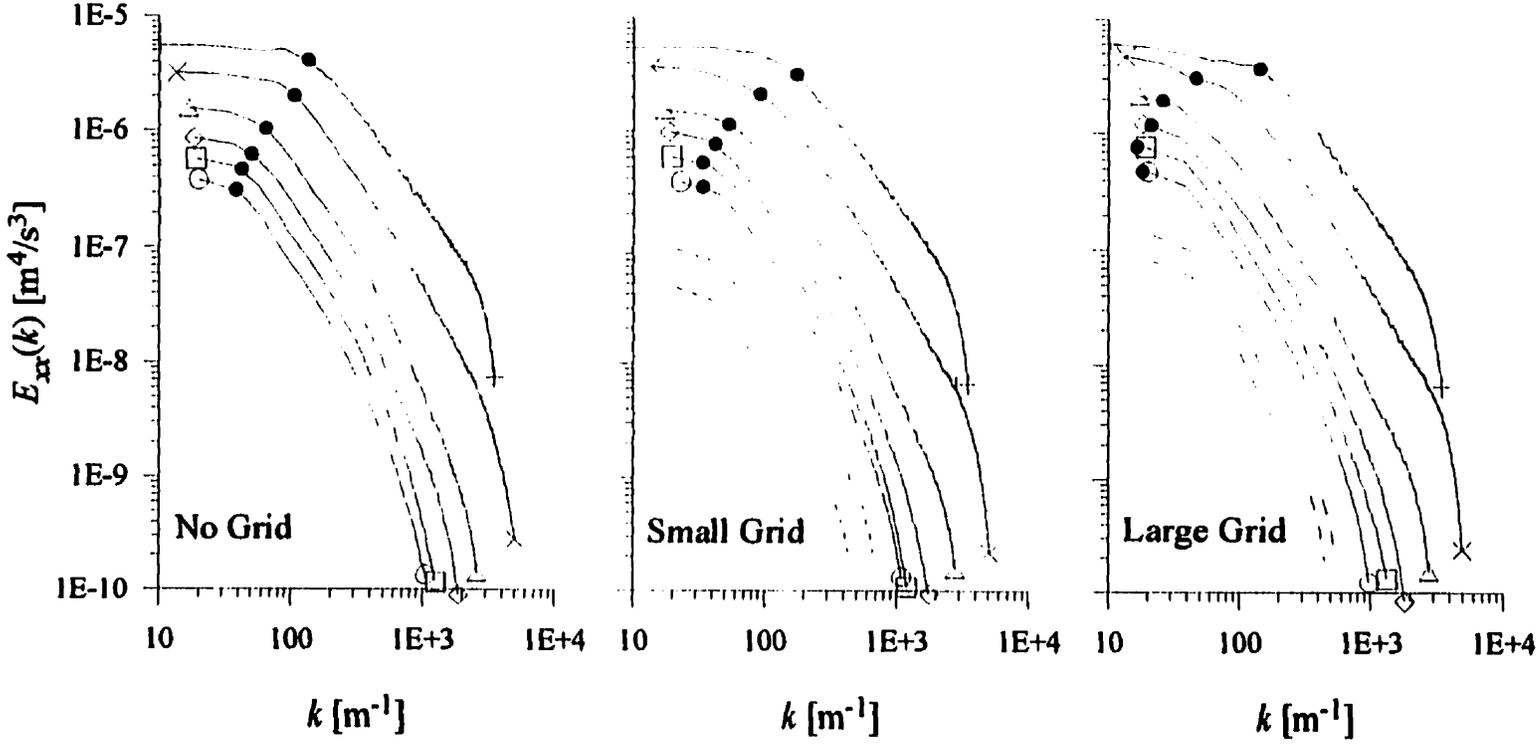

Figure 5.43: Average streamwise turbulent energy spectra for the small jet at $VR \approx 6$. x (cm): +, 10; ×, 20; △, 40; ◇, 60; □, 80; ○, 100. $(x-x_o)/\theta$: +, 3.3; ×, 7.3; △, 15.2; ◇, 23.4; □, 32.4; ○, 40.7. External spectra range: - - - -, small grid; – – –, large gird. Solid bullets, ●, give approximate locations of L_{xx} on spectra.

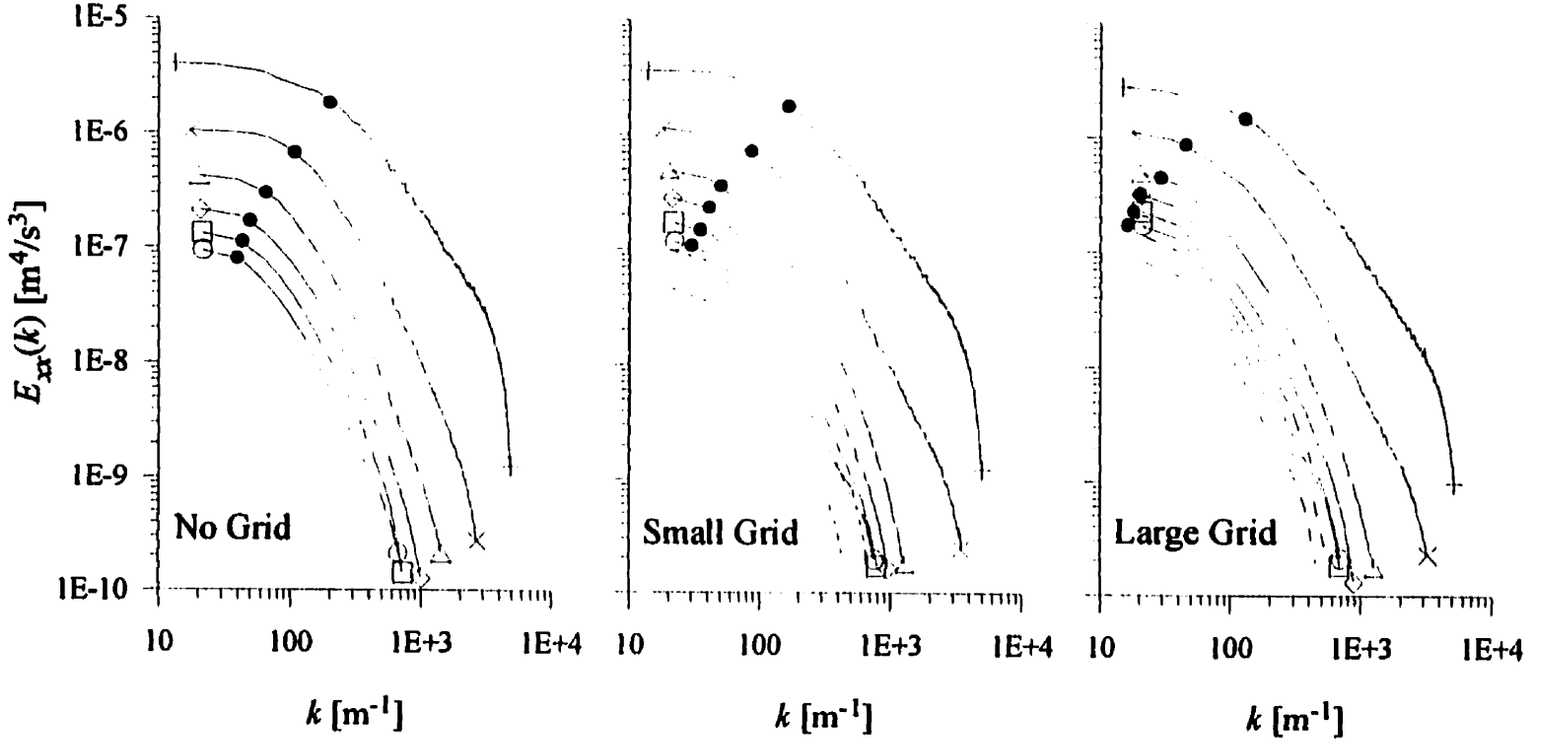

Figure 5.44: Average streamwise turbulent energy spectra for the small jet at $VR \approx 3$. x (cm): +, 10; ×, 20; △, 40; ◇, 60; □, 80; ○, 100. $(x-x_o)/\theta$: +, 9.9; ×, 19.6; △, 39.5; ◇, 60.3; □, 81.8; ○, 105.7. External spectra range: - - - -, small grid; – – –, large gird. Solid bullets, ●, give approximate locations of L_{xx} on spectra.

The average radial turbulent energy spectra, $E_{rr}(k)$, are presented in Figures 5.45 To 5.48 in a similar manner as the streamwise components. Note that the shape of the average radial turbulent energy spectra differ from the streamwise component by exhibiting a peak in the spectrum in the vicinity of k~100 m^{-1} which, in a given experimental set, shifts to smaller wavenumbers as distance from the jet exit is increased. Also, the location of the integral length scales occurs further down on $E_{rr}(k)$ than for $E_{xx}(k)$.

Aside from the slight differences in shape, the behaviour of $E_{rr}(k)$ is not radically different from $E_{xx}(k)$. For the large jet at VR≈6, the turbulent energy content of the external flow with the large and small grids installed is too small at all wavenumbers to dramatically affect the average jet spectra. As the non-dimensional distance is increased, as for the large jet at VR≈3 given in Figure 5.46 and the small jet at VR≈6 given in Figure 5.47, the average turbulent energy within the jet decreases to a level that is influenced by the level in the external flow. This is again evidenced by the greater amount of turbulent energy in the smaller wavenumbers (or larger length scales) in the average jet spectra when a grid is installed by the final few traversing locations. This is especially apparent in the jet with the large grid installed in the external flow. As the non-dimensional distance is increased further, as for the small jet at VR≈3 given in Figure 5.48, the turbulent energy within the jet continues to drop until we begin to see the shape of the average spectra emulating the shape of the spectra for the external flow.

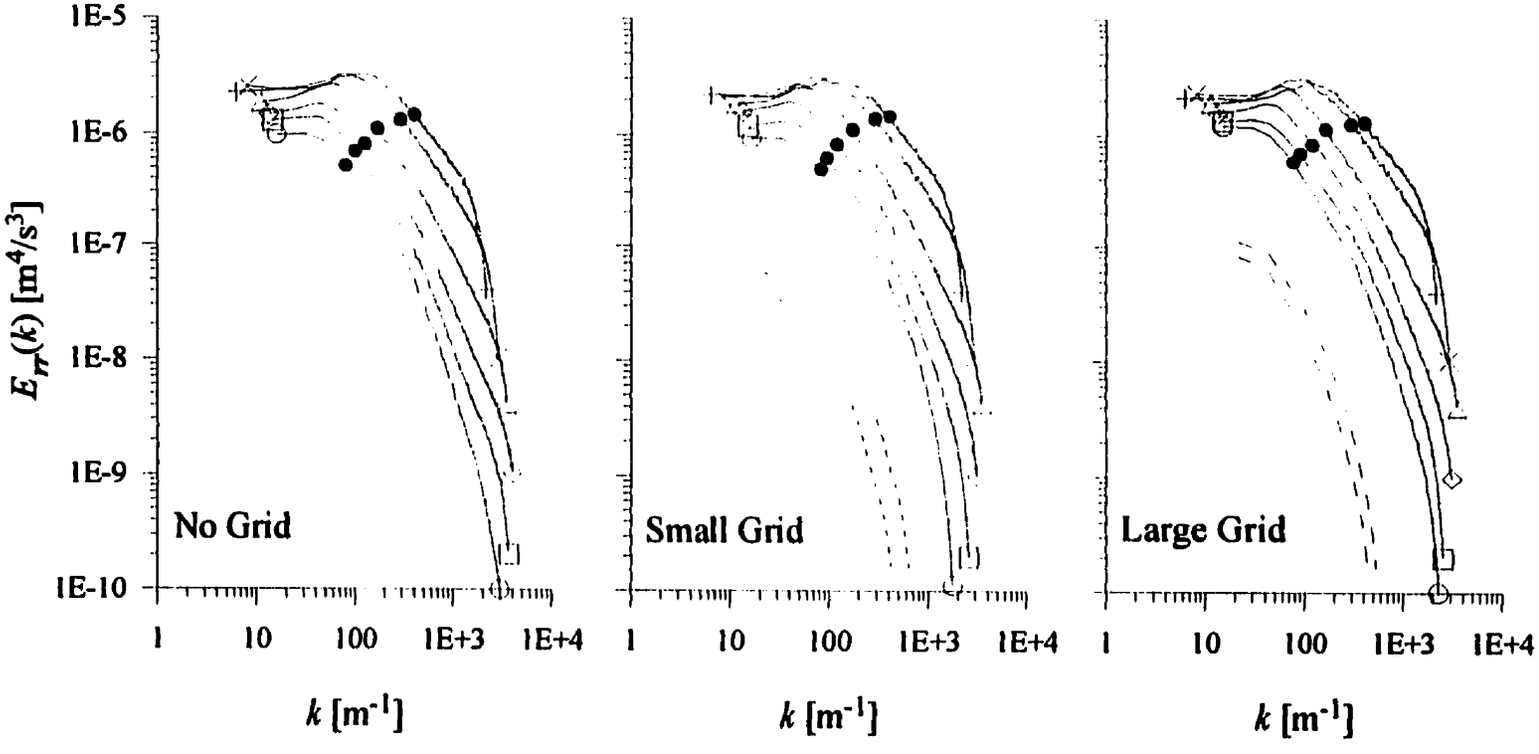

Figure 5.45: Average radial turbulent energy spectra for the large jet at $VR \approx 6$. x (cm): +, 10; ×, 20; △, 40; ◇, 60; □, 80; ○, 100. $(x-x_o)/\theta$: +, 0.8; ×, 2.3; △, 5.2; ◇, 8.6; □, 11.8; ○, 14.8. External spectra range: - - - -, small grid; – – –, large gird. Solid bullets, ●, give approximate locations of L_{rr} on spectra.

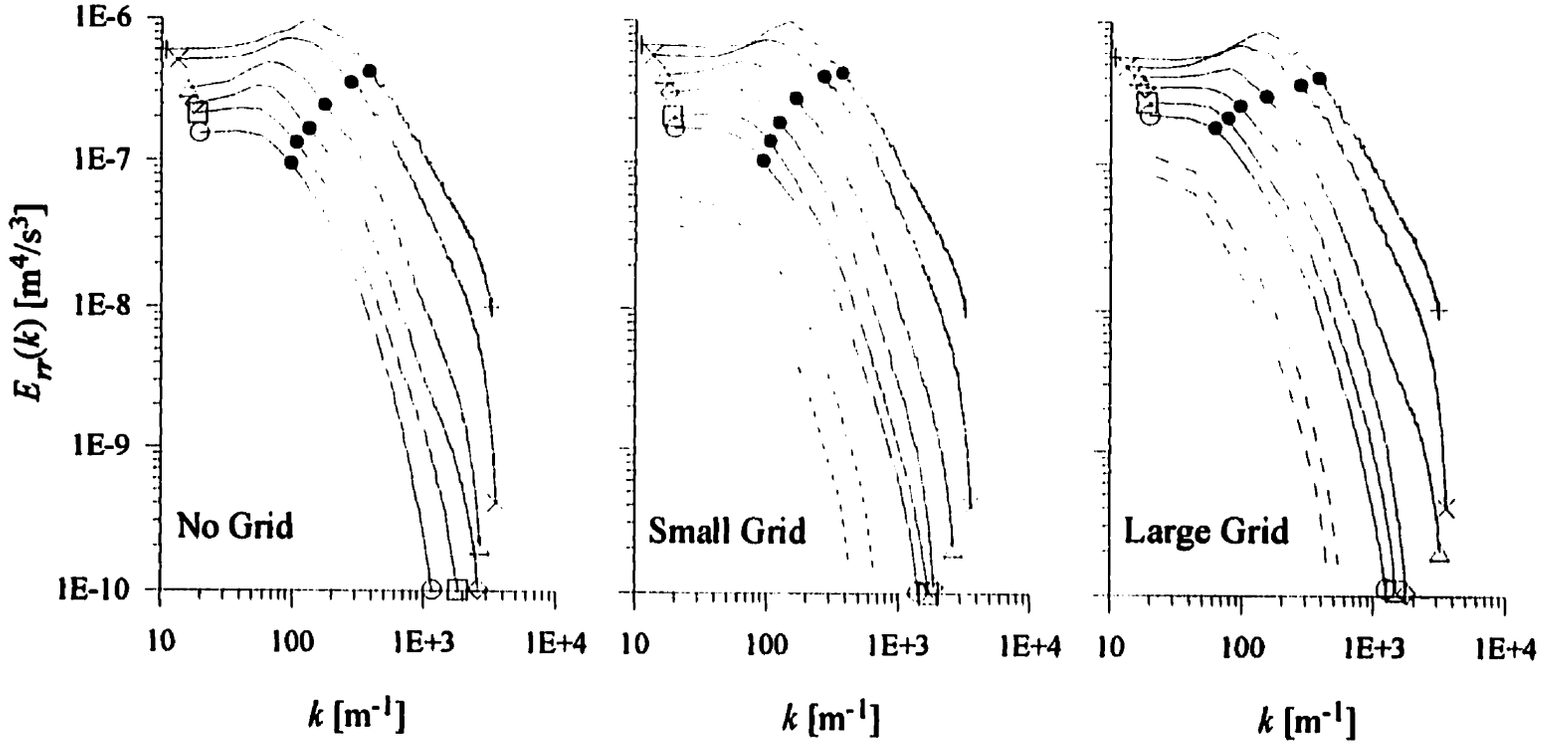

Figure 5.46: Average radial turbulent energy spectra for the large jet at $VR \approx 3$. x (cm): +, 10; ×, 20; △, 40; ◇, 60; □, 80; ○, 100. $(x-x_o)/\theta$: +, 4.6; ×, 8.1; △, 15.2; ◇, 22.2; □, 29.2; ○, 36.2. External spectra range: - - - -, small grid; - - -, large gird. Solid bullets, ●, give approximate locations of L_{rr} on spectra.

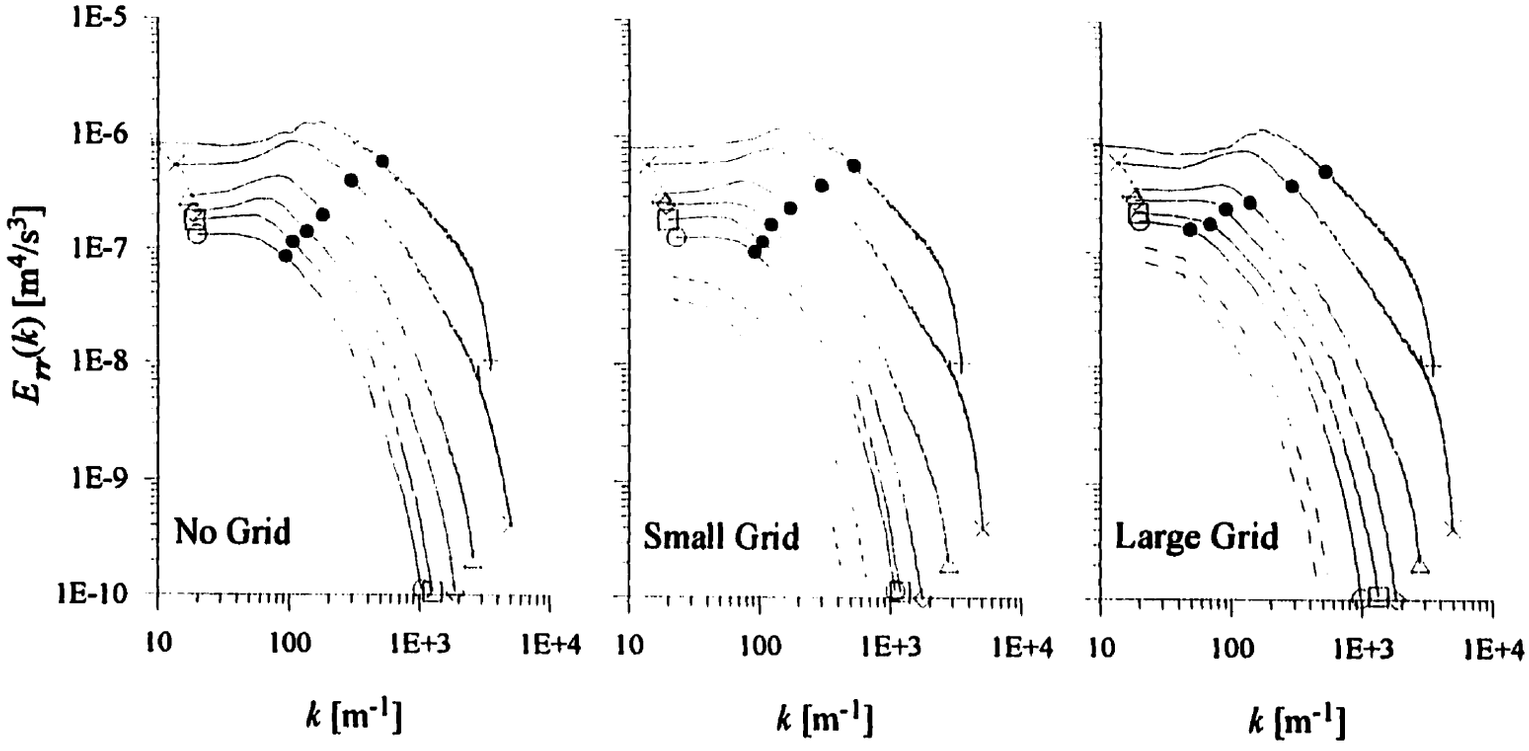

Figure 5.47: Average radial turbulent energy spectra for the small jet at $VR \approx 6$. x (cm): +, 10; ×, 20; △, 40; ◇, 60; □, 80; ○, 100. $(x-x_o)/\theta$: +, 3.3; ×, 7.3; △, 15.2; ◇, 23.4; □, 32.4; ○, 40.7. External spectra range: - - - -, small grid; – – –, large gird. Solid bullets, ●, give approximate locations of L_{rr} on spectra.

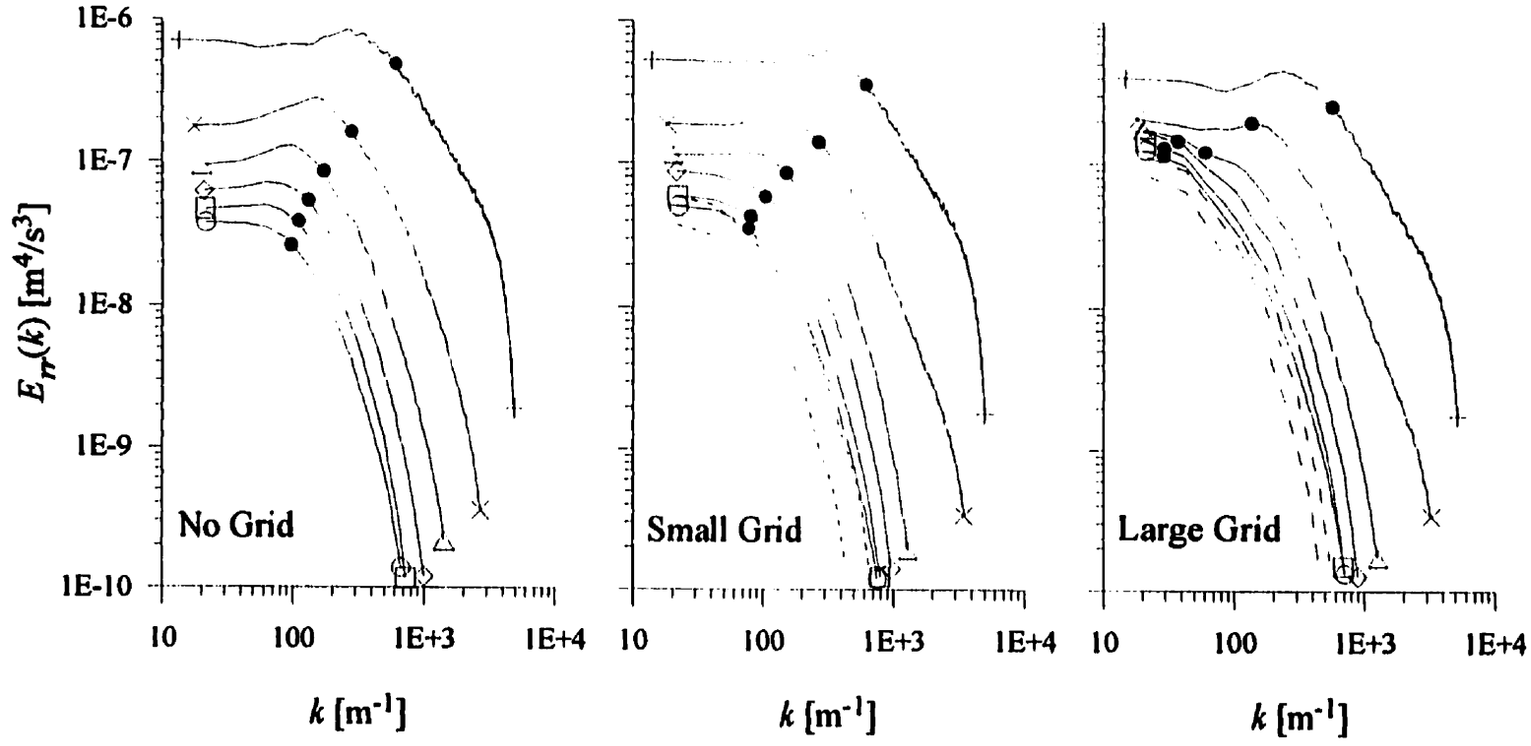

Figure 5.48: Average radial turbulent energy spectra for the small jet at $VR \approx 3$. x (cm): +, 10; ×, 20; △, 40; ◇, 60; □, 80; ○, 100. $(x-x_o)/\theta$: +, 9.9; ×, 19.6; △, 39.5; ◇, 60.3; □, 81.8; ○, 105.7. External spectra range: - - - -, small grid; – – –, large gird. Solid bullets, ●, give approximate locations of L_{rr} on spectra.

5.7 Normalizing Variables and Mathematical Similarity

The experimental results indicate that a form of similarity in the various profiles is obtained when the mean velocities are normalized by U_o and the turbulent velocities by $(U_o(U_o+U_e))^{1/2}$ with the radial position normalized by L_o. In addition, a common behaviour for U_e/U_o for jets in nearly laminar coflows is obtained when the downstream distance is normalized by the momentum radius, θ. Similarly, a common radial behaviour is obtained when the radius and downstream distance are both normalized by θ.

In Chapter 2, complete mathematical similarity of a jet in a coflow was considered with the end result being the derivation of equation (2.23) which gives the conditions under which complete similarity can be achieved. Substituting the above scales into the equation, however, does not satisfy the equation mathematically. Thus it must be concluded that the similarity indicated by the normalized experimental results is only partial similarity which may or may not apply outside the current experimental regime.

5.8 Summary of Experimental Results

Similarity of the excess mean velocity profiles are obtained when they are normalized by the centerline excess mean velocity, U_o, while similarity of the turbulent velocity profiles are obtained when they are normalized by a new scaling factor, $(U_o(U_o+U_e))^{1/2}$. Normalizing the turbulent velocity profiles by the conventional scale factor, U_o, failed to produce similar profiles by the end of the experimental regime. It is thus concluded that a jet in an external coflow has two velocity scales; one for mean velocities and one for the turbulent velocities. In addition, both the streamwise and radial integral length scales are found to be proportional to the jet radius.

For the jet in the absence of any grid-generated turbulence, the centerline excess mean velocity

follows $U_o \propto x^{-1}$ up to $(x-x_o)/\theta \approx 300$ with the radius following $R \propto x^{2/3}$ until $(x-x_o)/\theta \approx 100$ after which there is some indication that $R \propto x^{1/3}$. When a jet issues into a turbulent external coflow, one can expect, based on the present results, that:

a) the centerline excess mean velocity, U_o, will decay faster beyond $(x-x_o)/\theta \sim 20$ to 25.

b) the jet radius, R, will increase faster beyond $(x-x_o)/\theta \sim 20$ to 25.

c) the centerline turbulent velocities and Reynolds shear stresses, normalized by U_o, will increase faster beyond $(x-x_o)/\theta \sim 15$ to 20.

d) the average streamwise integral length scales, normalized by the jet radius, will increase faster after $(x-x_o)/\theta \sim 5$ to 10 while the average radial integral length scales will increase faster after $(x-x_o)/\theta \sim 15$ to 20.

in comparison to the same jet in a nearly laminar external coflow.

The present results clearly show that the effects of grid-generated turbulence on the development of a coflowing jet are not negligible and are dependent on the scales of turbulence in the two flow fields. The external turbulence that has the largest impact on the evolution of the jet occurs when the large grid is installed in the external coflow. For this case, the external coflow contains more turbulent energy located at larger length scales than for the case with the small grid installed, which in turn, contains more turbulent energy at larger length scales than for the case with no grid installed in the external. In fact, by the final traversing locations for the small jet at $VR \approx 3$, the average turbulent energy spectrum within in the jet has acquired the same shape and almost the same turbulent energy level as that found in the external coflow with the large grid installed thus indicating that the jet fluid is becoming indistinguishable from the external fluid.

Chapter 6: Integral Model Development

6.1 Introduction

Integral models, in combination with an entrainment velocity function, have been used extensively in the field of air pollution diffusion modelling to predict the trajectory and radial spread of jets and plumes in the natural environment. Their success can be attributed to their relatively simplistic formulation which is based on the Navier-Stokes equations and realistic simplifying assumptions. This produces a set of coupled ordinary differential equations that can be solved numerically using a Runge-Kutta solution algorithm. These equations are typically first order approximations to the fully turbulent equations of motion since it is assumed that all the effects of turbulence can be incorporated into the entrainment velocity function.

This chapter begins with a discussion of the phenomenological considerations inherent in the physics of two interacting turbulent fields. This will be followed by a brief review of the governing equations of motion and the simplifying assumptions appropriate for an isothermal, axisymmetrical jet in a coflowing external stream. Next, the postulation of the various entrainment velocity functions that are appropriate to the initial, intermediate and final phases of the jet behaviour will

be presented. This will be followed by the combination of the entrainment velocities for the three phases into a single continuous entrainment velocity function. Lastly, the predicted results will be compared to experimental data.

6.2 Phenomenological Considerations

Before an attempt is made at mathematically modelling a coflowing jet in a turbulent external flow, the phenomenological considerations inherent to diffusion, mixing, or entrainment of interacting turbulent flow fields will first be examined in order to elucidate the physics of the problem.

In general, the character of turbulence in any flow can be uniquely described by its turbulent energy spectrum which represents the distribution of turbulent energy over the range of frequencies or length scales that comprise the turbulent flow field. Diffusion or entrainment processes do not, however, occur over the entire spectrum range but tend to occur at scales comparable to the larger integral scales of the flow (Tennekes and Lumley, 1972, and Townsend, 1976). In addition, the turbulent energy spectrum, when integrated over the entire frequency or wavenumber range that comprises the spectrum, yields a value equal to the square of the turbulent velocity. Thus, for flows where diffusion and entrainment are the dominant concern, the character of the turbulence can be adequately described by a characteristic turbulent integral length scale and a characteristic turbulent velocity scale.

When two turbulent flow fields are interacting, such as a turbulent jet and a turbulent external coflow, the degree of interaction will be dictated by the relative magnitudes of the characteristic scales of turbulence in both flows. For the jet to be dynamically influenced by the external coflow, without resulting in the jet meandering, the external coflow must have eddies which correspond to or are on the same order of magnitude as those within the jet. Near the exit of the jet, the turbulent energy within the jet, generated primarily by the shear between the jet and external fluid, is much greater than that in the external coflow and centred about length scales that are much smaller than

those in the external coflow. Since the scales of turbulence in the two flow fields are so different, their interaction will be minimized. Thus the diffusion of the jet near the jet exit will be primarily determined by the self-generated turbulence of the jet. This defines the initial phase of jet diffusion (Slawson and Csanady, 1967 and 1971).

As the jet evolves downstream, the turbulent energy content of the jet fluid diminishes due to the decrease in shear between the jet fluid and the external fluid. In addition, the integral length scales within the jet, which scale with the radius of the jet, increase with distance downstream. Thus the turbulent energy content within the jet decreases and shifts to larger length scales with distance from the jet exit. At some downstream location, or downstream range, the turbulent energy within the jet will have decreased sufficiently and shifted to large enough length scales that they will correspond to those within the external coflow. At this point, the turbulence in the external coflow will begin to dynamically influence the jet behaviour. This is the start of the second stage of jet growth where the external turbulence eventually controls the diffusion and entrainment within the jet. Slawson and Csanady (1967 and 1971) subdivide this second stage into an intermediate phase, where the external turbulence with eddies in the inertial subrange of the turbulent energy spectrum dominates the jet mixing, and a final phase, where the energy containing eddies of the external turbulence dominate the mixing.

Realistically, however, the evolution of a jet in a turbulent external coflow is likely to contain considerable overlap between the various phases as one phase merges with another to dominate the diffusion of the jet fluid.

6.3 Governing Equations

To simplify the fully turbulent three-dimensional Navier Stokes equations into a form that is tractable, some simplifying yet realistic assumptions regarding the flow fields are required. For the coflowing jet, it is assumed that the flow is steady, incompressible, and fully turbulent shortly after

the jet exit with a Reynolds number sufficiently large that viscous effects can be neglected. It is also assumed that the jet is not subject to any mean flow in the azimuthal direction. The external mean flow is assumed to be uniform both in magnitude and direction. The first order equations representing the conservation of mass and the conservation of streamwise momentum can then be reduced to (see Appendix A):

$$\frac{d}{dx}\int_0^{R(x)} U(x,r)\,r\,dr = R\,v_e \tag{6.1}$$

and,

$$\frac{d}{dx}\int_0^{R(x)} U(x,r)\big(U(x,r)-U_e\big)\,r\,dr = 0 \tag{6.2}$$

respectively where $U(x,r)$ is the mean velocity, $R(x)$ is the radius of the jet, and v_e is an entrainment velocity function that needs to be specified. These two equations represent a first order approximation to the full governing equations and thus do not directly account for the effects of turbulence, either within the jet or in the external flow. The effects of turbulence can, however, be accounted for indirectly through the specification of an appropriate entrainment velocity function.

In order to evaluate the integrals in equations (6.1) and (6.2), an assumption about the mean velocity profiles is required. In Chapter 5 it was shown that the excess mean velocity profiles within the jet, for all experimental sets, are approximately similar after a short distance from the jet exit with a profile shape that is closely approximated by a Gaussian function. By assuming similarity of the mean velocity profiles, however, the detailed radial structure of the jet is suppressed since the profile becomes characterized by a single length scale and a single mean velocity scale. Thus any mean velocity profile shape can be used without loss of any additional physical information (Morton, 1961). In addition, a Gaussian profile can be represented by its mean and standard deviation or width which are essentially the parameters used to define a top-hat or

average profile. Thus a simple top-hat velocity profile will be assumed as is common for atmospheric releases. This greatly reduces the complexity of the integrations since all variables in a top-hat profile are assumed constant across the radius of the jet. It should also be noted that the assumption of similarity of the mean velocity profiles restricts the application of the integral model to downstream locations after which the experimental profiles exhibit similarity.

The conservation of mass equation, assuming a top-hat mean velocity profile, becomes:

$$\frac{d}{dx}\left(\overline{U}R^2\right) = 2Rv_e \tag{6.3}$$

where $\overline{U}$ is the top-hat or average mean velocity within the jet over $0 \le r \le R$. Similarly, the conservation of x-momentum becomes:

$$\frac{d}{dx}\left(\overline{U}\left(\overline{U} - U_e\right)R^2\right) = 0 \tag{6.4}$$

Equations (6.3) and (6.4) represent a pair of coupled ordinary differential equations that can be solved for $\overline{U}(x)$ and $R(x)$ once an entrainment velocity function has been specified.

6.4 The Entrainment Velocity Function

The right hand side of the conservation of mass equation (equation (6.3)) can be interpreted as an effective eddy diffusivity, K, (Slawson and Csanady, 1967) which is proportional to the product of a characteristic diffusion length scale and a characteristic turbulent velocity scale. This interpretation of equation (6.3) assumes that the jet radius is proportional to the characteristic diffusion length scale and that the entrainment velocity is proportional to the characteristic turbulent velocity scale responsible for the mixing in the jet. From the experimental data presented in Chapter 5, the ratio of the jet radial integral length scale (*i.e.* a diffusion length scale) to the jet radius, L_r/R, is nearly constant after an initial development region for the jets with no grid and the

small grid installed while for the jets with the large grid installed, the behaviour of L_{11}/R, while not strictly constant, can be approximated as such. Thus the first part of our interpretation on the continuity equation is reasonably satisfied. What remains to be determined is the functional form of the entrainment velocity such that it is proportional to the characteristic turbulent velocity dominating the mixing of the flow.

If the downstream evolution of the jet is divided into three phases such that the diffusion and entrainment in each phase is controlled by a unique characteristic velocity scale of turbulence, then a unique entrainment velocity function will be required for the initial, intermediate and final phases to fully predict the behaviour of a jet in a turbulent external coflow. The following sub-sections detail the development of v_e for each phase. For the initial phase, the predicted jet behaviour will be immediately compared to experimental data for jets in laminar coflows. For the intermediate and final phases, however, comparison with experimental data will wait until a complete entrainment velocity function is defined.

6.4.1 The Initial Phase

When the jet's self-generated turbulence dominates the mixing process, whether it be for a jet in laminar external coflow or for a jet in the initial phase in a turbulent external coflow, the entrainment velocity should ideally be proportional to a mean velocity or a mean velocity combination within the jet which, in turn, should be proportional to the turbulent velocity responsible for entraining external fluid. Setting the entrainment velocity proportional to a mean velocity combination greatly simplifies the problem since the solution neither requires the specification nor the prediction of any turbulent velocities within the jet.

A jet in a coflow has two characteristic mean velocities: that of the jet, $\overline{U}$, and that of the external coflow, U_e. The simplest technique to combine these two velocities is as a mean velocity difference or as the excess top-hat mean velocity given by $\overline{U}_o=\overline{U}-U_e$. Using this method, Morton (1961)

proposes an entrainment velocity of the form:

$$v_{e\_lam} = \alpha \overline{U}_o = \alpha\left(\overline{U} - U_e\right) \tag{6.5}$$

and suggests that the entrainment constant, α, is 0.116. Physically, Morton (1961) argues that the entrainment of external fluid arises from the turbulence that is produced by the shear generated by the difference in the characteristic mean velocities thus suggesting that the turbulent velocities need to scale with the mean velocity difference. This speculation, however, is not supported by the experimental data in Chapter 5 which clearly shows that the turbulent velocities do not scale with U_o.

The experimental results, however, do show that the turbulent velocities scale with $(U_o(U_o+U_e))^{1/2}$, the new turbulent velocity scale factor. If this scale factor is rewritten in terms of the average excess mean velocity, a new entrainment velocity function can be proposed as:

$$v_{e\_lam} = \alpha\left(\overline{U}_o\left(\overline{U}_o + U_e\right)\right)^{1/2} = \alpha\left(\overline{U}\left(\overline{U} - U_e\right)\right)^{1/2} \tag{6.6}$$

where the value of the entrainment constant, α, must be determined from the available data. This new entrainment velocity is now proportional to a mean velocity scale which has been experimentally shown to be proportional to the turbulent velocities within the jet which, in turn, are responsible for entraining external fluid into the jet.

The above two entrainment functions have been used in conjunction with equations (6.3) and (6.4) to predict the behaviour of $U_c/\overline{U}_o$ and R/θ for jets in a laminar external coflow. The data for the small jet at $VR\approx6$ at a downstream location of $(x-x_o)/\theta\approx3.5$ (roughly corresponding to the location where both the excess mean velocity and turbulent velocity profiles become similar) is used to initiate the solution algorithm for both entrainment functions. The results are given in Figures 6.1 and 6.2 for $U_c/\overline{U}_o$ and R/θ respectively along with the current experimental data with no grid installed and the experimental data of six other studies on jets in laminar external coflows.

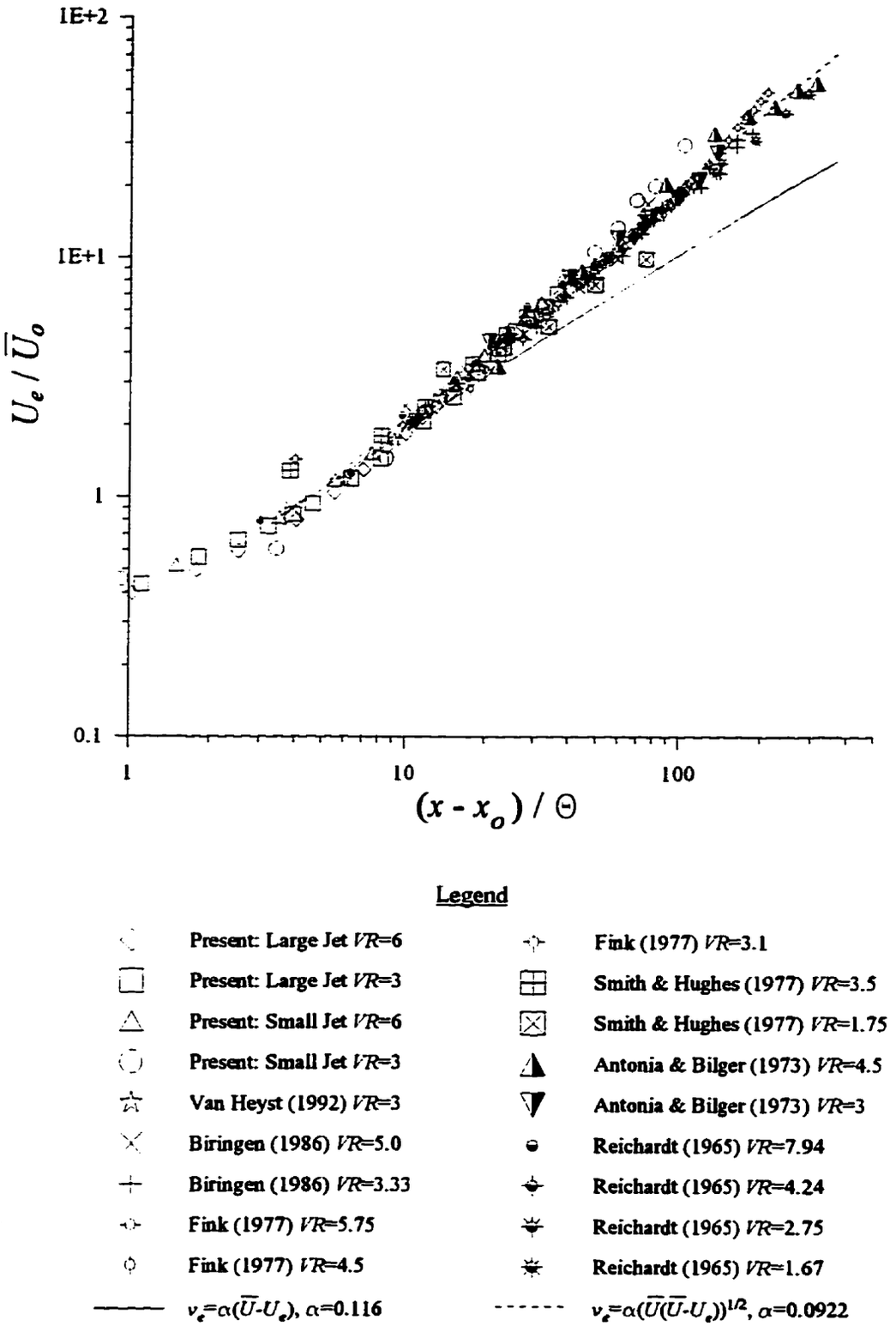

Figure 6.1: Comparison of predicted behaviour for $U_e/\overline{U}_o$ with experimental data for jets in laminar coflows.

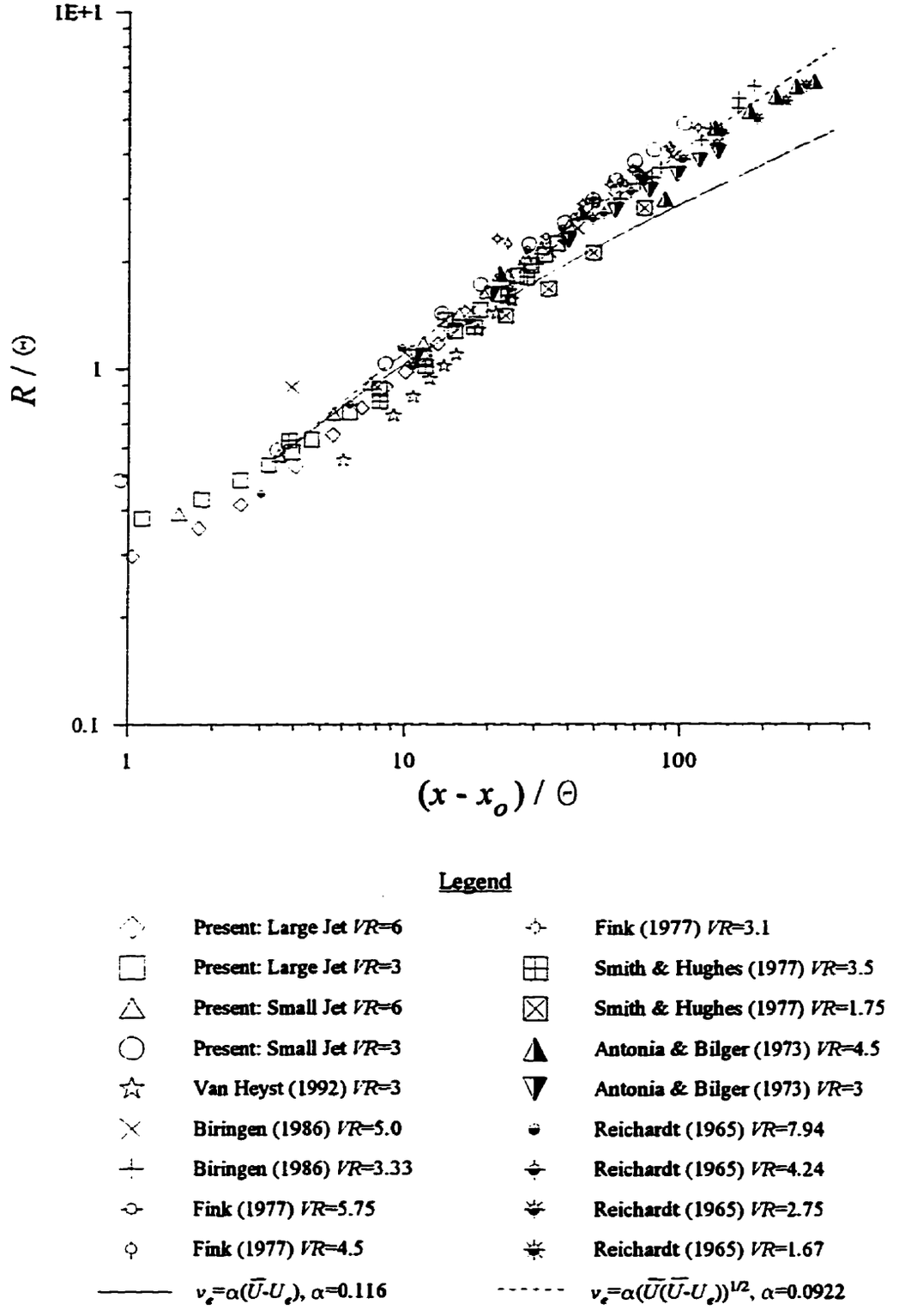

Figure 6.2: Comparison of predicted behaviour for R/θ with experimental data for jets in laminar coflows.

The predictions using the entrainment velocity function of Morton (1961) (equation (6.5)), given as the solid line in both figures, follows the data reasonably well up until $(x-x_o)/\theta \approx 20$ after which they start to increasingly under predict the behaviour of both $U_c/\overline{U}_o$ and R/θ as the distance downstream is increased. Increasing α to values greater than 0.116 in order to match the far downstream data results in an over prediction of $U_c/\overline{U}_o$ and R/θ closer to the source. Thus, over the given solution regime, the entrainment velocity function of Morton (1961) cannot correctly predict the behaviour of $U_c/\overline{U}_o$ and R/θ. Maczynski (1962) reached essentially the same conclusion by stating that α could not remain a constant but had to depend weakly on x.

As expected based on the discussion above, the predictions using equation (6.6), given as the dashed line in the two figures, better predicts the behaviour of $U_c/\overline{U}_o$ and R/θ over the entire solution regime than that based on Morton's entrainment velocity. The value of the entrainment constant, α=0.0922, is an average value from the studies given in the two figures. The range of values for the entrainment constant in all the studies is $0.08 \leq \alpha \leq 0.105$ where there appears to be some dependency on the jet model diameter and, to a lesser extent, the initial jet velocity ratio. As the jet diameter is increased or the initial velocity is increased, the magnitude of the entrainment constant decreases thus making α inversely dependent on the initial momentum. Presumably, if $(\overline{U}(\overline{U}-U_c))^{1/2}$ was a scale factor that resulted in true mathematical similarity, than the value of α would be constant.

6.4.2 The Intermediate Phase

In the intermediate phase, it is assumed that the external turbulence in the inertial subrange of the turbulent energy spectrum will dominate the diffusion and entrainment within the jet. The location of the inertial subrange within a spectrum is given by the wavenumber range $k_l \ll k \ll k_d$ where k_l is a typical wavenumber marking the range of the large energy containing eddies and k_d is a typical wavenumber marking the range of the small dissipative eddies. The concept behind the inertial

subrange as put forth by Kolmogoroff is that, at sufficiently high turbulent Reynolds number, the energy spectrum in the range of $k_l \ll k \ll k_d$ is independent of the fluid viscosity and is solely determined by the energy dissipation rate per unit mass, ϵ, which has the units of m^2/s^3 (Hinze, 1975).

Based solely on dimensional reasoning, a characteristic turbulent velocity or entrainment velocity can be defined for the intermediate phase of jet growth using the external energy dissipation rate, ϵ_e, and an external turbulent length scale, l_e, typical of the inertial subrange. This yields:

$$v_{e,int} \propto \left(\epsilon_e l_e\right)^{1/3} \tag{6.7}$$

Equation (6.7) can also be obtained by assuming that the effective turbulent diffusivity due to the external turbulence can be evaluated by supposing that the turbulent energy of the external eddies is "smeared" over a wavenumber range of width k (Fink, 1977). The turbulent energy content should therefore be proportional to both the maximum value of the power spectral density function, $E(k)$, in the interval as well as the wavenumber band width. Since the PSD function in the inertial subrange is a function of the dissipation rate only at a given wavenumber, *ie*:

$$E(k) \propto \epsilon^{2/3} k^{-5/3} \tag{6.8}$$

the effective eddy diffusivity can be evaluated from:

$$K \propto R\sqrt{E(k)k} \tag{6.9}$$

This gives a value of:

$$K \propto R\sqrt{\epsilon^{2/3} k^{-2/3}} = R\epsilon^{1/3} k^{-1/3} \tag{6.10}$$

Since k is a typical value in the wavenumber band width of the inertial subrange, its inverse will yield a typical turbulent length scale, l_e, of the inertial subrange. Also since $K \propto Rv_e$, the entrainment

velocity for the intermediate phase again becomes proportional to $(\epsilon_e l_e)^{1/3}$.

The selection of a length scale characteristic of the external turbulence in the inertial subrange, however, must still be made. Tennekes and Lumley (1972) state that the energy exchange between the mean flow and the turbulence is governed by the dynamics of the large eddies with scales comparable to the integral length scales. Furthermore, the authors go on to state that all experimental evidence suggests that the spectral energy transfer from the large scales down to the small dissipative scales, proceeds at a rate dictated by the energy of the large eddies and their time or length scale. Thus in the inertial subrange, where there is an equilibrium between the production and dissipation of turbulent energy, the characteristic length scale of the energy transfer is the integral length scale. The entrainment function for the intermediate phase of jet growth thus has the form:

$$v_{e.int} \propto \left(\epsilon_e L_e\right)^{1/3} \tag{6.11}$$

where L_e is an integral length scale in the external flow.

Based on similarity theory of turbulence and the theory of relative diffusion through the use of the Richardson-Batchelor relationship, Slawson and Csanady (1967 and 1971) suggest that, for an atmospheric release, the integral length scale in the atmosphere is proportional to the radius of the jet, R, in the intermediate phase of jet growth. This results in an entrainment velocity of the form:

$$v_{e.int} = \beta\, \epsilon_e^{1/3} R^{1/3} \tag{6.12}$$

where β is an entrainment constant for the intermediate phase. Note, however, that in the atmosphere there can be a substantial inertial subrange that spans several decades of wavenumbers (Batchelor, 1950).

For a laboratory situation, Fink (1977) suggests an entrainment function that essentially matches

the entrainment velocity of Slawson and Csanady (1967 and 1971). However, in a laboratory flow where the external turbulence is generated by a grid, a substantial inertial subrange does not exist which makes the assumption of proportionality between the external integral length scale and the radius of the jet questionable. The reason for this is that the external turbulence in the inertial subrange does not span a sufficiently wide range of wavenumbers to completely dominate the diffusion of the jet as it would in the case of the atmosphere.

For the current study, the proposed entrainment velocity function for the intermediate phase will thus follow the more fundamental formulation given by equation (6.11) by having the form:

$$v_{e.int} = \beta \, \epsilon_e^{1/3} L_{rr.e}^{1/3} \tag{6.13}$$

where $L_{rr.e}$ is the radial integral length scale of the external coflow which can be evaluated from the relationships developed in Chapter 4 for grid-generated turbulence. Preliminary prediction runs support this formulation since the value of β, when the external integral length scale is used, is constant. If the jet radius is used in equation (6.13) in lieu of the external integral length scale, β is no longer a constant but is strongly dependent on the specific grid installed in the external flow. Bear in mind, however, that since there is not a substantial inertial subrange in grid-generated turbulence, the fluid viscosity, which has been assumed to be nonessential based on the concept of the inertial subrange, may be an important variable in the determining the transfer of turbulent energy in the spectrum and thus in determining the magnitude of β.

The external energy dissipation rate for grid-generated turbulence can be estimated based on the isotropic relation (Hinze, 1975):

$$\epsilon_e = -\frac{3}{2} U_e \frac{d\overline{u^2}}{dx} \approx U_e \frac{d}{dx}\left(\frac{1}{2}\overline{u^2} + \overline{v_r^2} \right) \tag{6.14}$$

where use has been made of Taylor's theory of frozen turbulence and where the approximation takes into account the anisotropy in grid-generated turbulence. As with the integral length scales,

the values of the external turbulent velocities can be determined from the relationships developed in Chapter 4 for grid-generated turbulence.

6.4.3 The Final Phase

In the final phase of the jet development, the energy containing eddies of the external turbulence dominate the mixing of the jet.

Slawson and Csanady (1967 and 1971) give a final phase entrainment velocity of the form:

$$v_{e.fin} = \gamma v \frac{L}{R} \tag{6.15}$$

where γ is the entrainment constant for the final phase, v is a turbulent velocity, L is a diffusion length scale, and R is the radius of the jet. This form of the entrainment velocity is again based on the theories of turbulence similarity and relative diffusion for atmospheric releases.

However, in the final phase, it is assumed that the energy containing eddies in the external turbulence control the diffusion and entrainment within the jet. If this is the case, then the geometric scale of the jet should be proportional to the integral length scale of the turbulence which is dominating the mixing process. In other words $R \propto L_{rr.e}$ in the final phase. The logical choice for v is the external radial turbulent velocity since it is the component that crosses the jet boundary. The final phase entrainment velocity function can thus be simplified to:

$$v_{e.fin} = \gamma \left(\overline{v_{r.e}^2} \right)^{1/2} \tag{6.16}$$

where the constant of proportionality between the jet radius and the external integral length scale is absorbed into γ. The value of the external radial turbulent velocity can be determined from the relationships derived in Chapter 4 for grid-generated turbulence.

6.4.4 Combining the Entrainment Velocities

As mentioned previously, the three phase regional model is simplistic since it allows for no gradual merging of one phase into another. Ideally one entrainment velocity function valid for the entire flow field is desirable since it eliminates the necessary division of the flow field into its various phases. The single entrainment velocity would necessarily have asymptotic limits of the initial phase near the jet source and of the final phase far downstream. In addition, it must give a smooth transition from one phase to another.

Since the mixing effects of the three asymptotic phases of jet growth should be cumulative, a well known smoothing technique (Churchill and Usagi, 1972) to join the asymptotes is used and is given by:

$$v_e = \left[\left(v_{e.lam} \right)^n + \left(v_{e.int} \right)^n + \left(v_{e.fin} \right)^n \right]^{1/n} \tag{6.17}$$

where n is optimized and found equal to 2 for the present data. This results in a root-sum-square (RSS) summation which emphasizes the dominant phase of jet growth in the total entrainment velocity. The RSS summation method, although not typically used in the summation of entrainment velocities, has obtained wide acceptance and has been used extensively in the summation of different experimental errors in uncertainty analyses (Coleman and Steele, 1989).

To satisfy the asymptotic limit near the jet exit, a weighting function on $v_{e.fin}$ will be required so that its contributions will be initially small near the jet exit but increasingly grows until it dominates the entrainment velocity far downstream. A weighting function, w, of the form:

$$w = \left(\frac{U_e}{U_e + \left(\overline{U} \left(\overline{U} - U_e \right) \right)^{1/2}} \right)^2 \tag{6.18}$$

gives the correct asymptotic limits such that near the jet exit when $\overline{U} \gg U_e$, $w \to 0$ and far downstream

when $\overline{U} \rightarrow U_e$, $w \rightarrow 1$. A weighting function is not required for the intermediate entrainment velocity function since its initial contributions will be small in comparison to the initial phase value.

To satisfy the asymptotic limit far downstream, no weighting functions are required since the entrainment velocity function for the initial phase approaches zero as $\overline{U} \rightarrow U_e$ and the contribution from the intermediate phase becomes negligible in comparison to that of the final phase far downstream.

The final form of the entrainment velocity to be used for the entire flow regime is thus given by:

$$v_e = \left(\left[\alpha \left(\overline{U} \left(\overline{U} - U_e \right) \right)^{1/2} \right]^2 + \left[\beta \left(\epsilon_e L_{rr.e} \right)^{1/3} \right]^2 + \left[\gamma w \left(\overline{v_{r.e}^2} \right)^{1/2} \right]^2 \right)^{1/2} \qquad (6.19)$$

6.4.5 Comparison with Experimental Data

Using the simplified conservation equations of mass and streamwise momentum and using equation (6.19) to specify the entrainment velocity function, predicted values for R/θ and $U_c/\overline{U}_o$ have been generated for the current set of jet experiments and the experiments of Fink (1977). Table 6.1 summarizes the values of the entrainment constants used in the entrainment velocity function. Note that α varies inversely with the diameter of the jet model and with the initial velocity ratio as noted earlier and is thus considered a quasi-constant which is dependent on the initial jet momentum. The value of β remains constant for the current set of jet experiments in water but is decreased for the experiments of Fink (1977) conducted in air. This is due to the fact that in grid-generated turbulence there is not an inertial subrange of any substantial bandwidth thus making the fluid viscosity an important parameter and, in all probability, making the value of β dependent on the fluid viscosity. The value of γ for the final phase remains constant for all experiments.

The coupled ordinary differential equations, given by equations (6.3) and (6.4), are solved numerically using a fourth order Runge-Kutta algorithm. In order to initiate the integration, the

Jet Case	d_j (mm)	α	β	γ
small jet, $VR \approx 6$	9.5	0.087	0.65	1.40
small jet, $VR \approx 3$	9.5	0.090	0.65	1.40
large jet, $VR \approx 6$	22.2	0.081	0.65	1.40
large jet, $VR \approx 3$	22.2	0.083	0.65	1.40
Fink (1977), $VR \approx 5.75$	6.0	0.092	0.26	1.40
Fink (1977), $VR \approx 4.5$	6.0	0.094	0.26	1.40
Fink (1977), $VR \approx 3.1$	6.0	0.097	0.26	1.40

Table 6.1: Entrainment constant values used in the prediction of the various jet experiments.

solution algorithm requires a velocity and radius for the first point in the solution domain. For each of the current experimental sets, the start of the integration roughly corresponds to the location where the mean and turbulent velocity profiles become similar. This typically occurs within the first ten momentum radii of the jet exit. In the experiments of Fink (1977), the mean velocity information is reported much more frequently than the corresponding radial scales. To begin the integration near the first velocity data point (between ten and twenty momentum radii downstream from the jet exit), the radius at this location is extrapolated from the downstream data by assuming that the momentum integral is a constant at all downstream locations.

The predicted results are given in Figures 6.3 through 6.9 where the experimental data is given by symbols and the predictions given by lines. In all cases, the top graph illustrates the behaviour of R/θ while the bottom graphs depicts that of $U_e/\overline{U}_o$.

For the current large jet at $VR \approx 6$, the predictions for R/θ, given in Figure 6.3a, agree well with the experimental data while the predictions for $U_e/\overline{U}_o$, given in Figure 6.3b, are somewhat high for the jets with the grids installed. Although the difference in predictions for the jet with and without a grid installed are relatively small in this case, the model does show that the effects of the external turbulence begin very soon after the initial integration point. For the large jet at $VR \approx 3$, given in

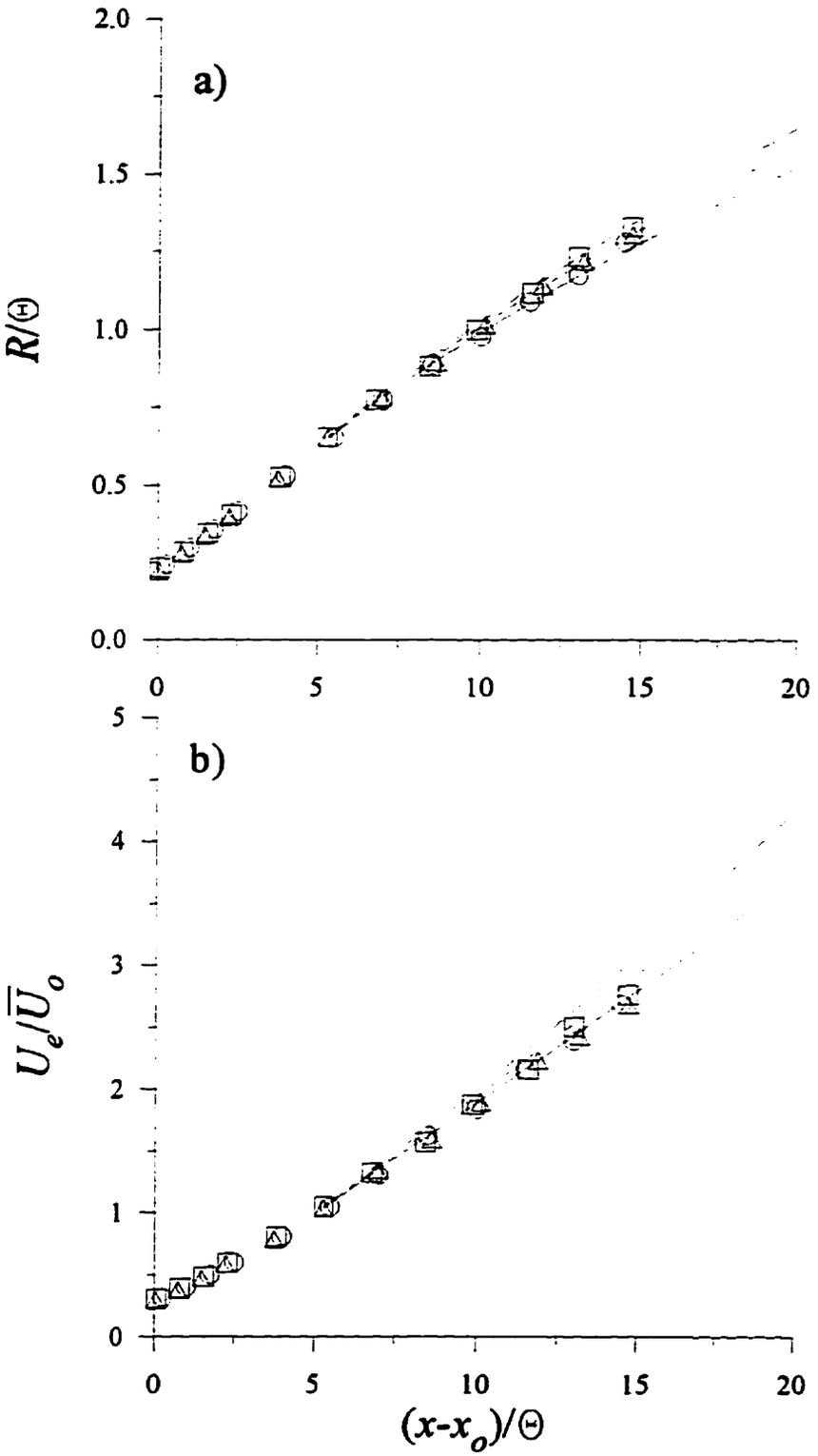

Figure 6.3: Comparison of predictions and experimental data for the large jet at $VR \approx 6$. Data: ○, no grid; △, small grid; □, large grid. Predictions: ——, no grid; - - - -, small grid; – – –, large grid.

Figure 6.4, the predictions of R/θ with the small and large grid installed are larger than the actual data while for the jet with no grid installed, the predictions closely matches the data. The predictions of $U_e/\overline{U}_o$, given in the lower figure, match well the experimental data for the jet with the small and large grid installed while the prediction for the jet with no grid installed is slightly low.

For the small jet at $VR \approx 6$, given in Figure 6.5, the predictions for R/θ match the data well in all cases of external turbulence. However, the predicted values of $U_e/\overline{U}_o$ are high for the jet with the small and large grids installed and somewhat low for the jet with no grid installed. The prediction for the jet with no grid installed, however, assumes that the external flow is perfectly laminar which is known to be not the case. For the small jet at $VR \approx 3$, given in Figure 6.6, we again see that the predictions of R/θ agree well with the data for the jet with the small and large grid installed while, for the jet with no grid installed, the prediction increasingly underestimates the data as downstream distance is increased. The predicted values for $U_e/\overline{U}_o$ also agree well with the data for the jet with the small and large grid installed. For the jet with no grid installed, we again see that the predicted value of $U_e/\overline{U}_o$ increasingly underestimate the data as downstream distance is increased. The experiments with the small jet at $VR \approx 3$ extend the farthest non-dimensional distance downstream from the jet exit. It is thus not surprising to see that the predictions based on a laminar external underestimate the data since the turbulence that is present in the external with no grid installed has a greater distance over which it can affect the jet.

Before examining the results based on the three jet runs of Fink (1977) who used one grid to generate external turbulence, it should be kept in mind that the data points have been taken from figures contained within a conference proceedings and thus not only contain experimental errors but errors associated with reading data points from the figures. In spite of this, the predicted results agree quite favourably with the experimental data of Fink (1977) with the exception of the radius prediction for the jet with the grid installed which is increasingly over predicted as distance downstream is increased. The reason for this is not entirely clear although the values of β and γ have been somewhat biased by the large quantity of mean velocity data in comparison to the small number of radius points. Figures 6.7, 6.8, and 6.9 give the comparisons of the predicted results to

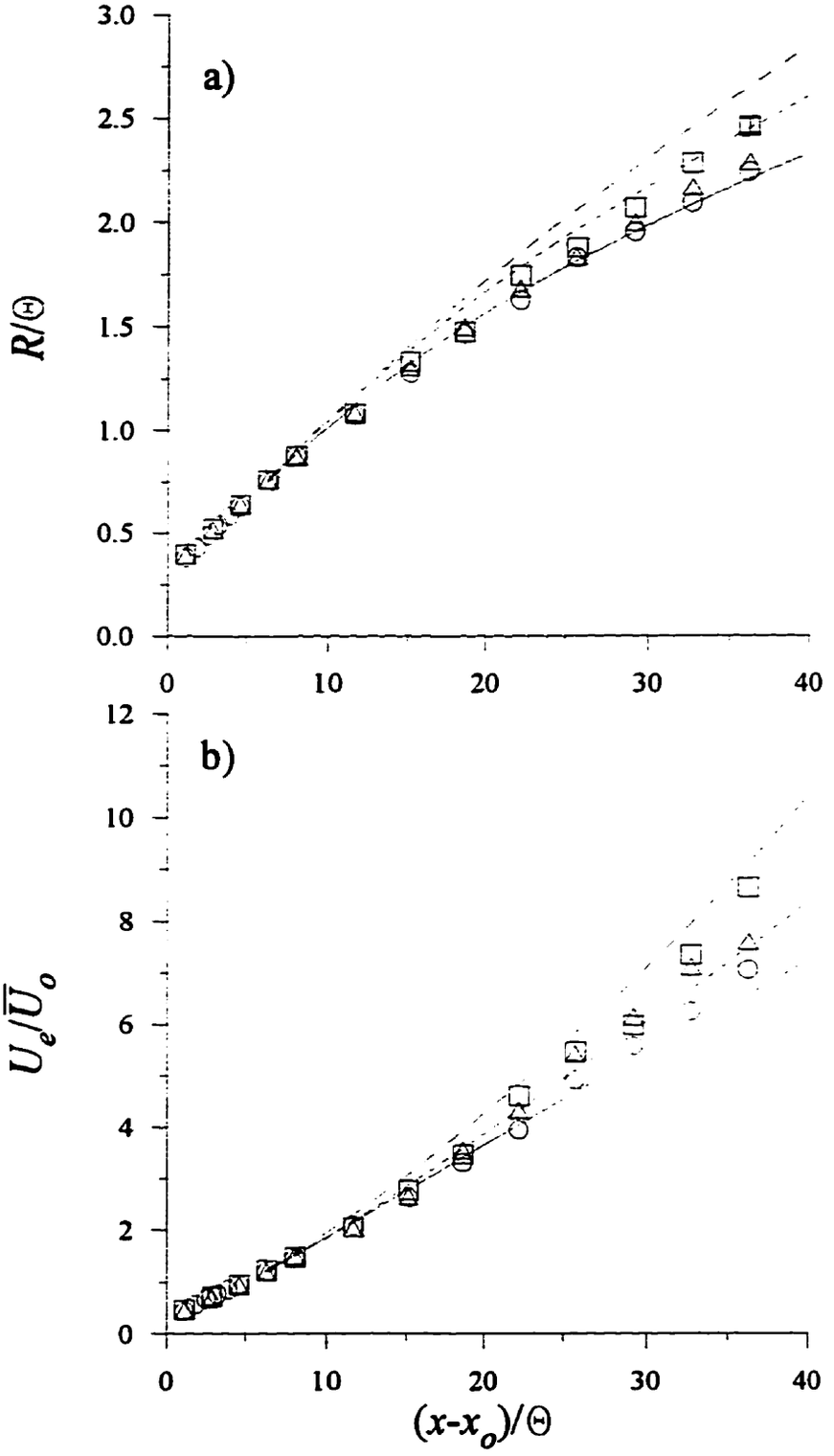

Figure 6.4: Comparison of predictions and experimental data for the large jet at $VR \approx 3$. Data: ○, no grid; △, small grid; □, large grid. Predictions: ——, no grid; - - - -, small grid; – – –, large grid.

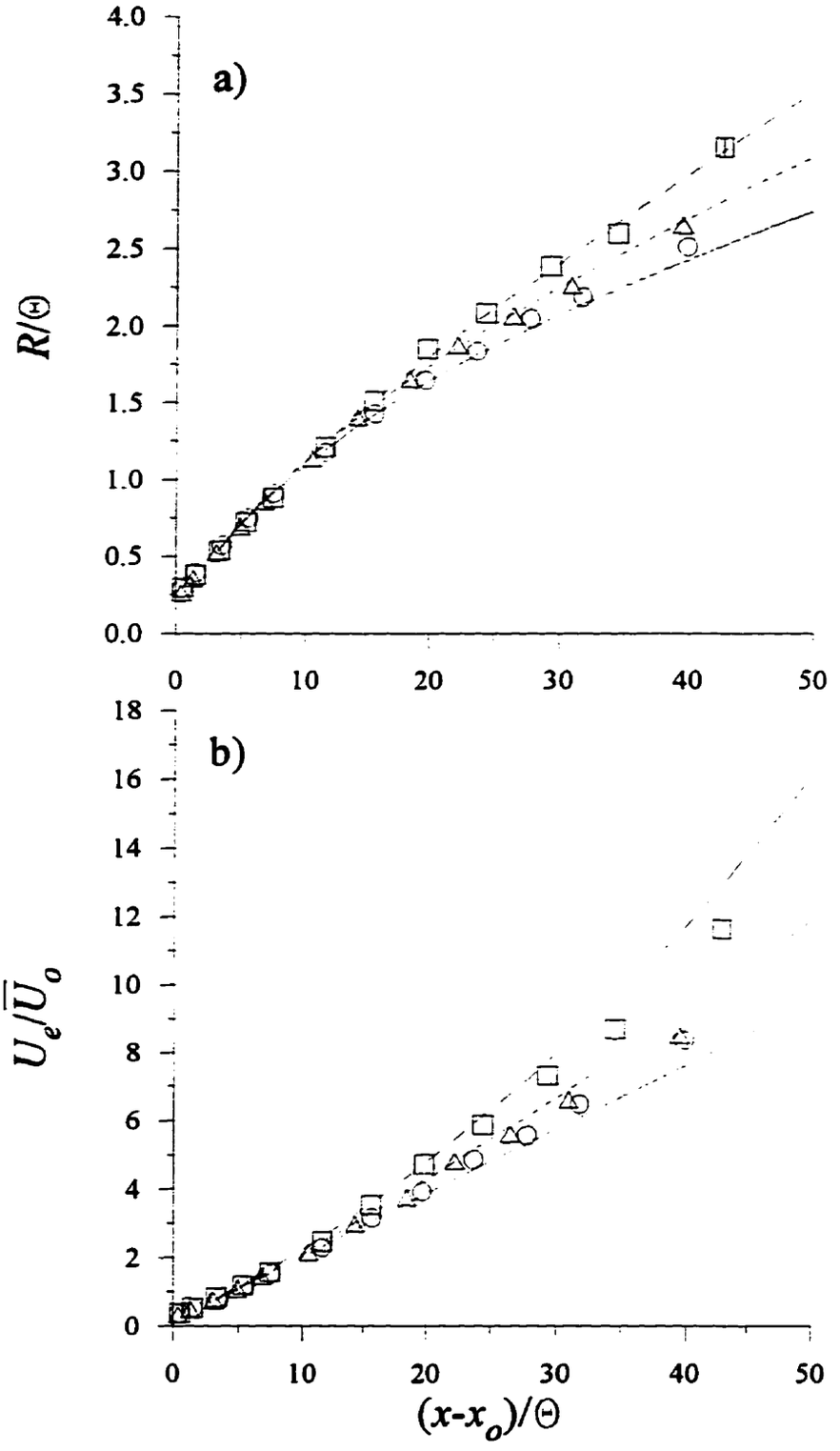

Figure 6.5: Comparison of predictions and experimental data for the small jet at $VR \approx 6$. Data: ○, no grid; △, small grid; □, large grid. Predictions: ——, no grid; - - - -, small grid; – – –, large grid.

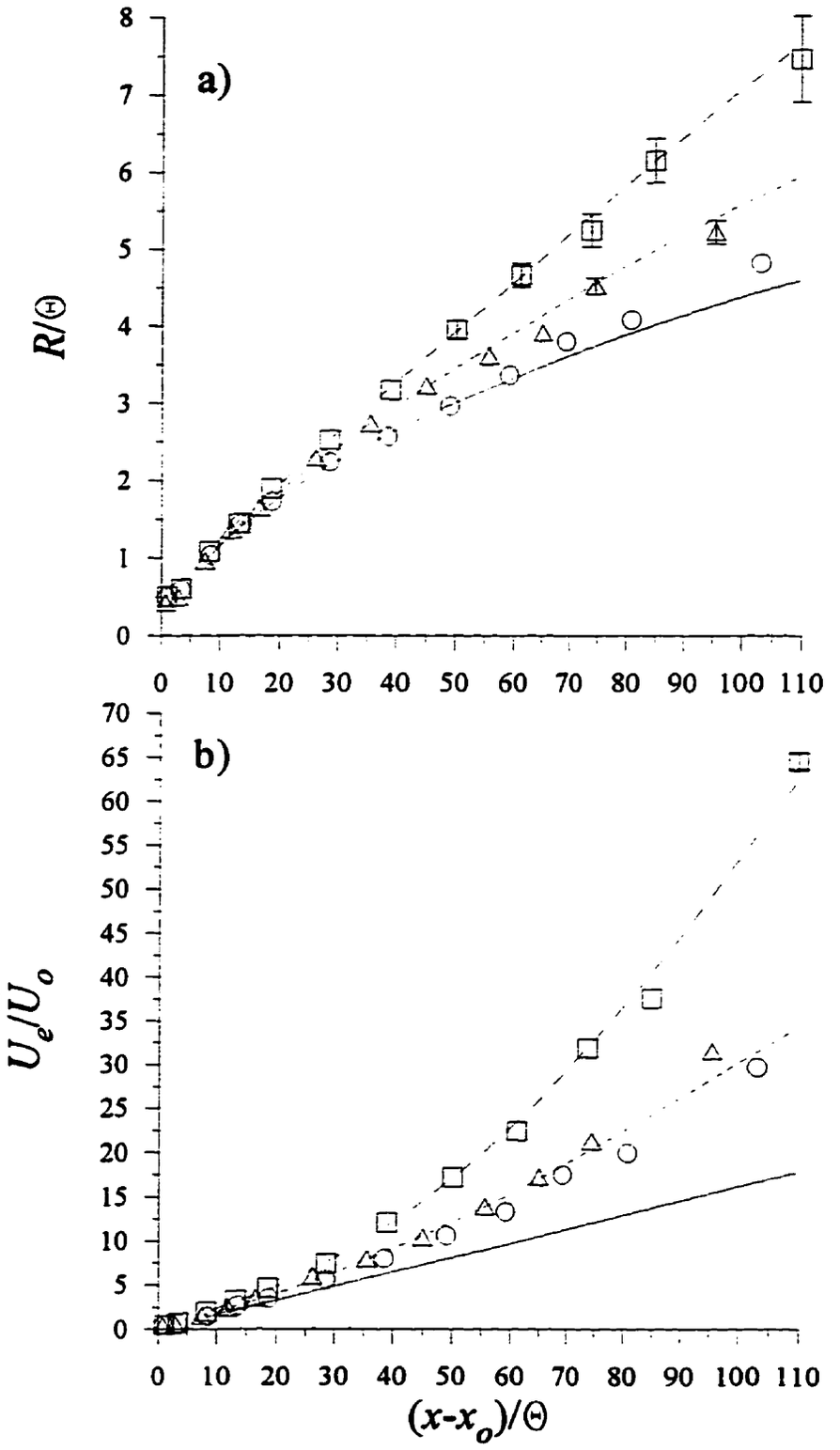

Figure 6.6: Comparison of predictions and experimental data for the small jet at $VR \approx 3$. Data: ○, no grid; △, small grid; □, large grid. Predictions: ——, no grid; - - - -, small grid; – – –, large grid.

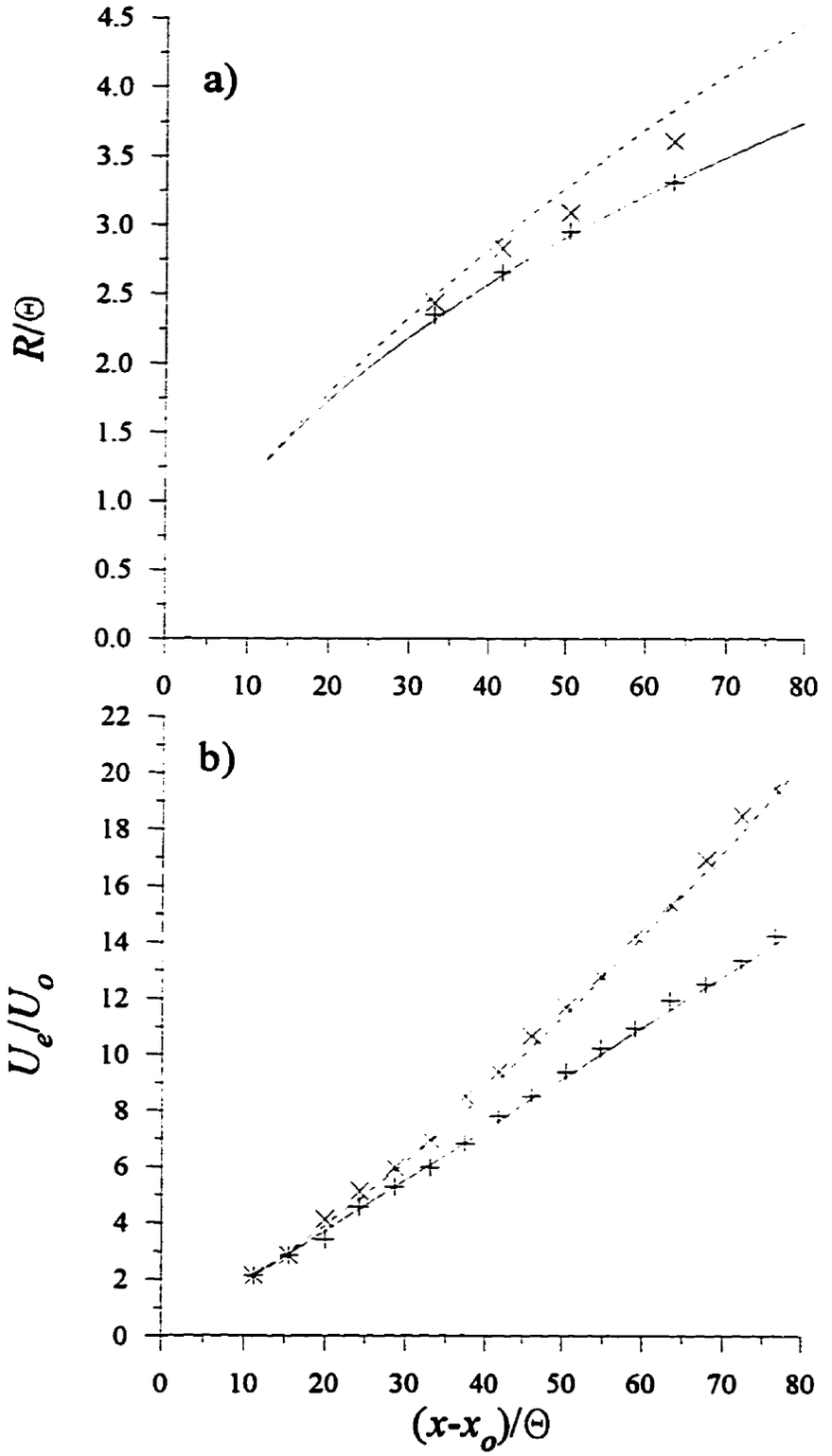

Figure 6.7: Comparison of predictions and experimental data for Fink's jet at $VR \approx 5.75$. Data: +, no grid; ×, grid. Predictions: ——, no grid; - - - -, grid.

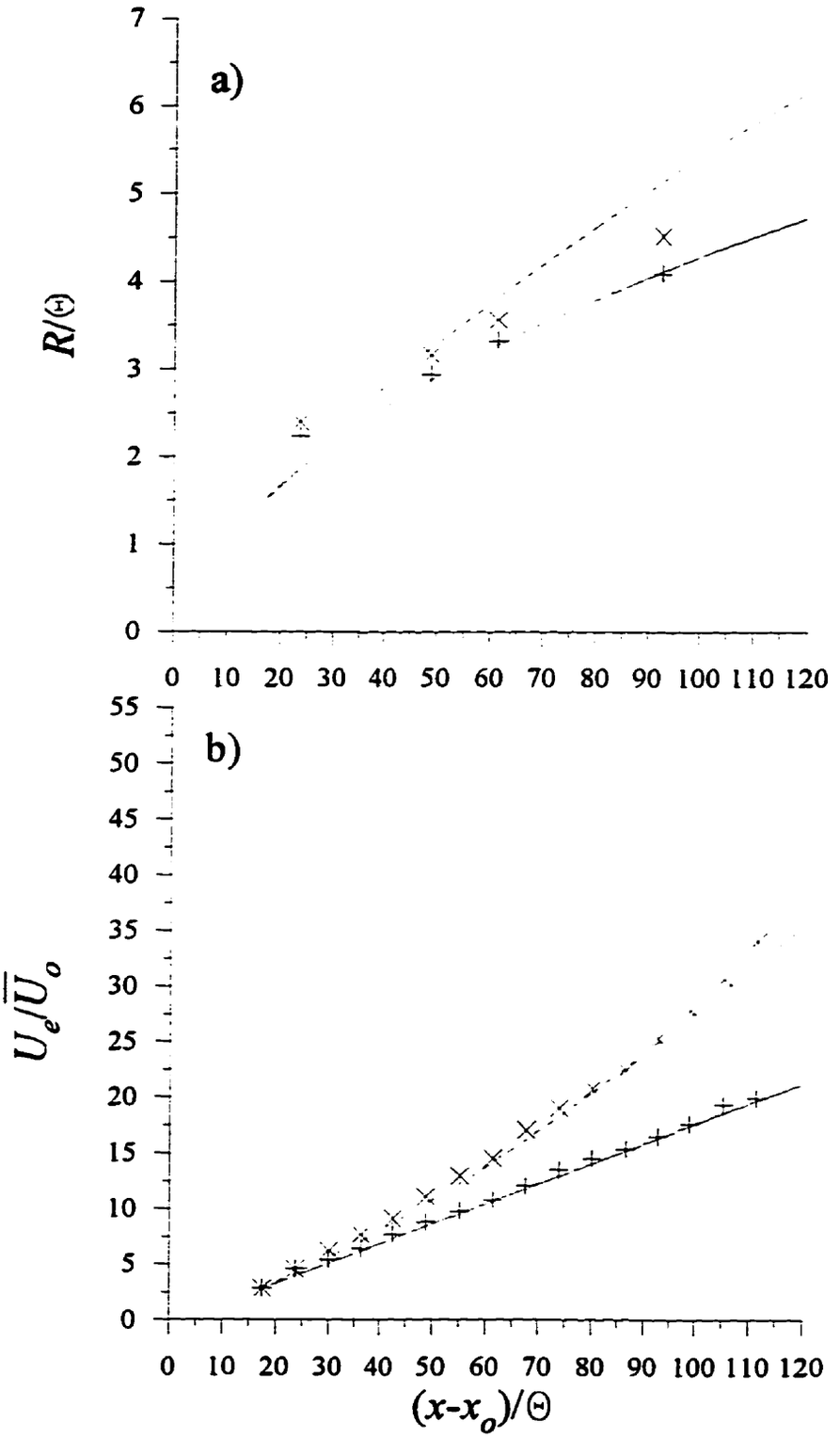

Figure 6.8: Comparison of predictions and experimental data for Fink's jet at $VR \approx 4.5$. Data: +, no grid; ×, grid. Predictions: ——, no grid; - - - -, grid.

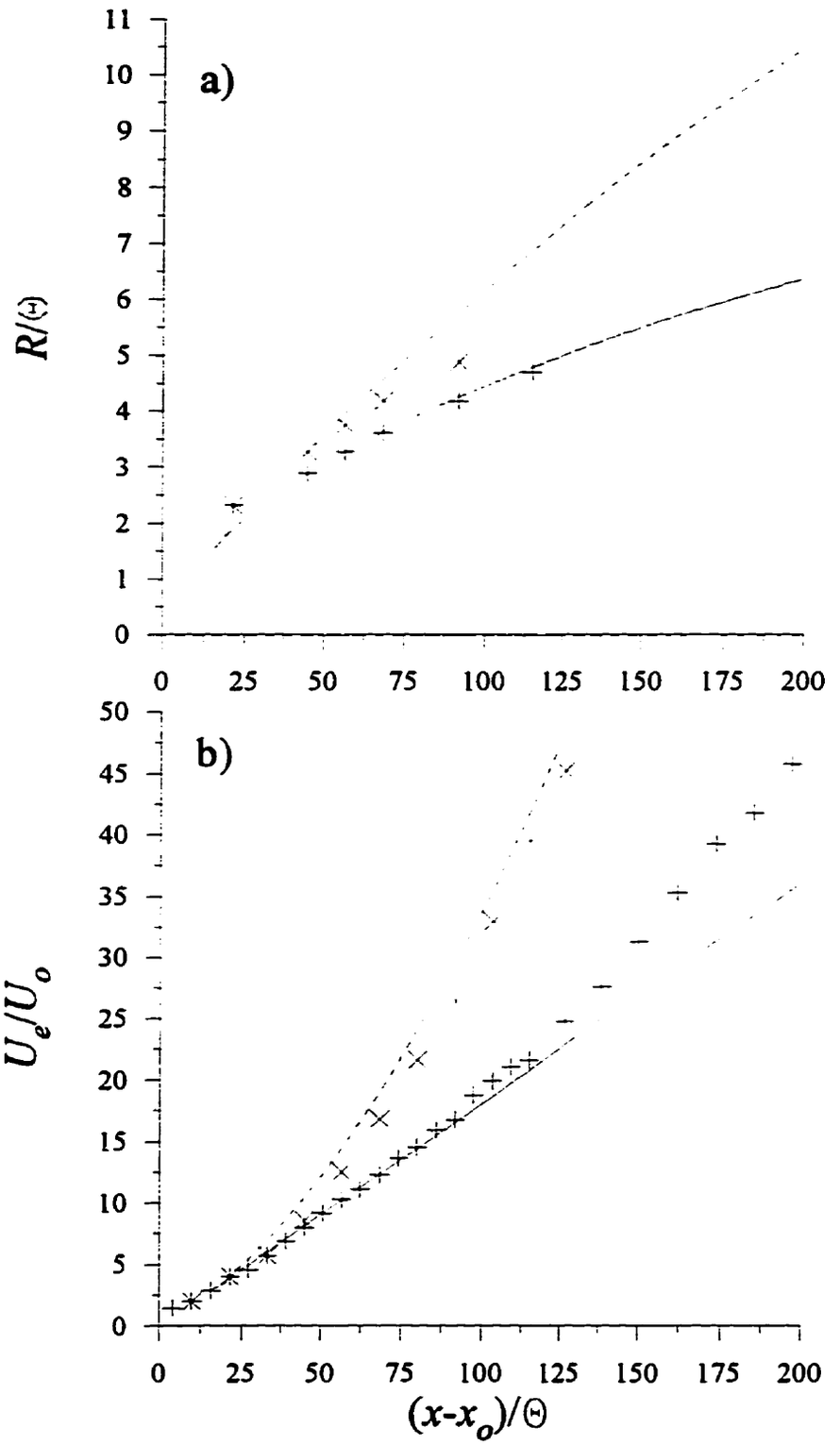

Figure 6.9: Comparison of predictions and experimental data for Fink's jet at $VR \approx 3.1$. Data: +, no grid; ×, grid. Predictions: ——, no grid; - - - -, grid.

the experimental data points for the jets at VR=5.75, 4.5, and 3.1 respectively. One additional comment for the jet at VR=3.1 is that the experimental data for $U_e/\overline{U}_o$ for the jet with no grid installed shows a marked increase in the rate of growth of $U_e/\overline{U}_o$ at around $(x-x_o)/\theta \approx 125$ which the predicted values fail to anticipate. The probable cause of this change in slope is that the very low levels of external turbulent energy with no grid installed are finally reaching a state where they can dynamically influence the behaviour of the jet by slowing the jet down and, presumably, increasing the radius.

6.4.6 Behaviour of the Entrainment Velocity

As a check to ensure that the contributions to the total entrainment velocity made by each phase of the model conforms with the theoretical discussion, the entrainment velocity for the small jet at $VR \approx 3$ with the large grid installed is presented in Figure 6.10. The total entrainment velocity is given as the solid line and the contributions from each phase of the model are given by the dashed lines. Note that the final phase contribution is weighted using equation (6.18).

As expected, near the jet exit, the contribution from the initial phase is dominant and, after $(x-x_o)/\theta \approx 50$, the final phase contribution becomes dominant. At no point is the total entrainment velocity dominated by the intermediate phase contribution since grid generated turbulence typically has a very small inertial subrange. Thus the contributions from each phase are in keeping with the theoretical development. The root-sum-square method of combining the entrainment velocities from each phase results in a smooth merging between phases which gives a smooth and continuous curve for the total entrainment velocity. Note that the transition region between the initial phase dominating the total entrainment velocity and the final phase dominating the total entrainment velocity lies approximately in the range of $15 \leq (x-x_o)/\theta \leq 50$.

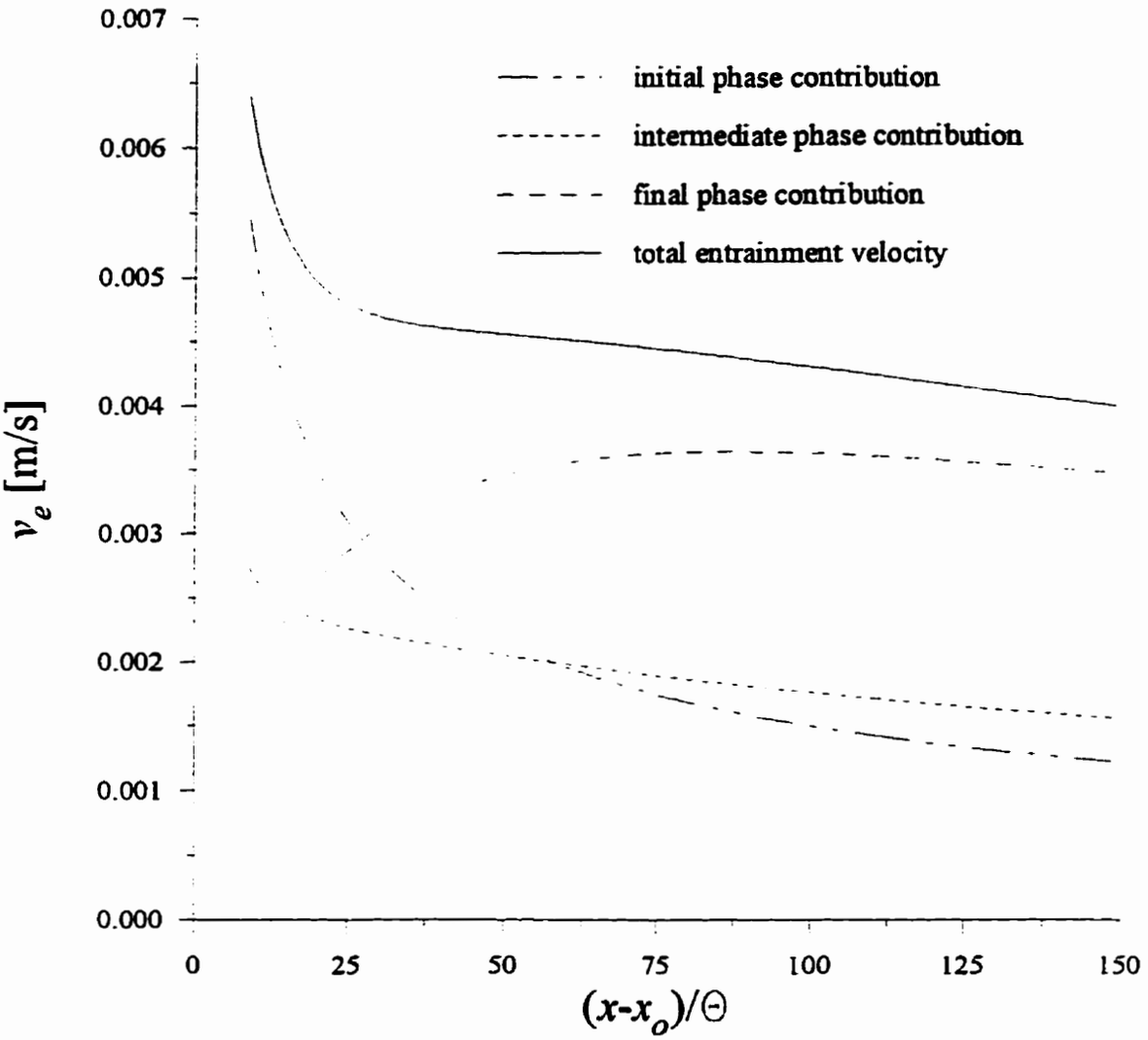

Figure 6.10: Behaviour of the various components of the entrainment velocity for the small jet at $VR \approx 3$ with the large grid installed.

6.5 Extension of the Model to Atmospheric and Oceanic Releases

In order to extend the current coflowing isothermal jet model to real atmospheric and oceanic releases, a complete description of the external turbulence is required. In a laboratory situation using grid-generated turbulence for the external flow, the behaviour of the turbulent velocities, integral length scales, and even the energy dissipation rate can be fairly accurately predicted using

available empirical formulae that have been developed based on the large quantity of experimental data. In atmospheric and oceanic flows, the description of the external turbulence cannot be predicted in general to the same level of certainty due to additional complexities such as convective forces, local topography, large scale horizontal pressure gradients, Coriolis forces, and vertical temperature stability. Thus if accurate external turbulence information is available over the entire solution regime for an atmospheric or oceanic release of an isothermal coflowing jet, the current model could be used to predict the behaviour of $\overline{U}$ and R. If the external flow has a substantial inertial subrange, then a value of β can be determined which should be independent of the fluid viscosity.

Most atmospheric and oceanic releases, however, have additional complexities that the model, as it stands now, cannot account for. These include buoyant forces in the jet (or plume), configurations other than coflowing (*ie.* a jet or plume in a cross flow), and non-uniform external flows (*ie.* turbulent boundary layers) which will require additional research in order to incorporate into the model.

6.6 Closure

For a coflowing jet in a laminar external flow, the behaviour of the mean velocity and the radius of the jet can be accurately predicted using an entrainment velocity of the form:

$$v_e = \alpha\left(\overline{U}\left(\overline{U} - U_e\right)\right)^{1/2} \tag{6.20}$$

where the entrainment constant is in the range of $0.080<\alpha<0.105$ and is inversely dependent, although weakly, on the jet diameter and the initial velocity ratio.

For a coflowing jet in a turbulent external flow, the behaviour of the mean velocity and the radius of the jet can be adequately predicted using a three phase entrainment model combined using the

root-sum-square method as given by equation (6.19). The model predicts that the transition from the initial phase of jet growth, where the self-generated turbulence within the jet controls the diffusion, to the final phase of jet growth, where the energy containing eddies in the external turbulence dominates the mixing, occurs over the range of $15 \leq (x-x_o)/\theta \leq 50$ which can, depending on the jet momentum, be fairly close to the exit of the jet.

Chapter 7: Closure

7.1 Summary and Conclusions

An experimental investigation into the effects that external turbulence has on the development and evolution of turbulent isothermal coflowing jets has been presented. The primary objective of this investigation was to vary the characteristic scales of turbulence in the external flow and in the jet so that the evolution of the jet ranged from being barely affected to being dramatically affected by the external turbulence. The other main objective was to accurately model the newly obtained experimental data using an integral model with an entrainment velocity function that allows for various mechanisms to dominate the diffusion process.

The main conclusions are:

1. The downstream behaviour of the turbulent intensities, the integral length scales, and the turbulent energy spectra in grid-generated turbulence is continuously affected by the grid's initial conditions, namely the grid Reynolds number and grid solidity, with the turbulence generated by each grid reaching a similar but unique state of self-preservation.

2. A turbulent jet issuing into an external coflow has two scaling velocities; one for the mean velocities and one for the turbulent velocities. The excess mean velocities within the jet were found to scale with the conventional scale factor, U_o, while the turbulent velocities were found to scale with a new scale factor, $(U_o(U_o+U_e))^{1/2}$.

3. Experimental results for an isothermal jet in a nearly laminar external coflow indicate that the decay in the excess centerline mean velocity is described by $U_o \propto x^{-1}$ as far downstream as $(x-x_o)/\theta \approx 300$ with the radius following $R \propto x^{2/3}$ up to $(x-x_o)/\theta \approx 100$ after which there is some indication that $R \propto x^{1/3}$. These results are not entirely expected based on asymptotic similarity relationships.

4. The effects of grid-generated turbulence on the evolution of a coflowing jet are not insignificant. Present experimental results indicate that when a jet issues into a turbulent external coflow, one can expect that:
   a) the jet centerline excess mean velocity, U_o, will decay faster beyond $(x-x_o)/\theta \sim 20$ to 25.
   b) the jet radius, R, will increase faster beyond $(x-x_o)/\theta \sim 20$ to 25.
   c) the jet centerline turbulent velocities and Reynolds shear stresses, normalized by U_o, will increase faster beyond $(x-x_o)/\theta \sim 15$ to 20.
   d) the average streamwise integral length scales in the jet, when normalized by the jet radius, will increase faster after $(x-x_o)/\theta \sim 5$ to 10 while the average radial integral length scales will increase faster after $(x-x_o)/\theta \sim 15$ to 20.

   in comparison to the same jet in a nearly laminar external coflow. In all cases, the effects are more pronounced when the large grid is installed than when the small grid is installed due to the greater amount of turbulent energy generated at larger length scales by the large grid.

5. The behaviour of a coflowing jet in a laminar external coflow is accurately predicted using the new entrainment velocity of the form:

$$v_{e.lam} = \alpha\left(\overline{U}\left(\overline{U} - U_e\right)\right)^{1/2} \tag{7.1}$$

where the value of the entrainment constant is inversely dependent on the initial momentum of the jet, namely the jet diameter and the initial velocity ratio, and thus varies between $0.080<\alpha<0.105$.

6. Predictions of the behaviour of a coflowing jet in a turbulent external coflow (made turbulent through the use of a grid) based on a three phase entrainment model where the individual terms are combined using a root-sum-square method to give:

$$v_e = \left(\left[\alpha\left(\overline{U}\left(\overline{U} - U_e\right)\right)^{1/2}\right]^2 + \left[\beta\left(\epsilon_e L_{rr.e}\right)^{1/3}\right]^2 + \left[\gamma w \left(\overline{v_{r.e}^2}\right)^{1/2}\right]^2 \right)^{1/2} \tag{7.2}$$

show acceptable agreement with experimental results. The range of values for α, based on available experimental data is again $0.080<\alpha<0.105$. The value for β, at least in grid-generated turbulence, is dependent on the fluid (for water, $\beta=0.65$ and for air, $\beta=0.26$) while the value for γ is constant and set equal to 1.40.

7.2 Contributions

There are two principal contributions of the present research. The first is a unique data set, consisting of mean velocities, Reynolds stresses, integral length scales, and turbulent energy spectra, that characterizes the evolution of various coflowing jets issuing into external flows with various levels of turbulence. This data set is unique because it contains experiments that have varied the scales of turbulence in the external flow as well as in the coflowing jet so that the evolution of the jet varies from being scarcely affected to being dramatically affected by the external turbulence. The second primary contribution is the development and validation of a new entrainment velocity function, used in conjunction with an integral model, that accurately predicts

the behaviour of jets in laminar external coflows and adequately predicts the behaviour of jets in turbulent external coflows.

In establishing these principal contributions, the following additional contributions have been made:

1. The experimental downstream behaviour of grid-generated turbulence has been shown to be dependent on the grid's initial conditions as speculated by George (1992).

2. A new scaling factor for the turbulent velocities in a coflowing jet has been postulated and verified with experimental data.

3. An order of magnitude analysis, using experimental results, has been conducted on the Navier-Stokes equations for a jet in an external coflow (given in Appendix A) to establish the relative importance of each term in the equations.

7.3 Recommendations for Future Research

The following recommendations are put forth for future research:

1. Additional experiments on jets in a laminar external coflow need to be conducted that systematically vary the jet model diameter and the initial velocity ratio in order to establish a functional relationship with α, the quasi-constant of proportionality for the entrainment in the initial phase of jet growth.

2. Since the effects of external turbulence have been documented and predicted for a simplified model of real atmospheric and oceanic releases, additional complexities can be introduced into the simplified model, such as source buoyancy, different release alignments (*ie.* jet in a cross-flow), and turbulent boundary layers, for future experimental and modelling

endeavours in order to better mimic real releases.

3. Additional experiments are needed that employ a technique to generate external turbulence that has an inertial subrange of substantial bandwidth in order to determine if the assumptions regarding grid-generated turbulence can be extended to other turbulence generating methods and to determine the true value of the entrainment constant for the intermediate phase. To achieve this end, full scale atmospheric or oceanic experiments will probably be required due to the impracticality of generating a substantial inertial subrange at a laboratory scale.

References

Abramovich, G.N., 1963, *The theory of turbulent jets*, The M.I.T. Press, Cambridge.

Adrian, R.J., 1983, "Laser velocimetry," *Fluid Mechanics Measurements*, R.J. Goldstein (ed.), Hemisphere Publishing Co., New York, pp 155-244.

Adrian, R.J. and Yao, C.S., 1987, "Power spectra of fluid velocities measured by laser Doppler velocimetry," *Experiments in Fluids*, Vol. 5, pp 17-28.

Antonia, R.A. and Bilger, R.W., 1973, "An experimental investigation of an axisymmetric jet in a co-flowing air stream," *Journal of Fluid Mechanics*, Vol. 61, Part 4, pp 805-822.

Antonia, R.A. and Bilger, R.W., 1974, "The prediction of the axisymmetric turbulent jet issuing into a co-flowing stream," *Aeronautical Quarterly*, Vol. 25, pp 69-80.

Baines, W.D. and Peterson, E.G., 1951, "An investigation of flow through screens," *Transactions of the ASME*, Vol. 73, pp 467-480.

Batchelor, G.K., 1950, "The application of the similarity theory of turbulence to atmospheric diffusion," *Quarterly Journal of the Royal Meteorological Society*, Vol. 76, pp 133-146.

Bendat, J.S. and Piersol, A.G., 1986, *Random Data*, John Wiley & Sons, Inc., Toronto.

Biringen, S., 1986, "An experimental investigation of a turbulent round jet in a coflowing

airstream," *ASME Paper 86-WA/FE-13.*

Bradshaw, P., 1994, "Turbulence: the chief outstanding difficulty of our subject," *Experiments in Fluids*, Vol. 16, pp 203-216.

Briggs, G.A., 1975, "Plume rise predictions," *American Meteorological Society Workshop on Meteorology and Environment Assessment*, Boston, USA.

Capp, S.P., 1983, *Experimental Investigation of the Turbulent Axisymmetric Jet*, PhD Thesis, State University of New York at Buffalo, Buffalo, USA.

Castro, I.P., 1989, *An Introduction to the Digital Analysis of Stationary Signals*, IOP Publishing Ltd., Cambridge, England.

Churchill, S.W. and Usagi, R., 1972, "A general expression for the correlation rates of transfer and other phenomena," *AIChE Journal*, Vol. 18, No. 6, pp 1121-1128.

Coleman, H.W. and Steele, W.G., 1989, *Experimentation and Uncertainty Analysis for Engineers*, John Wiley & Sons, Inc., Toronto.

Comt-Bellot, G. and Corrsin, S., 1966, "The use of a conrtraction to imporve the isotropy of grid generated turbulence," *Journal of Fluid Mechanics*, Vol. 25, part 4, pp 657-682.

Comte-Bellot, G. and Corrsin, S., 1971, "Simple Eularian time correlation of full- and narrow-band velcotiy signals in grid generated 'isotroic' turbulence," *Journal of Fluid Mechanics*, Vol. 48, Part 2, pp 237-337.

Davidson, G.A., 1986, "Gaussian versus top-hat profile assumptions in integral plume models," *Atmospheric Environment*, Vol. 20, No. 3, pp 471-478.

Djenidi, L. and Antonia, R.A., 1995, "LDA measurements: power spectra estimation," *Dantec Information*, Vol. 14, pp 12-15.

Edwards, R.V., 1992, " Is laser anemometry perfectible?" *Laser Anemometry*, Vol. 3, pp 11-14.

Fink, L.E., 1977, "Influence of external turbulence on mixing of axisymmetric coaxial jets," *Symposium on Turbulent Shear Flow*, Vol. 1, pp 2.11-2.21.

Forstall, W. and Shapiro, A.H., 1950, "Momentum and mass transfer in coaxial jets," *Journal of Applied Mathematics*, Vol. 17, pp 399-408.

Gartshore, I.S., 1966, "An experimental examination of the large-eddy equilibrium hypothesis," *Journal of Fluid Mechanics*, Vol. 24, part 1, pp 89-98.

George, W.K. and Lumley, J.L., 1973, "The laser Doppler velocimeter and its application to the measurement of turbulence," *Journal of Fluid Mechanics*, Vol. 60, pp 321-362.

George, W.K., 1989, "The self-preservation of turbulent flows and its relation to initial conditions and coherent structures," *Advances in Turbulence*, W.K. George and R. Arndt (eds.), Hemisphere Publishing Co., New York, pp 39-73.

George, W.K., 1992, "The decay of homogeneous isotropic turbulence," *Physics of Fluids*, Vol. 4, No. 7, pp 1492-1509.

Hill, P.G., 1965, "Turbulent jets in ducted streams," *Journal of Fluid Mechanics*, Vol. 22, Part 1, pp 161-186.

Hinze, J.O., 1975, *Turbulence, 2nd Edition*, McGraw-Hill Inc., Toronto.

Hirst, E., 1972, "Buoyant jets with three-dimensional trajectories," *Journal of the Hydraulics Division*, Vol. HY 11, pp 1999-2014.

Hussein, H.J., Capp, S.P., and George, W.K., 1994, "Velocity measurements in a high-Reynolds number, momentum-conserving, axisymmetrical, turbulent jet," *Journal of Fluid Mechanics*, Vol. 258, pp 31-75.

Johnson, P.L. and Johnston, J.P., 1989, "Active and inactive motions in a turbulent boundary layer - Interactions with free stream turbulence," *Seventh Symposium on Turbulent Shear Flows*, Stanford University, pp 20.2.1-20.2.6.

Keffer, J.F. and Baines, W.D., 1963, "The round turbulent jet in a cross-wind," *Journal of Fluid Mechanics*, Vol. 15, pp 481-496.

Kline, S.J., 1985, "The purposes of uncertainty analysis," *Journal of Fluids Engineering*, Vol. 107, pp 153-160.

Lewalle, J., 1990, "Decay of velocity and temperature fluctuations in grid turbulence," *AIAA Journal*, Vol. 28, No. 1, pp 106-112.

Maczynski, J.F.J., 1962, "A round jet in an ambient co-axial stream," *Journal of Fluid Mechanics*, Vol. 13, pp 597-608.

Moffat, R.J., 1988, "Describing the uncertainties in experimental results," *Experimental Thermal and Fluid Science*, Vol. 1, pp 3-17.

Morton, B.R., Taylor, G.I., and Turner, J.S., 1956, "Turbulent gravitational convection from

maintained and instantaneous sources," *Proceedings of the Royal Society of London, Series A*, Vol. 234, pp 1-23.

Morton, B.R., 1961, "On a momentum-mass flux diagram for turbulent jets, plumes and wakes," *Journal of Fluid Mechanics*, Vol. 10, pp 101-112.

Munson, B.R., Young, D.F., and Okiishi, T.H., 1990, *Fundamentals of Fluid Mechanics, 2nd Edition*, John Wiley and Sons, Inc., Toronto.

Nakamura, Y. and Ohya, Y., 1983, "The effects of turbulence on the mean flow past square rods," *Journal of Fluid Mechanics*, Vol. 137, pp 331-345.

Newman, B.G., 1967, "Turbulent jets and wakes in a pressure gradient," *Fluid Mechanics of Internal Flow*, G. Sovran (ed.), Elsevier Publishing Co., New York, pp 170-201.

Nickels, T.B. and Perry, A.E., 1996, "An experimental and theoretical study of the turbulent coflowing jet," *Journal of Fluid Mechanics*, Vol. 309, pp 157-182.

Patel, R.A., 1971, "Turbulent jets and wall jets in uniform streaming flow," *Aeronautical Quarterly*, Vol. 22, pp 311-326.

Patrick, W.P., 1985, "Error sources in laser velocimeter systems," *Workshop on Laser Velocimetry*, University of Connecticut, March 10-15.

Press, W.H., Teukolsky, S.A., Vetterling, W.T., and Flannery, B.P., 1986, *Numerical Recipes in Fortran, 2nd Edition*, Cambridge University Press, Cambridge.

Roach, P.E., 1987, "The generation of nearly isotropic turbulence by means of grids," *International Journal of Heat and Fluid Flow*, Vol. 7, No. 2, pp 117-125.

Rodi, W. and Spalding, D.B., 1970, "A two-parameter model of turbulence and its application to free jets," *Wärme-und Stoffübertragung*, Vol. 3, pp 85.

Rodi, W., 1972, *The Prediction of Free Turbulent Boundary Layers by Use of a Two-Equation Model of Turbulence*, PhD Thesis, Imperial College, London.

Sato, H., 1951, "Experimental study of the spectrum of isotropic turbulence," *Journal of the Physical Society of Japan*, Vol. 6, No. 5, pp 387-392.

Schatzmann, M., 1978, "The integral equations for round buoyant jets in stratified flows," *Journal of Applied Mathematics and Physics (ZAMP)*, Vol. 29, pp 608-630.

Schatzmann, M., 1979, "An integral model of plume rise," *Atmospheric Environment*, Vol. 13, pp

721-731.

Sirivat, A. and Warhaft, Z., 1983, "The effect of a passive cross-stream temperature gradient on the evolution of temperature variance and heat flux in grid turbulence," *Journal of Fluid Mechanics*, Vol. 128, pp 323-346.

Slawson, P.R. and Csanady, G.T., 1967, "On the mean path of buoyant, bent-over chimney plumes," *Journal of Fluid Mechanics*, Vol. 28, part 2, pp 311-322.

Slawson, P.R. and Csanady, G.T., 1971, "The effect of atmospheric conditions on plume rise," *Journal of Fluid Mechanics*, Vol. 47, part 1, pp 33-49.

Smith, D.J. and Hughes, T., 1977, "Some measurements in a turbulent circular jet in the presence of a co-flowing free stream," *Aeronautical Quarterly*, Vol. 28, pp 185-196.

So, R.M.C. and Hwang, B.C., 1989, "On incompressible, turbulent, heated round jets in a co-flowing stream," *Aeronautical Quarterly*, March, pp 100-110.

Spalding, D.B., 1971, "Concentration fluctuations in a round free jet," *Chemical Engineering Science*, Vol. 26, pp 95.

Squire, H.B. and Trouncer, J., 1944, "Round jets in a general stream," *ARC Technical Repot No. 1974*.

Tan, H.S. and Ling, S.C., 1963, "Final stage decay of grid-produced turbulence," *Physics of Fluids*, Vol. 6, No. 12, pp 1693-1699.

Taylor, G.I., 1922, "Diffusion by continuous movements," *Proceedings of the London Mathematical Society, Series 2*, Vol. 22, pp 196-212.

Tennekes, H. And Lumley, J.L, 1972, *A First Course in Turbulence*, MIT Press, Cambridge, Massachusetts.

Townsend, A.A., 1976, *The Structure of Turbulent Shear Flows, 2nd Edition*, Cambridge University Press, New York.

Van Heyst, W.J., 1992, *The Effects of External Turbulence on the Development of a Coflowing Jet*, MASc Thesis, University of Waterloo, Waterloo, Canada.

Warhaft, Z. and Lumley, J.L., 1978, "An experimental study of the decay of temperature fluctuations in grid-generated turbulence," *Journal of Fluid Mechanics*, Vol. 88, Part 4, pp 659-684.

Weckman, E.J., 1987, *The Structure of the Flowfield Near the Base of a Medium-Scale Pool Fire*, PhD Thesis, University of Waterloo, Waterloo, Canada.

Wright, S.J., 1994, "The effect of ambient turbulence on jet mixing," *Recent Research Advances in the Fluid Mechanics of Turbulent Jets and Plumes*, P.A. Davies and M.J. Valente Neves (eds.), Kluwer Academic Publishers, Netherlands, pp 13-27.

Appendix A: Integral Equations of Motion

A.1 Introduction

The development of the equations of motion for a jet in an external coflow can follow two distinct approaches. The first technique, termed the *control volume method*, involves taking a finite slice of the jet, dx, and balancing the fluxes of mass, momentum, and energy entering and leaving the control volume with what is being stored within the control volume. The resulting equations can then be integrated with respect to the radial coordinate, r, and solved numerically. This method has been primarily used in the development of governing equations for air pollution sources such as chimney plumes (see, for example, Slawson and Csanady, 1967 and 1971, and Briggs, 1975). The main advantage of the control volume method is that it is very clear how the flux balances are derived. The disadvantages are that it has a limited range of applicability (*i.e.* can only model simple external flow conditions) and that it does not explicitly demonstrate how the turbulence within the jet contributes to the growth and development of the jet.

The second method, referred to as the *differential method*, seeks to describe the flow pattern at every location in the field and hence uses the fully turbulent, three dimensional Navier-Stokes equations of

fluid mechanics which are first integrated with respect to the azimuthal direction, ϕ, and then with respect to the radial direction, r, with the aid of simplifying assumptions. This method has also been used to derive governing equations for air pollution sources (see, for example, Hirst, 1972, and Schatzmann, 1978) but has also been used in many other applications such as boundary layers (Hinze, 1975) and isothermal jets issuing into a quiescent background (Hussein *et al*, 1994). The main advantages of the differential method are that it can account for much more complicated flow situations such as complex ambient conditions and that it explicitly reveals the manner in which the turbulence within the jet contributes to the growth and development of the jet. The drawback of the method is that since it is mathematically more rigorous, arriving at the final equations is more complicated and tedious than in the control volume method.

A.2 Differential Approach

Since one of the primary objectives of the present research is to determine how the various turbulent quantities, both within the jet and in the external coflow, contribute to the development and growth of the jet, a detailed derivation of the equations of motion will be given following the differential approach.

A schematic of an axisymmetric isothermal turbulent jet, either in a laminar or turbulent coflow, is given in Figure A.1. The coordinate system is defined as (x,r,ϕ). The instantaneous velocities are decomposed into mean velocity components given by (U,V_r,V_ϕ) and fluctuating components given by (u,v_r,v_ϕ). The external mean flow is assumed to be uniform both in magnitude and direction (*i.e.* U_e and P_e are constants) although the turbulence quantities are assumed to vary with distance downstream as is appropriate for grid-generated turbulence. The jet flow is assumed to be steady, incompressible, and fully turbulent shortly after the jet exit with a Reynolds number sufficiently large so that the viscous terms can be neglected (Hinze, 1975). It is also assumed that the jet is not subjected to any mean swirl in the azimuthal direction (*i.e.* $V_\phi=0$ and $\partial(\ )/\partial\phi=0$ but $\overline{v_\phi^2}\neq 0$ necessarily).

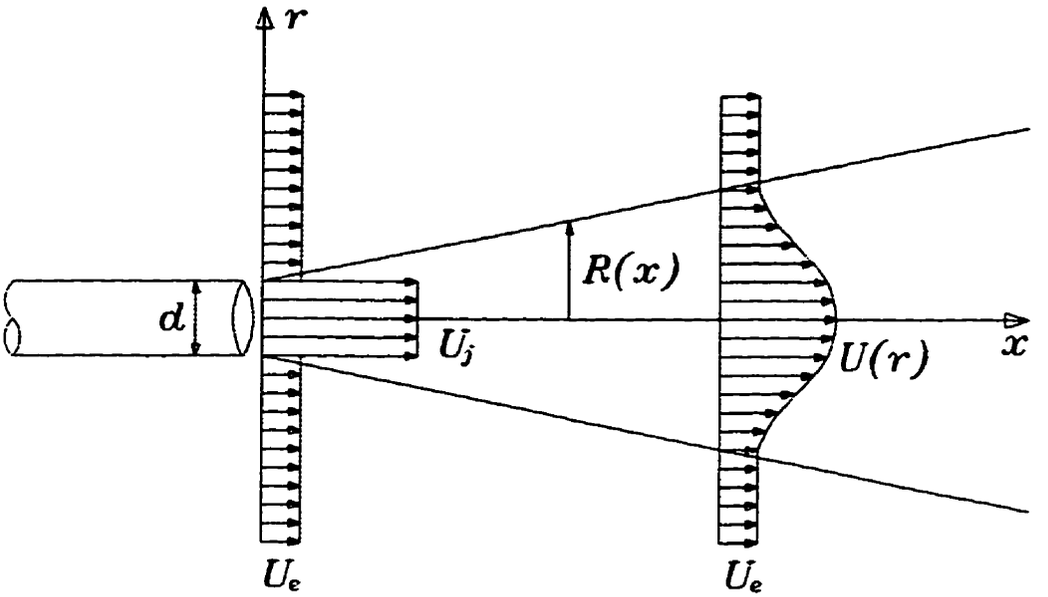

Figure A.1: Schematic of an axisymmetric isothermal jet issuing into a uniform external coflow.

The boundary conditions at the edge of the jet, where $r = R(x)$, are as follows:

$$U=U_e$$

$$P=P_e$$

$$\overline{u^2}=\overline{u_e^2}(x)$$

$$\overline{v_r^2}=\overline{v_{r,e}^2}(x)$$

$$\overline{v_\phi^2}=\overline{v_{\phi,e}^2}(x)$$

$$\overline{uv_r}=\overline{(uv_r)}_e(x)$$

Since the turbulence resulting from grid-generated turbulence is nearly isotropic and homogeneous in planes parallel to the grid, it will be assumed that the radial and azimuthal turbulent velocities are equal in magnitude (*i.e.* $\overline{v_{r,e}^2}(x)=\overline{v_{\phi,e}^2}(x)$) at a given downstream location. In addition, for a nearly laminar coflow, it is assumed that all turbulent velocity components are near zero (*i.e.* $\overline{u_e^2}(x)\approx\overline{v_{r,e}^2}(x)\approx\overline{v_{\phi,e}^2}(x)\approx\overline{(uv_r)}_e(x)\approx 0$) outside of the jet domain.

A.2.1 Integral Conservation of Mass Equation

Using the differential method and the assumptions outlined above, the equation representing the conservation of mass in a cylindrical coordinate system can be reduced to:

$$\frac{1}{r}\frac{\partial r V_r}{\partial r} + \frac{\partial U}{\partial x} = 0 \tag{A.1}$$

Taking this expression and multiplying it by rdr and integrating from r=0 to r=$R(x)$ yields:

$$\int_0^{R(x)} \frac{\partial r V_r}{\partial r} dr + \int_0^{R(x)} \frac{\partial U}{\partial x} r\, dr = 0 \tag{A.2}$$

The first term of equation (A.2) is readily integrated. The second term, in order to pull the derivative operator outside of the integral, requires the application of Leibnitz's rule for differentials of integrals since the upper limit is a function of x. The resulting expression, after some rearranging, is:

$$\frac{d}{dx}\int_0^{R(x)} U r\, dr = R\left(- V_r(R) + U_e \frac{dR}{dx} \right) \tag{A.3}$$

A.2.2 Integral Conservation of Momentum

The simplified equations describing the conservation of momentum in cylindrical coordinates are:

$$V_r \frac{\partial V_r}{\partial r} + U\frac{\partial V_r}{\partial x} = -\frac{1}{\rho}\frac{\partial P}{\partial r} - \frac{\partial \overline{v_r^2}}{\partial r} - \frac{\partial \overline{uv_r}}{\partial x} + \frac{\overline{v_\phi^2} - \overline{v_r^2}}{r} \tag{A.4}$$

for the radial direction and:

$$V_r \frac{\partial U}{\partial r} + U \frac{\partial U}{\partial x} = -\frac{1}{\rho}\frac{\partial P}{\partial x} - \frac{\partial \overline{u^2}}{\partial x} - \frac{1}{r}\frac{\partial r\overline{uv_r}}{\partial r} \qquad \text{(A.5)}$$

for the streamwise direction. The first step in deriving the integral form of the equations is to solve for the pressure distribution by multiplying the *r*-momentum equation by *dr* and integrating the resulting equation from some arbitrary reference point within the jet, say r_o, to the edge of the jet, $R(x)$. This gives:

$$\int_{r_o}^{R(x)} \left(U\frac{\partial V_r}{\partial x} + V_r\frac{\partial V_r}{\partial r} \right) dr = \int_{r_o}^{R(x)} \left(-\frac{1}{\rho}\frac{\partial P}{\partial r} - \frac{\partial \overline{uv_r}}{\partial x} - \frac{\partial \overline{v_r^2}}{\partial r} - \frac{\overline{v_r^2} - \overline{v_\phi^2}}{r} \right) dr \qquad \text{(A.6)}$$

For convenience, let:

$$T_1 = \int_{r_o}^{R(x)} \left(U\frac{\partial V_r}{\partial x} + V_r\frac{\partial V_r}{\partial r} \right) dr \qquad \text{and} \qquad T_2 = \int_{r_o}^{R(x)} \frac{\partial \overline{uv_r}}{\partial x} dr \qquad \text{(A.7)}$$

Integrating equation (A.6) then gives:

$$\left[-\frac{1}{\rho} P \right]_{r_o}^{R(x)} = T_1 + T_2 + \left[\overline{v_r^2} \right]_{r_o}^{R(x)} + \int_{r_o}^{R(x)} \frac{\overline{v_r^2} - \overline{v_\phi^2}}{r} dr \qquad \text{(A.8)}$$

Since r_o is an arbitrary position within the jet, let $P=P$ and $\overline{v_r^2}=\overline{v_r^2}$ at $r=r_o$, and using the boundary conditions previously defined for $r=R(x)$, the integrated *r*-momentum equation becomes:

$$\frac{P_e - P}{\rho} = -\left(T_1 + T_2\right) - \overline{v_{re}^2} + \overline{v_r^2} + \int_{r_o}^{R(x)} \frac{\overline{v_\phi^2} - \overline{v_r^2}}{r} dr \qquad \text{(A.9)}$$

Taking the derivative with respect to x gives an expression for the pressure gradient in the streamwise direction:

$$-\frac{1}{\rho}\frac{\partial P}{\partial x} = -\frac{\partial}{\partial x}\left(T_1 + T_2\right) + \frac{\partial}{\partial x}\left(\overline{v_r^2} - \overline{v_{re}^2}\right) + \frac{\partial}{\partial x}\int_{r_o}^{R(x)} \frac{\overline{v_\phi^2} - \overline{v_r^2}}{r}\,dr \qquad \text{(A.10)}$$

This expression can now be substituted into equation (A.5) which in turn can be multiplied by rdr and integrated from r=0 to r=$R(x)$ to yield:

$$\underbrace{\int_0^{R(x)}\left(U\frac{\partial U}{\partial x} + V_r\frac{\partial U}{\partial r}\right) r\,dr}_{\text{I}} + \underbrace{\int_0^{R(x)}\frac{\partial}{\partial x}\left(T_1 + T_2\right) r\,dr}_{\text{II}} + \underbrace{\int_0^{R(x)}\frac{\partial}{\partial x}\left(\overline{v_{re}^2} - \overline{v_r^2}\right) r\,dr}_{\text{III}}$$

$$+ \underbrace{\int_0^{R(x)}\frac{\partial \overline{u^2}}{\partial x} r\,dr}_{\text{IV}} + \underbrace{\int_0^{R(x)}\frac{\partial r\overline{uv_r}}{\partial r}\,dr}_{\text{V}} - \underbrace{\int_0^{R(x)}\left(\frac{\partial}{\partial x}\int_{r_o}^{R(x)}\frac{\overline{v_\phi^2} - \overline{v_r^2}}{r}\,dr\right) r\,dr}_{\text{VI}} = 0 \qquad \text{(A.11)}$$

To simplify this expression further, a term by term analysis is required.

Term I: Using the conservation of mass equation and the product rule for derivatives, term I can be simplified to:

$$\text{Term I} = \left[r\,U\,V_r\right]_0^{R(x)} + \int_0^{R(x)}\frac{\partial U^2}{\partial x} r\,dr \qquad \text{(A.12)}$$

Evaluating the term in the square brackets using the limits gives $U_e RV_r(R)$. However, by using the final form of the integral conservation of mass as given in equation (A.3), an alternative expression for $U_e RV_r(R)$ can be obtained and substituted for the first term in equation (A.12). The second term in equation (A.12) can be simplified using Leibnitz's rule to give:

$$\int_0^{R(x)}\frac{\partial U^2}{\partial x} r\,dr = \frac{d}{dx}\int_0^{R(x)} U^2 r\,dr - U_e^2 R\frac{dR}{dx} \qquad \text{(A.13)}$$

Substituting these results into equation (A.12) results in:

$$\textbf{Term I} = \frac{d}{dx}\int_0^{R(x)} U(U-U_e)\,r\,dr \qquad \text{(A.14)}$$

Term II: Since the upper limit is again a function of x, Leibnitz's rule is used to simplify the term to:

$$\text{Term II} = \frac{d}{dx}\int_0^{R(x)} \left(T_1+T_2\right) r\,dr - \left(T_1(R)+T_2(R)\right) R\frac{dR}{dx} \qquad \text{(A.15)}$$

Additional simplification of term II cannot be done at this point. An order of magnitude analysis will be conducted at the end to determine the relative importance that term II has on the integral momentum equation.

Term III and IV: Term III and IV can be combined into a single term. Taking the derivative operator outside of the integral using Leibnitz's rule and applying the boundary conditions at $r=R(x)$ gives:

$$\text{Term III \& IV} = \frac{d}{dx}\int_0^{R(x)} \left(\overline{u^2}-\overline{v_r^2}+\overline{v_{re}^2}\right) r\,dr + \overline{u_e^2}\,R\frac{dR}{dx} \qquad \text{(A.16)}$$

Term V: Term V can be integrated directly and evaluated using the boundary conditions:

$$\text{Term V} = \left[r\,\overline{u\,v_r}\right]_0^{R(x)} = R\left(\overline{u\,v_r}\right)_e \qquad \text{(A.17)}$$

Term VI: Using Leibnitz's rule to again extract the derivative operator outside the integral results in:

$$\text{Term VI} = \frac{d}{dx}\int_0^{R(x)} \left(\int_{r_o}^{R(x)} \frac{\overline{v_\phi^2}-\overline{v_r^2}}{r}\,dr \right) r\,dr - \left[\int_{r_o}^{R(x)} \frac{\overline{v_\phi^2}-\overline{v_r^2}}{r}\,dr \right]_{R(x)} R\frac{dR}{dx} \qquad \text{(A.18)}$$

At $r=R(x)$, it is assumed that the radial and azimuthal turbulent velocities are that of the external flow which are equal to each other due to planar isotropy. The contribution of the second term on the right hand side is thus zero. Using integration by parts, the first term on the right hand side can be rewritten so that term VI has the form (see Capp, 1983):

$$\textbf{Term VI} = \frac{d}{dx}\int_0^{R(x)} \frac{\overline{v_r^2} - \overline{v_\phi^2}}{2} r\,dr \tag{A.19}$$

The integral x-momentum equation, as given by equation (A.11), can now be reassembled to give:

$$\begin{aligned}\frac{d}{dx}\int_0^{R(x)} \left(U(U-U_e) + \overline{u^2} - \frac{\left(\overline{v_r^2} + \overline{v_\phi^2}\right)}{2} + \overline{v_{re}^2} + T_1 + T_2 \right) r\,dr \\ -\left(T_1(R) + T_2(R) + \overline{u_e^2}\right) R\frac{dR}{dx} + R\overline{(uv_r)_e} = 0\end{aligned} \tag{A.20}$$

A.2.3 Order of Magnitude Analysis

The purpose of this order of magnitude analysis is to establish the relative importance of each of the terms in equation (A.20). Let b and L be length scales that characterize the dimensions of the jet in the radial direction (*i.e.* the jet radius) and streamwise direction (*i.e.* the distance from the jet nozzle) respectively. The ratio of b/L from experiments for a jet in a nearly laminar coflow varies from 0.06 to 0.20 with a typical value of b/L=0.13. Also, let $\tilde{U}$ and $\tilde{u}^2$ be velocity scales that characterize the streamwise mean velocities (*i.e.* the excess mean velocity on the jet centerline) and the normal Reynolds stresses or square of the turbulent velocities (*i.e.* $\overline{u^2} \sim \overline{v_r^2} \sim \overline{v_\phi^2} \sim \tilde{u}^2$) respectively. Typical values for $\tilde{u}/\tilde{U}$ from experiments range from 0.10 to 0.40 for a jet in a nearly laminar coflow with a representative value being around $\tilde{u}/\tilde{U}$=0.25. In addition, since the magnitude of the Reynolds shear stress, in comparison to the normal stresses, depends on a correlation coefficient, C_{uv}, the Reynolds shear stress will scale as $\overline{uv_r} \sim C_{uv}\,\tilde{u}^2$. The absolute magnitude of C_{uv} will vary anywhere between zero for a isotropic turbulent flow, to a maximum of one for a perfectly correlated turbulent flow.

Table A.1 provides a summary of the relative order of magnitudes for each of the terms in equation (A.20). As indicated by the table, any term involving either T_1 or T_2 can be safely neglected since they

are two orders of magnitude smaller than the largest term. Terms involving the square of the turbulent velocities (*i.e.* the normal stresses) are a single order of magnitude smaller than the largest term. Previous studies on jets (Capp, 1983, and Antonia and Bilger, 1974) have estimated that these normal stresses account for approximately ten percent of the total momentum and will therefore be retained in the final equation. The relative magnitude of the Reynolds stress term can be seen to depend on C_{uv}. If it is assumed that the value of C_{uv} is not small, than this term must also be retained in the final equation. Thus the final form of the integral x-momentum equation is:

$$\frac{d}{dx}\int_0^{R(x)}\left[U(U-U_e)+\overline{u^2}-\frac{\overline{v_r^2}+\overline{v_\phi^2}}{2}+\overline{v_{re}^2}\right]r\,dr-\overline{u_e^2}\,R\frac{dR}{dx}+R\overline{(u\,v_r)_e}=0 \qquad \text{(A.21)}$$

To highlight the different sources contributing to the integral x-momentum equation, equation A.21 can be rewritten in the form:

$$\underbrace{\frac{d}{dx}\int_0^{R(x)}U(U-U_e)r\,dr}_{\text{I}}+\underbrace{\frac{d}{dx}\int_0^{R(x)}\left(\overline{u^2}-\frac{\overline{v_r^2}+\overline{v_\phi^2}}{2}\right)r\,dr}_{\text{II}}+$$
$$\underbrace{R\left(\left(\overline{v_{re}^2}-\overline{u_e^2}\right)\frac{dR}{dx}-R\frac{d\overline{v_{re}^2}}{dx}+\left(\overline{u\,v_r}\right)_e\right)}_{\text{III}}=0 \qquad \text{(A.22)}$$

where term I represents the contribution from the mean motion of the jet, term II gives the contribution of the Reynolds stresses within the jet, and term III gives the contribution from the Reynolds stresses in the external flow. For a nearly laminar external flow, the contribution from term III becomes negligible and the remaining terms can be integrated to obtain:

$$\int_0^{R(x)}\left[U(U-U_e)+\overline{u^2}-\frac{\overline{v_r^2}+\overline{v_\phi^2}}{2}\right]=\frac{M_o}{2\pi\rho}=\text{constant} \qquad \text{(A.23)}$$

where M_o is the momentum integral constant.

Term	Dimensional Magnitude	Relative Magnitude
$\frac{d}{dx}\int_0^{R(x)} U(U-U_e)r\,dr$	$O\left[\frac{b}{L}\left(\frac{\bar{U}}{\tilde{u}}\right)^2 b\,\tilde{u}^2\right]$	$O\left[2.08\,b\,\tilde{u}^2\right]$
$\frac{d}{dx}\int_0^{R(x)}\left(\overline{u^2}-\frac{\left(\overline{v_r^2}+\overline{v_\phi^2}\right)}{2}+\overline{v_{re}^2}\right)r dr$	$O\left[\frac{b}{L}b\,\tilde{u}^2\right]$	$O\left[0.13\,b\,\tilde{u}^2\right]$
$\frac{d}{dx}\int_0^{R(x)} T_1\,r\,dr$	$O\left[\left(\frac{b}{L}\right)^3\left(\frac{\bar{U}}{\tilde{u}}\right)^2 b\,\tilde{u}^2\right]$	$O\left[0.035\,b\,\tilde{u}^2\right]$
$\frac{d}{dx}\int_0^{R(x)} T_2\,r\,dr$	$O\left[\left(\frac{b}{L}\right)^2 b\,\tilde{u}^2\right]$	$O\left[0.017\,b\,\tilde{u}^2\right]$
$T_1(R)R\frac{dR}{dx}$	$O\left[\left(\frac{b}{L}\right)^3\left(\frac{\bar{U}}{\tilde{u}}\right)^2 b\,\tilde{u}^2\right]$	$O\left[0.035\,b\,\tilde{u}^2\right]$
$T_2(R)R\frac{dR}{dx}$	$O\left[\left(\frac{b}{L}\right)^2 b\,\tilde{u}^2\right]$	$O\left[0.017\,b\,\tilde{u}^2\right]$
$\overline{u_e^2}R\frac{dR}{dx}$	$O\left[\frac{b}{L}b\,\tilde{u}^2\right]$	$O\left[0.13\,b\,\tilde{u}^2\right]$
$R\overline{(u\,v_r)_e}$	$O\left[C_{uv}\,b\,\tilde{u}^2\right]$	$O\left[C_{uv}\,b\,\tilde{u}^2\right]$

Table A.1: Order of magnitude study on the integral *x*-momentum equation.

A.3 Control Volume Approach

In the control volume approach to deriving the integral equations of motion, all the effects of turbulence are considered to be lumped into one term which controls the entrainment of external fluid into the jet. This allows the resulting equations for the conservation of mass and x-momentum to be first order approximations which neglect the complicating turbulence terms. The entrainment velocity, v_e, is left as an unknown function in the derivation which must be later specified. The formulation for the entrainment velocity is often based on physically reasoning backed up experimental data.

Using the control volume approach (see, for example, Morton, 1961 and Briggs, 1975), the integral equations for the conservation of mass and x-momentum are given as:

$$\frac{d}{dx}\int_0^{R(x)} U\,r\,dr = R\,v_e \tag{A.24}$$

and:

$$\frac{d}{dx}\int_0^{R(x)} U\left(U-U_e\right)r\,dr = 0 \tag{A.25}$$

respectively. No assumption about the shape of the mean velocity profiles within the jet has been made at this time in order to facilitate a comparison with the same equations derived from the differential approach. Typically, a top-hat velocity profile within the jet is assumed which simplifies the integrals within the equations.

A.4 Comparison of the Methods

By comparing the equations for the conservation of mass derived from the differential approach (equation (A.3)) with that given for the control volume approach (equation (A.24)), an approximation for the entrainment velocity can be obtained:

$$v_e \sim -V_r(R) + U_e \frac{dR}{dx} \tag{A.26}$$

which can be rewritten in the form:

$$v_e \sim \frac{1}{U_e R}\left[\frac{d}{dx}\int_0^{R(x)} U^2 r\,dr + \frac{d}{dx}\int_0^{R(x)}\left(\overline{u^2} - \frac{\overline{v_r^2} + \overline{v_\phi^2}}{2}\right) r\,dr\right] + \frac{1}{U_e}\left[\left(\overline{v_{re}^2} - \overline{u_e^2}\right)\frac{dR}{dx} - R\frac{d\overline{v_{re}^2}}{dx} + (\overline{u v_r})_e\right] \tag{A.27}$$

with the aid of the results obtained from the differential derivation. Thus, the entrainment velocity is dependent on the mean motion of the jet and the external flow, the radius of the jet, the Reynolds normal stresses in the jet, and the Reynolds normal and shear stresses in the turbulent external flow. Equation (A.27) is an approximation of the entrainment velocity that is used here to highlight factors that contribute to the entrainment of external fluid. The exact formulation of an entrainment velocity function and the physical justifications behind it are dealt with in Chapter 6.

A.5 Velocity Profile Assumption

Up until this point, no assumption has been made regarding the shape of the jet mean velocity profiles except for the fact that they are assumed to be self-similar. Chapter 5 illustrated that the mean velocity profiles are approximately Gaussian in nature after an initial development zone. The use of

a velocity profile assumption has the effect of compressing all the experimental data measured in a radial profile down into a single characteristic velocity scale and a single characteristic radial length scale which, for a Gaussian profile, are U_o and L_o respectively. The end result is that the radial detail of the velocity profile is distilled into the characteristic scales of the assumed profile. Thus any velocity profile defined by a velocity scale and a radial length scale can be used without the loss of any additional experimental information. For this reason, it is often assumed, especially in atmospheric releases, that the mean velocity profile has a top-hat profile which can be characterized by $\overline{U}$ and R. An illustration of the Gaussian and top-hat velocity profiles is given Figure A.2. The main advantage of the top-hat profile is that it reduces the complexity of the integrals in the conservation of mass and streamwise momentum equations since the mean velocity is assumed constant within the jet. Davidson (1986) has shown that even for buoyant jets in a cross-flow, the predicted results using a top-hat profile are essentially identical to the results predicted from a Gaussian profile, except perhaps near the source.

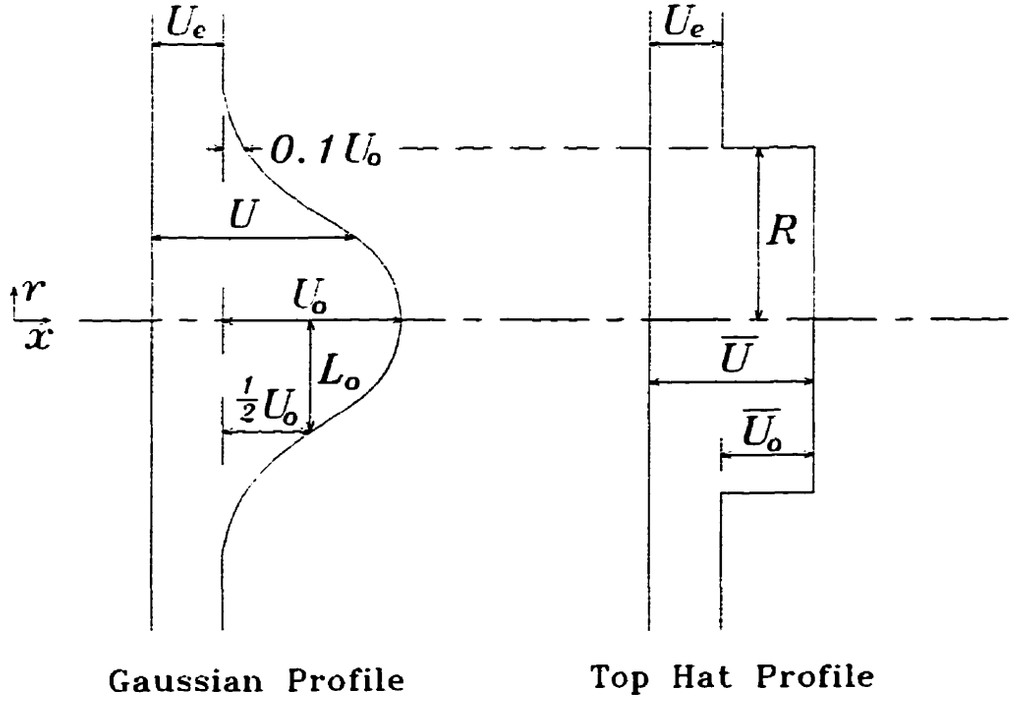

Figure A.2: Schematic and nomenclature of velocity profiles commonly assumed.

Using a top-hat mean velocity profile assumption, the equations for the conservation of mass and streamwise momentum can be simplified to:

$$\frac{d}{dx}\left(R^2\overline{U}\right) = 2Rv_e \tag{A.28}$$

and:

$$\frac{d}{dx}\left(\overline{U}\left(\overline{U}-U_e\right)R^2\right) = 0 \tag{A.29}$$

respectively. Equation (A.29) can be integrated directly to obtain the momentum integral, M_o:

$$\overline{U}\left(\overline{U}-U_e\right)R^2 = \frac{M_o}{\pi\rho} \tag{A.30}$$

which is a constant for a particular combination of a jet and an external flow.

Appendix B: LDA Signal Noise Contamination

B.1 Introduction

At an early stage in the experiments, it was noticed that the measured power spectra tended to level off at the same turbulent energy level at the higher frequencies. This phenomenon became more evident as the turbulent energy within the flow decreased. It quickly became apparent that a particular measured spectrum consisted of the true spectrum of the turbulence being measured as well as a flatter spectrum characteristic of white or random noise with roll off.

In order to pinpoint the source of the white noise contamination, various experiments were conducted that varied the photomultiplier gain, the shift frequency, the sample frequency, the make and model of the counter, and the water flume velocity. In addition, the water flume facility was grounded and the experiments were conducted with and without the overhead fluorescent lights on. The results of all these experiments showed that the LDA signal was still being contaminated by white noise. Finally, a known laminar pipe flow with a Reynolds number of approximately 800 was measured with the LDA. The resulting spectrum, given in Figure B.1, is not negligibly small

as theoretically expected for laminar flows, but is typical of white noise with roll off occurring after a frequency of approximately 10 HZ. Thus is was concluded that the source of the noise contamination is inherent in the LDA system and not due to some external factor.

B.2 Noise in the LDA System

The presence of a particle in the LDA control volume occurs at random times. In order to generate a regular interval times series from this randomly occurring data, the LDA counters employ a simple

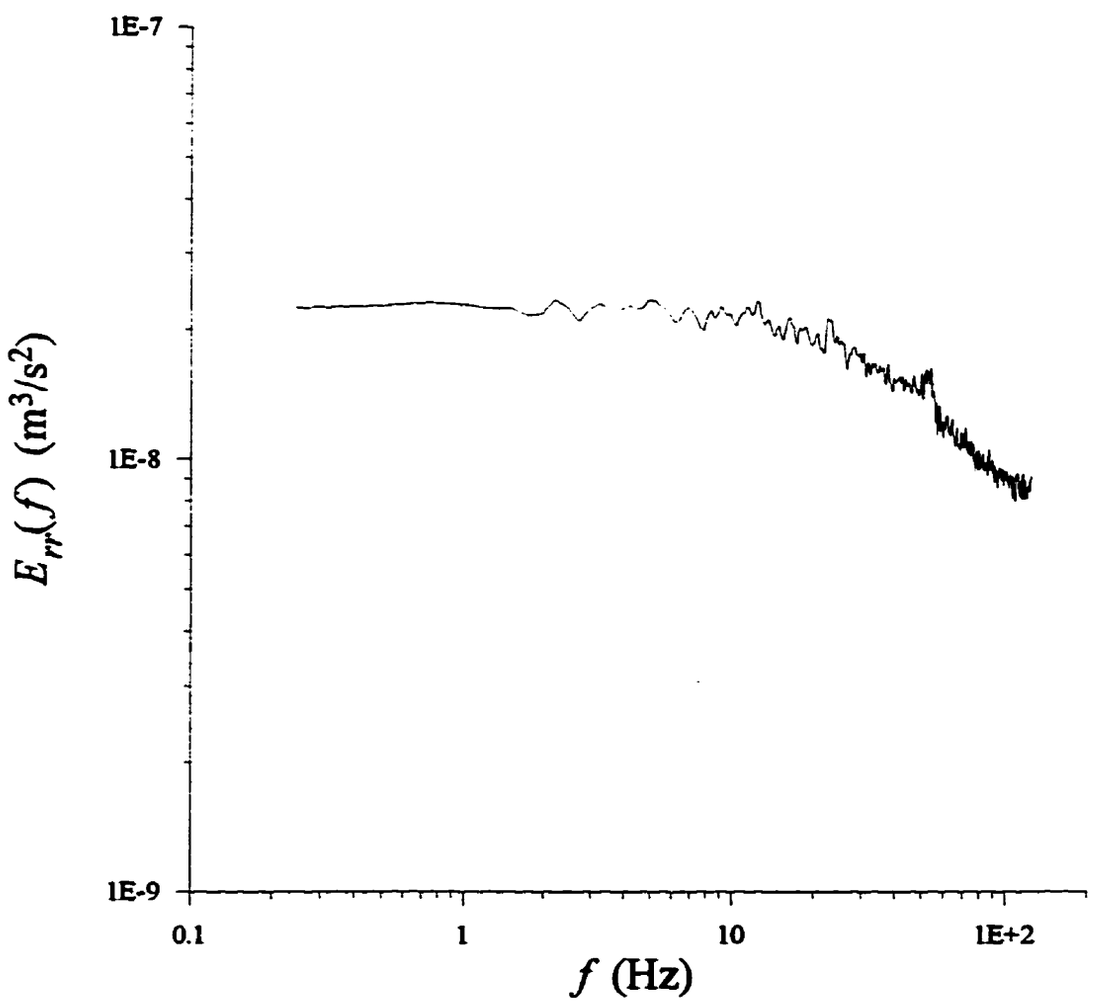

Figure B.1: Noise spectrum as measured using the current LDA set up for a known laminar pipe flow operating at $Re \approx 800$.

sample and hold processing technique whereby the last valid Doppler signal is held until a new Doppler burst occurs. This technique represents a simple form of interpolation between the data points and is an appropriate procedure when the average time between data points is small enough to resolve the structure of the velocity fluctuations.

In order to understand possible sources of noise that can be introduced into the measured signal by the LDA system, the implications arising from the data density, defined as the mean number of samples occuring in one Talyor micro time scale of the flow (Adrian, 1983), and the burst density, N_e, defined as the average number of scatter particles within the control volume at any one time, must be examined.

The average time bewteen Doppler bursts can be compared to the small scale turbulence structure of the flow by using the data density which is calculated from:

$$\textbf{data density} = \dot{N}\,\Im_\lambda \tag{B.1}$$

where $\dot{N}$ is the mean valid signal arrival rate and $\Im_\lambda$ is the Taylor micro time scale. If the data density is greater than five, the data density is considered high and if it is less than 0.5, the data denstiy is considered to be low (Edwards, 1992). A high data density implies that the particles passing through the control volume are close enough together that a simple interpolation scheme, such as the sample and hold technique, can be used to fill in any missing data occuring between valid bursts without introducing serious statistical errors.

The burst density, N_e, can be estimated from (Adrian, 1983):

$$N_e = \frac{2\,a\,\dot{N}}{U\,\Im_\lambda} \tag{B.2}$$

where a is the minor elliptical diameter of the control volume in the direction of the mean flow and is estimated at 0.235 mm for the current LDA set up. A low burst density ($N_e \ll 1$) is desired since

the probability of more than one particle in the control volume is small. A high burst density (N_e»1) may result in ambiguity or phase errors being introduced into the measured signal. The errors, caused by more than one particle being present in the control volume, generate a white noise spectrum which is the result of the random frequency modulation generated by the random overlap of multiple bursts (Adrian and Yao, 1987).

The results from the grid-generated turbulence experiments using the small grid are used as an illustrative example. The oscilloscope, connected to the counter output, can be used to determine the average time between valid Doppler bursts originating at the control volume with the result being approximately 10 ms. The inverse of this gives the mean valid signal arrival rate and is $\dot{N}$=100 Hz. The Taylor micro time scale can be estimated using empirical equations given by Roach (1987) for the small grid with a mean velocity of U_e≈0.07 m/s to give $\Im_\lambda$≈0.20 s. The data density is therefore on the order of 20 and is thus considered high. The burst density yields a value of 3.4 which is also on the high side and thus the possibility of ambiguity error contamination of the measured data exists. The use, however, of amplitude discriminators (*ie.* Schmitt triggers), and the use of multiple zero crossing comparison logic (*ie.* 5/8 comparison) in the Dantec counters greatly reduce these errors.

Adrian and Yao (1987) have shown, however, that the sample and hold process effectively acts as a low pass filter to the true spectrum with a low pass frequency determined by $\dot{N}/2\pi$ and, in addion, introduces a white noise component into the measured velocity signal. The low pass filtering is caused by the result of the information loss that occurs over the hold periods while the white noise is created by the random steps that occur at new Doppler bursts and is often referred to as 'step' noise. In the limit of high data density, the step noise is reduced and vanishes completely in the limit. As the data density decreases, however, theory predicts that the sample and hold process attenuates the noise spectrum with a role off that is characteristic of a first order low pass filter and increases the energy content of the low frequencies by adding more step noise (Adrian and Yao, 1987).

Thus the current white noise contamination of the LDA signal is most likely due to step noise with some contributions coming from ambiguity noise that eludes the Dantec counter logic. Assuming that the noise and the velocity being measured are statistically independent of each other, the measured signal will correspond to the sum of the true signal and the white noise component. This assumption is useful since it makes the recovery of the true signal possible from the contaminated measured signal.

Before addressing the techniques available for the recovery of the true signal, it is useful to have an impression of how the magnitude of the noise spectrum compares with other measured spectra. This is given in Figure B.2 which gives typical measured spectra on the jet centerline (large jet,

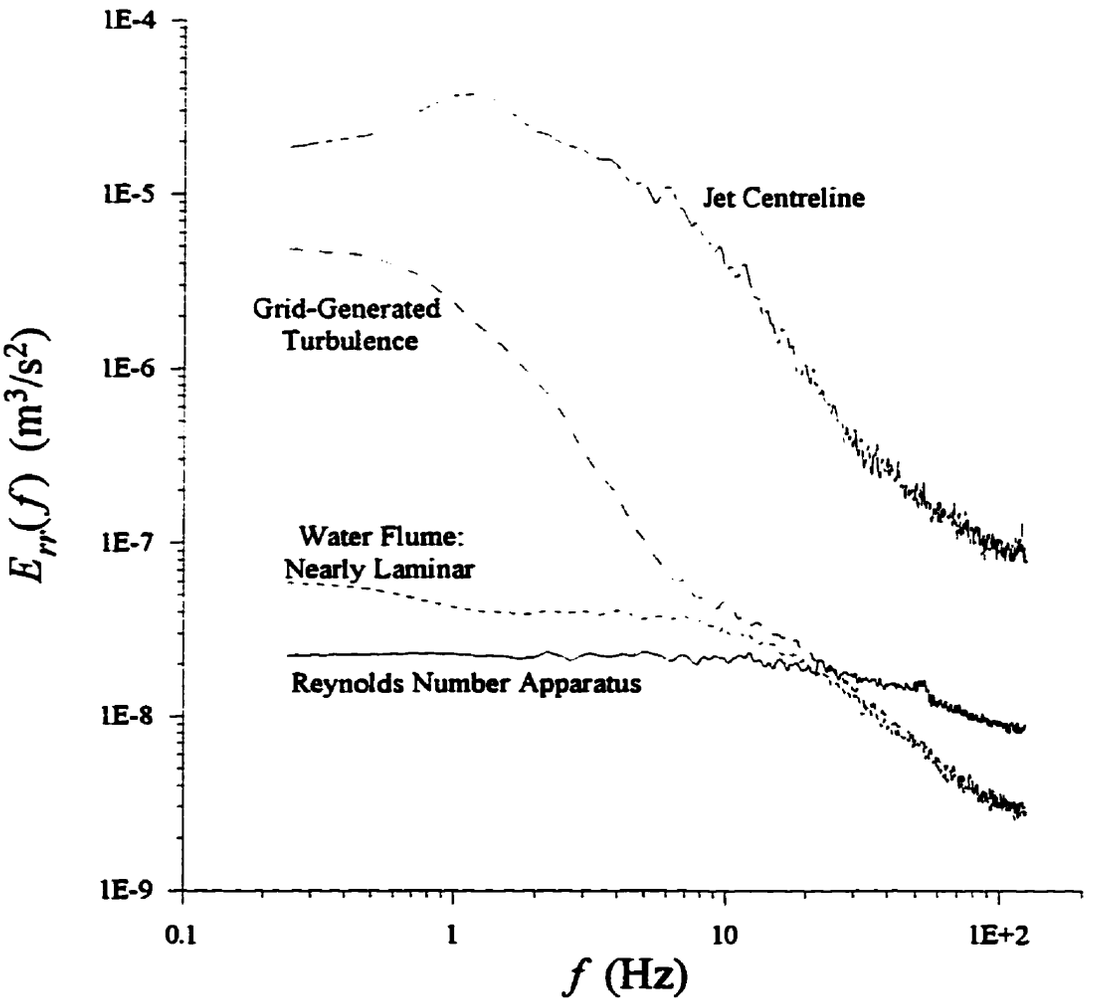

Figure B.2: Measured spectra in the external flow with and without a grid installed, on the jet centerline, and in a known laminar flow.

$VR \approx 3$, no grid, and at x=40.2 cm), in the external flow with the small grid installed (x_g=70 cm), in the low turbulence external flow with no grid installed, and for comparison purposes, the noise spectrum measured in the Reynolds number apparatus ($Re \approx 800$). Note that the spectrum for the low turbulence external flow, although displaying a slight shoulder in the turbulent energy content for $f<1$, is similar to the noise spectrum but with more turbulent energy at the low frequencies and a sharper roll off in energy at the higher frequencies. This implies that, for the external flow with no grid installed, most of the spectrum is swamped by white noise with only the portion of the spectrum with $f<1$ being part of the true signal. For the external flow with a grid installed, it is fairly easy to identify that at $f \approx 10$ the noise spectrum starts to swamp the true spectrum. The spectrum on the jet centerline, due to its large turbulent energy content at all frequencies, is little affected by the noise spectrum.

B.3 Recovery of the True Signal

One simple technique for recovering the true spectrum from the measured spectrum is to subtract the noise spectrum from the measured spectrum (Djenidi and Antonia, 1995, and George and Lumley, 1973). This technique, however, requires that the noise spectrum be known before hand and is of limited use since it only corrects the turbulent energy spectrum and leaves all the other statistics contaminated with the noise.

Another method of recovering not only the true energy spectrum, but also all other statistics, is to low pass filter the data using a Savitsky-Golay or least-squares filter (Press *et al*, 1986). The premise upon which the 'smoothing' effect of low pass filtering is based is that the underlying variable is slowing varying and corrupted by noise. The assumption of a slowly varying time series is not unrealistic in the present case since those flows that are contaminated most with noise have the least amount of turbulent energy and thus less fluctuation in the time series. Each data point in the time series can then be replaced by a local average of the surrounding data points. Since nearby points in the time series will measure very nearly the same underlying value, averaging can

reduce the level of noise without biasing the value obtained (Press *et al*, 1986).

The filter starts in the time domain using the measured times series data. The idea is to approximate the true underlying signal over a moving window by a polynomial of order n (typically a quadratic or quartic polynomial). The window of data points is specified by $nl+nr+1$ where nl and nr are the number of data points used to the left and to the right of the current point. The resulting least-square fit polynomial is valid for the current data point only. For the next data point, the window is shifted to the right by one and a whole new least-square fit polynomial is determined.

From a computer coding point of view, a subroutine is used to calculate the filter coefficients based on the desired polynomial (order, n, and number of points to be used, $nl+nr+1$) which are used to determine the cut off frequency of the filter. A fast Fourier transform (FFT) is performed on the time series and on the coefficient matrix and the results are convoluted in frequency domain. The final product of the convolution undergoes an inverse FFT back into the time domain. This produces a filtered time series which can be processed to obtain the desired statistical quantities. A more detailed discussion of the Savitzky-Golay filter is given in Press *et al* (1986).

As an example of the filtering process, the spectrum for grid-generated turbulence, given in Figure B.2, is passed through a Savitzky-Golay filter with n=4 and nl=nr=28. The result is given in Figure B.3 which clearly shows that the shoulder in the measured spectrum resulting from white noise contamination is removed in the filtered spectrum.

Although the results of the filtering process are encouraging for the coflowing jet and for grid-generated turbulence, it is less so for the external flow with no grid installed. The main reason for this is that little of the true spectrum is present above the white noise spectrum, thus making it difficult to correctly fit a polynomial to the underlying trend in the data. For this reason, only the mean velocity and turbulent velocities are reported for the external flow with no grid installed since the spectra and autocorrelation functions cannot be accurately restored.

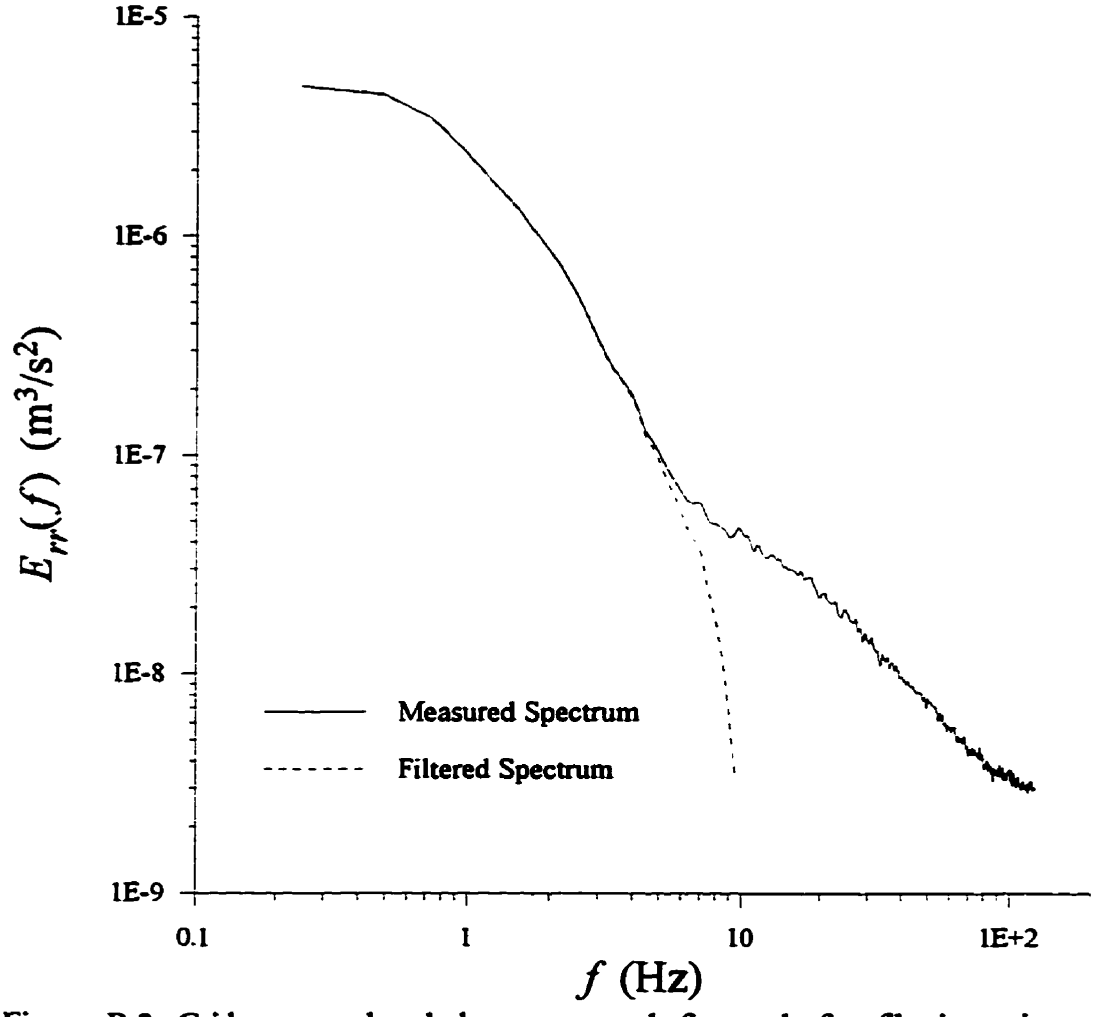

Figure B.3: Grid-generated turbulence spectra before and after filtering using a Savitzky-Golay filter.

Appendix C: Uncertainty Analysis

C.1 Introduction

This appendix addresses the issue of uncertainty contained within the measured experimental variables and how this uncertainty is propagated into the reported results. The appendix will begin with a brief definition of the types of uncertainty encountered. This will be followed by an estimation of the uncertainties in the mean and turbulent velocities and the power spectral density (PSD) functions as measured using the LDA. After this, equations to estimate the uncertainty in the reported results will be given which are based on the data reduction equations and absolute sensitivity coefficients.

All measurements of a variable contain a certain amount of inaccuracies or errors. Error can be defined as the difference between the true value of the variable and the value recorded for a given measurement and, thus, is a fixed number. Uncertainty, on the other hand, gives a possible range of values that the error may have for a given measurement based on a given confidence interval.

Uncertainty in measurements are due to two fundamental types of errors. The first type are random

or precision errors, S, which show up in a measurement as scatter about the average value and are usually caused by the characteristics of the measuring system in combination with changes in the quantity being measured. Precision errors can be determined using statistical methods. The second type of errors are fixed or bias errors, B, and show up in measurements as a displacement between the average measured value and the average true value. Bias errors are considered to remain constant for a given experiment and must be estimated since no simple statistical methods exist to define them. (A more detailed discussion on errors can be found in Coleman and Steele, 1989.)

Each measured variable can have many different sources of precision and bias errors. Each type of error is combined using the root-sum-square (RSS) method which is given by:

$$S = \left(\sum_{i=1}^{n} S_i^2 \right)^{1/2} \tag{C.1}$$

for precision errors and by:

$$B = \left(\sum_{i=1}^{n} B_i^2 \right)^{1/2} \tag{C.2}$$

for bias errors. The total combined uncertainty, δ, is given by:

$$\delta_{RSS} = \left(B^2 + (tS)^2 \right)^{1/2} \tag{C.3}$$

where the Student t value is a function of the degrees of freedom used in calculating S. For a 95% confidence interval and for sample sizes greater than thirty, t is set equal to 2.

C.2 Uncertainty Analysis of the LDA Measurements

C.2.1 Mean and Turbulent Velocities

Precision errors in the LDA velocity measurements arise primarily due to data processing errors and can be determined using standard statistical techniques. Bias errors, however, are predominantly the result of seeding effects on the flow, the specific geometry of the laser beams with respect to the flow and with respect to each other, and electronic effects that can be associated with the configuration of the counter processors. The bias error analysis on the LDA data will follow that of Van Heyst (1992), Weckman (1987), and Patrick (1985).

C.2.1.1 Precision Errors

The uncertainty resulting from precision errors in the LDA velocity measurements are estimated using the methods outlined in Castro (1989). The relative precision error in the mean velocity, S_U / U, is determined from:

$$\frac{S_U}{U} = \frac{z_{\alpha/2}}{\sqrt{N}} \frac{\left(\overline{u^2}\right)^{1/2}}{U} \tag{C.4}$$

where U is the mean velocity, $(\overline{u^2})^{1/2}$ is the turbulent velocity, N is the number of samples which comprise the sum ($N = 40960$), and $z_{\alpha/2}$ is the standard normal variate for a (100 - α) percent confidence interval which, for a 95% confidence interval, has a value of $z_{\alpha/2} = 1.96$. The relative precision error for the mean velocity thus ranges in value between $0.0001 \le S_U / U \le 0.0020$ since it is dependent on the magnitude of the turbulent velocity.

The relative precision error for the turbulent velocity, $S_{rms} / (\overline{u^2})^{1/2}$, is calculated by:

$$\frac{S_{rms}}{\left(\overline{u^2}\right)^{1/2}} = \frac{z_{\alpha/2}}{\sqrt{2N}} \qquad \text{(C.5)}$$

This yields a constant value of $S_{rms}/(\overline{u^2})^{1/2} = 0.0068$.

C.2.1.2 Bias Errors

To estimate the bias errors, typical values of the optical configuration parameters and counter parameters are required. Nominal values and tolerances for the LDA optical configuration parameters are given in Table C.1 with the LDA counter parameters given in Table C.2. These values are considered representative of the range of values covered in the experiments.

Parameter	Green Beam (Vertical)		Blue Beam (Horizontal)	
	Nominal	Tolerance	Nominal	Tolerance
Laser Wavelength (nm)	514.5	±13	488	±12
Beam Separation (mm)	72	±0.7	72	±0.7
Focal Length (mm)	600	±6	600	±6
C.V. Position, $\Delta x=\Delta y=\Delta z$ (mm)		±0.1		±0.1
Intersection Angle (degrees)	7.0	±0.10	7.0	±0.10
Shift Frequency (kHz)	60	0.6	60	0.6
Calibration Factor (m/s/MHZ)	4.21	±0.16	4.03	±0.15

Table C.1: LDA optical configuration parameters.

Parameters	Typical Value
Number of fringes, m	8
High pass filter setting, f_L (kHz)	4
Low pass filter setting, f_U (kHz)	256
Signal-to-noise ratio, SNR	10
Doppler frequency, f_D - green beam (kHz)	96
Doppler frequency, f_D - blue beam (kHz)	97
Mean velocity, U (m/s)	0.150
Turbulent velocity, $(\overline{u'^2})^{1/2}$ and $(\overline{v_r'^2})^{1/2}$ (m/s)	0.015

Table C.2: Typical LDA counter processor parameters.

C.2.1.2.a Seeding Errors

Seeding effects can result in bias errors being introduced into the LDA velocity measurements due to flow distortion errors, seed particle lag errors, and individual realization errors.

Flow distortion errors are typically caused by artificial seeding of a flow field where the injection velocity of the seed particles is different than that of the mean velocity in the flow field. In the water flume facility, artificial seeding is unnecessary since the natural hydrosol present in the water provides ample seed particles. Errors due to flow distortion are therefore negligible.

Seed particle lag errors are the result of the inability of a seed particle to accurately follow the flow field. This typically occurs when the seed particle density is much greater than the fluid density, when the flow is highly turbulent, or when large velocity gradients are present in the flow. Patrick (1985), however, states that in most liquid flows the seed particles will track the flow with minimum lag. Since water is used as the working medium in all the experiments, the seed particle bias error is assumed negligible.

Individual realization errors arise from the fact that proportionately more fast seed particles than slow seed particles are counted in a uniformly seeded flow when an arrival time sampling method is used (Patrick, 1985). This causes the average velocity to be biased towards the high side. However, when a regular time sampling technique is used with a sampling frequency set much smaller than the validation rate, the individual bias error can be assumed to be negligible since there is an equal probability of detecting a fast moving seed particle as there is of a slow moving particle (Weckman, 1987). For this reason, the configuration of the LDA counters was set to a regular time sampling technique with the sampling frequency never exceeding one half of the validation frequency.

The relative bias errors associated with seeding effects are summarized in Table C.3.

Type of Bias	Magnitude	
	Mean Velocity	Turbulent Velocity
Flow distortion bias	negligible	negligible
Seed particle lag	negligible	negligible
Individual realization bias	negligible	n.a.
RSS Total	negligible	negligible

Table C.3: Summary of bias errors due to seeding effects.

C.2.1.2.b Bias Errors due to the LDA Geometry

Bias errors arising from the specific geometry of the intersecting laser beams with respect to each other and with respect to the flow can be categorized as (Patrick, 1985, and Weckman, 1987):

a) finite probe volume errors

b) positioning bias (both location bias and orientation bias)

c) fringe spacing uncertainty

d) nonparallel fringe errors (velocity broadening)

e) negative velocity bias

f) incomplete signal bias

Finite probe volume errors arise since the velocities are measured over a finite control volume diameter. If significant velocity gradients exist within the control volume, errors will result in the measured value. These errors, however, are minimized by utilizing a beam expander in conjunction with the LDA optics to minimize the diameter of the probe volume. The resulting probe diameter is approximately 0.25 mm and is a fraction of the integral length scales encountered in the flow fields (see Chapters 4 and 5). Finite probe volume errors are thus considered negligible.

The position bias can be divided up into a location bias and an orientation bias for both the mean and the turbulent velocities. The location bias is estimated by (Patrick, 1985):

$$\frac{B_{LB}^{U}}{U} = \pm \frac{\partial U_i}{\partial x_j} \Delta x_j \qquad \text{(C.6)}$$

for the mean velocity and by:

$$\frac{B_{LB}^{rms}}{\left(\overline{u^2}\right)^{1/2}} = \pm \frac{\partial \left(\overline{u^2}\right)^{1/2}}{\partial x_j} \Delta x_j \qquad \text{(C.7)}$$

for the turbulent velocities where U_i is the primary velocity component being measured, $(\overline{u^2})^{1/2}$ is the turbulent velocity and Δx_j is the position in the x_j direction. Maximum values for the location bias are obtained in the jet flow as it merges with the external flow. For a typical velocity profile in the jet, the normalized location biases are estimated at $B_{LB}^{U}/U \approx \pm 0.0010$ and $B_{LB}^{rms}/(\overline{u^2})^{1/2} \approx \pm 0.0005$. The orientation bias is considered negligible since the control volume was carefully aligned with the mean flow direction (Weckman, 1987).

The fringe spacing uncertainty is a result of either a variation in the fringe spacing or by nonparallel fringes (frequency broadening) within the control volume. The variation in the fringe spacing is governed by the intersection angle and the wavelength of the laser beams and can be estimated by (Patrick, 1985):

$$\frac{B_{FS}^{U}}{U} = \frac{B_{FS}^{rms}}{\left(\overline{u^2}\right)^{1/2}} = \pm \frac{\left|\Delta \frac{\theta}{2}\right|}{\sin\left(\frac{\theta}{2}\right)} \qquad \text{(C.8)}$$

for both the mean and turbulent velocities where $\theta/2$ is half of the intersection angle of the two incident laser beams and $\Delta\theta/2$ is the tolerance associated with the half angle. From the experimental parameters, the normalized fringe spacing bias is ± 0.0143 for both velocities.

For the fringes to be parallel, the laser beams must intersect at their respective waists. During alignment of the optics, the location of the beam waists were found and adjusted so that they coincided with the point of intersection. This ensured that the fringes would be parallel in the control volume. In addition, no large gradients in the index of refraction were present since all the experiments were isothermal. The bias error caused by nonparallel fringes is therefore assumed to be negligible.

In highly turbulent flows with near zero means or flows with recirculation, it is possible to get negative velocities which can be reflected about the origin thus making them look positive. This introduces a negative velocity bias into the average velocity. Using frequency shifting, where the zero velocity is shifted away from the zero frequency, eliminates negative velocity errors. Since frequency shifting was used in all the experiments, the negative velocity bias is negligible.

Incomplete velocity bias results when a seed particle passes through the control volume at an angle other than perpendicular to the fringe orientation. Depending on the incident angle of the particle, the number of fringes in the control volume, the minimum number of fringes needed to produce a

valid signal, and the ratio of the fringe velocity to the particle velocity, the seed particle may not be able to cross enough fringes for the counter processor to validate it as a genuine velocity sample. For the current parameters, the probability of detecting a particle with an incident angle of 30° from the normal of the fringe orientation is better than 99.9% (Van Heyst, 1992, and Patrick, 1985). The incomplete velocity bias errors are therefore considered negligible.

A summary of the bias errors associated with the specific geometry is given in Table C.4.

Type of Bias	Magnitude	
	Mean Velocity	Turbulent Velocity
Finite probe volume bias	negligible	negligible
Location bias	±0.0010	±0.0005
Orientation bias	negligible	negligible
Fringe spacing uncertainty	±0.0143	±0.0143
Nonparallel fringe bias	negligible	negligible
Negative velocity bias	negligible	n.a.
Incomplete signal bias	negligible	negligible
RSS Total	±0.0143	±0.0143

Table C.4: Summary of bias errors due to the specific geometry of the laser beams.

C.2.1.2.c Bias Errors due to the Counter Processors

Bias errors associated with the electronic counter processors, used to convert the voltage signal from the photomultiplier into a velocity, can be categorized as:

a) clock synchronization errors

b) quantizing errors

c) threshold limit errors

d) electronic noise induced errors

e) filter setting errors

Clock synchronization errors are the result of a mismatch between the randomly occurring Doppler bursts and the start of the clock cycle. Estimations of the normalized clock synchronization errors for the mean and turbulent velocities can be made from (Patrick, 1985):

$$\frac{B_{CS}^{U}}{U} = +\frac{f_D}{2mf_c}\left(1 + \frac{\overline{u^2}}{U^2}\right) \quad (C.9)$$
$$-0$$

and

$$\frac{B_{CS}^{rms}}{\left(\overline{u^2}\right)^{1/2}} = +\frac{f_D}{2mf_c}\left(1 - \frac{\overline{u^2}}{U^2}\right) \quad (C.10)$$
$$-0$$

respectively where f_D is the Doppler frequency, f_c is the reference clock frequency (500 MHZ), and m is the number of fringes required by the processor for a valid signal. For a typical flow situation, the normalized clock synchronization errors are therefore estimated at +0.000012 for both the mean and the turbulent velocities.

Quantizing errors arise from the determination of the frequency of the analog Doppler signal using a digital reference clock. The quantizing errors resulting from the current configuration and counters are extremely small (on the order of 10^{-10}; Van Heyst, 1992) and are thus considered negligible.

Threshold limit errors are the result of using non-zero volt Schmitt triggers to digitize the Doppler burst. The normalized threshold limit errors can be estimated by (Patrick, 1985):

$$\frac{B_{TL}^{U}}{U} = +\frac{1}{12m} + \frac{1}{96m^2} \quad (C.11)$$
$$-0$$

for the mean velocity and by:

$$\frac{B_{TL}^{rms}}{\left(\overline{u^2}\right)^{1/2}} = +0 \qquad -\frac{1}{576\,m^2} \tag{C.12}$$

for the turbulent velocity. Based on $m = 8$, the normalized threshold limit biases are +0.0106 and −0.00003 for the mean and turbulent velocities respectively.

Electronic noise induced errors occur at low signal-to-noise ratios (SNR) where the electronic noise can be mixed with the Doppler signal to cause significant LDA bias errors. The error mechanism involved in electronic induced errors is still under investigation (Patrick, 1985) but can be estimated by:

$$\log\left(\frac{B_{EN}^{U}}{U}\right) = 3.126\log\left(\frac{23.32}{SNR}\sqrt{\frac{f_U + f_L}{2f_D}}\right) - 4.0 \tag{C.13}$$

for the mean velocity component and by:

$$\log\left(\frac{B_{EN}^{rms}}{\left(\overline{u^2}\right)^{1/2}}\right) = 5.67\log\left(\frac{16.56}{SNR}\sqrt{\frac{f_U + f_L}{2f_D}}\right) - 5.0 \tag{C.14}$$

for the turbulent velocity component where f_U and f_L are the upper and lower cutoff frequencies. Based on the counter parameters the electronic noise induced errors are ±0.00227 for the mean velocity and ±0.00041 for the turbulent velocity.

Filter errors are caused by the improper setting of the cutoff frequency of the high pass pedestal removal filter. If the filter is set too high, the Doppler burst caused by a slow particle will be distorted by the filter or even dropped out causing a high biased velocity estimate. If the filter is set too low,

some of the bursts from the faster particles will pass through the filter with residual pedestals which again causes the velocity to be biased (Patrick, 1985). However, with proper filter settings, the filter error is negligible.

Table C.5 summarizes the results for the bias errors due to the counter processors.

Type of Bias	Magnitude	
	Mean Velocity	Turbulent Velocity
Clock synchronization error	+0.000012	+0.000012
Quantizing error	negligible	negligible
Threshold limit error	+0.0106	-0.00003
Electronic noise induced error	±0.00227	±0.00041
Filter error	negligible	negligible
RSS Total	+0.0108 -0.0023	±0.0004

Table C.5: Summary of bias errors due to the counter processors.

C.2.1.3 Total Normalized Velocity Bias Errors

A summary of the bias errors from the three different sources is given in Table C.6. The major source of bias error is that due to the LDA specific geometry which, in turn, is predominantly caused by the uncertainty in the fringe spacing.

Source of Bias	Magnitude	
	Mean Velocity	Turbulent Velocity
Seeding effects	negligible	negligible
LDA specific geometry	±0.0143	±0.0143
Counter processors	+0.0108 -0.0023	±0.0004
RSS Total	+0.0179 -0.0145	±0.0143

Table C.6: Normalized bias errors in the mean and turbulent velocities.

C.2.2 PSD Functions

The uncertainty in the power spectral density (PSD) function, $E(f)$, is estimated based on techniques outlined in Bendat and Piersol (1986). The normalized precision error can be determined from:

$$\frac{S_{PSD}}{E(f)} = \frac{1}{\sqrt{n_d}} \tag{C.15}$$

where n_d is the number of distinct subrecords. All the time series from the experiments are analysed using $n_d = 40$ with subrecord sizes of 1024. The estimate of the normalized precision error is thus $S_{PSD}/E(f) = 0.158$ which is quite large for any one PSD function. However, if an average of several PSD functions is taken, the precision error is reduced by (Coleman and Steele, 1989):

$$\bar{S}_{PSD} = \frac{S_{PSD}}{\sqrt{N}} \tag{C.16}$$

where N is the number of PSD functions in the average.

The normalized bias error in the PSD functions can be estimated by:

$$\frac{B_{PSD}}{E(f)} = -\frac{1}{3}\left(\frac{B_e}{B_r}\right)^2 \qquad \text{(C.17)}$$

where B_e is the resolution bandwidth and B_r is the half-power point bandwidth. Weckman (1987) has estimated this to be $B_{PSD}/E(f) \approx 0.02$ based on the power spectral density processing software and using the same number and size of subrecords.

C.2.3 Summary of Uncertainty Analysis for the LDA Measurements

A summary of the uncertainty analysis for the mean and turbulent velocities as well as the power spectral density functions is given in Table C.7. The numbers in the table are fractions of the measured variable and represent the range that the errors may take on based on a 95% confidence interval.

Measured Variable	Precision Error, S	Bias Error, B	Total Error, δ_{RSS}
Mean velocity	±0.0020 (max) ±0.0001 (min)	+0.0179 −0.0145	+0.018 −0.015
Turbulent velocities	±0.0068	±0.0143	±0.020
PSD functions	±0.1580 (single)	±0.0200	±0.317

Table C.7: Summary of the normalized uncertainty for the measured variables (numbers listed are a fraction of the variable).

C.3 Propagation of Errors into Reported Results

For the general case, consider an experimental result, q, which is a function of j variables:

$$q = q(y_1, y_2, \ldots, y_j) \tag{C.18}$$

Equation C.18 represents the data reduction equation used to evaluate q from the measured values of y_j. The propagation of precision errors into q is given by:

$$S_q = \left[\left(\frac{\partial q}{\partial y_1} S_{y_1} \right)^2 + \left(\frac{\partial q}{\partial y_2} S_{y_2} \right)^2 + \ldots + \left(\frac{\partial q}{\partial y_j} S_{y_j} \right)^2 \right]^{1/2} \tag{C.19}$$

The derivation of equation C.19 assumes that the data reduction equation is continuous and that its derivatives are also continuous over the domain of interest, that the measured y_j are independent of each other, and that their associated uncertainty are also mutually independent (Coleman and Steele, 1985). The partial derivatives of q with respect to the variables y_j are defined as the absolute sensitivity coefficients.

Although the above case tracks the propagation of precision errors into q, the same equation can be written for either the bias errors or the total errors by replacing S with B and δ respectively.

The following sections present equations for the propagation of precession error into the reported results. For more detailed information on the propagation of errors, see Coleman and Steels (1989), Moffat (1988), and Kline (1985).

C.3.1 Mean Velocity Results

C.3.1.1 Excess Mean Velocity

The excess mean velocity is defined as the difference between the mean velocity of the jet and that of the external flow. The normalized precision error for the excess mean velocity can be evaluated from:

$$\left(\frac{S_{U-U_e}}{U-U_e}\right)=\left(\frac{1}{U-U_e}\frac{\partial(U-U_e)}{\partial U}S_U\right)^2+\left(\frac{1}{U-U_e}\frac{\partial(U-U_e)}{\partial U_e}S_{U_e}\right)^2 \qquad \text{(C.20)}$$

The partial derivatives become 1 and -1 for differentiation with respect to U and U_e respectively. The equation can therefore be simplified to:

$$\left(\frac{S_{U-U_e}}{U-U_e}\right)^2=\left(\frac{S_U}{U-U_e}\right)^2+\left(\frac{-S_{U_e}}{U-U_e}\right)^2 \qquad \text{(C.21)}$$

C.3.1.2 Ratio of External Mean Velocity to Centerline Excess Mean Velocity

The normalized precision error for U_e/U_o can be estimated from:

$$\left(\frac{S_{U_e/U_o}}{U_e/U_o}\right)^2=\left(\frac{U_o}{U_e}\frac{\partial(U_e/U_o)}{\partial U_e}S_{U_e}\right)^2+\left(\frac{U_o}{U_e}\frac{\partial(U_e/U_o)}{\partial U_o}S_{U_o}\right)^2 \qquad \text{(C.22)}$$

which can be simplified to:

$$\left(\frac{S_{U_e/U_o}}{U_e/U_o}\right)^2=\left(\frac{S_{U_e}}{U_e}\right)^2+\left(\frac{-S_{U_o}}{U_o}\right)^2 \qquad \text{(C.23)}$$

where the centerline excess mean velocity precision error can be calculated from equation C.21.

C.3.1.3 Jet Velocity Half Width and Jet Radius

Both the jet velocity half width, L_o, and the jet radius, R, are defined by a radial location based on some value of $(U-U_e)/U_o$. The percent uncertainty in locating L_o and R is therefore that of the mean velocity ratio which can be determined from:

$$\left(\frac{S_{(U-U_e)/U_o}}{(U-U_e)/U_o}\right)^2 = \left(\frac{S_{U-U_e}}{U-U_e}\right)^2 + \left(\frac{-S_{U_o}}{U_o}\right)^2 \qquad \text{(C.24)}$$

where the two terms on the right hand side can be evaluated using equation C.21.

C.3.1.4 Momentum Radius

For the purposes of an uncertainty analysis, the momentum radius can be approximated as:

$$\theta \approx \frac{R}{U_e}\left(\overline{U}^2 - \overline{U}\,U_e\right)^{1/2} \qquad \text{(C.25)}$$

where $\overline{U}$ is the average or top-hat velocity in the jet. Using this equation, the propagation of precision errors into the momentum radius can be determined from:

$$\left(\frac{S_\theta}{\theta}\right)^2 = \left(\frac{S_R}{R}\right)^2 + \left(\frac{2\overline{U}-U_e}{2\left(\overline{U}-U_e\right)}\right)^2\left[\left(\frac{S_{\overline{U}}}{\overline{U}}\right)^2 + \left(\frac{S_{U_e}}{U_e}\right)^2\right] \qquad \text{(C.26)}$$

The precision error for the average velocity can be calculated from $S_{\overline{U}} = S_U / N^{1/2}$ where N is the number of points averaged to get $\overline{U}$.

C.3.2 Turbulent Velocity Results

C.3.2.1 Local Turbulent Intensities

The local turbulent intensity is defined as the turbulent velocity normalized by the jet excess centerline velocity. For convenience of notation, let $I_x=(\overline{u^2})^{1/2}/U_o$. The normalized precision error in the streamwise local turbulent intensity is given by:

$$\left(\frac{S_{I_x}}{I_x}\right)^2=\left(\frac{S_{(\overline{u^2})^{1/2}}}{(\overline{u^2})^{1/2}}\right)^2+\left(\frac{S_{U_o}}{U_o}\right)^2 \qquad \text{(C.27)}$$

A similar equation can be written for the radial local turbulent intensity where $I_r=(\overline{v_r^2})^{1/2}/U_o$.

The turbulent velocities can also be normalized by the velocity scale $(U_o(U_o+U_e))^{1/2}$ to obtain another local turbulent intensity. Again, for convenience, let $I_x^*=(\overline{u^2})^{1/2}/(U_o(U_o+U_e))^{1/2}$. The normalized precision error in the streamwise direction is given by:

$$\left(\frac{S_{I_x}^*}{I_x^*}\right)^2=\left(\frac{S_{(\overline{u^2})^{1/2}}}{(\overline{u^2})^{1/2}}\right)^2+\left(\frac{2U_o+U_e}{2U_o}\frac{S_{U_{cl}}}{U_{cl}}\right)^2+\left(\frac{S_{U_e}}{2U_o}\right)^2 \qquad \text{(C.28)}$$

where U_{cl} is the centerline mean velocity. A similar equation can be written for the radial local turbulent intensity where $I_r^*=(\overline{v_r^2})^{1/2}/(U_o(U_o+U_e))^{1/2}$.

C.3.2.2 Local Normalized Reynolds Stress

The local normalized Reynolds stress is given as the Reynolds stress term normalized by the square of the centerline velocity. For convenience, let $I^2=\overline{u\,v_r}/U_o^2$. The propagation of precision error can then be determined from:

$$\left(\frac{S_{I^2}}{I^2}\right)^2 = \left(2\frac{S_{(\overline{uv_r})^{1/2}}}{(\overline{uv_r})^{1/2}}\right)^2 + \left(2\frac{S_{U_o}}{U_o}\right)^2 \qquad \text{(C.29)}$$

where the precision error for $(\overline{u\,v_r})^{1/2}$ has the same value as that for the turbulent velocities.

As with the turbulent velocities, the Reynolds stress term can also be normalized using the velocity scale $(U_o(U_o+U_e))^{1/2}$. Again for convenience, let $I^{*2}=\overline{u\,v_r}/(U_o(U_o+U_e))$. The precision error propagation can then be evaluated using:

$$\left(\frac{S_{I^{*2}}}{I^{*2}}\right)^2 = \left(2\frac{S_{(\overline{uv_r})^{1/2}}}{(\overline{uv_r})^{1/2}}\right) + \left(\frac{2U_o+U_e}{U_o}\frac{S_{U_d}}{U_{cl}}\right)^2 + \left(\frac{S_{U_e}}{U_o}\right)^2 \qquad \text{(C.30)}$$

C.3.3 Integral Length Scale Results

C.3.3.1 Autocorrelation Functions

The autocorrelation function in the streamwise direction is given by:

$$R_{xx} = \frac{\overline{u(x;t)\,u(x;t+\Delta t)}}{\overline{u^2}} \qquad \text{(C.31)}$$

For the purposes of an uncertainty analysis, equation C.31 will have the same level of uncertainty as:

$$R_{xx} \sim \frac{(\overline{u_1^2})^{1/2}(\overline{u_2^2})^{1/2}}{\overline{u^2}} \qquad \text{(C.32)}$$

The propagation of precision error can therefore be estimated from:

$$\left(\frac{S_{R_{xx}}}{R_{xx}}\right)^2 = 6\left(\frac{S_{(\overline{u^2})^{1/2}}}{(\overline{u^2})^{1/2}}\right)^2 \qquad \text{(C.33)}$$

A similar equation can be derived for the autocorrelation in the radial direction, R_{rr}.

C.3.3.2 Integral Length Scales

The streamwise integral length scale is estimated from:

$$\begin{aligned} L_{xx} &= U\int_0^{\infty} R_{xx}(\tau)\,d\tau \\ &\approx U\frac{\Delta\tau}{2}\left(R_{xx}(0) + R_{xx}(n) + 2\sum_{i=1}^{n-1} R_{xx}(i)\right) \end{aligned} \qquad \text{(C.34)}$$

where the approximate equation is that arrived at using a trapezoidal rule for numerical integration. For the purposes of an error analysis, the term in brackets can be approximated as $2R_{xx}n$. The propagation of precision errors can then be determined from:

$$\left(\frac{S_{L_{xx}}}{L_{xx}}\right)^2 = \left(\frac{S_{R_{xx}}}{R_{xx}}\right)^2 + \left(\frac{S_U}{U}\right)^2 \qquad \text{(C.35)}$$

A similar equation can be derived for the integral length scales in the radial direction, L_{rr}.